Spring 2013

An overset grid method coupling an orthogonal curvilinear grid solver and a Cartesian grid solver

Akira Hanaoka
University of Iowa

AN OVERSET GRID METHOD COUPLING AN ORTHOGONAL CURVILINEAR GRID SOLVER AND A CARTESIAN GRID SOLVER

by

Akira Hanaoka

An Abstract

Of a thesis submitted in partial fulfillment of the
requirements for the Doctor of Philosophy degree
in Mechanical Engineering in
the Graduate College of
The University of Iowa

May 2013

Thesis Supervisor: Professor Frederick Stern

The objective of the current study is development of a coupled orthogonal curvilinear/Cartesian grid solver. The solver requires a thin orthogonal boundary layer grid and a non-uniform Cartesian grid to resolve the boundary layer on a solid surface and the flow region away from the surface, respectively. Flows inside the orthogonal boundary layer and Cartesian background grids are solved by different CFD solvers which are coupled by an overset grid method. SUGGAR code writes the grid domain connectivity information into a file that identifies grid points necessary for the overset grid interpolation. In order to satisfy mass conservation across the overlapping region, the pressure Poisson equations and the overset interpolation equations are encompassed from both of the solvers and solved simultaneously by an iterative method.

Accuracy of the coupled orthogonal curvilinear/Cartesian grid solver was evaluated in terms of flows past circular cylinders because the orthogonal boundary layer grids can be generated easily due to its simple cylindrical shape. In this study, additional numerical simulations were also performed by the original orthogonal curvilinear and Cartesian grid solvers in order to obtain the benchmark data to compare with the results of the coupled orthogonal curvilinear/Cartesian grid solver.

The coupled orthogonal curvilinear/Cartesian grid solver was applied to steady and unsteady laminar flows at Re = 40 and 200, single-phase turbulent flows at subcritical Re = 3900 and supercritical Re = 5×10^5 and 1×10^6, and two-phase flows at (Re, Fr) = (2.7×10^4, 0.20), (2.7×10^4, 0.80), and (4.58×10^5, 1.64). Those numerical results are in good agreement with the experimental and numerical results in the literature.

Effects of the grid resolution on the numerical results were analyzed in this study. The analysis showed the more accurate resolution of near-wall regions by the boundary layer grids for the coupled orthogonal curvilinear/Cartesian grid solver. It also presented the similar trends of the flow at the subcritical Re with the vertical resolution to those observed in the literature.

The coupled orthogonal curvilinear/Cartesian grid solver predicted much delayed separations of the boundary layers at both the supercritical Re, which caused the narrower wakes and the shorter recirculation regions than those at the subcritical Re. The features of surface pressure corresponded to the postponed separations.

The solver developed in this study showed the similar trends in the two-phase flows at Fr = 0.20 and 0.80 to those observed by the past numerical studies. The trends of the vortex shedding, deviating shear layers, and the expanded wake on the free surface are more prominent in the flow at Fr = 0.80 than that at Fr = 0.20.

The mean flow on the free surface at Fr = 1.64 shows the high magnitudes of the streamwise vorticity and the transverse velocity, which are responsible for the attenuation of periodic vortex shedding. The difference of the gradients of two Reynolds shear stresses and the streamwise vortex stretching are the main mechanism for generation of the mean streamwise vorticity on the free surface. In addition, the source terms due to the strong streamwise vorticity mainly generate both transverse and vertical vortices on the free surface.

Abstract Approved: _____

Thesis Supervisor

_____

Title and Department

_____

Date

AN OVERSET GRID METHOD COUPLING AN ORTHOGONAL CURVILINEAR GRID SOLVER AND A CARTESIAN GRID SOLVER

by

Akira Hanaoka

A thesis submitted in partial fulfillment of the
requirements for the Doctor of Philosophy degree
in Mechanical Engineering in
the Graduate College of
The University of Iowa

May 2013

Thesis Supervisor: Professor Frederick Stern

Graduate College
The University of Iowa
Iowa City, Iowa

CERTIFICATE OF APPROVAL

PH.D. THESIS

This is to certify that the Ph. D. thesis of

Akira Hanaoka

had been approved by the Examining Committee for the thesis requirement for the Doctor of Philosophy degree in Mechanical Engineering at the May 2013 graduation.

Thesis Committee:

Frederick Stern, Thesis Supervisor

Jianming Yang

George Constantinescu

James Buchholz

Pablo M. Carrica

To my parents, Nobuaki Hanaoka and Terue Hanaoka

ACKNOWLEDGMENTS

I would like to express the deepest appreciation to my advisor, Professor Frederick Stern, who had supported me throughout my thesis with his patience and knowledge. I would also like to give my thanks to my collaborators, Dr. Shanti Bhushan and Dr. Jianming Yang. This thesis would not have been possible without their guidance, support, and constructive discussion. I would also like to convey my sincere gratitude to my advisory committee members, Professor George Constantinescu, James Buchholz, and Pablo Carrica.

I would like to express my appreciation to Dr. Yusuke Tahara in NMRI (National Maritime Research Institute) who used to be my advisor at Osaka Prefecture University and inspired me to study in Ph. D. program at the University of Iowa. I am grateful to so many friends and colleagues in IIHR and the University of Iowa for the great time we share in Iowa.

I am indebted to my parents, Nobuaki Hanaoka and Terue Hanaoka, for their encouragement and support especially for the life in the United States of America.

This work is sponsored by the US Office of Naval Research through research grant N000141-01-00-1-7 under the administration of Dr. Patrick Purtell. The numerical simulations were performed using DoD HPC resources.

TABLE OF CONTENTS

LIST OF TABLES

LIST OF FIGURES

CHAPTER 1

INTRODUCTION

1.1 Background and Motivation

Computational fluid dynamics (CFD) solvers with high fidelity are required to perform accurate simulations of turbulent flows. Such CFD solvers should include high-order numerical schemes, accurate turbulence modeling, and good scalability of high performance computing (HPC). Simplicity of generating computational grids is also important for complex geometries such as those observed in ship hydrodynamics. Generation of a body-fitted structured grid around the complex geometry surface is difficult, and mesh quality, namely mesh orthogonality and mesh smoothness, often becomes an issue. Extensive researches made for the quality of the structured grids can be reviewed in Zhang et al. (2006, 2012). On the other hand, unstructured grids show greater flexibility to geometry shapes and are easier to generate around the complex surfaces than the structured grids (Mavriplis, 1997). However, implementation of high-order numerical schemes and accurate turbulence models such as large eddy simulation (LES) is difficult to the unstructured grid solvers (Caraeni and Hill, 2010; Mahesh et al., 2004). CFD solvers using a Cartesian grid with an immersed boundary method (IBM) involve extremely easy grid generation and allow implementation of high-order numerical schemes easily (Mittal and Iaccarino, 2005; Gullbrand et al., 2001). Also, HPC scalability of the Cartesian grid solvers is better than that of the curvilinear structured grid solvers (Bhushan et al., 2011). Because of these features, the Cartesian grid solvers with IBM are well suited for accurate numerical simulations of turbulent flows, such as LES (Gullbrand et al., 2001; Moin, 2002; Balaras, 2004; Ramakrishnan et al., 2009; Yang and Stern, 2009). However, the Cartesian grid solvers require very large grids to adequately resolve boundary layers at high Reynolds numbers. Adaptive local grid refinement near the solid wall can lead to reduction of the grid size (Iaccarino et al.,

2004; Ghias et al., 2007), but still the near-wall grid resolution is very expensive. Moreover, the fine near-wall resolutions require very small time steps to simulate unsteady or developing flows accurately. Thus, it is important for the Cartesian grid solvers to implement a method to resolve the viscous boundary layers around the solid surfaces appropriately.

A wall function (WF) approach (Stern et al., 2009) can be used to capture effects of the boundary layers in the framework of an IBM based Cartesian grid solver. In Bhushan et al. (2011), the simulation was performed for a surface combatant model DTMB 5415 in the straight-ahead condition by using a Cartesian grid solver with the WF method. The numerical results show that the WF method has limitations in accurately predicting the flow separation and the turbulence quantities. This is expected since the WF methods are more suited for body-fitted curvilinear grids in which uniform first grid spacing can be maintained throughout the solid surface.

A coupled curvilinear/Cartesian grid method was proposed by Yang and Stern (2009) as an alternative approach to resolve the boundary layers. In this method, curvilinear structured grids are used to resolve the boundary layers on the solid surfaces and Cartesian grids to compute the flow regions out of the boundary layers. Different CFD solvers are applied to the body-fitted curvilinear grids and the Cartesian background grids. Those solvers can be coupled using the boundary conditions, a hybrid grid method, or an overset grid method.

Coupling multiple CFD solvers by the boundary conditions requires two things (Schlüter et al., 2005b). The first is to define an interface which enables communication and exchange of the flow variables between the solvers. Previous work (Shankaran et al., 2001; Schlüter et al., 2003a; Schlüter et al., 2003b) has established the algorithms which specify the interface and allow information exchange between two or more CFD solvers. The second thing for the coupling is to specify the appropriate boundary conditions used by the solvers at the interface. Schlüter and Pitsch (2005), and Schlüter et al. (2004,

2005a, 2005b) discussed the boundary conditions at the interface to couple an LES flow solver and the Reynolds Averaged Navier Stokes (RANS) flow solver. Schlüter et al. (2005b) validated the developed coupling method for a flow in an axisymmetric expansion and a swirl flow at an expansion with a subsequent contraction and demonstrated its applicability in a turbomachinery case. However, this approach is not appropriate for a coupled curvilinear/Cartesian grid method because it requires the plane interface between the computational domains for each solver.

Zhang and Wang (2004) proposed a hybrid adaptive Cartesian/quad/triangular grid method to solve two-dimensional flows with moving objects. In the hybrid grid method, a body-fitted structured grid is generated first near a solid body to resolve the viscous boundary layer. An adaptive Cartesian grid is then generated to cover the whole computational domain. The Cartesian cells which overlap the body-fitted grid are removed from the computational domain, and the gap is produced between the body-fitted grid and the Cartesian grid. The triangular unstructured grids are used to fill the gap. In the dynamic moving boundary flow problems, the body-fitted grid moves with the moving body, whereas the Cartesian grid remains stationary. Meanwhile, the triangular unstructured grids are deformed according to the motion of the moving body with a spring analogy approach (Batina, 1991). Zhang and Wang (2004) demonstrated the hybrid grid generation approach and the developed time-integration algorithm for a supersonic flow around a cylinder and inviscid flow and turbulent flow over an oscillating NACA0012 airfoil. Zhang et al. (2009) extended the above hybrid grid generation method to morphing bodies for two-dimensional external bio-fluid simulations. Delaunay graph interpolation approach (Liu et al., 2006) was implemented to improve the efficiency of the grid generation and to deal with very large motions. The extended hybrid dynamic grid generation method was validated for several external bio-fluid problems with multiple bodies. However, those hybrid grid approaches were

developed for simulations using finite volume methods. Also, they can be performed only for two-dimensional flows, and the extension to three-dimensional cases is difficult.

In the overset grid methods, there is no need to match grids at the interface of the neighboring grid blocks (Baker, 2005). This lack of any constraint at the grid block interfaces allows both body-fitted curvilinear grids and Cartesian background grids to be constructed easily. Moreover, the overset grid methods do not need to either deform or regenerate the grids to solve the problems even with moving objects. Therefore, good grid quality can be maintained during the entire simulation process. However, there are two issues to implement the overset grid methods: (1) an additional module is required to interpolate information from one grid block boundary to another; (2) the interpolation can violate conservative nature of the governing equations solved in the CFD solvers. Those issues should be resolved to couple the curvilinear grid solver and the Cartesian grid solver using the overset grid interpolation.

The Structured, Unstructured, and Generalized overset Grid AssembleR (SUGGAR) code was developed as an overset grid assembly program by Noack (2005). The SUGGAR code can create a single composite grid from multiple overlapping structured, unstructured, and/or general polyhedral grids for both node-centered and cell-centered flow solvers. It has been incorporated into existing flow solvers, and the solvers with the overset grid capability have been validated for several problems including static or dynamic objects (Pandya et al., 2005; Carrica et al., 2007; Mulvihill and Yang, 2007; Koomullil et al., 2008).

1.2 Objective and Approach

The objective of this study is development of a coupled orthogonal curvilinear/Cartesian grid solver. The solver requires a thin structured boundary layer grid and a non-uniform Cartesian grid to resolve the boundary layer on a solid surface and the flow region away from the surface, respectively. The boundary layer grid is so thin that the grid orthogonality is maintained everywhere inside the grid. The Cartesian

background grid part is solved by a Cartesian grid CFD solver, which is called CFDShip-Iowa version 6 (V6-IBM hereafter) developed on the basis of an immersed boundary method for ship hydrodynamics. Another CFD solver requiring a body-fitted orthogonal curvilinear grid is applied into the boundary layer grid. This solver is named CFDShip-Iowa version 6.2 (V6-OC hereafter) and has been developed from V6-IBM by Suh et al. (2011). Therefore V6-OC has the similar architecture to that of V6-IBM. An overset grid method is used to couple V6-IBM and V6-OC. In the overset grid method, all the flow variables are interpolated from one grid block to another through the interface between the boundary layer grid and the Cartesian background grid. SUGGAR code writes the grid domain connectivity information into a file that identifies grid points necessary for the overset grid interpolation. In order to satisfy mass conservation across the overlapping part, a pressure Poisson equation is solved in a strongly coupled manner using the PETSc toolkit (Balay et al., 2012). In this strongly coupled manner, the pressure Poisson equations and the overset interpolation equations are encompassed from both V6-IBM and V6-OC and solved together by an iterative method. Thus, both mass conservation and overset interpolation relation are satisfied in both of the CFD solvers. The coupled orthogonal curvilinear/Cartesian grid solver developed in this study is named CFDShip-Iowa version 6.2.5 (V6.2.5 hereafter).

After the development of V6.2.5, its accuracy is assessed by considering several different flows. Table 1 summarizes all the numerical simulations performed in this study. Validations of V6.2.5 are carried out in terms of flows past a circular cylinder because orthogonal boundary layer grids can be generated due to its simple geometry shape. In addition, many results about the circular cylinder flows have been obtained experimentally or numerically for decades. Those data are available in the literature in order to validate V6.2.5. In this study, additional simulations using V6-IBM and V6-OC are also performed to obtain benchmark data to validate V6.2.5. The initial validations are performed for steady and unsteady laminar flows at Re = 40 and 200, respectively.

Effects of the grid resolution and the domain size on the steady laminar flow are discussed in terms of the boundary layer grid. The validations of V6.2.5 are also presented for turbulent flows past a circular cylinder. Numerical simulations are performed by V6.2.5 with large eddy simulation turbulence modeling for single-phase flows at Re = 3900, 5×10^5, and 1×10^6, and two-phase flows at Fr = 0.2, 0.8, and 1.64. Those Reynolds numbers and Froude numbers are based on the cylinder diameter, the free stream velocity, and water kinematic viscosity. Those turbulent flows have been chosen for the current validation studies because relatively many detailed benchmark results are available from both experimental measurement and numerical simulations in the literature. This study also analyzes effects of the grid resolution, Re, and the free surface on the turbulent flows.

Outline

Chapter 2 discusses the mathematical models and numerical methods implemented in V6-IBM, V6-OC, and V6.2.5. Chapter 3 shows validation results of V6.2.5 about single-phase flows past a circular cylinder. The flow behavior varied by Re is also overviewed. Chapter 4 presents validation results of V6.2.5 about two-phase flows past a circular cylinder. Chapter 5 shows overall conclusions and future work.

Table 1.1 Summary of numerical simulations

<table>
<tr><th>Geometry</th><th>Fr</th><th>Re</th><th>Solver</th><th>Results</th></tr>
<tr><td rowspan="10">circular cylinder
single-phase flow</td><td rowspan="10">-</td><td rowspan="3">40</td><td>V6-IBM</td><td rowspan="10">• steady recirculation
• unsteady vortex shedding
• comparison with V6-IBM, V6-OC, and experimental and numerical results in the literature
• effects of boundary layer grid resolution and domain size</td></tr>
<tr><td>V6-OC</td></tr>
<tr><td>V6.2.5</td></tr>
<tr><td rowspan="3">200</td><td>V6-IBM</td></tr>
<tr><td>V6-OC</td></tr>
<tr><td>V6.2.5</td></tr>
<tr><td rowspan="3">3900</td><td>V6-IBM</td><td rowspan="5">• LES of turbulent flows
• comparison with V6-IBM, V6-OC, and experimental and numerical results in the literature
• effects of grid resolution
• effects of Re</td></tr>
<tr><td>V6-OC</td></tr>
<tr><td>V6.2.5</td></tr>
<tr><td>5×10^5</td><td rowspan="2">V6.2.5</td></tr>
<tr><td>1×10^6</td></tr>
<tr><td rowspan="3">circular cylinder
two-phase flow</td><td>0.20</td><td rowspan="2">2.70×10^4</td><td rowspan="3">V6.2.5</td><td rowspan="3">• LES of turbulent flows
• computation of free surfaces
• comparison with experimental and numerical results in the literature
• effects of free surfaces</td></tr>
<tr><td>0.80</td></tr>
<tr><td>1.64</td><td>4.58×10^5</td></tr>
</table>

CHAPTER 2

COMPUTATIONAL METHODS

2.1 Cartesian Grid Solver

CFDShip-Iowa version 6 is recently developed as a flow solver based on a combined sharp interface immersed-boundary/level-set Cartesian grid method for the large eddy simulations (LES) of three-dimensional two-phase flows interacting with moving bodies (Yang and Stern, 2009). The second-order direct forcing, sharp interface immersed boundary method in Yang and Balaras (2006) is used to treat both stationary and moving bodies. The fluid-fluid interface is captured using a high-order level-set method with third-order TVD (Total Variation Diminishing) Runge-Kutta and fifth-order HJ (Hamilton-Jacobi) WENO (Weighted Essentially Non-Oscillatory) schemes. The ghost-fluid method (Kang et al., 2000; Liu et al., 2000) is adopted to treat jump conditions across the fluid-fluid interfaces, where the density keeps its sharp jump while the viscosity is smoothed over a transition band by the smoothed Heaviside function.

2.1.1 Mathematical Models

CFDShip-Iowa version 6 solves Navier-Stokes equations in an inertial reference frame, by which incompressible viscous flows of two immiscible fluids, e.g. air and water, are governed:

$$\frac{\partial \boldsymbol{u}}{\partial t} + \boldsymbol{u} \cdot \nabla \boldsymbol{u} = \frac{1}{\rho} \nabla \cdot (-p\boldsymbol{I} + \boldsymbol{T}) + \boldsymbol{g} \tag{2.1}$$

$$\nabla \cdot \boldsymbol{u} = 0 \tag{2.2}$$

where t is the time, $\boldsymbol{u}$ is the velocity vector, p is the pressure, $\boldsymbol{I}$ is the unit diagonal tensor, ρ is the density, $\boldsymbol{g}$ represents the gravity acceleration, and $\boldsymbol{T}$ is the viscous stress tensor defined as

$$\boldsymbol{T} = 2\mu\boldsymbol{S} \tag{2.3}$$

with μ the dynamic viscosity and $\boldsymbol{S}$ the strain rate tensor given by

$$\boldsymbol{S} = \frac{1}{2}[\nabla \boldsymbol{u} + (\nabla \boldsymbol{u})^T] \tag{2.4}$$

where the superscript T represents transpose operation.

Interfaces between two immiscible fluids are defined as the zero level set of a signed distance function, ϕ, or the level-set function. The level-set function is advanced by its evolution equation (Osher and Sethian, 1988):

$$\frac{\partial \phi}{\partial t} + (\boldsymbol{u} \cdot \nabla)\phi = 0 \tag{2.5}$$

The reinitialization equation (Sussman et al., 1994) for the level-set function is iteratively solved to keep ϕ as a signed distance function in the course of its evolution:

$$\frac{\partial \phi}{\partial \tau} + S(\phi_0)(|\nabla \phi| - 1) = 0 \tag{2.6}$$

where τ is the pseudo-time for the iteration and $S(\phi_0)$ is the numerically smeared-out sign function:

$$S(\phi_0) = \frac{\phi_0}{\sqrt{\phi_0^2 + (\Delta h)^2}} \tag{2.7}$$

with ϕ_0 the initial value of ϕ and Δh a small amount, usually the grid cell size, to smear out the sign function.

Each phase of constant density and viscosity can be easily defined by the level-set function in the computational domain, and sharp jumps of the fluid properties occur at the phase interface. For simplicity and efficiency, the density keeps its sharp jump, whereas the viscosity is smoothed over a transition band across the interface in this study:

$$\begin{aligned} \rho &= \rho_G + (\rho_L - \rho_G)H(\phi) \\ \mu &= \mu_G + (\mu_L - \mu_G)H_\varepsilon(\phi) \end{aligned} \tag{2.8}$$

where the subscripts G and L represent gas and liquid phase, respectively. The stepwise Heaviside function is defined as:

$$H(\phi) = \begin{cases} 1 & \text{if} \quad \phi \geq 0 \\ 0 & \text{if} \quad \phi < 0 \end{cases} \tag{2.9}$$

The smoothed Heaviside function (Sussman et al., 1994) is

$$H_\varepsilon(\phi) = \begin{cases} 1 & \text{if} \quad \phi > \varepsilon \\ \frac{1}{2}\left[1 + \frac{\phi}{\varepsilon} + \frac{1}{\pi} sin\left(\frac{\pi\phi}{\varepsilon}\right)\right] & \text{if} \quad |\phi| \le \varepsilon \\ 0 & \text{if} \quad \phi < -\varepsilon \end{cases} \tag{2.10}$$

where ε is the transition band where the viscosity is smoothed. In this study, the level-set function is defined as negative in the air and positive in the water.

Since the fluids considered here are viscous and no phase change occurs, the velocity across the interface is continuous:

$$[\boldsymbol{u}] = 0 \tag{2.11}$$

where $[\cdot]$ indicates the jump at the interface, i.e., $f_L^I - f_G^I$ for a variable f with the superscript I denoting interface.

The exact jump condition for stress is

$$\left[\boldsymbol{n} \cdot \left(-p\boldsymbol{I} + \mu(\nabla\boldsymbol{u} + (\nabla\boldsymbol{u})^T)\right) \cdot \boldsymbol{n}\right] = \sigma\kappa \tag{2.12}$$

where σ is the coefficient of surface tension, $\boldsymbol{n}$ is the unit normal vector to the interface, and κ is the local curvature on the interface. Those geometric properties can be estimated readily from the level-set function:

$$\boldsymbol{n} = \frac{\nabla\phi}{|\nabla\phi|} \tag{2.13}$$

$$\kappa = \nabla \cdot \left(\frac{\nabla\phi}{|\nabla\phi|}\right) \tag{2.14}$$

The gravity term can be removed from Eq. (2.1) by incorporating the gravity into the jump condition as

$$\left[\boldsymbol{n} \cdot \left(-p_d\boldsymbol{I} + \mu(\nabla\boldsymbol{u} + (\nabla\boldsymbol{u})^T)\right) \cdot \boldsymbol{n}\right] = \sigma\kappa + [\rho]\boldsymbol{X} \cdot \boldsymbol{g} \tag{2.15}$$

where p_d represents the dynamic pressure (for simplicity, p is used hereafter), $[\rho]$ is the density jump at the interface, and $\boldsymbol{X}$ is the position vector normal to the reference plane of zero hydrostatic pressure.

With a continuous viscosity and velocity field, the stress jump conditions Eq. (2.12) reduce to

$$[p] = p_L^I - p_G^I = -\sigma\kappa - [\rho]\boldsymbol{X}\cdot\boldsymbol{g} \tag{2.16}$$

In the LES approach adopted into CFDShip-Iowa version 6, the Navier-Stokes equations are spatially filtered such that the large, energy carrying eddies are resolved and the small-scale, dissipative eddies are modeled by a subgrid-scale (SGS) model. The following equations can be obtained after applying the filter operation to Eqs. (2.1) and (2.2):

$$\frac{\partial\overline{\boldsymbol{u}}}{\partial t} + \overline{\boldsymbol{u}}\cdot\nabla\overline{\boldsymbol{u}} = -\frac{1}{\rho}\nabla\bar{p} + \frac{1}{\rho}\nabla\cdot[\mu(\nabla\overline{\boldsymbol{u}} + (\nabla\overline{\boldsymbol{u}})^T)] - \nabla\cdot\bar{\tau} \tag{2.17}$$

$$\nabla\cdot\overline{\boldsymbol{u}} = 0 \tag{2.18}$$

Note that the gravity acceleration is not included in Eq. (2.17) and it is assumed that the gravity term is incorporated into the jump condition for the stress, Eq. (2.16). $\bar{f}$ denotes the filter operation on a variable f, $\bar{\tau} = \overline{(\boldsymbol{uu})} - \overline{(\boldsymbol{u})(\boldsymbol{u})}$ is the SGS stress tensor, whose deviatoric part is parametrized by following the Smagorinsky procedure (Smagorinsky, 1963) as:

$$\bar{\tau} - \frac{1}{3}trace(\bar{\tau})\boldsymbol{I} = -2\nu_t\overline{\boldsymbol{S}} \tag{2.19}$$

The turbulent eddy viscosity is defined as

$$\nu_t = C\Delta^2|\overline{\boldsymbol{S}}| \qquad \text{and} \qquad |\overline{\boldsymbol{S}}| = \sqrt{2\overline{\boldsymbol{S}}\cdot\overline{\boldsymbol{S}}} \tag{2.20}$$

The model parameter *C* in the eddy viscosity definition (2.20) has to be determined to close the equations. In CFDShip-Iowa version 6, the Lagrangian dynamic SGS model (Meneveau et al., 1996) is used as it can handle complex geometries without the requirement of homogeneous direction(s). Therefore, Eq. (2.17) can be rewritten as the following form

$$\frac{\partial\overline{\boldsymbol{u}}}{\partial t} + \overline{\boldsymbol{u}}\cdot\nabla\overline{\boldsymbol{u}} = -\frac{1}{\rho}\nabla\bar{p} + \frac{1}{\rho}\nabla\cdot[\mu(\nabla\overline{\boldsymbol{u}} + (\nabla\overline{\boldsymbol{u}})^T)] + \nabla\cdot[\nu_t(\nabla\overline{\boldsymbol{u}} + (\nabla\overline{\boldsymbol{u}})^T)] \tag{2.21}$$

with the trace of SGS stress tensor incorporated into $\bar{p}$.

2.1.2 Numerical Methods

A finite difference method is used to discretize the Navier-Stokes equations on a non-uniform staggered Cartesian grid, in which three components of velocity (u, v, w) in the x, y, and z directions are defined at centers of cell faces normal to their own directions and all other variables (p, ϕ, ρ, μ, ν_t) are defined at cell centers. Fig. 2.1 shows the staggered arrangement of the variables on a two-dimensional x-y grid.

A four-step fractional-step method (Choi and Moin, 1994) is employed for velocity-pressure coupling, in which a pressure Poisson equation is solved to enforce the continuity equation. For time advancement, a second-order semi-implicit scheme is adopted to integrate the momentum equations with the second-order Crank-Nicolson scheme for the diagonal viscous terms and the second-order Adams-Bashforth scheme for the other viscous terms and the convection terms. The processes in the four-step fractional-step method are as follows:

1. Predictor:

$$\frac{\hat{u}_i - u_i^n}{\Delta t} = \frac{1}{2}\left(3A_i^n - A_i^{n-1}\right) + \frac{1}{2}\left(C_i^{n+!} + C_i^n\right) - Grad_i(p^n) \tag{2.22}$$

2. First corrector:

$$\frac{u_i^* - \hat{u}_i}{\Delta t} = Grad_i(p^n) \tag{2.23}$$

3. Pressure Poisson equation:

$$\frac{\partial}{\partial x_i} Grad_i(p^{n+1}) = \frac{1}{\Delta t}\frac{\partial u_i^*}{\partial x_i} \tag{2.24}$$

4. Second corrector:

$$\frac{u_i^{n+1} - u_i^*}{\Delta t} = -Grad_i(p^{n+1}) \tag{2.25}$$

where superscript *n* denotes time step, subscript *i* = 1, 2, 3 represents *i*-coordinate, and *A* and *C* denote terms treated by the Adams-Bashforth and Crank-Nicolson schemes, respectively, i.e.,

$$\boldsymbol{A} = -\overline{\boldsymbol{u}} \cdot \nabla \overline{\boldsymbol{u}} + \frac{1}{\rho}\nabla \cdot [\mu(\nabla \overline{\boldsymbol{u}})^T] + \nabla \cdot [\nu_t(\nabla \overline{\boldsymbol{u}})^T] \tag{2.26}$$

$$\boldsymbol{C} = \frac{1}{\rho}\nabla \cdot [\mu(\nabla \overline{\boldsymbol{u}})] + \nabla \cdot [\nu_t(\nabla \overline{\boldsymbol{u}})] \tag{2.27}$$

$\hat{u}_i$ and u_i^* are the first and second intermediate velocities, respectively. $Grad_i(p)$ is a pressure gradient term defined at the center of a cell face (collocated with *i*th velocity component). The surface tension and gravity terms do not appear in Eq. (2.22) explicitly since they are incorporated into the pressure gradient term $Grad_i(p)$ through the jump condition across the interface. For instance, as shown in Fig. 2.2, the following definition of the pressure gradient in the x direction can be used to implement the jump condition given by Eq. (2.16):

$$\begin{aligned} Grad_x(p)_{i+1/2,j} &= \frac{1}{\hat{\rho}_{i+1/2,j}} \frac{\left(p_{i+1,j} - [p]H_{i+1,j}\right) - \left(p_{i,j} - [p]H_{i,j}\right)}{\Delta x} \\ &= \frac{1}{\hat{\rho}_{i+1/2,j}} \frac{\left(p_{i+1,j} - p_{i,j}\right) - [p]\left(H_{i+1,j} - H_{i,j}\right)}{\Delta x} \end{aligned} \tag{2.28}$$

where H is the Heaviside function defined in Eq. (2.9), the pressure jump across the interface between cell centers (i, j) and $(i + 1, j)$ is based on Eq. (2.16):

$$[p] = -\sigma\kappa^I - [\rho]\left(x^I g_x + y^I g_y + z^I g_z\right) \tag{2.29}$$

with (x^I, y^I, z^I) the interface position vector normal to the reference piezometric plane. The cell face density is defined as

$$\hat{\rho}_{i+1/2,j} = \rho_L \theta_{i+1/2,j} + \rho_G\left(1 - \theta_{i+1/2,j}\right) \tag{2.30}$$

with

$$\theta_{i+1/2,j} = \begin{cases} 1 & \text{if} \quad \phi_{i,j} \geq 0 \quad \text{and} \quad \phi_{i+1,j} \geq 0 \\ 0 & \text{if} \quad \phi_{i,j} < 0 \quad \text{and} \quad \phi_{i+1,j} < 0 \\ \dfrac{\phi_{i,j}}{|\phi_{i,j}| + |\phi_{i+1,j}|} & \text{if} \quad \phi_{i,j} \geq 0 \quad \text{and} \quad \phi_{i+1,j} < 0 \\ \dfrac{\phi_{i+1,j}}{|\phi_{i,j}| + |\phi_{i+1,j}|} & \text{if} \quad \phi_{i,j} < 0 \quad \text{and} \quad \phi_{i+1,j} \geq 0 \end{cases} \tag{2.31}$$

It is evident from the definition of the Heaviside function *H* that Eqs. (2.28) and (2.30) recover their usual one-fluid forms when the cell centers (*i*, *j*) and (*i*+1, *j*) are in the same phase, i.e. either air or water.

To solve Eq. (2.22), the convection term and diffusion term have to be discretized. An arithmetic mean is used to obtain values of velocity components, density, and viscosity at locations where these values are not defined from the neighboring collocation points with the exception of the interfacial density as defined by Eq. (2.30). The diffusion and convective terms are discretized by the standard second-order central difference scheme and a third-order QUICK (Quadratic Upwind Interpolation for Convective Kinematics) scheme (Leonard, 1979), respectively. As shown in Fig. 2.3, Φ represents a general velocity component, and a different index system (*I*, *J*) than that in Fig. 2.1 is used to indicate the staggered variable arrangement. Using $\nabla_x(u\Phi)$ as an example, the discretization can be written as

$$\nabla_x(u\Phi) = \frac{1}{\Delta x}\left(U_{I+1/2,J}\Phi_{I+1/2,J} - U_{I-1/2,J}\Phi_{I-1/2,J}\right) \tag{2.32}$$

where *U* means a cell face advecting *u* velocity component from an arithmetic mean. With an upwind procedure, the right side cell face flux, $\Phi_{I+1/2,J}$, can be evaluated using the QUICK scheme as follows:

$$\Phi_{I+1/2,J} = \begin{cases} \frac{1}{8}\left(-\Phi_{I-1,J} + 6\Phi_{I,J} + 3\Phi_{I+1,J}\right) & \text{if} \quad U_{I+1/2,J} \geq 0 \\ \frac{1}{8}\left(-\Phi_{I+2,J} + 6\Phi_{I+1,J} + 3\Phi_{I,J}\right) & \text{if} \quad U_{I+1/2,J} < 0 \end{cases} \tag{2.33}$$

on a uniform grid. Lagrangian polynomial interpolation can be used to obtain the non-constant coefficients in the above equation for non-uniform grids.

To invert the momentum equations due to the implicit treatment of the diagonal viscous terms, the approximate factorization method (Beam and Warming, 1976) is used. Eq. (2.22) can be rewritten in the following form:

$$\left[1 - \frac{\Delta t}{\rho}\nabla \cdot (\mu\nabla)\right]\hat{u}_i = u_i^n + \Delta t(RHS)_i^n \tag{2.34}$$

where $(RHS)_i^n$ includes all terms evaluated explicitly in Eq. (2.22). In order to illustrate the factorization method, a uniform grid is used and terms due to SGS stresses are not included in Eq. (2.34). With the approximate factorization method, the above equation can be expressed as:

$$\left[1-\frac{\Delta t}{\rho}\frac{\partial}{\partial x}\left(\mu\frac{\partial}{\partial x}\right)\right]\left[1-\frac{\Delta t}{\rho}\frac{\partial}{\partial y}\left(\mu\frac{\partial}{\partial y}\right)\right]\left[1-\frac{\Delta t}{\rho}\frac{\partial}{\partial z}\left(\mu\frac{\partial}{\partial z}\right)\right]\hat{u}_i = u_i^n + \Delta t(RHS)_i^n \tag{2.35}$$

A splitting error of order $O(\Delta t^3)$ is introduced into the system in this factorization procedure, which does not affect the second-order temporal accuracy of the overall algorithm.

The pressure Poisson equation, Eq. (2.24), is discretized using a standard second-order central-difference scheme. On a staggered grid, the right-hand side of Eq. (2.24) can be computed readily using the cell face velocity components. The left-hand side can be discretized by applying the divergence operator to Eq. (2.28) (Liu et al., 2000). In the x direction of a uniform grid,

$$\begin{aligned}\frac{1}{\Delta x}Grad_x(p^{n+1})_{i+\frac{1}{2},j} &= \frac{1}{\Delta x}\frac{1}{\hat{\rho}_{i+1/2,j}}\frac{\left(p_{i+1,j}^{n+1}-p_{i,j}^{n+1}\right)-[p]\left(H_{i+1,j}-H_{i,j}\right)}{\Delta x}\\ &= \frac{1}{(\Delta x)^2}\frac{p_{i+1,j}^{n+1}-p_{i,j}^{n+1}}{\hat{\rho}_{i+1/2,j}}-\frac{[p]}{(\Delta x)^2}\frac{H_{i+1,j}-H_{i,j}}{\hat{\rho}_{i+1/2,j}}\end{aligned} \tag{2.36}$$

where the second term due to the pressure jump condition is moved to the right-hand side of the pressure Poisson equation. Since the level set function is solved before the pressure Poisson equation, the position and curvature of the interface and then the pressure jumps through the interface can be computed in advance. Thus, re-evaluation of the right-hand side is not necessary.

The level-set evolution and reinitialization equations are solved using third-order TVD Runge-Kutta scheme (Shu and Osher, 1988) for the time advancement and fifth-order HJ-WENO scheme (Jiang and Peng, 2000) for the spatial discretization. The local (narrow band) level-set method by Peng et al. (1999) is used to identify a narrow band of

several grid cell widths around the zero level set at each time step, where the level set evolution and reinitialization equations are solved. Due to the narrow band method, the additional solution of the level-set function with the current high order schemes does not pose a significant overhead to CFDShip-Iowa version 6.

A sharp interface immersed boundary method by Yang and Balaras (2006) is used to treat an immersed body on a non-uniform Cartesian grid. In this approach, the grid generation for complex geometries is trivial since the requirement that the grid points coincide with the boundary, which is imperative for body-fitted methods, is relaxed; while the solution near the immersed boundary is reconstructed using momentum forcing in a sharp-interface manner. Since the detailed procedure is given in Yang and Balaras (2006), and Yang and Stern (2009), the overview is summarized here.

The first step is to establish the grid-interface relation with a given immersed boundary description, such as parametrized curve/surface or triangulation. In this step, all Cartesian grid nodes are split into three categories shown in Fig. 2.4: (1) fluid-points, which are points in the fluid phase; (2) forcing points, which are grid points in the fluid phase with one or more neighboring points in the solid phase; (3) solid-points, which are points in the solid phase. CFDShip-Iowa version 6 is applied to all grid points without distinguishing fluid, forcing, or solid points. The effect of the immersed boundary on the flow is mimicked by introducing a discrete forcing function to the momentum equation, Eq. (2.22). A provisional velocity field $\tilde{u}_i$ for the first intermediate velocity is $\hat{u}_i$ solved first with all terms treated by the Crank-Nicolson scheme in Eq. (2.22) using the explicit forward Euler scheme; then the discrete forcing function is evaluated by substituting $\tilde{u}_i$ with u_f (Kim et al., 2001). The velocity u_f is computed by a linear interpolation scheme given in Yang and Balaras (2006). In the linear interpolation scheme, an interpolation stencil is setup for a forcing point by three points: the projection of the forcing point onto the interface (point 1 in Fig.2.4) and two neighboring fluid points (points 2 and 3 in Fig.2.4). The provisional velocity is used for points 2 and 3. Point 1 uses the local

velocity of the immersed body that is already known from the prescribed or predicted motion

The time step Δt is restricted by the CFL (Courant-Friedrichs-Lewy) condition, gravity, and surface tension. With a CFL restriction of 0.5, the following relationship can be established as discussed in Kang et al. (2000).

$$\Delta t \leq 0.5 \left(\frac{C_{cfl} + \sqrt{\left(C_{cfl}\right)^2 + 4\left(G_{cfl}\right)^2 + 4\left(S_{cfl}\right)^2}}{2} \right)^{-1} \tag{2.37}$$

with the convective time step restriction

$$C_{cfl} = max\left(\frac{|u|}{\Delta x} + \frac{|v|}{\Delta y} + \frac{|w|}{\Delta z} \right) \tag{2.38}$$

the time step restriction due to gravity

$$G_{cfl} = \sqrt{\frac{|g_x|}{\Delta x} + \frac{|g_y|}{\Delta y} + \frac{|g_z|}{\Delta z}} \tag{2.39}$$

and the time step restriction due to surface tension

$$S_{cfl} = \sqrt{\frac{\sigma|\kappa|}{\rho_G \left(min(\Delta x, \quad \Delta y, \quad \Delta z) \right)^2}} \tag{2.40}$$

One of the major objectives of the development of CFDShip-Iowa version 6 is to make use of the on-coming petascale computers and provide fast turnaround for simulation-based design in ship hydrodynamics. Efficiency and sustainable development of the solver are among the major considerations in the software design. Modern programming language Fortran 95 is chosen and a modulized approach is followed for the code development.

The simple topologic structure of Cartesian grids is favorable for coarse-grain parallelization. The parallelization is done via a domain decomposition technique using the Message Passing Interface (MPI) library. A simple domain decomposition technique is used in CFDShip-Iowa version 6 where the Cartesian grid is divided into uniform

pieces, each of which resides in one processor. Optimal load balance can be achieved except for a small amount of overhead due to interface and immersed boundary treatment, which may be unevenly distributed over processors.

A parallel tri-diagonal system solver is used with the approximate factorization of momentum equations, no iterations are needed for the inversion of the momentum equations. For the pressure Poisson equation, a highly efficient, scalable multigrid-preconditioned Krylov subspace solver from PETSc has been included in the code. Usually, the Poisson solver takes most of the CPU time in a single time step.

Parallel I/O based on MPI 2 is implemented. Instead of the usual approaches that one process collects all data from all processes and write to one file, or, each process write its data to its own file, in the current approach all processes write its data to one single file, which is highly scalable and can greatly simplify the I/O operation and minimize the post-processing overhead.

2.2 Orthogonal Curvilinear Grid Solver

The original CFDShip-Iowa version 6 has been extended into orthogonal curvilinear coordinate system (ξ_1, ξ_2, ξ_3) by Suh et al. (2011). The CFD solver is currently developed as CFDShip-Iowa version 6.2. All governing equations are expressed in the orthogonal curvilinear coordinate system. The momentum equations solve the contravariant velocity components u_i (i = 1, 2, 3) in the directions of ξ_1, ξ_2, and ξ_3, respectively. Since the computational domain is discretized by an orthogonal curvilinear grid fitted to the body shape, the immersed boundary method of CFDShip-Iowa version 6 is no longer needed and the no-slip condition on the body surface has been adopted.

2.2.1 Mathematical Models

The governing equations in CFDShip-Iowa version 6.2 are the unsteady, three-dimensional, incompressible Navier-Stokes equations written in the orthogonal curvilinear coordinate system:

$$\frac{\partial u_i}{\partial t} + \nabla(j)[u_i u_j] - \frac{1}{\rho}\nabla(j)[\tau_{ij}] = -\frac{1}{\rho}\frac{\partial p}{\partial \xi(i)} + g_i + H_j(i)\left[u_j u_j - \frac{\tau_{ij}}{\rho}\right] - H_i(j)\left[u_i u_j - \frac{\tau_{ij}}{\rho}\right] \tag{2.41}$$

$$\nabla(i)[u_i] = 0 \tag{2.42}$$

where g_i (i = 1, 2, 3) is the gravity vector in the direction of the orthogonal curvilinear coordinate ξ_i, ρ the density, p the pressure, and t the time. In addition,

$$H_i(j) = \frac{1}{h_i h_j}\frac{\partial h_i}{\partial \xi_j} \tag{2.43}$$

$$\nabla(i)[\cdot] = \frac{1}{J}\frac{\partial}{\partial \xi_i}\left[\left(\frac{J}{h_i}\right)\right] \tag{2.44}$$

and $\partial\xi(i) = h_i\partial\xi_i$ and $h_i = \partial x_i/\partial\xi_i$ with x_i a Cartesian coordinate following Pope (1978). The Jacobian of the coordinate transformation is defined as $J = h_i h_j h_k$,. The viscous stress tensor τ_{ij} is defined as follows:

$$\tau_{ij} = \mu\left[\frac{\partial u_i}{\partial \xi(j)} + \frac{\partial u_j}{\partial \xi(i)} - u_i H_i(j) - u_j H_j(i) + 2u_l H_i(l)\delta_{ij}\right] \tag{2.45}$$

where μ is the dynamic viscosity and δ_{ij} is the Kronecker delta function.

The fluid-fluid interface is tracked as the zero level set of the level-set function. The level-set function is evolved by the following equation:

$$\frac{\partial \phi}{\partial t} + u_i \frac{\partial \phi}{\partial \xi(i)} = 0 \tag{2.46}$$

The reinitialization equation (Sussman et al., 1994) is iteratively solved to keep the level-set function as a signed distance function.

Like CFDShip-Iowa version 6, the density and viscosity are defined according to the level-set function, and sharp jumps of the fluid properties occur at the interface. Thus, the density keeps its sharp jump while the viscosity is smoothed over a transition band across the interface.

In order to handle fully inhomogeneous turbulence, Suh et al. (2011) adopted the Lagrangian dynamic SGS model based on Sarghini et al. (1999) as it averages the model

coefficient along the flow pathline (Meneveau et al., 1996). In this LES approach, the Navier-Stokes equations are spatially filtered so that the large, energy-carrying eddies are resolved while the small-scale, dissipative eddies are modeled by the SGS model. The following equations can be obtained after applying the filter operation to Eq. (2.41):

$$\frac{\partial \bar{u}_i}{\partial t} + \nabla(j)\left[\bar{u}_i \bar{u}_j\right] - \frac{1}{\rho}\nabla(j)\left[\bar{\tau}_{ij}\right] - \frac{1}{\rho}\nabla(j)\left[\tilde{\tau}_{ij}\right] = -\frac{1}{\rho}\frac{\partial \bar{p}}{\partial \xi(i)} + g_i + H_j(i)\left[\bar{u}_j \bar{u}_j - \frac{\bar{\tau}_{ij}}{\rho} - \tilde{\tau}_{ij}\right] - H_i(j)\left[\bar{u}_i \bar{u}_i - \frac{\bar{\tau}_{ij}}{\rho} - \tilde{\tau}_{ij}\right] \tag{2.47}$$

with $\bar{\tau}_{ij} = \mu \bar{S}_{ij}$ and $\tilde{\tau}_{ij} = \nu_t \tilde{\tau}_{ij}$ with ν_t the turbulent eddy viscosity, respectively.

2.2.2 Numerical Methods

CFDShip-Iowa version 6.2 implements the same numerical methods as those of CFDShip-Iowa version 6. Therefore, a finite-difference method is used to discretize the governing equations on a non-uniform staggered orthogonal grid. The contravariant velocity components are defined at centers of cell faces in their orthogonal curvilinear coordinate directions. All other variables are defined at cell centers. A semi-implicit time advancement scheme is used to integrate the momentum equations with the second-order Crank-Nicolson scheme for the diagonal viscous terms and the second-order Adams-Bashforth scheme for other terms. A four-step fractional-step method (Choi and Moin, 1994) is employed for velocity-pressure coupling, in which a pressure Poisson equation is solved to enforce the continuity equation.

The convective terms are discretized using the fifth-order Hamilton-Jacobi Weighted-ENO (HJ-WENO) scheme (Jiang and Peng, 2000). The other terms are discretized using the second-order central difference scheme. A semi-coarsening multigrid solver from the HYPER library (Falgout et al., 2006) is used to solve the pressure Poisson equation.

Both the level-set evolution and reinitialization equations are solved using the third-order TVD Runge-Kutta scheme (Shu and Osher, 1988) for time advancement and

the fifth-order HJ-WENO scheme (Jiang and Peng, 2000) for spatial discretization. The local level-set method by Peng et al. (1999) defines a narrow band around the fluid-fluid interface, in which the level-set and reinitialization equations are solved.

2.3 Coupled Orthogonal Curvilinear/Cartesian Grid Solver

CFDShip-Iowa version 6.2.5 is a coupled orthogonal curvilinear/Cartesian grid solver based on CFDShip-Iowa version 6, a Cartesian grid solver, and CFDShip-Iowa version 6.2, an orthogonal curvilinear grid solver, both of which are for LES of two-phase incompressible flows as discussed above. CFDShip-Iowa version 6.2.5 requires two grid blocks: a thin orthogonal boundary layer grid to resolve a boundary layer on a body surface and a Cartesian background grid to compute the flow region out of the boundary layer grid. Then CFDShip-Iowa version 6.2.5 applies CFDShip-Iowa version 6.2 and CFDShip-Iowa version 6 into the boundary layer grid and the Cartesian background grid, respectively. Those solvers are coupled by the grid connectivity information given by Structured, Unstructured, and Generalized overset Grid AssembleR (SUGGAR) code (Noack, 2005).

2.3.1 Mathematical Models

Since CFDShip-Iowa version 6.2.5 executes CFDShip-Iowa version 6 and CFDShip-Iowa version 6.2 simultaneously, the coupled solver solves the continuity equations and the momentum equations in a Cartesian coordinate system and an orthogonal curvilinear coordinate system, i.e. Eqs. (2.1), (2.2), (2.41), and (2.42).

The interface between two immiscible fluids is defined as the zero level set of the level-set function. The level-set function is advanced by the evolution equations: Eq. (2.5) and Eq. (2.46). The reinitialization equations written in the Cartesian coordinate system and the orthogonal curvilinear coordinate system are iteratively solved to keep the level-set function as a signed distance function. Each phase of the constant density and viscosity is defined according to the level-set function.

Since CFDShip-Iowa version 6.2.5 implements an LES method in each solver, the Navier-Stokes equations in both of the solvers are spatially filtered such that the large, energy-carrying eddies are resolved while the small-scale, dissipative eddies are modeled by an SGS model. The Smagorinsky model (Smagorinsky, 1963) is used to model the SGS stress tensor in Eq. (2.17) and Eq. (2.47). The model parameter, such as C in Eq. (2.20), is determined as a constant in CFDShip-Iowa version 6.2.5 because it was found that evaluation of the parameter by a dynamic model leads to large differences in the turbulent eddy viscosity across the overlapping region due to the secondary filtering (Bhushan et al., 2011). In this study, the model parameter is equal to 0.03.

2.3.2 Numerical Methods

The numerical methods in CFDShip-Iowa version 6.2.5 are the same as those in its component solvers, i.e. CFDShip-Iowa version 6 and CFDShip-Iowa version 6.2. A finite difference method is used to discretize the governing equations on the overlapping non-uniform staggered grids. The four-step fractional-step method of Choi and Moin (1994) is employed for velocity-pressure coupling, in which pressure Poisson equation is solved to enforce the continuity equation. A semi-implicit time advancement scheme is adopted to integrate the momentum equations with the second-order Crank-Nicolson scheme for the diagonal viscous terms and the second-order Adams-Bashforth scheme for the other viscous terms and the convection terms. The diffusion terms are discretized by the standard second-order central difference scheme. The convective terms are discretized by the third-order QUICK scheme (Leonard, 1979) in both the curvilinear grid solver and the Cartesian grid solver because the overset interpolation in CFDShip-Iowa version 6.2.5 give the boundary conditions onto two grid layers, as discussed later.

Both the level-set evolution and reinitialization equations are solved using the third-order TVD Runge-Kutta scheme (Shu and Osher, 1988) for the time advancement and the third-order QUICK scheme for the spatial discretization due to the same reason as the momentum equations. The local level-set method by Peng et al. (1999) is used to

identify a narrow band of several grid cell widths around the fluid-fluid interface at each time step, in which the level-set and the reinitialization equations are solved.

Fig. 2.5 (a) shows a boundary layer grid overlapping with a Cartesian background grid for CFDShip-Iowa version 6.2.5 simulation of flow past a circular cylinder. As shown in Fig. 2.5 (a), the whole boundary layer grids are included inside the Cartesian background grids for all the CFDShip-Iowa version 6.2.5 simulations. The grid connectivity information is obtained by three overset grid assembly processes performed by the SUGGAR code, an overset grid assembly program originally designed for moving body simulations. At the beginning of the processes, the SUGGAR code identifies hole points within the grids, which are excluded from the numerical computations. In Fig. 2.5 (b), the Cartesian grid points highlighted by green become the hole points because they are inside the boundary layer grid or the circular cylinder. The next step in the overset grid assembly process is identification of fringe points which receive flow variables interpolated from other grids. Once all the fringe points are specified, the final step searches donor points which interpolate the flow variables to the corresponding fringe points and identifies the interpolation weights of the donor points. Fig. 2.5 (b) and (c) show the fringe points (blue) and active points (red) on which the governing equations are solved. The fringe points provide the Dirichlet boundary conditions that the component solvers of CFDShip-Iowa version 6.2.5 use. The details of the overset grid assembly process in the SUGGAR code are described in Noack (2005).

Fig. 2.6 shows the overall solution strategy in CFDShip-Iowa version 6.2.5. Since the current study handles only flow problems with static bodies, it is sufficient that the SUGGAR code is executed before the numerical simulations. The grid connectivity information specifies which grid point is the hole, fringe, or active point, and what the interpolation weights of the donors are, as described above. The grid connectivity information is written in a file which CFDShip-Iowa version 6.2.5 reads together with the input data necessary for the simulation. Since both CFDShip-Iowa version 6 and

CFDShip-Iowa version 6.2 perform the domain decompositions using the MPI library, CFDShip-Iowa version 6.2.5 splits all the processors into the solvers which are executed simultaneously. Since both of the solvers have the same numerical methods, the overset interpolation can be performed in a straightforward manner; each flow variable is interpolated after it is solved by the governing equations. For the velocity components, the interpolation is also done for the intermediate velocities in the predictor step and the first corrector step of the four-step fractional-step method to obtain the smooth velocity distribution across the overlapping part of the grid blocks.

The overset interpolation in CFDShip-Iowa version 6.2.5 is performed for the variables at the centers of the cells. Therefore, the velocity components at the cell centers need to be calculated from those at the centers of the cell faces which are solved by the momentum equations. Moreover, CFDShip-Iowa version 6.2 incorporated in CFDShip-Iowa version 6.2.5 as the curvilinear grid solver computes the contravariant velocity components along the curvilinear coordinate system (ξ, η, ζ). Those contravariant velocity components have to be transformed into those in the Cartesian coordinate system (x, y, z) before the overset interpolation. The contravariant velocity components (u, v, w) at the cell centers are obtained by the arithmetic mean. Then, the velocity components can be transformed into those (U, V, W) along (x, y, z) as

$$\begin{pmatrix} U \\ V \\ W \end{pmatrix} \equiv \begin{bmatrix} \frac{\partial x}{\partial \xi} & \frac{\partial x}{\partial \eta} & \frac{\partial x}{\partial \zeta} \\ \frac{\partial y}{\partial \xi} & \frac{\partial y}{\partial \eta} & \frac{\partial y}{\partial \zeta} \\ \frac{\partial z}{\partial \xi} & \frac{\partial z}{\partial \eta} & \frac{\partial z}{\partial \zeta} \end{bmatrix} \begin{pmatrix} u \\ v \\ w \end{pmatrix} \tag{2.48}$$

Similarly,

$$\begin{pmatrix} u \\ v \\ w \end{pmatrix} \equiv \begin{bmatrix} \frac{\partial \xi}{\partial x} & \frac{\partial \xi}{\partial y} & \frac{\partial \xi}{\partial z} \\ \frac{\partial \eta}{\partial x} & \frac{\partial \eta}{\partial y} & \frac{\partial \eta}{\partial z} \\ \frac{\partial \zeta}{\partial x} & \frac{\partial \zeta}{\partial y} & \frac{\partial \zeta}{\partial z} \end{bmatrix} \begin{pmatrix} U \\ V \\ W \end{pmatrix} \tag{2.49}$$

The matrix elements in Eq. (2.49) are defined as

$$\begin{aligned}
\frac{\partial \xi}{\partial x} &\equiv \frac{1}{J}\left(\frac{\partial y}{\partial \eta}\frac{\partial z}{\partial \zeta} - \frac{\partial y}{\partial \zeta}\frac{\partial z}{\partial \eta}\right) \\
\frac{\partial \xi}{\partial y} &\equiv -\frac{1}{J}\left(\frac{\partial x}{\partial \eta}\frac{\partial z}{\partial \zeta} - \frac{\partial x}{\partial \zeta}\frac{\partial z}{\partial \eta}\right) \\
\frac{\partial \xi}{\partial z} &\equiv \frac{1}{J}\left(\frac{\partial x}{\partial \eta}\frac{\partial y}{\partial \zeta} - \frac{\partial x}{\partial \zeta}\frac{\partial y}{\partial \eta}\right) \\
\frac{\partial \eta}{\partial x} &\equiv -\frac{1}{J}\left(\frac{\partial y}{\partial \xi}\frac{\partial z}{\partial \zeta} - \frac{\partial y}{\partial \zeta}\frac{\partial z}{\partial \xi}\right) \\
\frac{\partial \eta}{\partial y} &\equiv \frac{1}{J}\left(\frac{\partial x}{\partial \xi}\frac{\partial z}{\partial \zeta} - \frac{\partial x}{\partial \zeta}\frac{\partial z}{\partial \xi}\right) \\
\frac{\partial \eta}{\partial z} &\equiv -\frac{1}{J}\left(\frac{\partial x}{\partial \xi}\frac{\partial y}{\partial \zeta} - \frac{\partial x}{\partial \zeta}\frac{\partial y}{\partial \xi}\right) \\
\frac{\partial \zeta}{\partial x} &\equiv \frac{1}{J}\left(\frac{\partial y}{\partial \xi}\frac{\partial z}{\partial \eta} - \frac{\partial y}{\partial \eta}\frac{\partial z}{\partial \xi}\right) \\
\frac{\partial \zeta}{\partial y} &\equiv -\frac{1}{J}\left(\frac{\partial x}{\partial \xi}\frac{\partial z}{\partial \eta} - \frac{\partial x}{\partial \eta}\frac{\partial z}{\partial \xi}\right) \\
\frac{\partial \zeta}{\partial z} &\equiv \frac{1}{J}\left(\frac{\partial x}{\partial \xi}\frac{\partial y}{\partial \eta} - \frac{\partial x}{\partial \eta}\frac{\partial y}{\partial \xi}\right)
\end{aligned} \tag{2.50}$$

where

$$\begin{aligned}
J = &\frac{\partial x}{\partial \xi}\frac{\partial y}{\partial \eta}\frac{\partial z}{\partial \zeta} + \frac{\partial x}{\partial \eta}\frac{\partial y}{\partial \zeta}\frac{\partial z}{\partial \xi} + \frac{\partial x}{\partial \zeta}\frac{\partial y}{\partial \xi}\frac{\partial z}{\partial \eta} \\
&- \frac{\partial x}{\partial \xi}\frac{\partial y}{\partial \zeta}\frac{\partial z}{\partial \eta} - \frac{\partial x}{\partial \eta}\frac{\partial y}{\partial \xi}\frac{\partial z}{\partial \zeta} - \frac{\partial x}{\partial \zeta}\frac{\partial y}{\partial \eta}\frac{\partial z}{\partial \xi}
\end{aligned} \tag{2.51}$$

To satisfy mass conservation across the overlapping grid region, a pressure Poisson equation is solved in a strongly coupled manner using the PETSc toolkit (Balay et al., 2012). In this strong coupling of the pressure Poisson equation, the pressure

Poisson equations and the overset interpolation equations are encompassed from both CFDShip-Iowa version 6 and CFDShip-Iowa version 6.2 and solved together by an iterative method. Therefore, both the continuity equation and the overset interpolation relation are satisfied in both of the CFD solvers. In the coupled pressure Poisson equation, the left hand side (LHS) matrix consists of 1-point stencils for the hole points, 9-point stencils for the fringe points, 7-point stencils for the active points shown in Fig. 2.5. The LHS matrix is assembled only at the first time step as the grids are static, whereas the right hand side (RHS) vector is updated at every time step.

The pressure Poisson equation at the active points in Fig. 2.5 is expressed as

$$\Delta V\left[\frac{\partial}{\partial x}Grad_x P^{(n+1)}+\frac{\partial}{\partial y}Grad_y P^{(n+1)}+\frac{\partial}{\partial z}Grad_z P^{(n+1)}\right] = \frac{\Delta V}{\Delta t}\left(\frac{\partial u}{\partial x}+\frac{\partial v}{\partial y}+\frac{\partial w}{\partial z}\right) \tag{2.52}$$

where ΔV is the volume of the cell and $P^{(n+1)}$ is the pressure at time step (n+1). For a non-uniform Cartesian grid, the pressure gradients are computed as below:

$$\frac{\partial}{\partial x}Grad_x P^{(n+1)} = \underbrace{\frac{1}{\rho_{i+\frac{1}{2}}}\frac{1}{\Delta x_{i+\frac{1}{2}}}}_{C11}P_{i+1,j,k}-\underbrace{\left(\frac{1}{\rho_{i+\frac{1}{2}}}\frac{1}{\Delta x_{i+\frac{1}{2}}}+\frac{1}{\rho_{i-\frac{1}{2}}}\frac{1}{\Delta x_{i-\frac{1}{2}}}\right)}_{D1}P_{i,j,k}+\underbrace{\frac{1}{\rho_{i-\frac{1}{2}}}\frac{1}{\Delta x_{i-\frac{1}{2}}}}_{C12}P_{i-1,j,k} \tag{2.53a}$$

$$\frac{\partial}{\partial y}Grad_y P^{(n+1)} = \underbrace{\frac{1}{\rho_{j+\frac{1}{2}}}\frac{1}{\Delta y_{j+\frac{1}{2}}}}_{C21}P_{i,j+1,k}-\underbrace{\left(\frac{1}{\rho_{j+\frac{1}{2}}}\frac{1}{\Delta y_{j+\frac{1}{2}}}+\frac{1}{\rho_{j-\frac{1}{2}}}\frac{1}{\Delta y_{j-\frac{1}{2}}}\right)}_{D2}P_{i,j,k}+\underbrace{\frac{1}{\rho_{j-\frac{1}{2}}}\frac{1}{\Delta y_{j-\frac{1}{2}}}}_{C22}P_{i,j-1,k} \tag{2.53b}$$

$$\frac{\partial}{\partial z}Grad_z P^{(n+1)} = \underbrace{\frac{1}{\rho_{k+\frac{1}{2}}}\frac{1}{\Delta z_{k+\frac{1}{2}}}}_{C31}P_{i,j,k+1}-\underbrace{\left(\frac{1}{\rho_{k+\frac{1}{2}}}\frac{1}{\Delta z_{k+\frac{1}{2}}}+\frac{1}{\rho_{k-\frac{1}{2}}}\frac{1}{\Delta z_{k-\frac{1}{2}}}\right)}_{D3}P_{i,j,k}+\underbrace{\frac{1}{\rho_{k-\frac{1}{2}}}\frac{1}{\Delta z_{k-\frac{1}{2}}}}_{C22}P_{i,j,k-1} \tag{2.53c}$$

where the diagonal component of the LHS matrix is D = ΔV(D1 + D2 + D3), and six non-zero coefficients C1 ~ C6 of the matrix are ΔV*C11, ΔV*C12, ΔV*C21, ΔV*C22, ΔV*C31, and ΔV*C32, respectively. The LHS matrix for the orthogonal curvilinear grid solver is obtained similarly. The pressures at the fringe points are interpolated as:

$$P_{i,j,k} = W1 \times P_{d1} + W2 \times P_{d2} + W3 \times P_{d3} + W4 \times P_{d4} + W5 \times P_{d5} + W6 \times P_{d6} + W7 \times P_{d7} + W8 \times P_{d8} \tag{2.54}$$

where (i, j, k) is the fringe point index, d1 ~ d8 represent the donor points, and W1 ~ W8 are the interpolation weights of the donor points. At the hole points:

$$P_{i,j,k} = 0 \tag{2.55}$$

Then, the LHS matrix and the RHS vector are assembled as below:

$$\underbrace{\begin{bmatrix} \overbrace{\cdots C1..C2..C3..D..C4..C5..C6\cdots}^{\text{Cartesian}} & \cdots\cdots 0\cdots\cdots \\ \cdots\cdots 1\cdots\cdots & \cdots\text{-}W1..\text{-}W2\cdots\cdots\text{-}W7..\text{-}W8\cdots \\ \cdots\cdots 1\cdots\cdots & \cdots\cdots 0\cdots\cdots \\ \cdots\cdots 0\cdots\cdots & \underbrace{\cdots C1..C2..C3..D..C4..C5..C6\cdots}_{\text{Orthogonal Curvilinear}} \\ \cdots\text{-}W1..\text{-}W2\cdots\cdots\text{-}W7..\text{-}W8\cdots & \cdots\cdots 1\cdots\cdots \end{bmatrix}}_{\text{LHS}} \begin{matrix} \text{Fluid}\rightarrow \\ \text{Overset}\rightarrow \\ \text{Blanked}\rightarrow \\ \text{Fluid}\rightarrow \\ \text{Overset}\rightarrow \end{matrix} \begin{bmatrix} P_{Fluid} \\ P_{Overset} \\ P_{Blanked} \\ P_{Fluid} \\ P_{Overset} \end{bmatrix}$$

$$= \underbrace{\begin{bmatrix} \text{div(u)} \\ 0 \\ 0 \\ \text{div(u)} \\ 0 \end{bmatrix}}_{\text{RHS}} \tag{2.56}$$

The above linear system is solved using Krylov subspace based GMRES iterative method with ASM preconditioner.

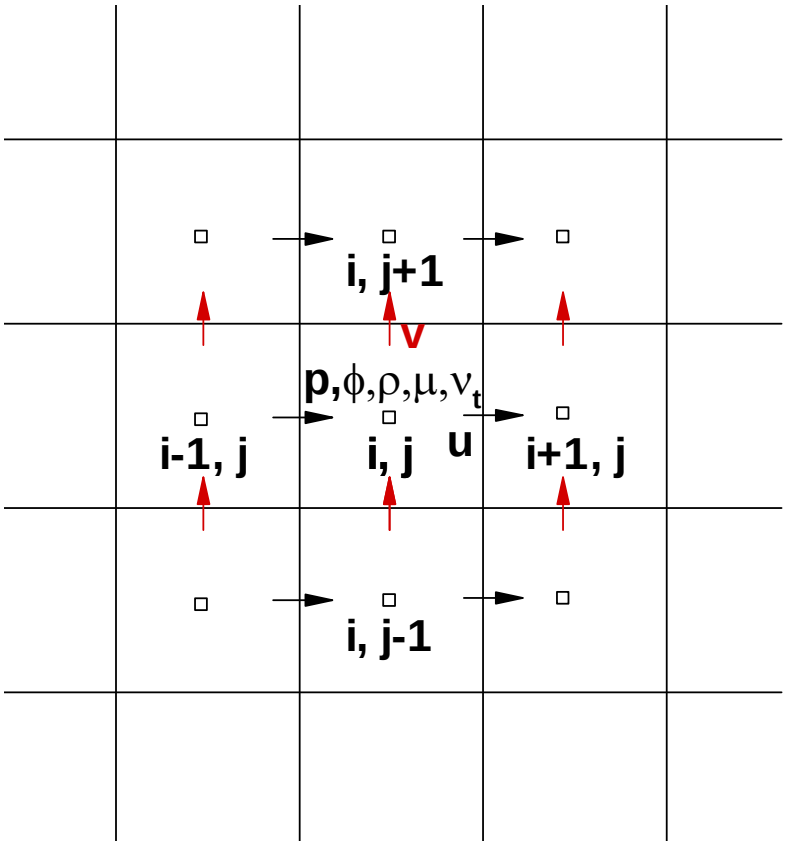

Figure 2.1 Arrangement of variables on staggered Cartesian grid

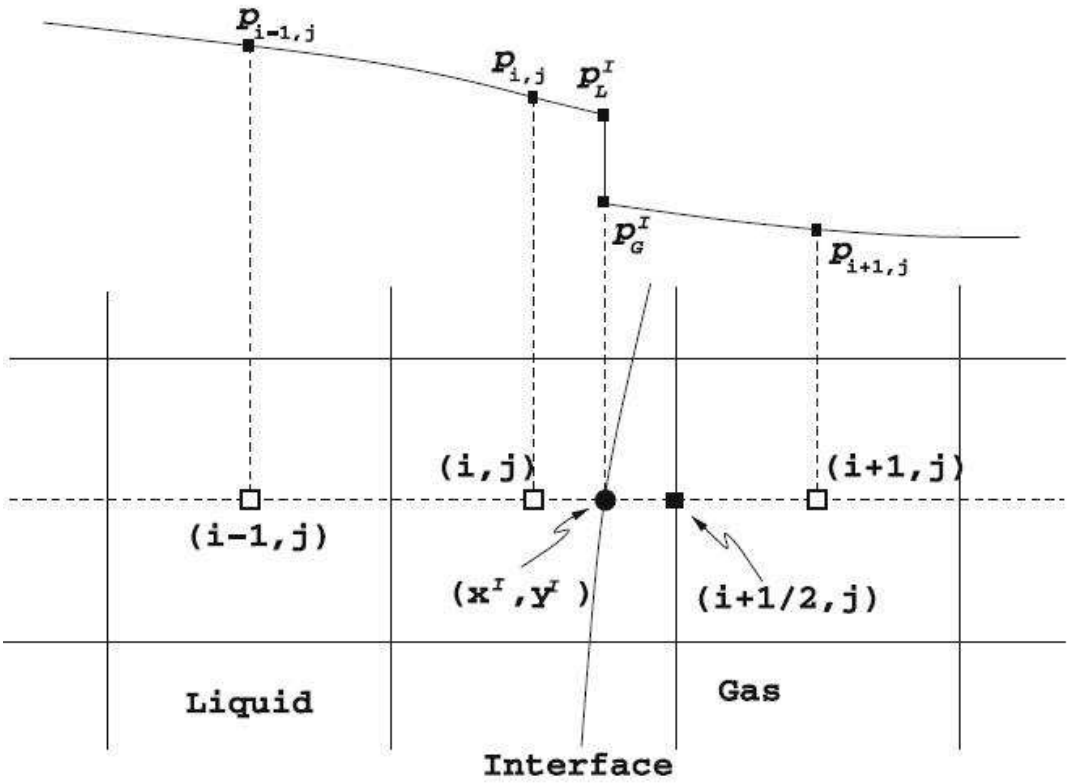

Figure 2.2 Schema of the jump condition treatment for the case $H_{i,j} = 1$ and $H_{i+1,j} = 0$

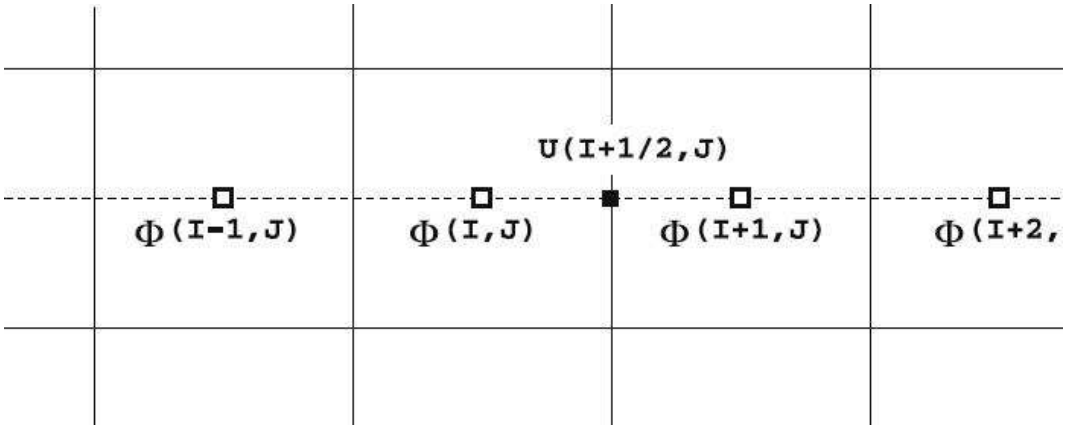

Figure 2.3 Schema of the QUICK scheme for the convection terms

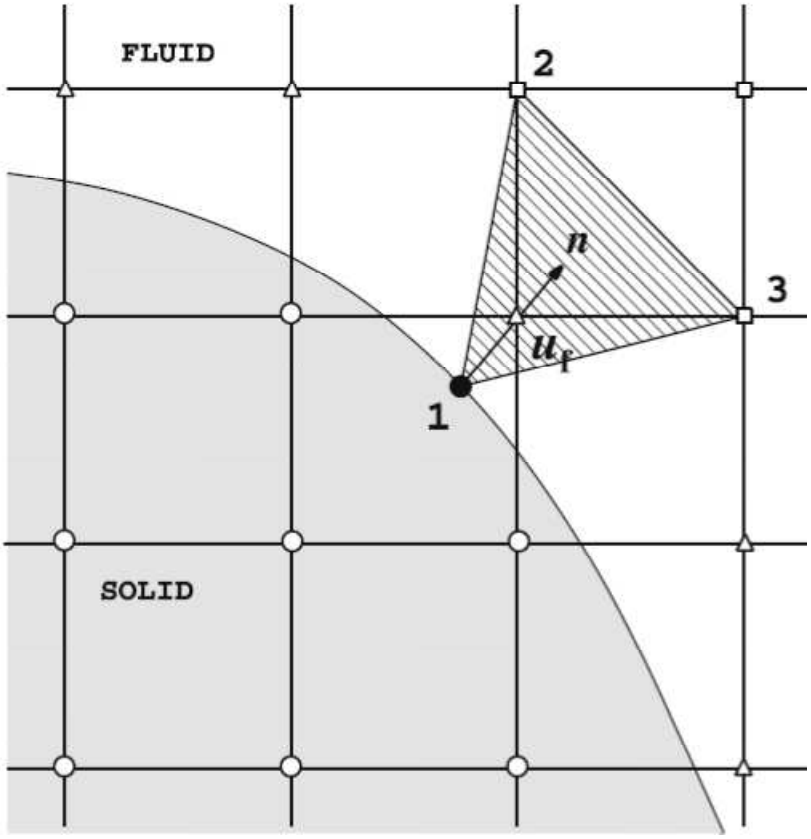

Figure 2.4 Grid-interface relation and the interpolation stencil for u_f (point 1, 2, and 3): ○ solid points; □ fluid points; Δ forcing points

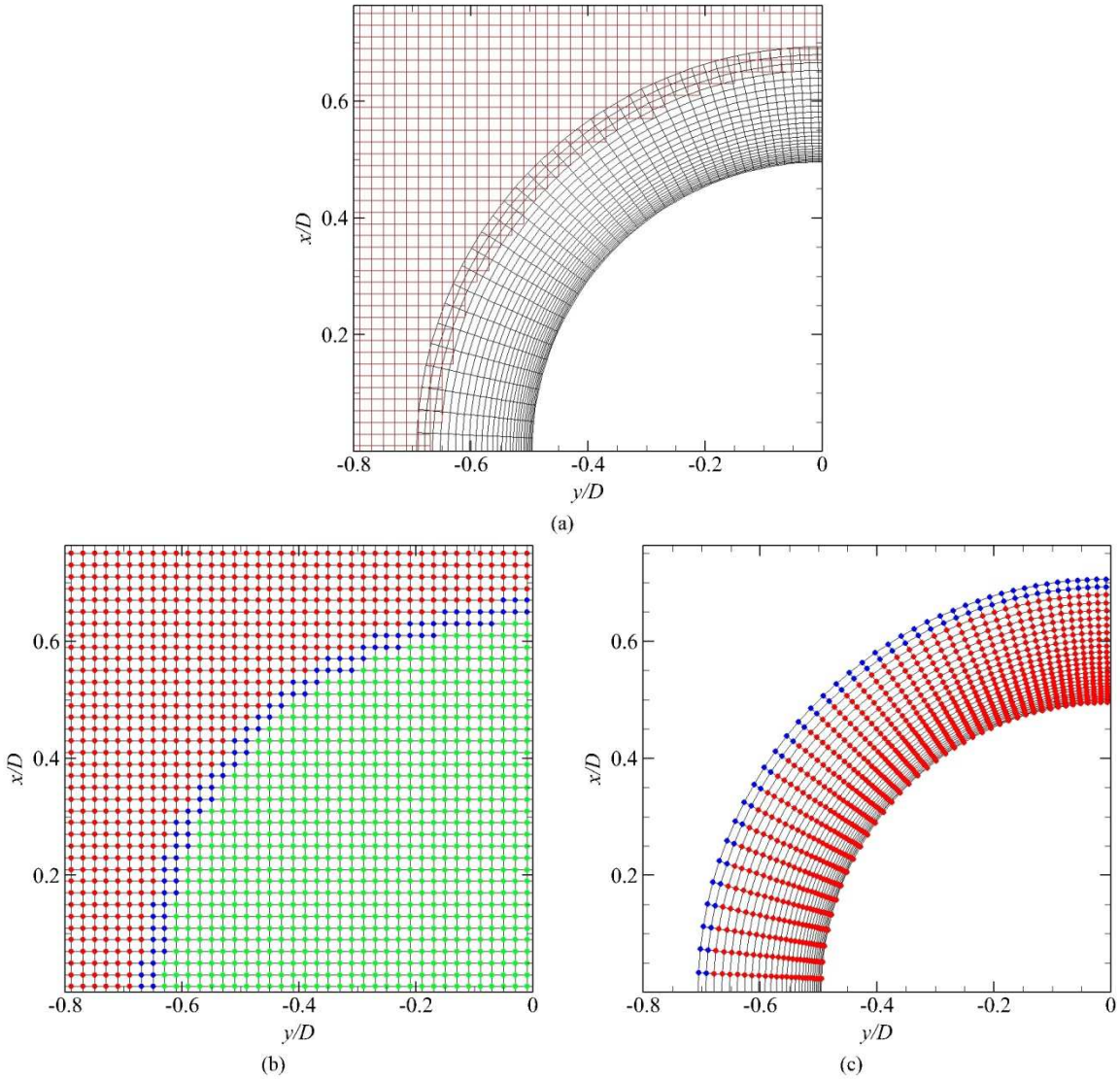

Figure 2.5 Overset grids for flow past a circular cylinder: (a) Overset grid configuration; (b) active points (red), fringe points (blue), and hole points (green) in the Cartesian background grid; (c) active points (red) and fringe points (blue) in the boundary layer grid

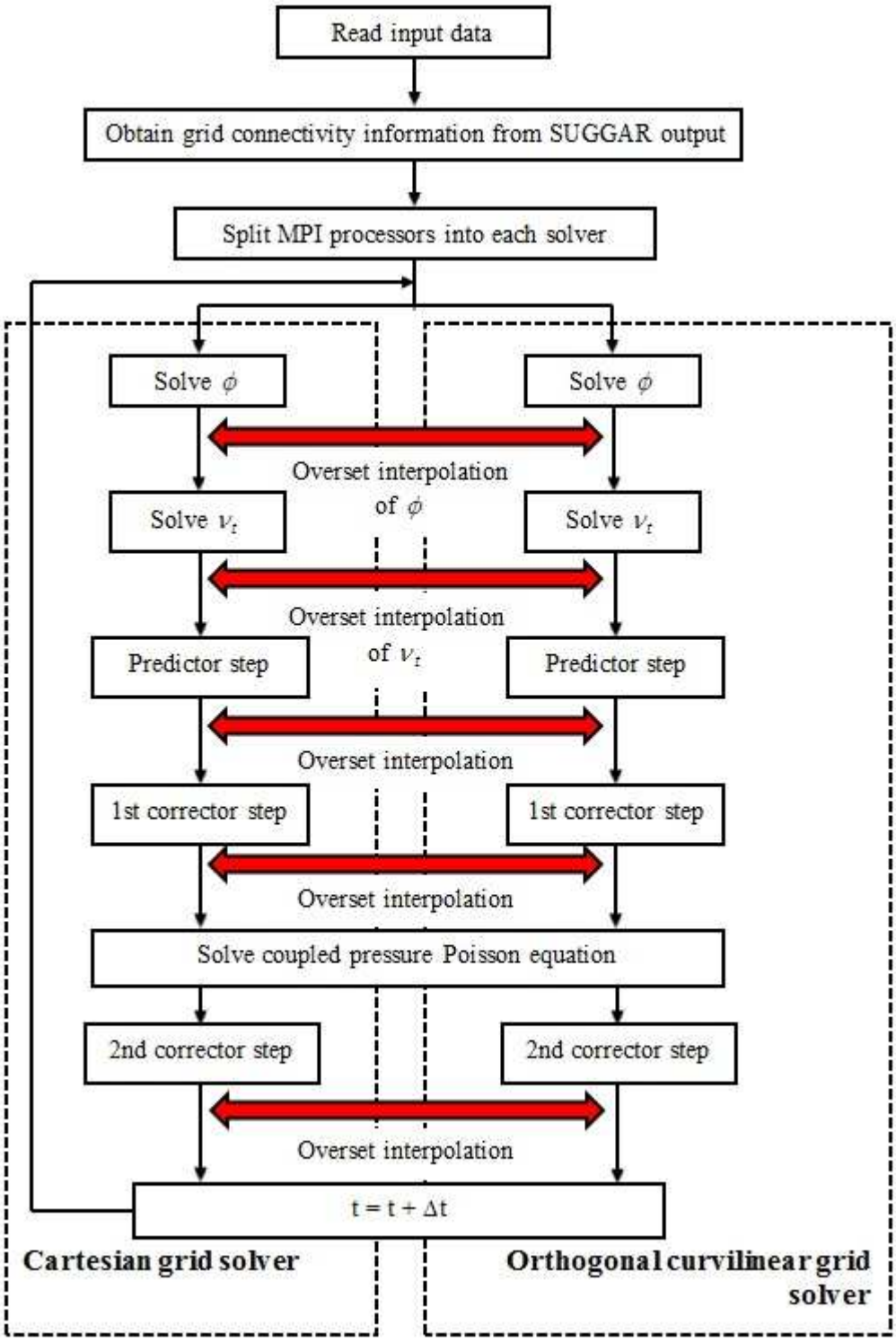

Figure 2.6 Solution strategy of coupled orthogonal curvilinear/Cartesian grid solver

CHAPTER 3
NUMERICAL SIMULATIONS OF SINGLE-PHASE FLOWS PAST CIRCULAR CYLINDERS

3.1 Introduction

A flow past a circular cylinder is an ideal case to validate CFDShip-Iowa version 6.2.5 (V6.2.5) because it involves an orthogonal curvilinear boundary layer grid based on cylindrical coordinate system. Since single-phase flows past circular cylinders have been extensively studied both experimentally and numerically for several decades due to simplicity of its geometry and its importance of engineering application, there are a lot of experimental data and numerical results available in the literature for comparison purposes. Thus, the viability and accuracy of V6.2.5 are initially investigated by considering the single-phase flows past a circular cylinder.

The single-phase flow past a circular cylinder exhibits vastly different behavior depending on Reynolds number ($Re = UD/\nu$) based on free stream velocity (U), the cylinder diameter (D), and kinematic viscosity of the fluid (ν) (Williamson, 1996). A steady laminar flow exists up to $Re \approx 49$ with a pair of symmetric counter-rotating vortices attached behind the cylinder. As Re increases, the laminar flow becomes unsteady, and periodic Karman vortex shedding appears behind the cylinder. The shear layer separating from the cylinder becomes unstable at around Re = 1000, resulting in three-dimensional turbulent wake. The flow regime up to $Re = 2\times10^5$ is referred to as subcritical. The subcritical flow involves a thin laminar boundary layer attached on the cylinder surface, transition to turbulence after separation of the boundary layer, a recirculation region behind the cylinder, and large-scale Karman vortices interacting with small-scale vortices along the directions of the flow and the cylinder axis. Between $Re = 2\times10^5$ and 4×10^5, the boundary layer reattaches after the separation and separates again further downstream. The resulting separation-reattachment bubble and narrower wake

than the laminar case cause drastically decreased drag. Flow regime between Re = 4×10^5 and 1×10^6 is referred to as supercritical. In the supercritical regime, the boundary layer on the cylinder surface becomes turbulent prior to the separation (Catalano et al., 2003). The boundary layer separates much further downstream and, as a result, the wake is narrower than that in the subcritical regime.

Validations of V6.2.5 are performed for two-dimensional steady (Re = 40) and unsteady (Re = 200) laminar flows, and subcritical (Re = 3900) and supercritical (Re = 5×10^5 and 1×10^6) turbulent flows past a circular cylinder because relatively many results about those flows have been obtained by either numerical simulations or experimental measurement for decades.

3.2 Numerical Simulations of Two-Dimensional Laminar Flows

Numerical simulations are performed by V6.2.5 to compute two-dimensional steady (Re = 40) and unsteady (Re = 200) laminar flows past a circular cylinder. Additional numerical simulations are also performed by CFDShip-Iowa version 6 (V6-IBM) and CFDShip-Iowa version 6.2 (V6-OC) to compare with the V6.2.5 results. The numerical results obtained by V6.2.5 are also compared with experimental data and benchmark numerical results in the literature. The experimental data available for Re = 40 include drag coefficient in Tritton (1959) and characteristics of the symmetric counter-rotating vortices in the wake in Coutanceau and Bouard (1977). The benchmark numerical results of the drag coefficient and the characteristics of the recirculation region are available from Dennis and Chang (1970), Fornberg (1980), Linnick and Fasel (2005), Xu and Wang (2006), and Xu (2008). Distributions of vorticity magnitude and pressure on the cylinder surface are predicted and compared with the numerical results in the literature, which were obtained by solvers using a body-fitted grid (Braza et al., 1986) and an immersed boundary method (IBM) (Xu, 2008). No experimental data is available

for Re = 200, but ample numerical results are available in the literature (Braza et al., 1986; Russell and Wang, 2003; Linnick and Fasel, 2005; Xu and Wang, 2006; Le et al., 2006; Xu, 2008).

Simulation conditions for the Re = 40 and 200 cases are summarized in Table 3.1. Each simulation has its own case name. For both cases, the size of the Cartesian grid for the V6-IBM simulations is $-20 \leq x/D \leq 20$ and $-11 \leq y/D \leq 11$. The domain is discretized by 204×260×3 points in the streamwise, transverse, vertical directions, respectively. An O-type grid with radius 20D is used for the V6-OC simulations. Three different grid resolutions coarse (128×128×3), medium (256×128×3), and fine (512×128×3) in the radial direction are taken into account for the simulations at Re = 40. The medium grid is used for the Re = 200 case.

V6.2.5 uses orthogonal curvilinear boundary layer and Cartesian grids to resolve the boundary layers on the cylinder and the other region away from the cylinder, respectively. In order to investigate the accuracy of V6.2.5, the size and resolution of the Cartesian background grid are the same as those used in the laminar simulations by V6-IBM. For the Re = 40 case, effects of the domain size (0.1D, 0.15D, and 0.2D) and grid resolution of the boundary layer grid on the numerical results are studied to identify limitation of the boundary layer domain size. As discussed later, boundary layer domain size of 0.2D is found to be sufficiently thin for the circular cylinder simulations and will be used for the rest of the circular cylinder cases.

Fig. 3.1 shows X-Y horizontal planes of the grid domains and the boundary conditions used by V6-IBM, V6-OC, and V6.2.5. For V6-IBM, uniform inlet and convective outlet boundary conditions are specified at I-MIN and I-MAX planes, respectively. Slip wall boundary conditions (i.e., zero velocity in the normal direction to the face and the Neumann condition for the other directions) are specified at the rest of the domain boundaries. A sharp-interface immersed boundary method in Yang and Stern (2009) is implemented to achieve the boundary conditions on the wall surface. For V6-

OC, no-slip boundary condition is applied to J-MIN plane which is the wall surface. Dirichlet inlet boundary conditions with uniform streamwise velocity is specified for $150° \leq \theta \leq 210°$ and convective outlet boundary conditions elsewhere for J-MAX plane far away from the wall, where θ is the tangential angle starting from the downstream direction. The bottom and top planes are specified as the same slip boundary conditions as that for V6-IBM. For V6.2.5, the Cartesian background grid is used to specify the inlet, outlet, and slip wall boundary conditions. The boundary layer grid is used to specify the no-slip boundary conditions on the wall surface. The Cartesian grid and orthogonal curvilinear grid solvers communicate with each other via the overset boundary condition at J-MAX plane of the boundary layer grid.

The boundary conditions described above are used in common by all the simulations of flows past a circular cylinder.

A pair of symmetric counter-rotating vortices behind the cylinder at Re = 40 is predicted by all the solvers on all the grids as shown in Fig. 3.2. Table 3.2 summarizes characteristics of the recirculation region, separation angle ($\Theta°$) from the trailing edge of the cylinder, drag coefficient (C_D), and pressure ($C_{D,p}$) and friction components ($C_{D,f}$) of C_D predicted at Re = 40 by the current solvers. Table 3.2 also shows the experimental data and the benchmark numerical results of the Re = 40 case in the open literature. The characteristics of the recirculation region include its length (L) from the trailing edge and location (0.5+a, b/2) of the vortex centers as shown in Fig. 3.3. Fig. 3.3 also shows the separation angle from the cylinder trailing edge. The predictions of vorticity magnitude (ω_s) and pressure (P_s) on the cylinder surface are compared with the benchmark numerical results obtained by body-fitted grid (Braza et al., 1986) and IBM (Xu, 2008) solvers in Fig. 3.4 and 3.6.

V6-IBM predicts L, b and C_D within 2% of the experimental data, while the streamwise location of the vortex centers (a) is underpredicted by 8% and Θ by 5.4%. The prediction of P_s compares well with Xu (2008) result which also uses an IBM solver,

but the minimum value is lower than that obtained by Braza et al. (1986). The peak ω_s is underpredicted by 9.6% compared to the benchmark numerical results. V6-OC predictions of C_D are within 5.5% of the experimental data on all the grids. C_D is dominated by $C_{D,p}$ which accounts for 65% of the total. The characteristics of the recirculation region are predicted within 20%, 13%, and 5.6% of the experimental data by 40-OC-C, 40-OC-M, and 40-OC-F, respectively. The predictions of P_s show no change between all the grids and the results agree very well with that of Braza et al. (1986). The peak ω_s improves by 1.63% between 40-OC-C and 40-OC-M. Both 40-OC-M and 40-OC-F results compare very well with that of Braza et al. (1986).

V6.2.5 overpredicts C_D by 6.8% of the experimental data on all the boundary layer grids, but the predictions agree very well with the benchmark numerical results. The predictions of the recirculation region characteristics and the separation angle do not show significant dependence on resolution and size of the boundary layer grid. The results are within 6.6% of the experimental data and in good agreement with the benchmark numerical results. The predictions of P_s show no significant change by the resolution of the boundary layer grid and compare very well with the result of Braza et al. (1986). The predictions of ω_s improve by 3.07% between 40-CS-C and 40-CS-M and less than 1.3% between 40-CS-M and 40-CS-F. The results of 40-CS-M and 40-CS-F compare very well with the benchmark numerical results. Both P_s and ω_s show no significant change by the size of the boundary layer grid. Fig. 3.5 shows the streamwise and transverse components of velocity around the circular cylinder at Re = 40. The predictions of the flow patterns also present no significant change by the resolution and the size of the boundary layer grid.

Overall, the predictions by V6.2.5 compare well with the experimental data and the benchmark numerical results in the literature. As shown in Fig. 3.6, V6.2.5 shows 10% better predictions of P_s and ω_s than those by V6-IBM on the same background grid resolution. This indicates that the near-wall region is resolved properly by the boundary

layer grids for V6.2.5. The results of V6.2.5 at Re = 40 imply that boundary layer domain size of 0.2D is sufficiently thin to resolve the boundary layer. Thus, the boundary layer grid size of 0.2D will be used for higher Re circular cylinder flow cases.

Periodic Karman vortex shedding is predicted by all the solvers for the Re = 200 case. The V6.2.5 predictions are shown in Fig. 3.7 for demonstration. Table 3.3 summarizes mean values and fluctuation amplitude of C_D and lift coefficient (C_L) and Strouhal number (St) at Re = 200. Table 3.3 also summarizes benchmark numerical results at Re = 200 available in the literature. St compares within 1.5% between the solvers and the benchmark numerical results. V6-IBM predicts the mean value and amplitude of C_D within 5% of the benchmark numerical results, but C_L amplitude is over-predicted by 8.5%. V6-OC predictions of mean C_D and the amplitude are underpredicted by 9.3% and 2.4%, respectively. The C_L amplitude prediction is over predicted by 12%. V6.2.5 underpredicts mean C_D by 8%. V6.2.5 predicts 2% higher C_D amplitude and 13.6% higher C_L amplitude.

V6.2.5 predictions of C_D and C_L show up to 13.6% deviation from the benchmark numerical results but are in good agreement with the benchmark data. In the time history of C_D and C_L at Re = 200 shown in Fig. 3.8, V6.2.5 and V6-OC unsteady amplitudes compare within 3% of predictions by Xu (2008), whereas V6-IBM unsteady amplitudes are underpredicted by 6%.

3.3 Large Eddy Simulations of Turbulent Flow at a Subcritical Reynolds Number

Numerical simulations are performed to compute a turbulent flow past a circular cylinder at a subcritical Re = 3900. The turbulent flow in the subcritical Re = 3900 regime is a well-studied validation case (refer to Kravchenko and Moin (2000) and reference therein) and has detailed experimental data and large eddy simulation (LES) results. The benchmark data of flow parameters include drag coefficient (C_D), base pressure coefficient (C_{pb}), Strouhal number (St), separation angle (θ_{sep}) from the cylinder

front, length (L) of the mean recirculation region, and minimum streamwise velocity (U_{min}) inside the recirculation region. Those data can be obtained from Kravchenko and Moin (2000), Ong and Wallace (1996), Cardell (1993), Son and Hanratty (1969), and Hansen and Forsythe (2004). The pressure profile on the cylinder surface is available for a slightly higher Re = 4020 originally from Norberg shown in Kravchenko and Moin (2000). For Re = 3900, Lourenco and Shih (the data taken from Kravchenko and Moin (2000)) provide detailed particle image velocimetry measurement of mean velocity and Reynolds stresses in the wake near the cylinder. Ong and Wallace (1996) show hot wire measurement of the mean velocity and the Reynolds stresses in the far wake away from the cylinder.

Kravchenko and Moin (2000) compare their own LES results with the experimental data and the LES results of Beaudan and Moin (1994), and Mittal and Moin (1997). They identify effects of the vertical grid resolution parallel to the cylinder axis on the numerical results at the subcritical Re= 3900. This will be discussed later.

The V6.2.5 results at the subcritical Re are compared with the experimental data and the benchmark LES results in the literature. In additional to the V6.2.5 simulations, the V6-IBM and V6-OC simulations are also performed at the same Re to analyze the accuracy of V6.2.5. For all the solvers, computational grids with different vertical resolutions are generated, and the numerical results are compared and analyzed with regard to the effects of the vertical grid resolution, especially on Karman vortex shedding in the flow.

Table 3.4 shows the summary of simulation conditions for Re = 3900. The domain size for the V6-IBM simulations is $-20 \leq x/D \leq 20$, $-20 \leq y/D \leq 20$, and $-3 \leq z/D \leq 3$ in the streamwise, transverse, and vertical directions, respectively. In order to analyze the effects of the vertical grid resolution, two different grids 288×248×24 and 288×248×48 are used for 3900-IBM-C and 3900-IBM-M, respectively. The V6-OC simulations are performed using O-grids with the radius 20D in the horizontal plane. The

domain size in the vertical direction is $-3 \leq z/D \leq 3$. Three different grids consisting of 1.57M, 3.14M and 12.6M points are used for 3900-OC-C, 3900-OC-M, and 3900-OC-F, respectively. Note that 3900-OC-C and 3900-OC-M have different vertical grid resolutions. The additional simulation 3900-OC-F is performed to analyze effects of the grid resolution in the horizontal directions on the numerical results.

The Cartesian domain size and grid resolutions for the V6.2.5 simulations are the same as those for the V6-IBM simulations, again, in order to investigate the accuracy of V6.2.5. The boundary layer grid resolutions for the V6.2.5 simulations 3900-CS-C and 3900-CS-M correspond to the near-wall resolutions of 3900-OC-C and 3900-OC-M, respectively.

Fig. 3.9 – 3.14 show predictions of the instantaneous flow at Re =3900. Long shear layers separating from both sides of the cylinder and the Karman vortex shedding are clearly seen in Fig. 3.9 – 3.11. The Karman vortices are affected largely by the velocity component in the vertical direction. Fig. 3.12 shows the vertical velocity on the center plane of the wake and indicates three-dimensionality of the flow at Re = 3900. The unsteady recirculation region in Fig. 3.13 and alternating regions of positive and negative transverse velocity corresponding to the Karman vortices in Fig. 3.14 can be clearly observed. In addition, 3900-OC-F prediction captures more small structures in the wake due to the finer grid resolution far away from the cylinder.

The instantaneous statistics were accumulated over approximately eight vortex shedding cycles ($T = 40D/U_\infty$). The flow quantities were also averaged over the vertical direction.

Table 3.5 compares the experimental data and the LES results of C_D, C_{pb}, St, θ_{sep}, and characteristics of the mean recirculation region, i.e., L, and U_{min}. Instantaneous values of C_D shown in Fig. 3.15 (a) were accumulated to obtain the mean value of C_D in Table 3.5. Fast Fourier transform (FFT) was performed to lift coefficients, and the values of St in Table 3.5 were determined as the peak in Fig. 3.15 (b). The predictions of C_D and

C_{pb} by V6-IBM show improvement by the grid refinement in the vertical direction. St is predicted within 4.7% of the experimental data by both 3900-IBM-C and 3900-IBM-M. The predictions of θ_{sep} indicate that the boundary layer separates earlier from the cylinder surface in 3900-IBM-M, and the prediction by 3900-IBM-M is closer to the experimental data. The V6-IBM results show that L increases between 3900-IBM-C and 3900-IBM-M, indicating that the increase is due to refinement of the vertical grid resolution. Compared to the experimental data, the deviations of L predicted by 3900-IBM-C and 3900-IBM-M are 18.6% and 10%, respectively. The overprediction of L by the finer vertical grid resolution is consistent with the LES results in Kravchenko and Moin (2000). U_{min} predicted by 3900-IBM-M is closer to the experimental data.

Predictions of the flow parameters in 3900-OC-C and 3900-OC-M show similar trends to those observed in 3900-IBM-C and 3900-IBM-M. C_D and C_{pb} improve significantly with the vertical grid refinement and the former compares within 6% of the experimental data in 3900-OC-M. St is predicted within 7% of the experimental data by both 3900-OC-C and 3900-OC-M. 3900-OC-M prediction of θ_{sep} compares within 1% of the experimental data. Compared to the experimental data, 3900-OC-C underpredicts L by 11.4%, whereas 3900-OC-M overpredicts L by 50%. Again, the trend of L with the vertical grid refinement is consistent with that observed by Kravchenko and Moin (2000). U_{min} is predicted well in 3900-OC-C but is overpredicted by 20% in 3900-OC-M. A similar overprediction was observed in the benchmark LES simulation (Kravchenko and Moin, 2000) and was explained as the result of early transition in the separated shear layers due to external disturbances to the experiment, as discussed later. The time history of the drag coefficients in Fig. 3.15 shows higher fluctuations in 3900-OC-C than in 3900-OC-M. This is because the transition in the shear layers occurs earlier in 3900-OC-C than in 3900-OC-M, as discussed later. Effects of the vertical grid resolution on the transition have been found by Kravchenko and Moin (2000) and will be discussed later in

this study. 3900-OC-F shows similar values of the flow parameters to those in 3900-OC-M, which indicates that grid refinement in horizontal directions does not affect the computations significantly.

The predictions by 3900-CS-C and 3900-CS-M show similar trends with the vertical grid refinement to those observed in the V6-IBM results and, as a consequence, the V6-OC results. The 3900-CS-M predictions are closer to the experimental data, and the differences of C_D, C_{pb}, St and θ_{sep} are within 2.02%, 0.1%, 4.65% and 6.51%, respectively. Compared to the experimental data, L and U_{min} are overpredicted by up to 42% in 3900-CS-M, while the differences are up to 8% in 3900-CS-C. Again, the overpredictions of L and U_{min} are consistent with the benchmark LES results in Kravchenko and Moin (2000). The time history of the drag coefficients shows higher fluctuations in 3900-CS-C than in 3900-CS-M.

In Fig. 3.16 - 3.20, the mean flow statistics predicted by V6.2.5, V6-OC, and V6-IBM are compared with the experimental data (Ong and Wallace, 1996) and the benchmark LES results (Beaudan and Moin, 1994; Mittal and Moin, 1997; Kravchenko and Moin, 2000). The experimental data of Norberg, and Lourenco and Shih were taken from Kravchenko and Moin (2000). Both V6-IBM predictions of surface pressure in Fig. 3.16 are in good agreement with the experimental data. On the center line of the wake, the minimum streamwise velocity of 3900-IBM-M in Fig. 3.17 is located in the more downstream region than 3900-IBM-C. As shown in Fig. 3.18, the predictions of the streamwise velocity profiles improve significantly with the vertical grid refinement especially beyond x/D = 1. In Fig. 3.19, the transverse velocity profiles predicted by 3900-IBM-C agree better with the experimental data than those by 3900-IBM-M, whereas the 3900-IBM-M predictions compare well with the benchmark LES results by Kravchenko and Moin (2000). Kravchenko and Moin (2000) attributed the discrepancies between the experimental data and the LES results to external disturbances to the experiment measurement. It is expected that such disturbances may cause transition of

the separating shear layer to turbulence occurring closer to the cylinder, which results in shorter shear layers and more prominent V-shaped profiles of the streamwise velocity. 3900-IBM-C predicts shorter shear layers than 3900-IBM-M in Fig. 3.20, and, as a consequence, the recirculation region length L of 3900-IBM-C is shorter than that of 3900-IBM-M in Table 3.5. The shorter shear layers imply that the transition to turbulence occurs earlier in 3900-IBM-C than 3900-IBM-M. Note that the only difference of the grids between 3900-IBM-C and 3900-IBM-M is the resolution in the vertical direction. Thus, the predictions of the resolved turbulence in the flow at Re = 3900 are dominated mainly by the velocity component in the vertical direction. This is consistent with observations of Kravchenko and Moin (2000). Furthermore, the Karman vortex is attached onto the cylinder surface in the 3900-IBM-C result. This results in the larger unsteadiness in C_D of 3900-IBM-C in Fig. 3.15 (a).

The turbulence statistics are compared in Fig. 3.21 and 3.22. The experimental data in the near (x/D = 1.54) and far wake ($6 \leq x/D \leq 10$) are taken from Hansen and Forsythe (2004), and Ong and Wallace (1996), respectively. At x/D = 1.54, the streamwise Reynolds normal stress $R_{xx} = \overline{u'u'}$ has the peak values at two transverse locations. The Reynolds shear stress $R_{xy} = \overline{u'v'}$ shows an almost linear decrease between the maximum and minimum values. The transverse Reynolds normal stress $R_{yy} = \overline{v'v'}$ shows the peak on the center plane. V6-IBM predictions of R_{xx} are significantly improved by the vertical grid refinement. The predictions of other Reynolds stress components by 3900-IBM-M are also in better agreement with the experimental data than 3900-IBM-C. In the far wake at x/D = 6, 7 and 10, 3900-IBM-M predictions agree better with the experimental data for both R_{xx} and R_{xy}.

The trends in the numerical results of 3900-OC-C and 3900-OC-M are similar to those observed in the results of V6-IBM simulations. In Fig. 3.16, the V6-OC predictions of the surface pressure, especially in the separated flow region, are improved by the vertical grid refinement, and both 3900-OC-M and 3900-OC-F agree very well with the

experimental data. The streamwise velocity profiles of 3900-OC-M and 3900-OC-F in Fig. 3.17 and 3.18 show the minimum values in the more downstream locations of the wake center line and more prominent U-shaped transverse profiles until x/D = 1.06 than those of the experimental data. No significant differences can be observed in the results of the streamwise velocity between 3900-OC-M and 3900-OC-F except the lower minimum value of 3900-OC-F. The transverse velocity profile of 3900-OC-C compares better with the experimental data especially at x/D = 1.06 than those of 3900-OC-M and 3900-OC-F, while the 3900-OC-M and 3900-OC-F results are in very good agreement with the LES results of Kravchenko and Moin (2000). In Fig. 3.20, 3900-OC-C shows the shorter shear layers than 3900-OC-M, and it is definitely caused by the vertical grid refinement.

Both 3900-CS-C and 3900-CS-M in Fig. 3.16 are in good agreement with the experimental data. The mean streamwise velocity on the center line of the wake in Fig. 3.17 shows that 3900-CS-C is closer to the experimental data than both 3900-IBM-C and 3900-OC-C and 3900-CS-M is closer to the LES results than both 3900-IBM-M and 3900-OC-M. This is also true for the transverse profiles of the streamwise and transverse velocities in Fig. 3.18 and 3.19. Note that, for both of the velocity components, 3900-CS-C shows the most similar profiles to those of the experimental data in the near wake region ($x/D \leq 2.02$). 3900-CS-C predicts the shorter shear layers than 3900-CS-M in Fig. 3.20. Again, this is caused by earlier transition to turbulence in the shear layers owing to the coarser vertical grid resolution. The earlier transition also results in the V-shaped profiles of the streamwise velocity near the cylinder. As shown in Fig. 3.21, the profiles of Reynolds stresses at x/D = 1.54 show that 3900-CS-M is closer to the experimental data than 3900-CS-C. Both 3900-CS-C and 3900-CS-M predict R_{xx} in good agreement with the experimental data at x/D = 6 and 7, but the predictions are lower at x/D = 10 due to the relatively coarse grid resolution in the far wake region. Both of the predictions of R_{xy} agree well with the experimental data.

3.4 Large Eddy Simulations of Turbulent Flows at Supercritical Reynolds Numbers

In order to demonstrate the performance of V6.2.5 in very high Re complex turbulent flows, numerical simulations are performed by V6.2.5 for the turbulent flows past a circular cylinder at the supercritical Re = 5×10^5 and 1×10^6, i.e., 5E5-CS and 1E6-CS shown in Table 3.6. The numerical results of 5E5-CS and 1E6-CS are compared with the experimental data of the surface pressure in Warschauer and Leene (1971) and Zdravkovich (1997). The V6.2.5 results are also compared with the LES results of Catalano et al. (2003). Effects of Re on the turbulent flows past a circular cylinder are analyzed by comparing the V6.2.5 results of the higher supercritical Re flows with those of the lower subcritical Re flow, i.e., 3900-CS-M.

Table 3.6 shows the simulation conditions for the flows at the supercritical Re. For both 5E5-CS and 1E6-CS, the Cartesian domain size is $-5 \le x/D \le 15$, $-10 \le y/D \le 10$, and $-1 \le z/D \le 1$. Catalano et al. (2003) show the delayed separation and the resulting narrower wake at the supercritical Re than lower Re, such as subcritical Re = 3900 and 1.4×10^5 (Kravchenko and Moin, 2000; Breuer, 2000). Because of this, the domain size of V6.2.5 in the transverse direction is smaller than that used for the lower Re = 3900. The vertical domain length is also shorter than that for the Re = 3900 case because of the reduced vertical correlation lengths in the higher Re flows. The same vertical domain length was used by Catalano et al. (2003). The grid consists of 10.2M points.

Fig. 3.23 compares profiles of the mean pressure on the cylinder surface at the supercritical Re. The experimental data of Flachsbart was obtained from Zdravkovich (1997). The predictions of 5E5-CS and 1E6-CS are in good agreement with the experimental data at similar Re, respectively. The 1E6-CS result also agrees well with the LES result of Catalano et al. (2003) at the same Re. The experimental data of Flachsbart at Re = 6.7×10^5 contains a kink near 105°. This indicates the presence of a separation

bubble. It is difficult for both experiments and numerical simulations to reproduce the separation bubble due to sensitivity to disturbances (Catalano et al., 2003).

The surface pressures are compared between the V6.2.5 predictions and the experimental data at similar Re in Fig. 3.24. The pressure gradients in the front part are larger at the supercritical Re = 5×10^5 and 1×10^6 than that at the subcritical Re = 3900. Near the cylinder trailing edge, the pressures at the supercritical Re are higher than that at the subcritical Re. The adverse pressure gradients at the supercritical Re exist between 90° and 125°, whereas it is located between 75° and 100° at the subcritical Re. This leads to the later separations of the boundary layers at the supercritical Re, as shown later.

Fig. 3.25 compares the instantaneous vertical vorticity and the mean streamwise velocity between Re = 3900, 5×10^5, and 1×10^6. Compared with the subcritical Re = 3900, the flows at the supercritical Re = 5×10^5 and 1×10^6 exhibits the delayed separations of the boundary layers. The postponed separations result in the narrower wakes and the shorter recirculation regions at both of the supercritical Re than those at the subcritical Re. At the supercritical Re, the shear layers interact with each other near the outer edge of the recirculation regions. The interactions of the shear layers result in vortices shed into the wake.

Fig. 3.26 and 3.27 show the iso-surfaces of the instantaneous vorticity magnitude ($\omega = 2.5$) and the second invariant of the velocity gradient tensor ($Q = 1$), respectively. Note that the cylinder lengths are 6D and 2D at the subcritical and supercritical Re, respectively. The vortical structures at the subcritical Re show Karman vortex streets clearly, whereas the structures at the supercritical Re are not similar to the Karman type of the vortex shedding. Shear layers separating from both sides of the cylinder develop in the streamwise direction at both of the supercritical Re. Many small-scale vortices exist inside the recirculation regions between the shear layers. The iso-surfaces of the second invariant of the velocity gradient tensor show the quasi-vertical vortical structures, which indicate the vortices in the shear layers.

Three instantaneous velocity components on the center plane of the wake are compared between the subcritical Re = 3900 and the supercritical Re = 5×10^5 and 1×10^6 in Fig. 3.28 – 3.30. Negative streamwise velocity can be observed behind the cylinder at both supercritical and subcritical Re, which indicates the recirculation region. The minimum streamwise velocities inside the recirculation regions are larger at the supercritical Re ($U_{min} \approx -0.4$) than that ($U_{min} \leq -0.8$) at the subcritical Re. Alternating regions of positive and negative transverse velocity can be observed clearly in the wake at the subcritical Re, whereas they are not clearly shown at both supercritical Re. The magnitudes of the maximum and minimum transverse velocities are higher at the subcritical Re. The vertical velocity component contours at the supercritical Re show the remarkable three-dimensionality of the turbulent flows and the smaller flow structures which correspond to the small-scale vortices in the wake at the high Re.

Fig. 3.31 – 3.33 show two Reynolds normal stresses and the Reynolds shear stress in the wake at Re = 3900, 5×10^5 and 1×10^6. All of the Reynolds stresses are symmetric about the center axis of the wakes. The peak values of the Reynolds stresses are smaller at the supercritical Re = 5×10^5 and 1×10^6 than those at the subcritical Re = 3900. At all the Re, the transverse Reynolds normal stress achieves the peak value along the center line of the wake, and the peaks of the streamwise Reynolds normal stress and the Reynolds shear stress exist off the wake center axis.

Mean flow fields and Reynolds stresses at the supercritical Re = 5×10^5 and 1×10^6 are presented in Fig. 3.34 and 3.35, respectively. The flows at both Re show similar characteristics. The streamwise velocity is negative behind the cylinder, which indicates the existence of the recirculation regions. In the recirculation regions, the transverse velocity magnitude is very low and large amounts of the small-scale vortices are generated. The Reynolds stresses show the peak values near the edges of the recirculation regions where the velocity gradients are high, and the normal components are larger than the shear component.

The vorticity transport equation can be derived by taking the curl of the time-averaged Navier-Stokes equation. For a steady flow of constant density, the transport equation of the vertical vorticity can be written as:

$$\left(U\frac{\partial \Omega_z}{\partial x}+V\frac{\partial \Omega_z}{\partial y}+W\frac{\partial \Omega_z}{\partial z}\right) \quad \text{(A)}$$

$$=\left(\Omega_x\frac{\partial W}{\partial x}+\Omega_y\frac{\partial W}{\partial y}+\Omega_z\frac{\partial W}{\partial z}\right) \quad \text{(B)}$$

$$+\nu\left(\frac{\partial^2 \Omega_z}{\partial x^2}+\frac{\partial^2 \Omega_z}{\partial y^2}+\frac{\partial^2 \Omega_z}{\partial z^2}\right) \quad \text{(C)}$$

$$+\frac{\partial}{\partial z}\left(\frac{\partial \overline{u'w'}}{\partial y}-\frac{\partial \overline{v'w'}}{\partial x}\right) \quad \text{(D)}$$

$$+\frac{\partial^2}{\partial x \partial y}\left(\overline{u'u'}-\overline{v'v'}\right) \quad \text{(E)}$$

$$+\left(\frac{\partial^2}{\partial y^2}-\frac{\partial^2}{\partial x^2}\right)\overline{u'v'} \quad \text{(F)} \qquad (3.1)$$

where Ω_x, Ω_y, and Ω_z are the streamwise, transverse, and vertical components of the mean vorticity, respectively. Term (A) in Eq. (3.1) represents the material derivative of the mean vertical vorticity. The third term of term (B) is the vorticity amplification by the vertical stretching, while the other terms provide vortex-line bending effects. Term (C) suggests the vorticity damping by the viscous diffusion. Terms (D), (E), and (F) are the vorticity production by inhomogeneities in the Reynolds stress field (Launder and Rodi, 1983). Longo et al. (1998) analyzed the physical mechanism of the mean streamwise vortices in a solid/free-surface juncture flow using the vorticity transport equation. Suh et al. (2011) and Koo (2011) used the transport equations of all vorticity components to explain the mechanism to generate the vortices in the flows past an interface piercing circular cylinder. In this study, the transport equation of the mean vertical vorticity is used to analyze the mechanism to generate the vortices in the single-phase flows at the very high supercritical Re = 5×10^5 and 1×10^6.

Fig. 3.36 and 3.37 show the source terms for the mean vertical vorticity at Re = 5×10^5 and 1×10^6, respectively. Both of the supercritical Re results present the similar

features. The x and y components of term (B) by the vortex bending are negligibly small, while the z component of term (B) by the vortex stretching is relatively larger than the other components due to the strong vertical vortices in the shear layers, as shown in Fig. 3.34 and 3.35. The source terms produced by the Reynolds stresses are also large in the wake region. Note that the small-scale vortices in the recirculation region between the shear layers are dominantly generated by the Reynolds stresses. The mean vertical vortices in the shear layers are produced dominantly by the term (E) $\partial^2/\partial x\partial y(\overline{u'u'} - \overline{v'v'})$ and the term (F) $(\partial^2/\partial y^2 - \partial^2/\partial x^2)\overline{u'v'}$ due to the high gradients of the streamwise Reynolds normal stress ($\overline{u'u'}$) and the Reynolds shear stress ($\overline{u'v'}$) in the part of the flows.

3.5 Summary

Validations of V6.2.5 have been performed for the single-phase flows past a circular cylinder. The validations cover the two-dimensional steady (Re = 40) and unsteady (Re = 200) laminar flows and the turbulent flows at the subcritical Re = 3900 and the supercritical Re = 5×10^5 and 1×10^6. This study has also analyzed the effects of the domain size and the grid resolution of the boundary layer grid on the numerical results at Re = 40 and the effects of the vertical grid resolution on the numerical results at Re = 3900. The numerical results obtained by V6.2.5 have been compared with those by V6-IBM, a Cartesian grid solver, and V6-OC, an orthogonal curvilinear grid solver. The results have also been compared with the numerical results and the experimental data in the literature.

At Re = 40, the numerical results obtained by V6.2.5 show no significant dependence on the resolution and the size of the boundary layer grid. V6.2.5 predicts a pair of the symmetric counter-rotating vortices behind the cylinder, and the characteristics of the recirculation region are predicted within 6.6% of the experimental data. The predictions of the drag coefficient are 6.8% higher than the experimental data, but they agree very well with the numerical results of the past studies. Compared to the numerical results in the literature, V6.2.5 predicts up to 10% better vorticity magnitude

and pressure distributions on the cylinder surface than V6-IBM with the same Cartesian grid. This indicates that the near-wall region is resolved properly by the boundary layer grids for V6.2.5.

Periodic Karman vortex shedding was reproduced by V6.2.5 at Re = 200. V6.2.5 predicts the drag coefficient, the lift coefficient, and Strouhal number in good agreement with the numerical results of several past studies.

At Re = 3900, V6.2.5 reproduces the long shear layers separating from both sides of the circular cylinder and the Karman vortices interacting with the vertical velocity component. V6.2.5 has predicted the mean flow parameters including the drag coefficient, the base pressure coefficient, the Strouhal number, the separation angle from the cylinder leading edge, the length of the mean recirculation region, and the minimum streamwise velocity inside the recirculation region. The predictions of the mean flow parameters compare within 6.5% of the experimental data. The numerical results by V6.2.5 have also been compared with the experimental data and the results by V6-IBM, V6-OC, and the numerical study of Kravchenko and Moin (2000) in terms of the profiles of the velocity components and the Reynolds stresses in the wake region. The study of the effects of the vertical grid resolution has shown better agreement of the coarser grid results with the experimental data. On the other hand, the results given by the finer grids agree better with the LES results by Kravchenko and Moin (2000). These trends with the vertical grid resolution are consistent with those in Kravchenko and Moin (2000), and it has been explained that both the coarser grid predictions and the experimental data exhibit earlier transitions of the shear layer to turbulence than the finer grid predictions, which result in significantly smaller recirculation regions.

In order to demonstrate the performance of V6.2.5 in the turbulent flows at very high Re, the numerical simulations have been performed for the flows at the supercritical Re = 5×10^5 and 1×10^6. Compared to the flow at the subcritical Re = 3900, much delayed separations of the boundary layers have been predicted at the supercritical Re = 5×10^5

and 1×10^6. The delayed separations lead to the narrower wakes and the shorter recirculation regions at the very high Re. The predictions of V6.2.5 have been compared with the experimental and numerical results in terms of the pressure profiles on the cylinder surface. V6.2.5 has shown the good agreement with the experimental data and the LES results by Catalano et al. (2003). In this study, the effects of Re on the turbulent flows have also been analyzed by comparing the V6.2.5 numerical results at the subcritical Re (=3900) and the supercritical Re (= 5×10^5 and 1×10^6). The surface pressure shows the features corresponding to the separation at each Re. Many small-scale vortices are generated between the shear layers right behind the cylinder at the supercritical Re, while they are not generated at the subcritical Re. The Reynolds stress contours show the similar distributions, but the magnitudes are smaller at the supercritical Re. The mechanism to generate the vertical vortices at the supercritical Re has been analyzed using the vorticity transport equation. The analysis has revealed that the vertical vortices in the wake are generated mainly by the gradients of the Reynolds stresses and the vertical stretching effect.

Table 3.1 Simulation conditions for the laminar flows at Re = 40 and 200

Case	Re	Solver	Domain size	Boundary layer domain	Grid resolution	
					$N_x \times N_y \times N_z$	$N_r \times N_\theta \times N_z$
40-IBM	40	V6-IBM	$-20 \le x/D \le 20$ $-11 \le y/D \le 11$	-	204×260×3	-
40-OC-C		V6-OC	O-type grid r/D = 20	-	-	128×128×3
40-OC-M					-	256×128×3
40-OC-F					-	512×128×3
40-CS-C		V6.2.5	$-20 \le x/D \le 20$ $-11 \le y/D \le 11$	0.20D	204×260×3	13×128×3
40-CS-M					204×260×3	22×128×3
40-CS-F1					204×260×3	32×128×3
40-CS-F2				0.15D	204×260×3	24×128×3
40-CS-F3				0.10D	204×260×3	17×128×3
200-IBM	200	V6-IBM	$-20 \le x/D \le 20$ $-11 \le y/D \le 11$	-	204×260×3	-
200-OC		V6-OC	O-type grid r/D = 20	-	-	256×128×3
200-CS		V6.2.5	$-20 \le x/D \le 20$ $-11 \le y/D \le 11$	0.20D	204×260×3	22×128×3

Table 3.2 Characteristics of the recirculation region, separation angles, drag coefficients, and pressure and friction components at Re = 40

	L	a	b	Θ°	C_D	$C_{D,p}$	$C_{D,f}$
Experiment	2.13	0.76	0.59	53.8	1.48	-	-
Numerical results (E)	2.28 ± 0.07 (7.04%)	0.72 ± 0.01 (-5.26%)	0.58 ± 0.02 (-1.69%)	54.3 ± 1.3 (0.93%)	1.60 ± 0.10 (8.11%)	-	-
40-IBM (E)	2.11 (-0.94%)	0.70 (-7.89%)	0.58 (-1.69%)	50.9 (-5.39%)	1.51 (2.03%)	0.97	0.54
40-OC-C (E)	1.86 (-12.7%)	0.61 (-19.7%)	0.55 (-6.78%)	51.7 (-3.90%)	1.55 (4.73%)	1.01	0.54
40-OC-M (E)	2.05 (-3.76%)	0.66 (-13.2%)	0.58 (-1.69%)	52.4 (-2.60%)	1.56 (5.41%)	1.02	0.54
40-OC-F (E)	2.01 (-5.63%)	0.73 (-3.95%)	0.57 (-3.39%)	54.0 (0.37%)	1.56 (5.41%)	1.02	0.54
40-CS-C (E)	2.24 (5.16%)	0.72 (-5.26%)	0.59 (0%)	53.7 (-0.19%)	1.58 (6.76%)	1.04	0.54
40-CS-M (E)	2.24 (5.16%)	0.72 (-5.26%)	0.59 (0%)	53.7 (-0.19%)	1.58 (6.76%)	1.04	0.54
40-CS-F1 (E)	2.24 (5.16%)	0.72 (-5.26%)	0.59 (0%)	54.0 (0.37%)	1.58 (6.76%)	1.04	0.54
40-CS-F2 (E)	2.24 (5.16%)	0.71 (-6.58%)	0.59 (0%)	54.2 (0.74%)	1.58 (6.76%)	1.04	0.54
40-CS-F3 (E)	2.23 (4.69%)	0.72 (-5.26%)	0.59 (0%)	54.0 (0.37%)	1.58 (6.76%)	1.04	0.54

Table 3.3 Drag and lift coefficients and Strouhal numbers at Re = 200

	C_D		C_L		St
	Mean	Amplitude	Mean	Amplitude	
Numerical results	1.455 ± 0.115	0.042 ± 0.012	0	0.59 ± 0.16	0.200 ± 0.002
200-IBM	1.41	0.040	0	0.64	0.200
200-OC	1.32	0.041	0	0.66	0.197
200-CS	1.34	0.043	0	0.67	0.199

Table 3.4 Simulation conditions for turbulent flows at Re = 3900

Case	Solver	Domain size	Boundary layer domain	Grid resolution	
				$N_x \times N_y \times N_z$	$N_r \times N_\theta \times N_z$
3900-IBM-C	V6-IBM	$-20 \le x/D \le 20$ $-20 \le y/D \le 20$ $-3 \le z/D \le 3$	-	288×248×24	-
3900-IBM-M				288×248×48	-
3900-OC-C	V6-OC	O-type grid r/D = 20 $-3 \le z/D \le 3$	-	-	256×256×24
3900-OC-M				-	256×256×48
3900-OC-F				-	512×512×48
3900-CS-C	V6.2.5	$-20 \le x/D \le 20$ $-20 \le y/D \le 20$ $-3 \le z/D \le 3$	0.2D	288×248×24	20×256×24
3900-CS-M				288×248×48	20×256×48

Table 3.5 Drag coefficients, Strouhal numbers, separation angle from the cylinder front and characteristics of the mean recirculation region at Re = 3900

	C_D	$-C_{pb}$	St	θ_{sep}	L/D	$-U_{min}$
Experiment	0.99 ± 0.05	0.88 ± 0.05	0.215 ± 0.005	86.0° ± 2°	1.4 ± 0.1	0.24 ± 0.1
LES (E)	1.00 ~ 1.04 (3.03%)	0.93 ~ 0.95 (6.82%)	0.203 ~ 0.210 (-3.95%)	85.8° ~ 88.0° (1.05%)	1.35 ~ 1.40 (-1.79%)	0.32 ~ 0.37 (43.8%)
3900-IBM-C (E)	1.20 (21.2%)	1.00 (13.6%)	0.225 (4.65%)	115° (33.7%)	1.14 (-18.6%)	0.46 (91.7%)
3900-IBM-M (E)	1.02 (3.03%)	0.87 (-1.14%)	0.225 (4.65%)	110° (27.9%)	1.54 (10.0%)	0.28 (16.7%)
3900-OC-C (E)	1.20 (21.2%)	1.03 (17.0%)	0.200 (6.98%)	90.0° (4.65%)	1.24 (-11.4%)	0.24 (0%)
3900-OC-M (E)	0.93 (-6.06%)	0.88 (0%)	0.200 (6.98%)	86.7° (0.81%)	2.10 (50.0%)	0.29 (20%)
3900-OC-F (E)	0.94 (-5.05%)	0.85 (3.41%)	0.198 (-7.91%)	86.5° (0.58%)	2.14 (52.9%)	0.36 (50%)
3900-CS-C (E)	1.18 (19.2%)	0.92 (4.55%)	0.208 (-3.26%)	97.0° (12.8%)	1.51 (7.86%)	0.25 (4.17%)
3900-CS-M (E)	0.97 (-2.02%)	0.88 (0%)	0.225 (4.65%)	91.6° (6.51%)	1.89 (35.0%)	0.34 (41.7%)

Table 3.6 Simulation conditions for turbulent flows at Re = 5.0×10^5 and 1.0×10^6

Case	Re	Solver	Domain size	Boundary layer domain	Grid resolution	
					$N_x\times N_y\times N_z$	$N_r\times N_\theta\times N_z$
5E5-CS	5.0×10^5	V6.2.5	$-5 \le x/D \le 15$ $-10 \le y/D \le 10$ $-1 \le z/D \le 1$	0.2D	220×200×200	28×256×200
1E6-CS	1.0×10^6					

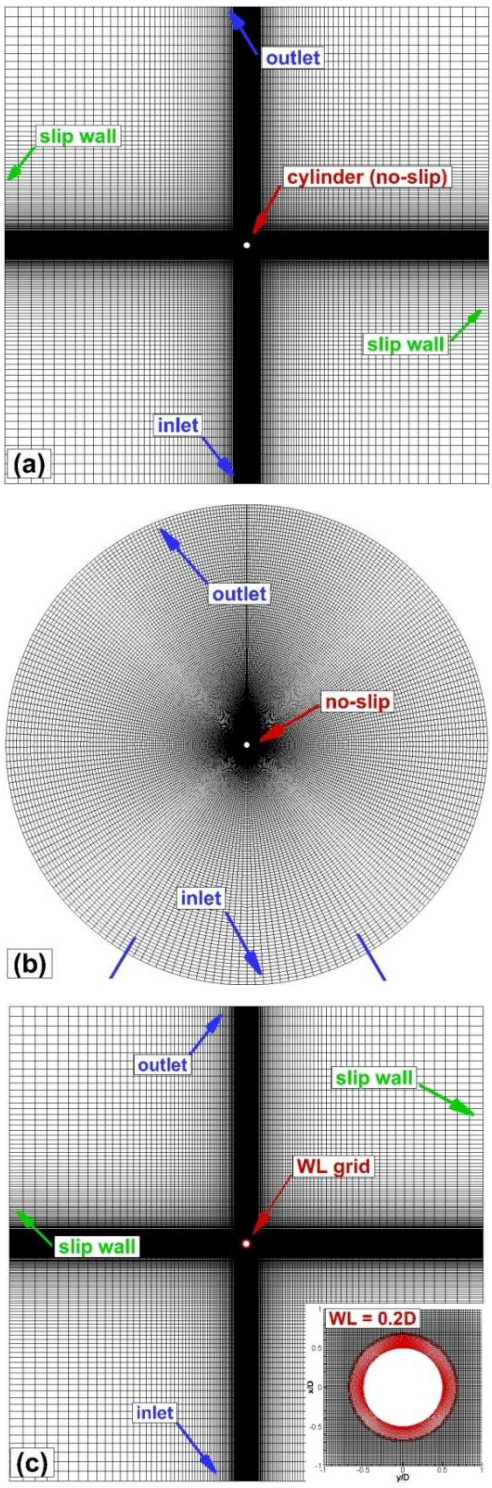

Figure 3.1 Computational grids and boundary conditions for (a) V6-IBM, (b) V6-OC, and (c) V6.2.5. The inset shows the boundary layer domain size of 0.2D.

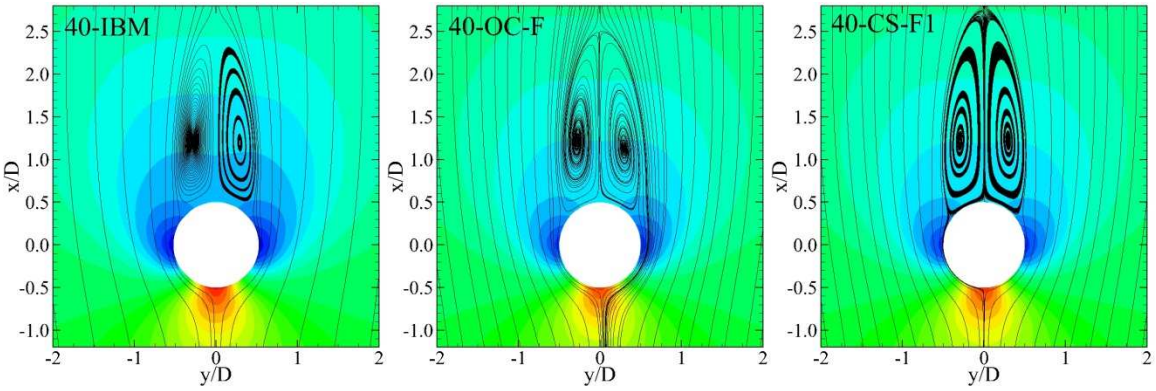

Figure 3.2 Streamlines and pressure contours around the circular cylinder at Re = 40. The range of the pressure contours is from -0.45 to 0.65 with the interval 0.05.

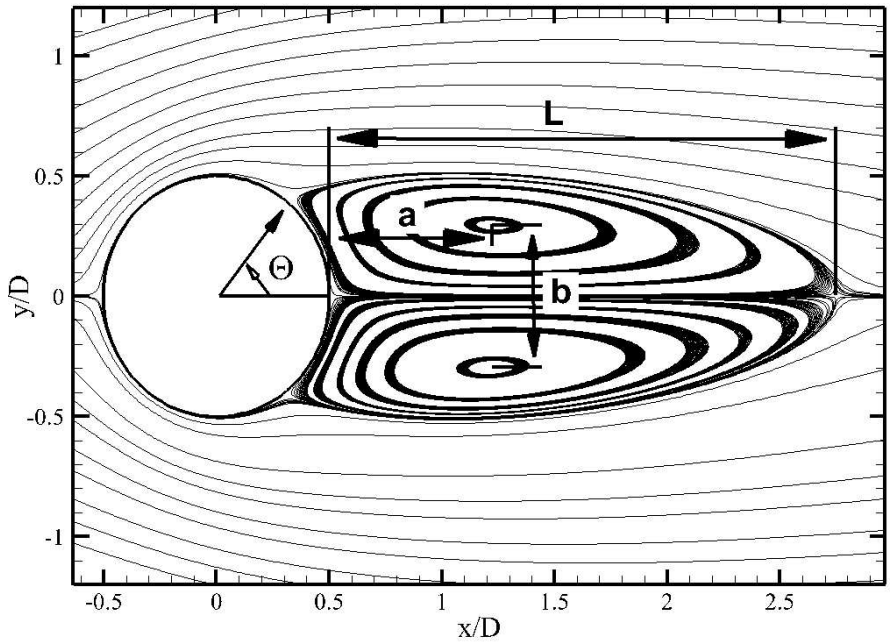

Figure 3.3 Characteristics of the recirculation region at Re = 40

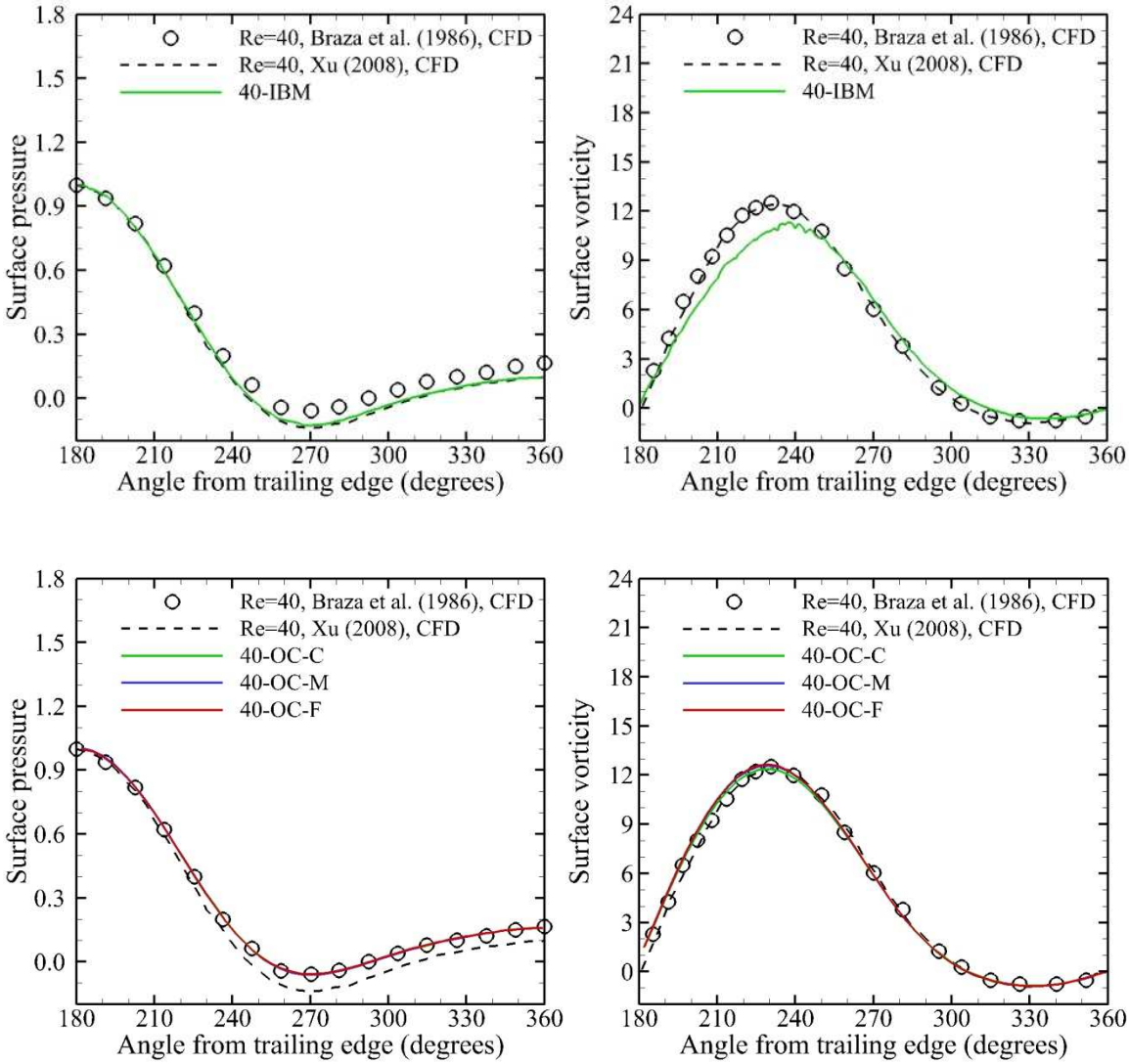

Figure 3.4 Distribution of pressure (left column) and vorticity magnitude (right column) on the circular cylinder surface at Re = 40

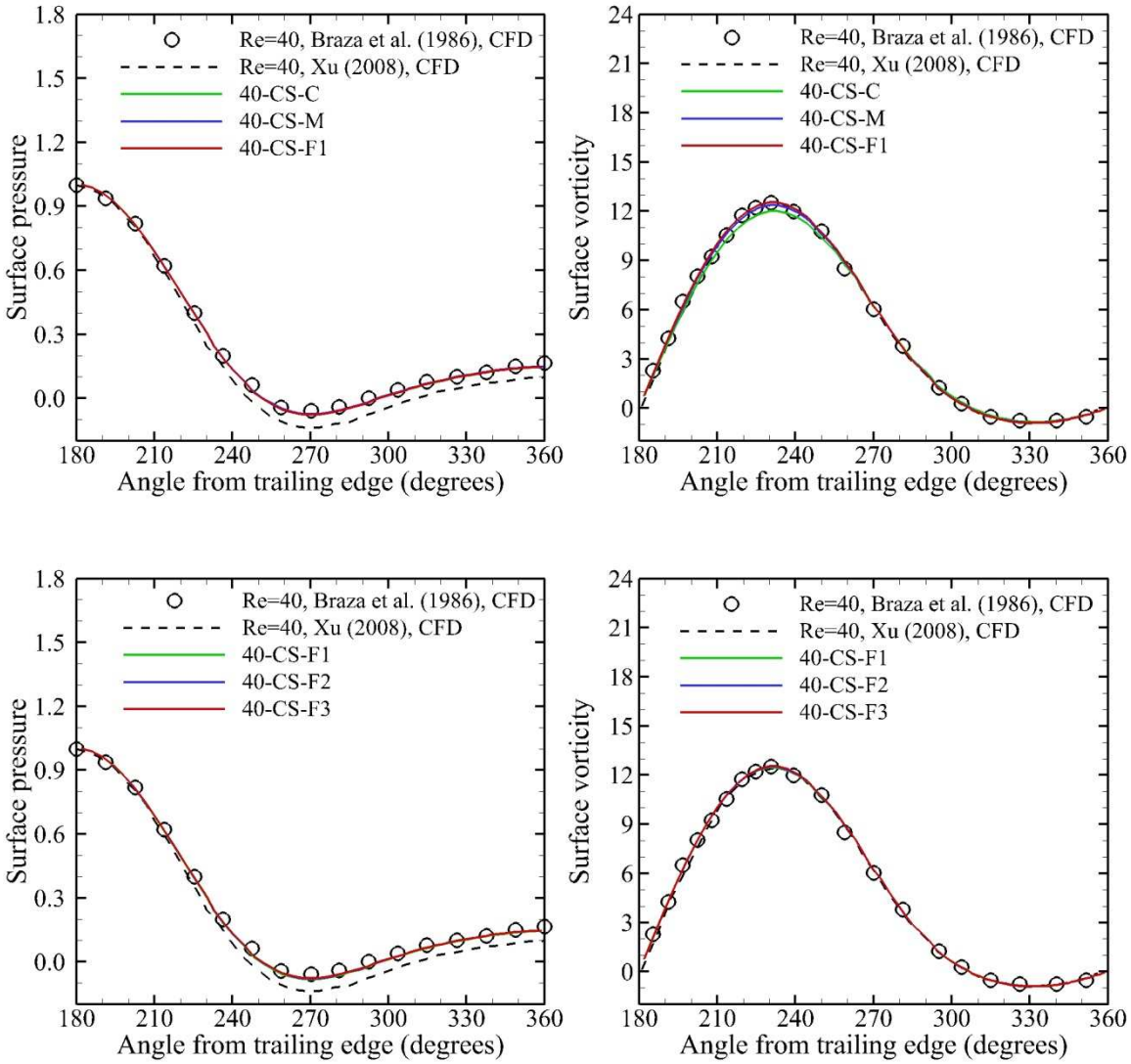

Figure 3.4 Continued

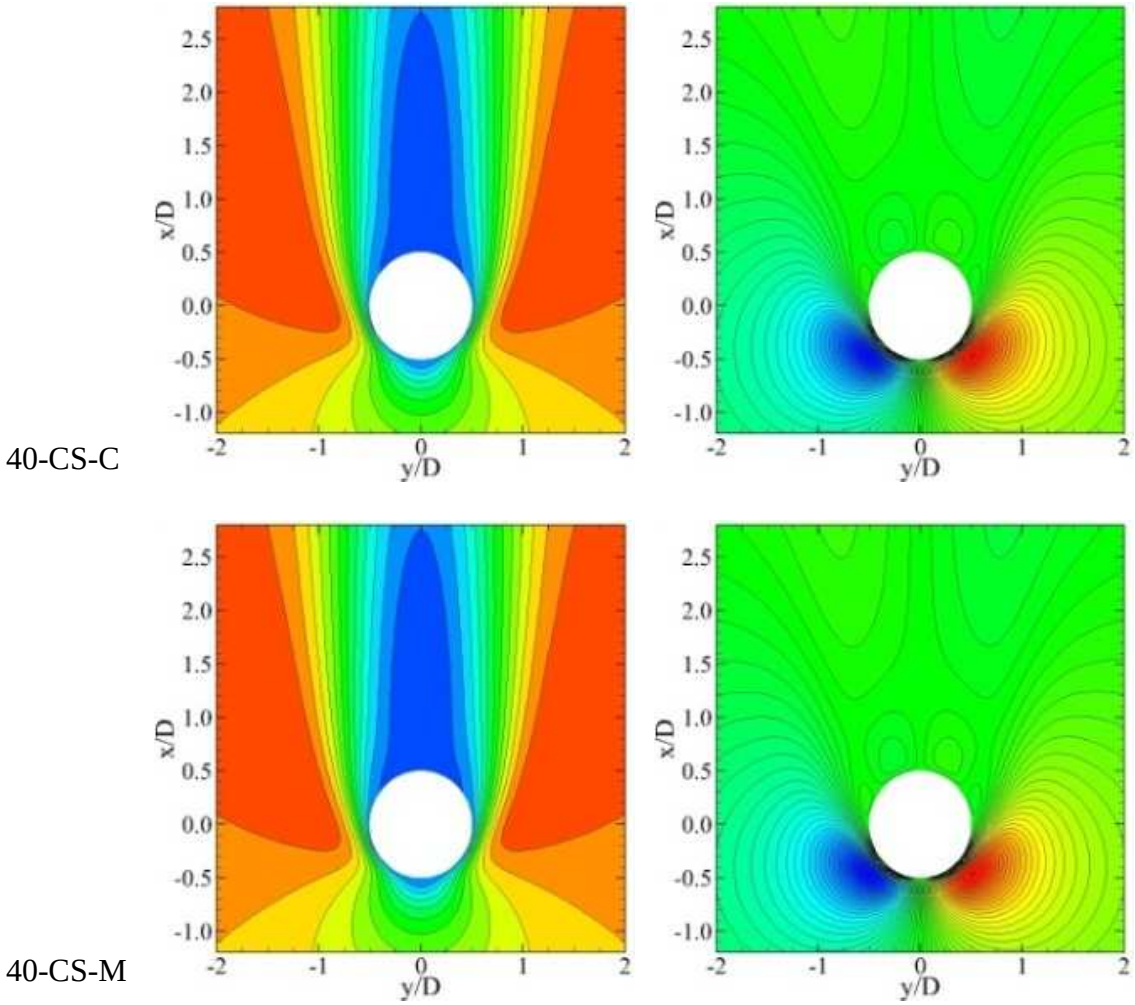

Figure 3.5 Streamwise (left column) and transverse (right column) components of velocity around the circular cylinder at Re = 40. The contour range is -0.1 - 1.2 with the interval 0.1 and -0.55 - 0.55 with the interval 0.02 for the streamwise and transverse components, respectively.

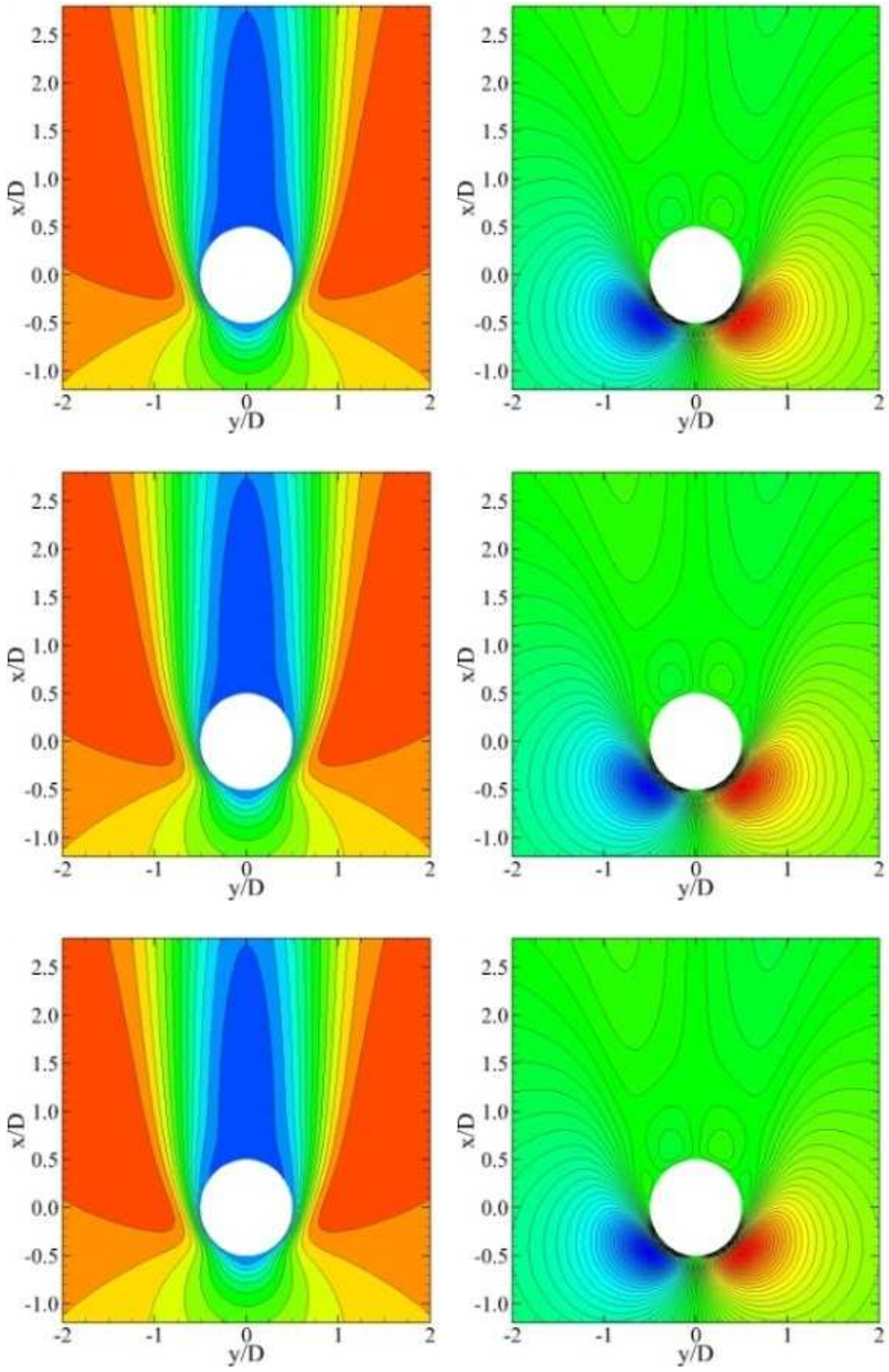

Figure 3.5 Continued

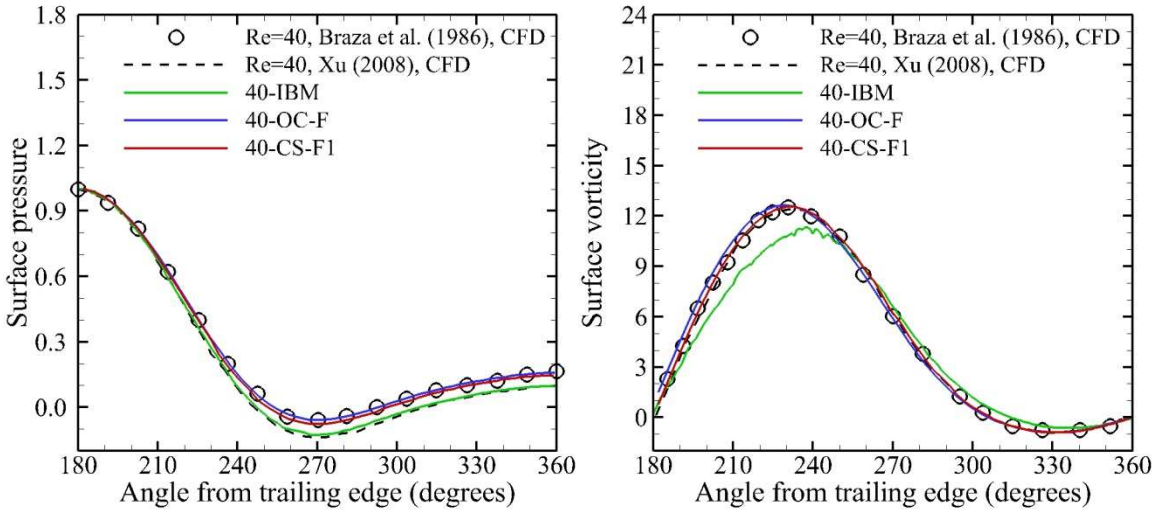

Figure 3.6 Comparison of pressure (left column) and vorticity magnitude (right column) on the circular cylinder surface at Re = 40 among the current solvers

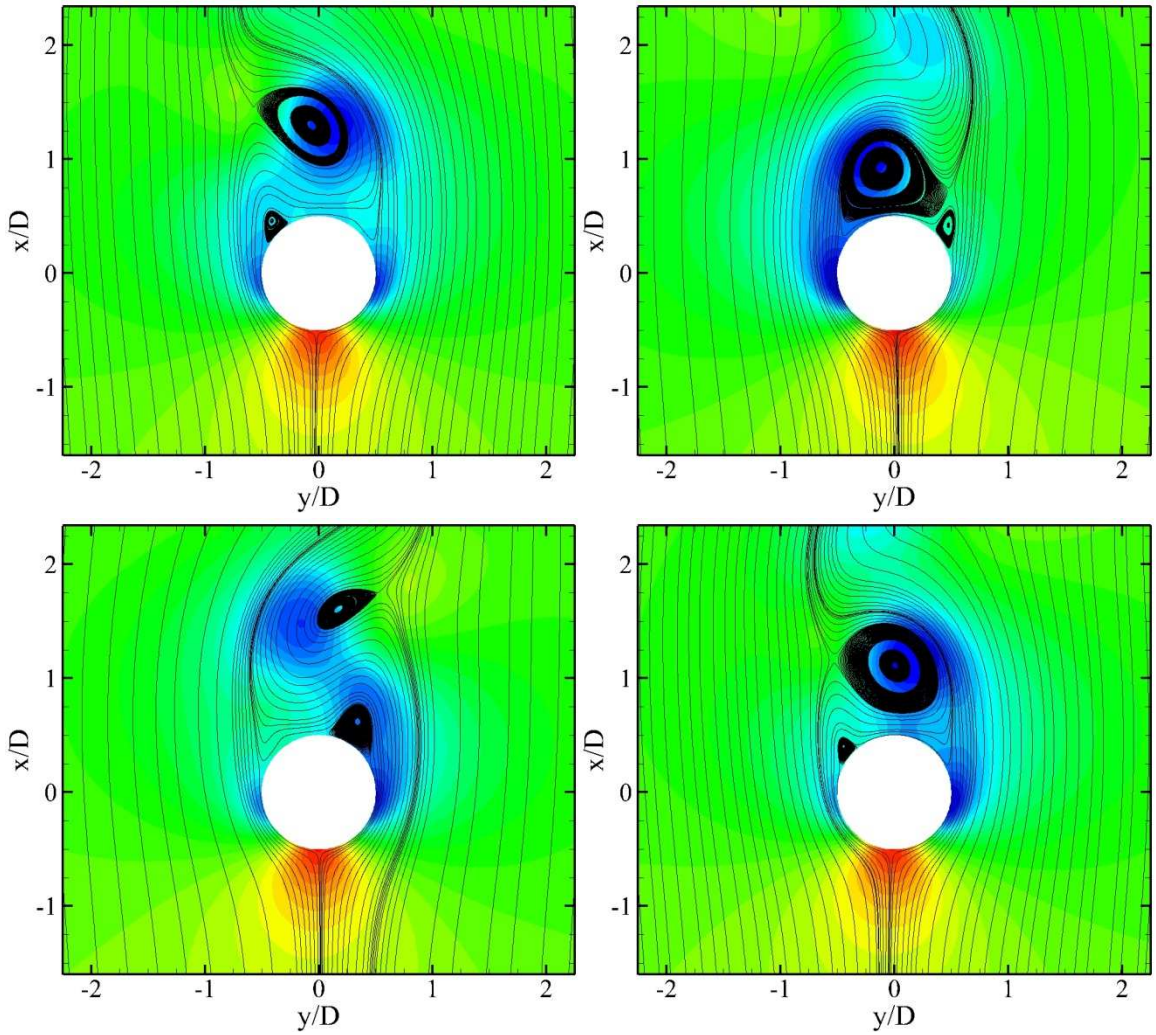

Figure 3.7 Vortex shedding obtained by 200-CS. The contours show pressure distribution with the range -0.65~0.65 and interval 0.05.

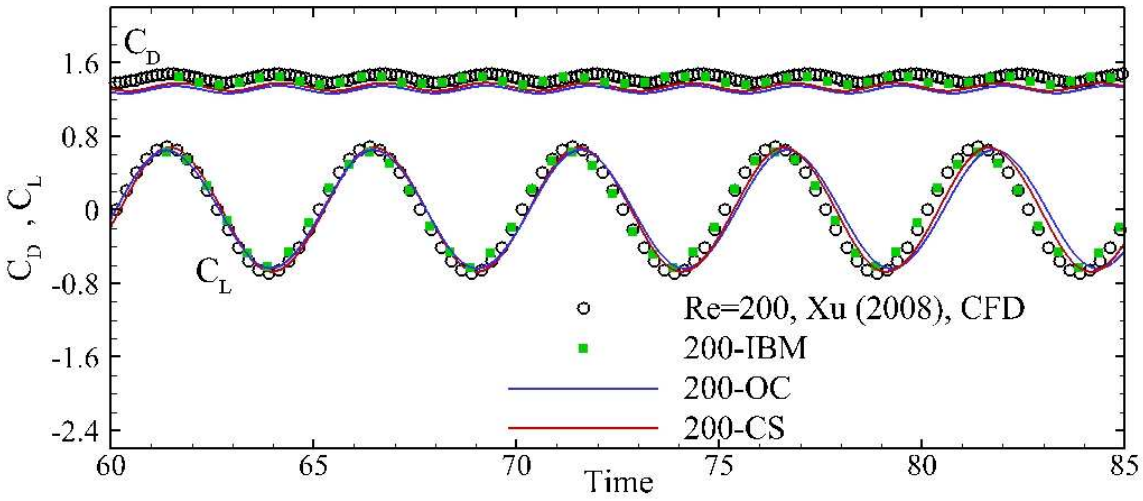

Figure 3.8 Time histories of drag and lift coefficients compared with those obtained by Xu (2008)

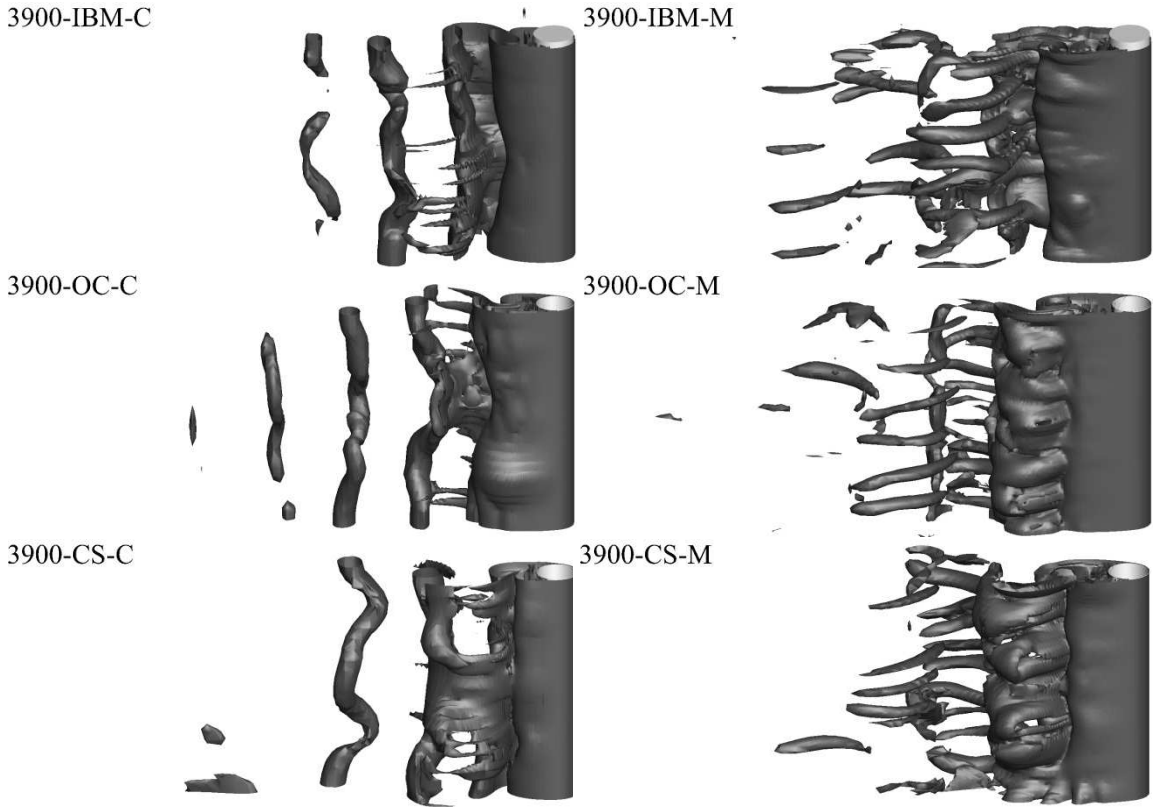

Figure 3.9 Iso-surfaces of instantaneous vorticity magnitude (ωD/U = 2.5) around the cylinder

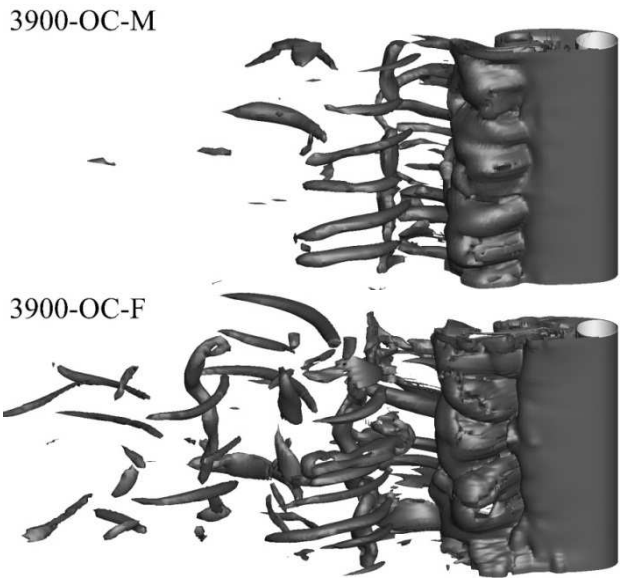

Figure 3.10 Comparison of iso-surfaces of instantaneous vorticity magnitude (ωD/U = 2.5) around the cylinder between 3900-OC-M and 3900-OC-F

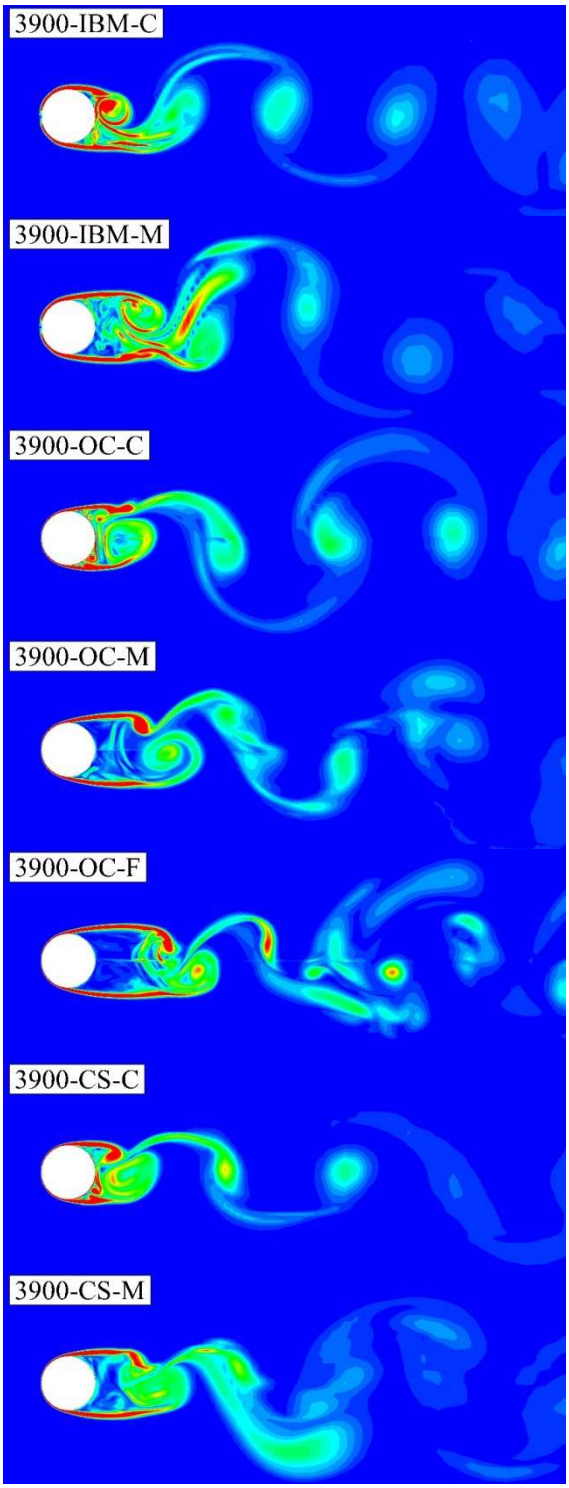

Figure 3.11 Instantaneous vorticity magnitude in the wake. The contour range is 0.5 – 10 with interval 0.5.

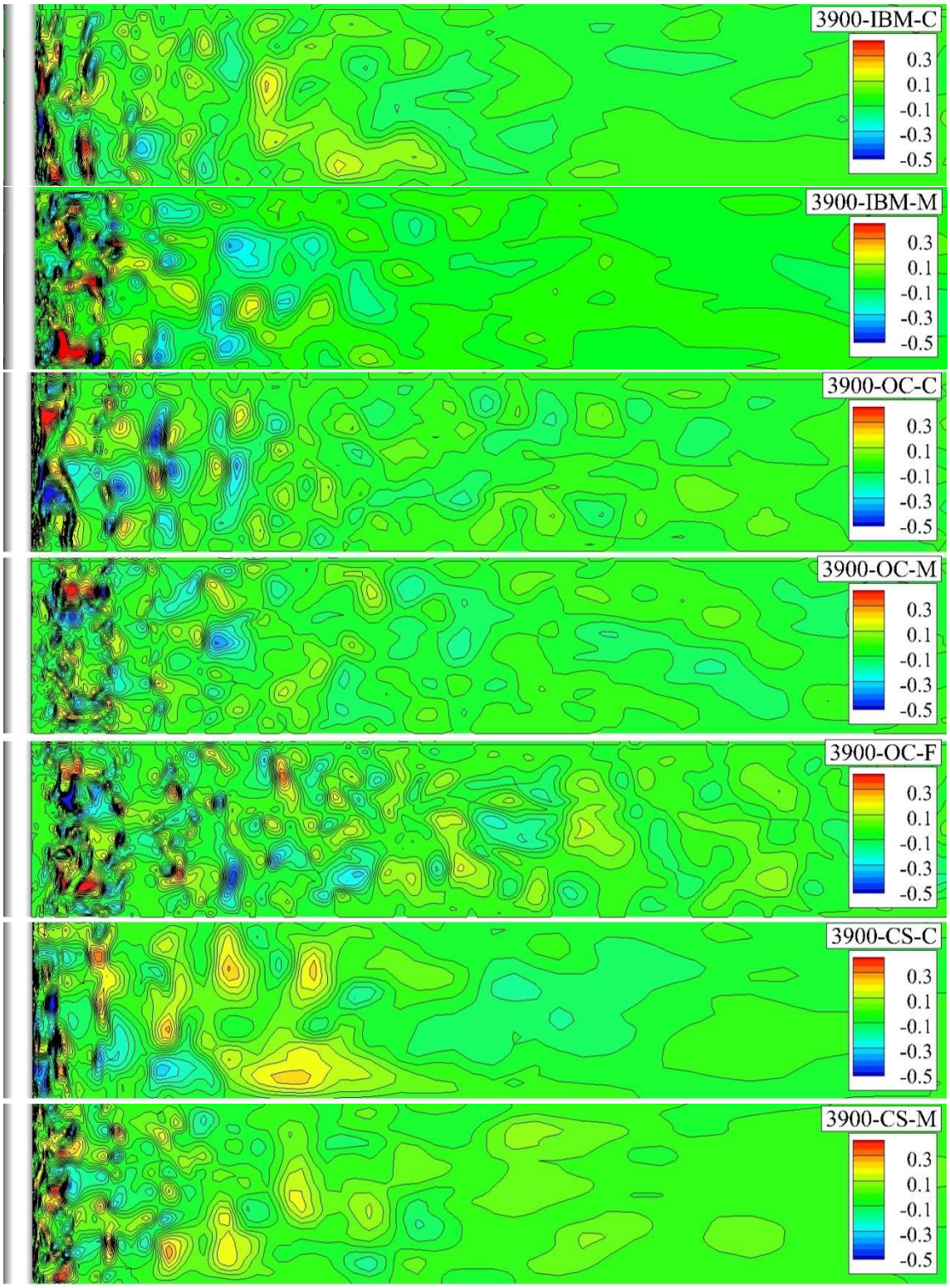

Figure 3.12 Instantaneous vertical velocity on the center plane of the wake

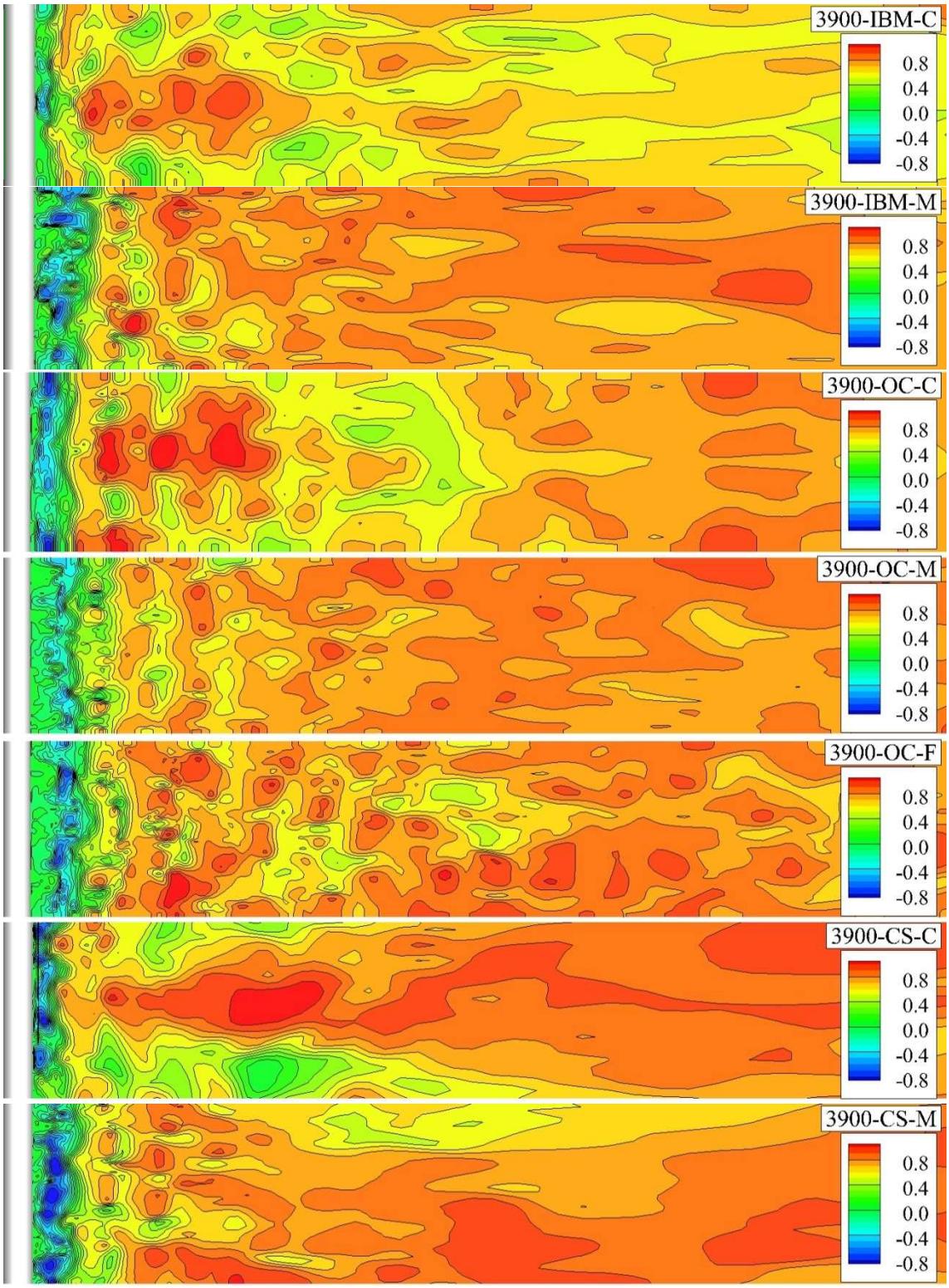

Figure 3.13 Instantaneous streamwise velocity on the center plane of the wake

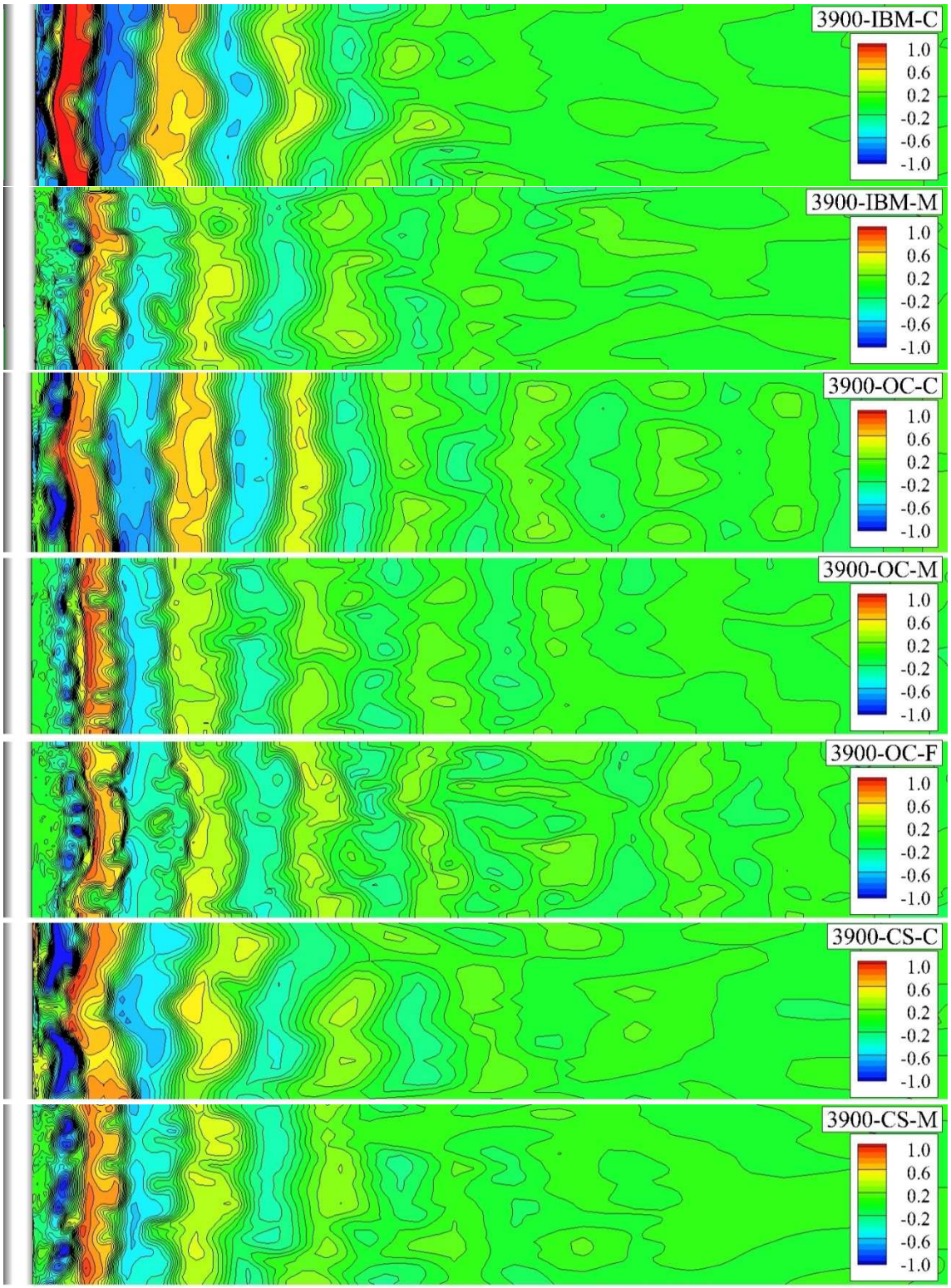

Figure 3.14 Instantaneous transverse velocity on the center plane of the wake

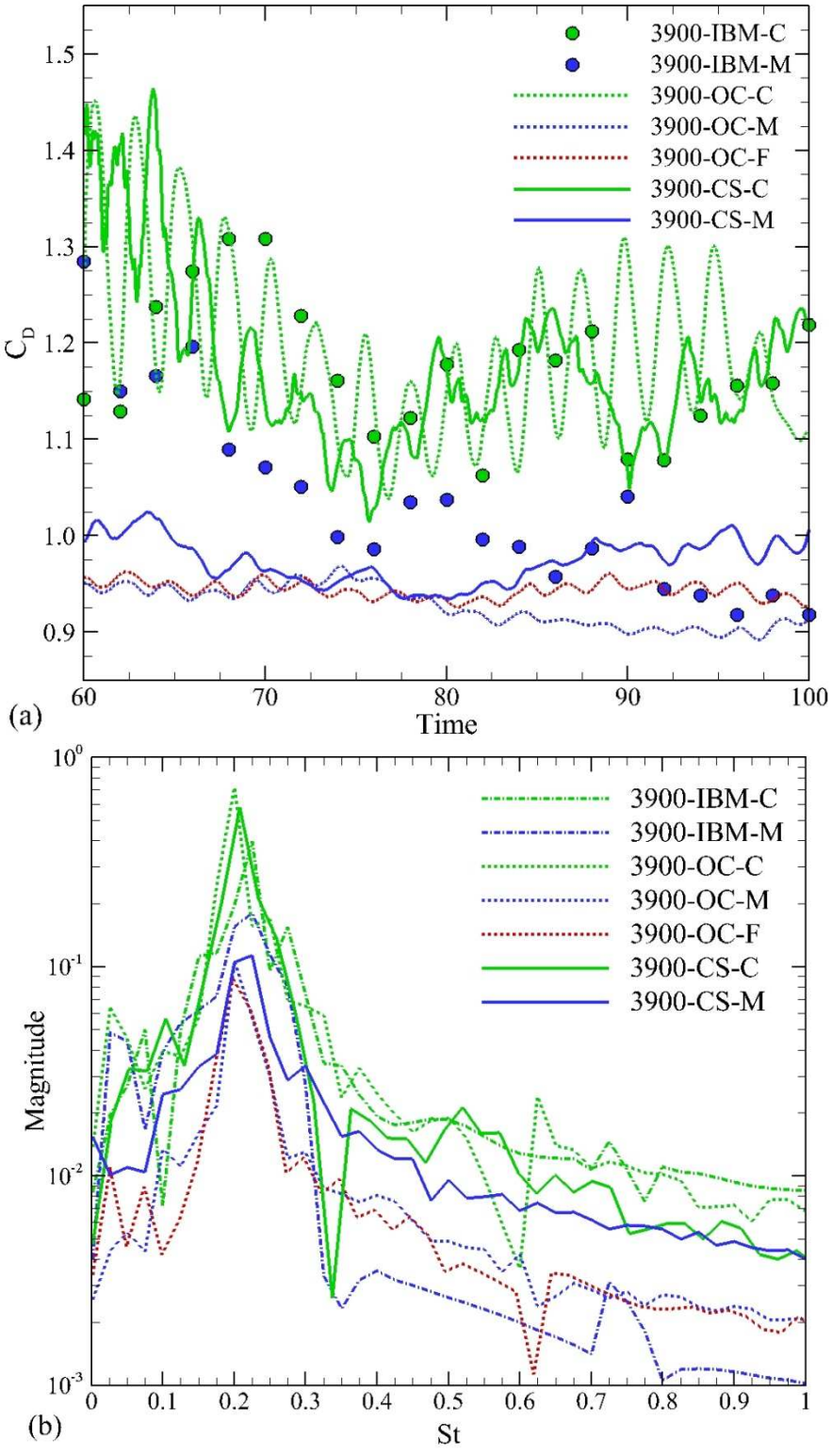

Figure 3.15 Force coefficients: (a) Time history of drag coefficients; (b) FFT of lift coefficients

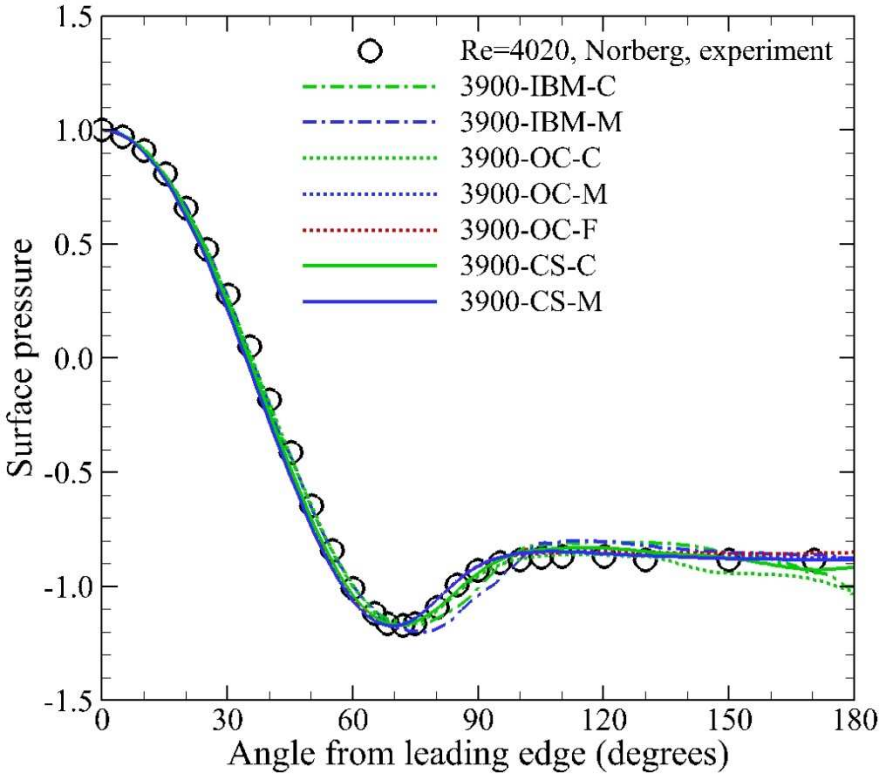

Figure 3.16 Pressure distribution on the cylinder surface

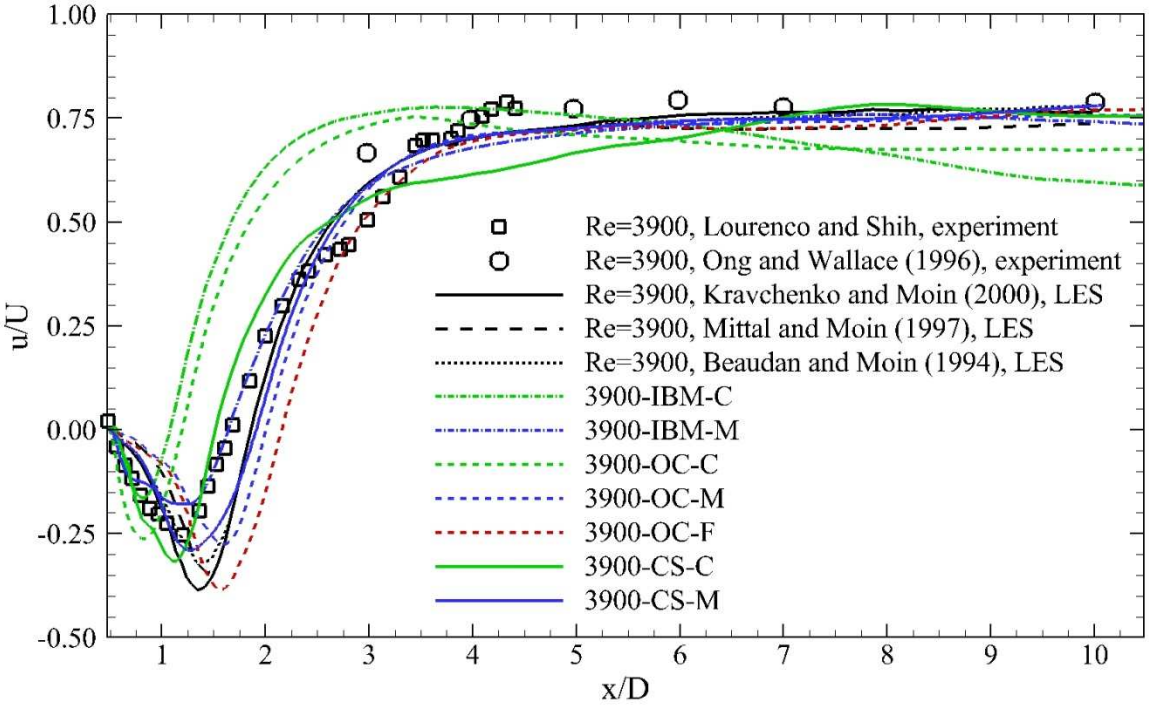

Figure 3.17 Mean streamwise velocity on the wake center line

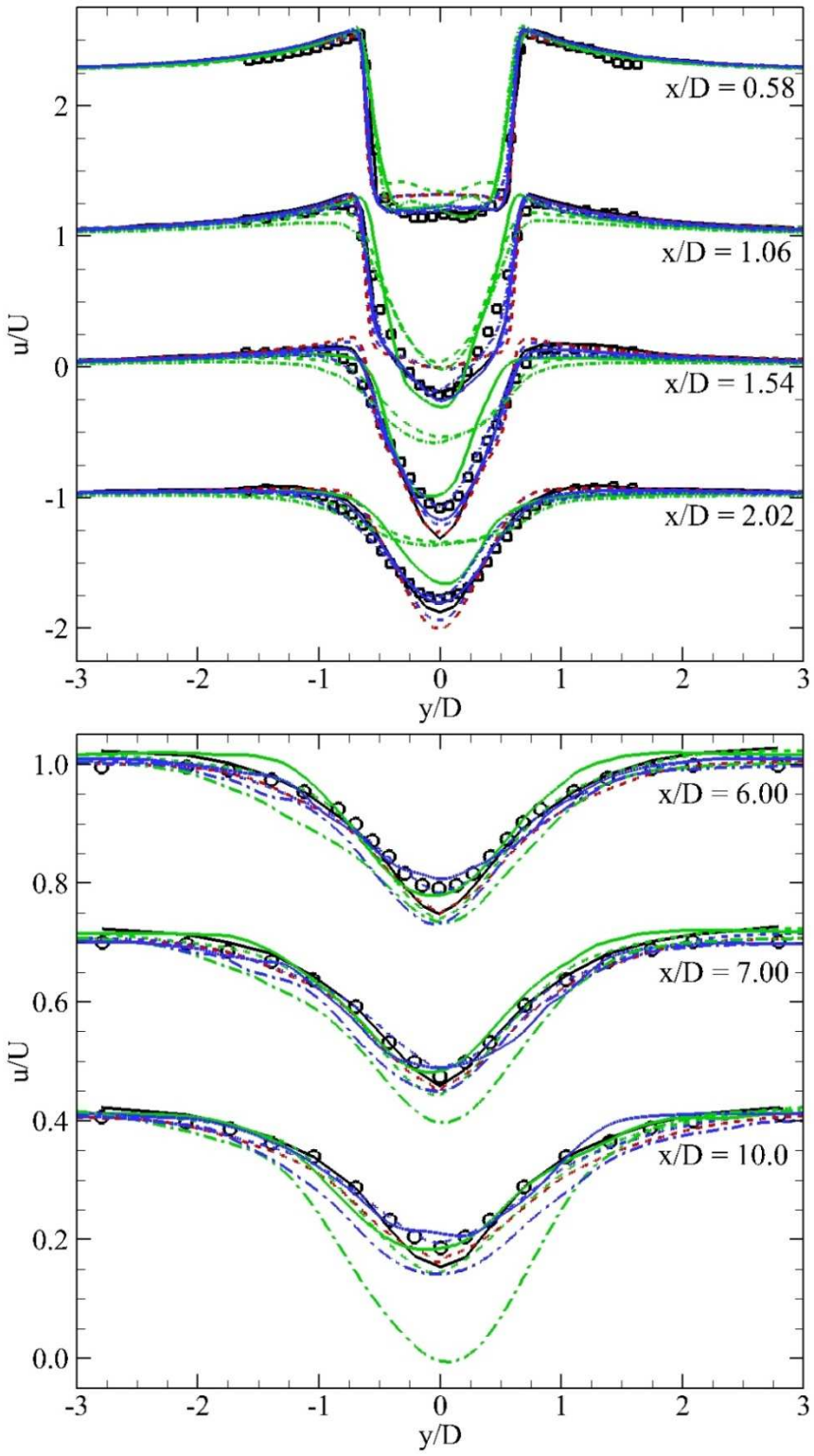

Figure 3.18 Mean streamwise velocity at transverse sections in the wake. Refer to the caption in Figure 3.17 for details.

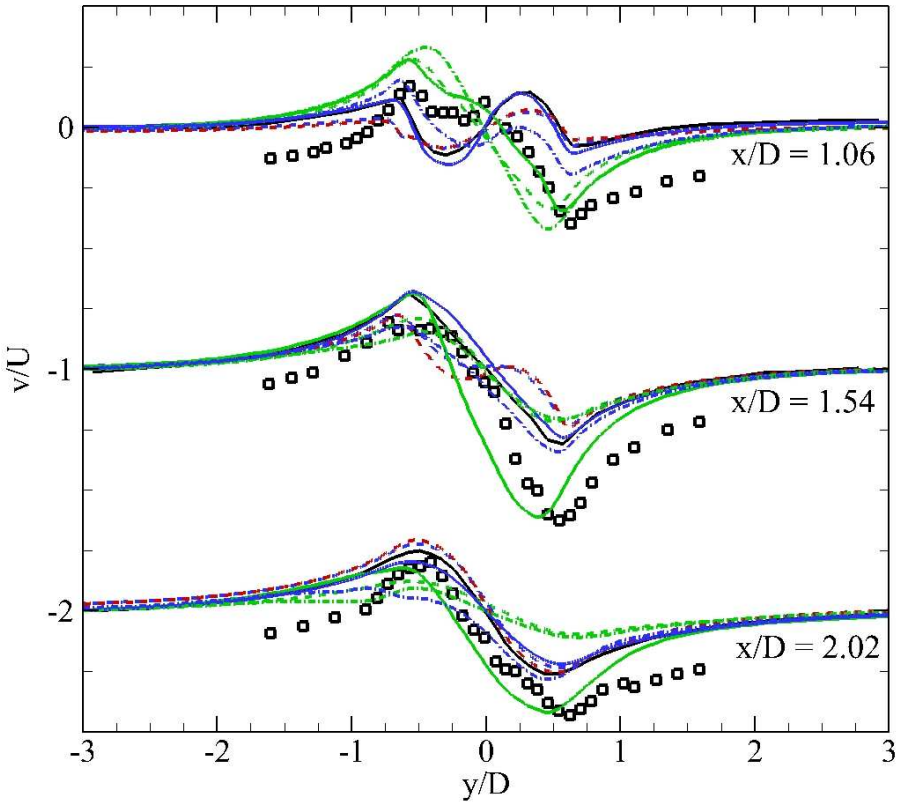

Figure 3.19 Mean transverse velocity at transverse sections in the wake. Refer to the caption in Figure 3.17 for details.

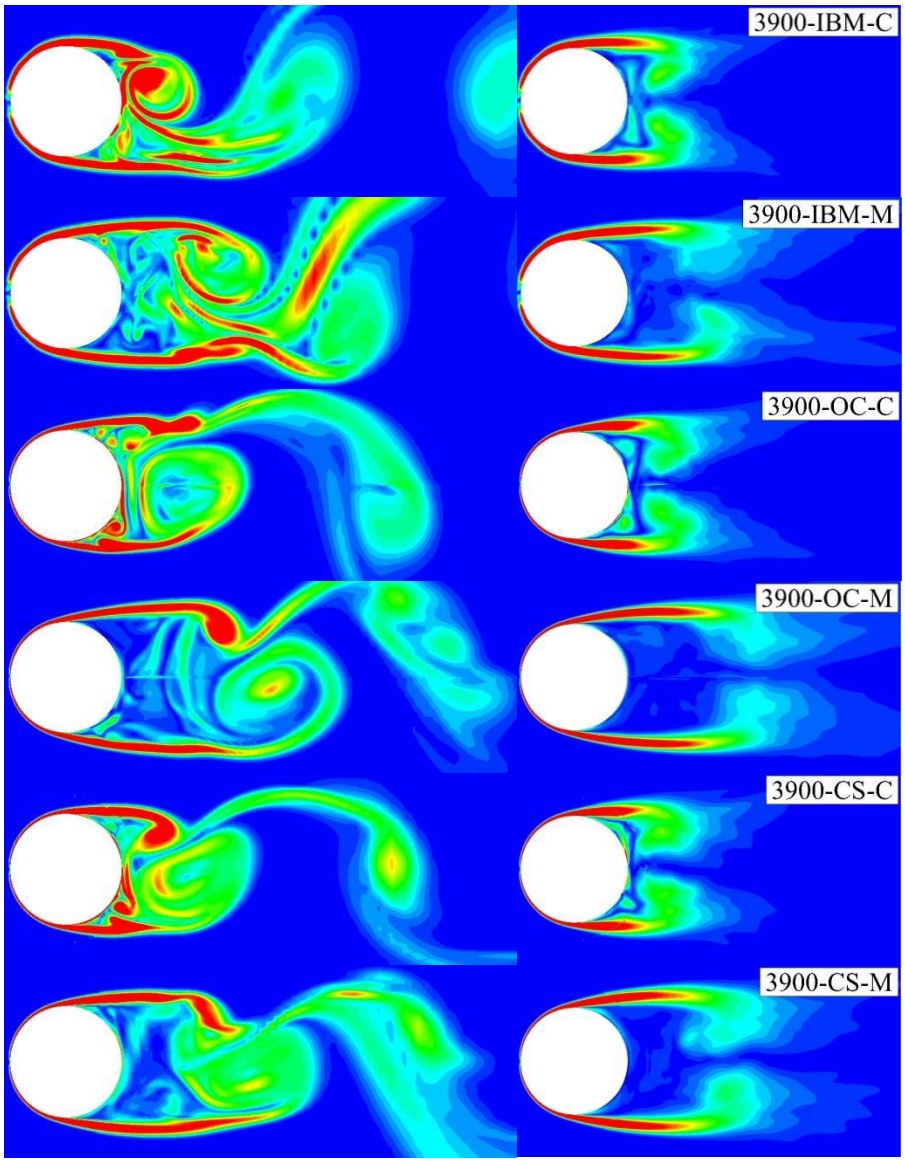

Figure 3.20 Instantaneous (left column) and mean (right column) vorticity magnitude contours

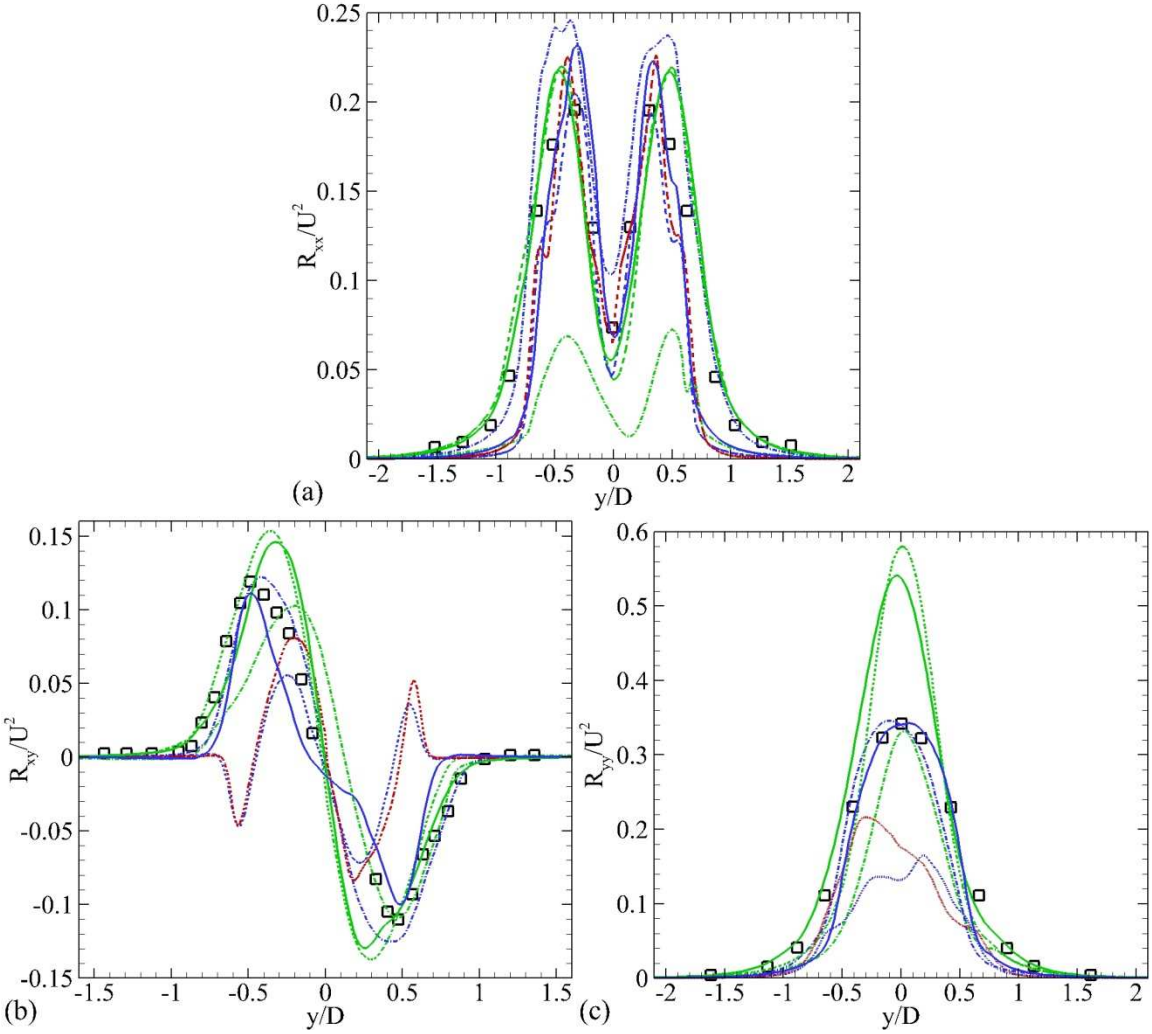

Figure 3.21 Reynolds stresses at x/D = 1.54: (a) streamwise normal stress component; (b) shear stress component; (c) transverse normal stress component. The square symbols show experimental data taken from Hansen and Forsythe (2004). Refer to the caption in Figure 3.17 for details.

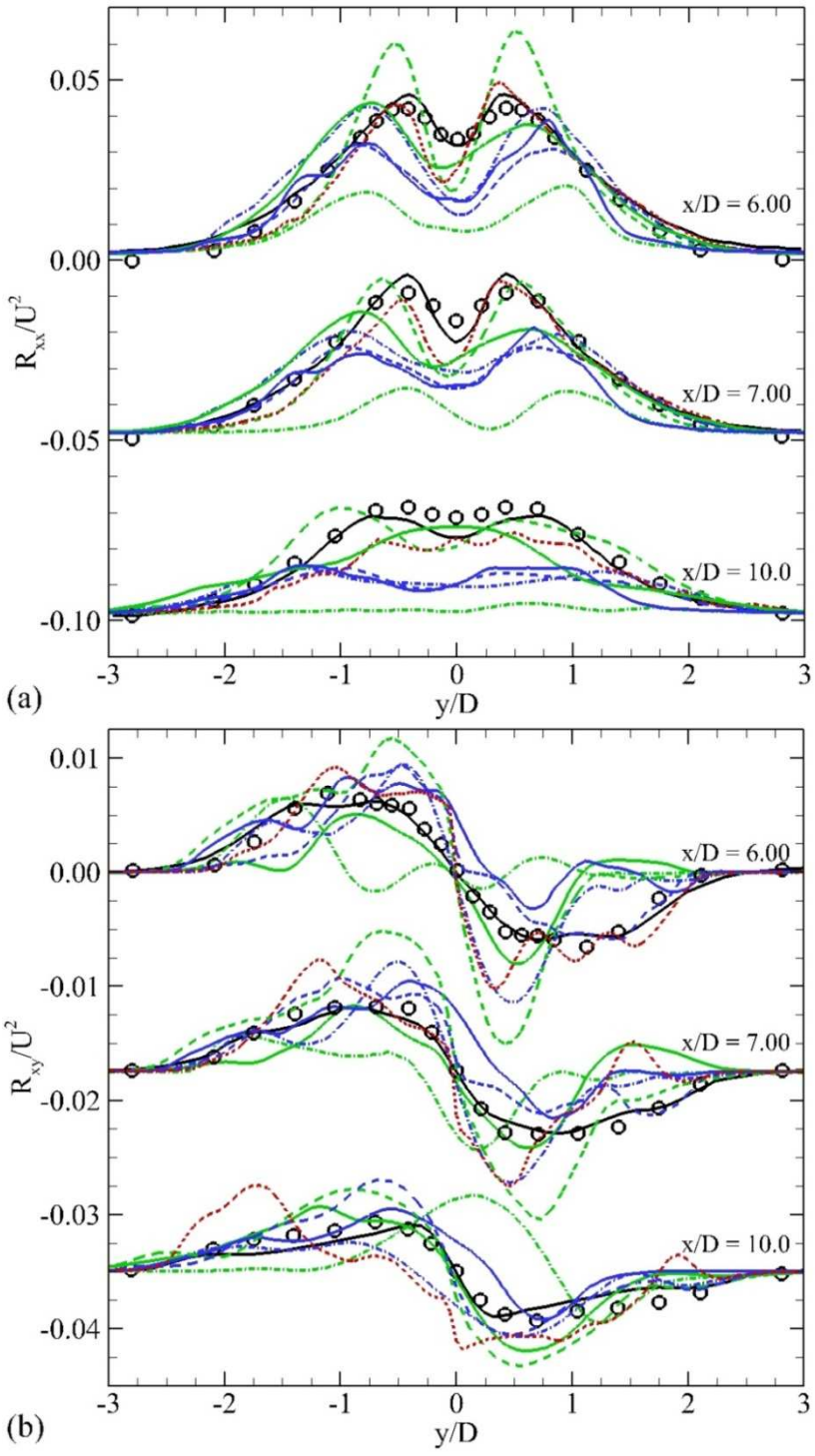

Figure 3.22 Reynolds stresses at three locations in the far wake: (a) streamwise normal stress component; (b) shear stress component. Refer to the caption in Figure 3.17 for details.

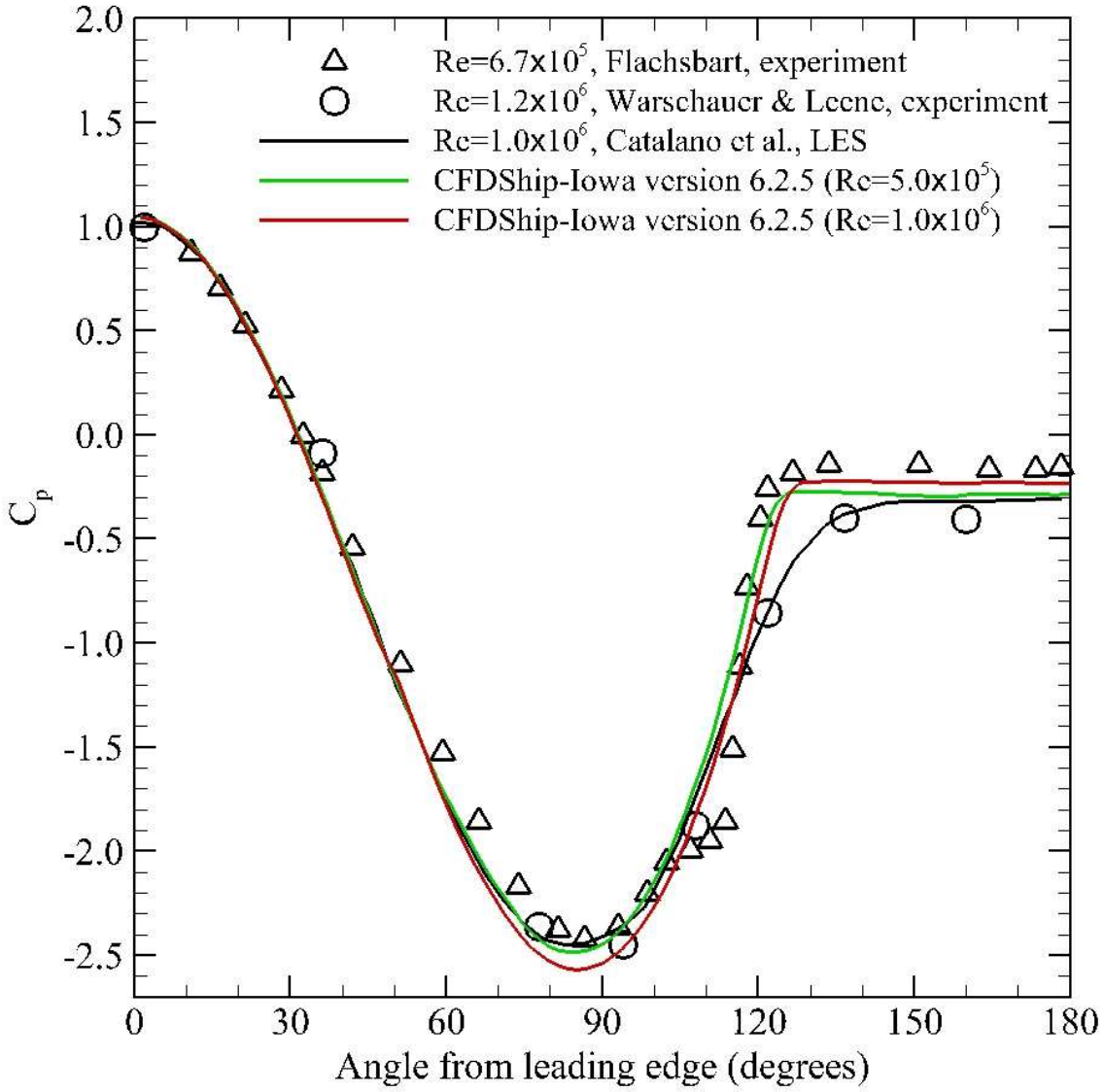

Figure 3.23 Pressure distributions on the cylinder surface at supercritical Re

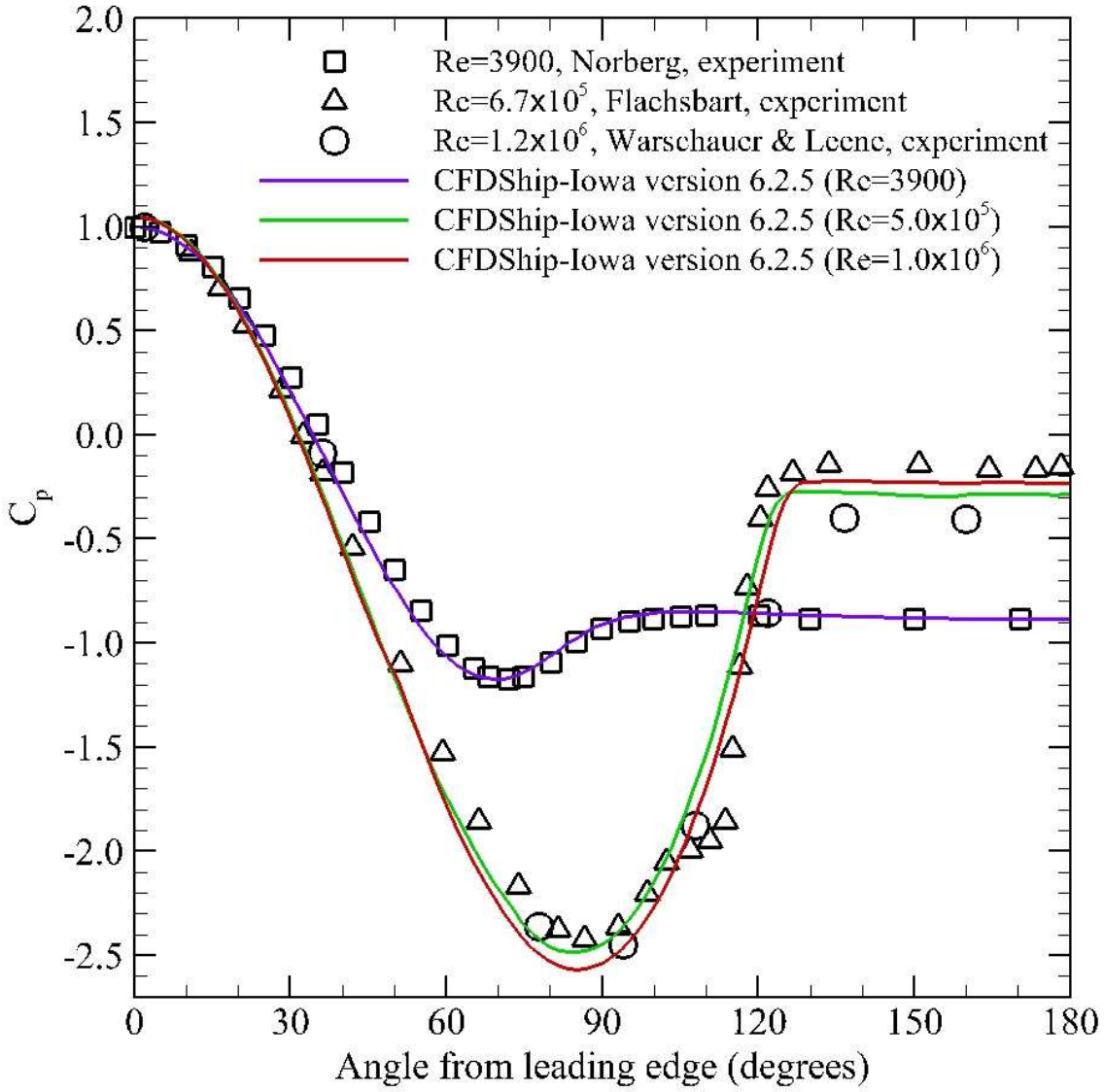

Figure 3.24 Comparison of the mean pressure distributions on the cylinder surface

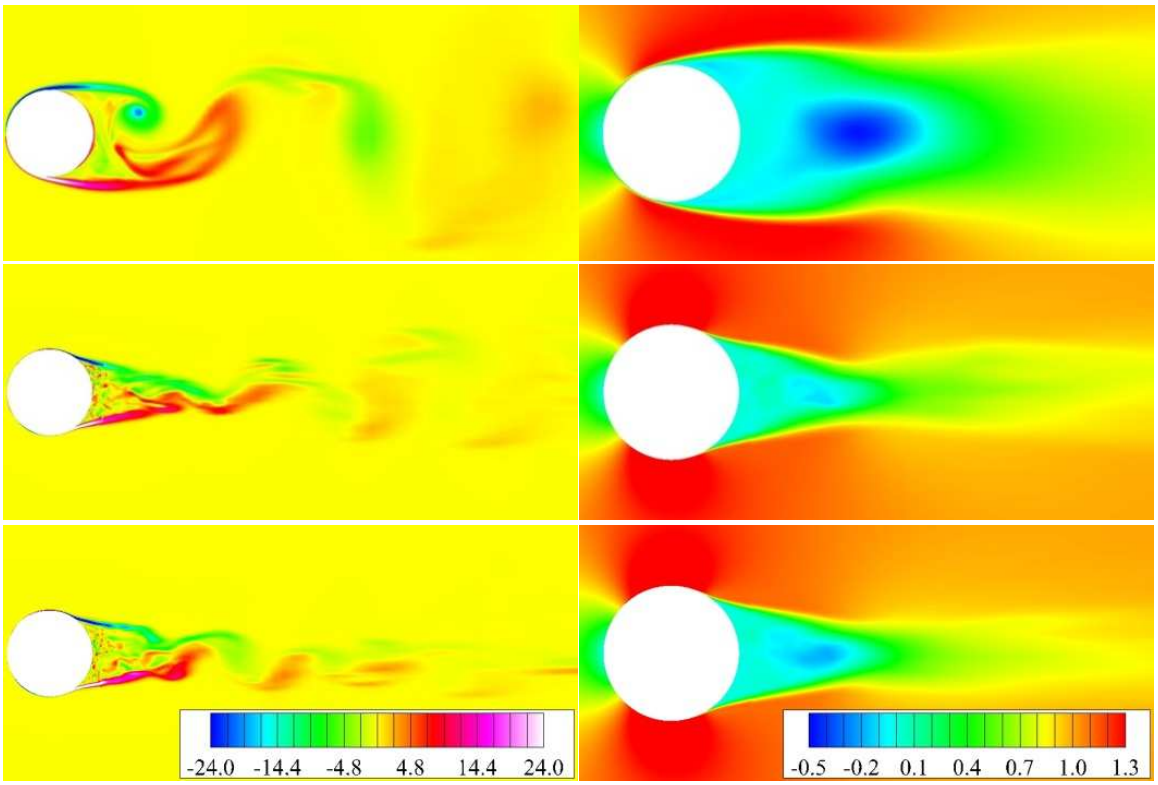

Figure 3.25 Comparison of flows: (top) 3900-CS-M; (middle) 5E5-CS; (bottom) 1E6-CS

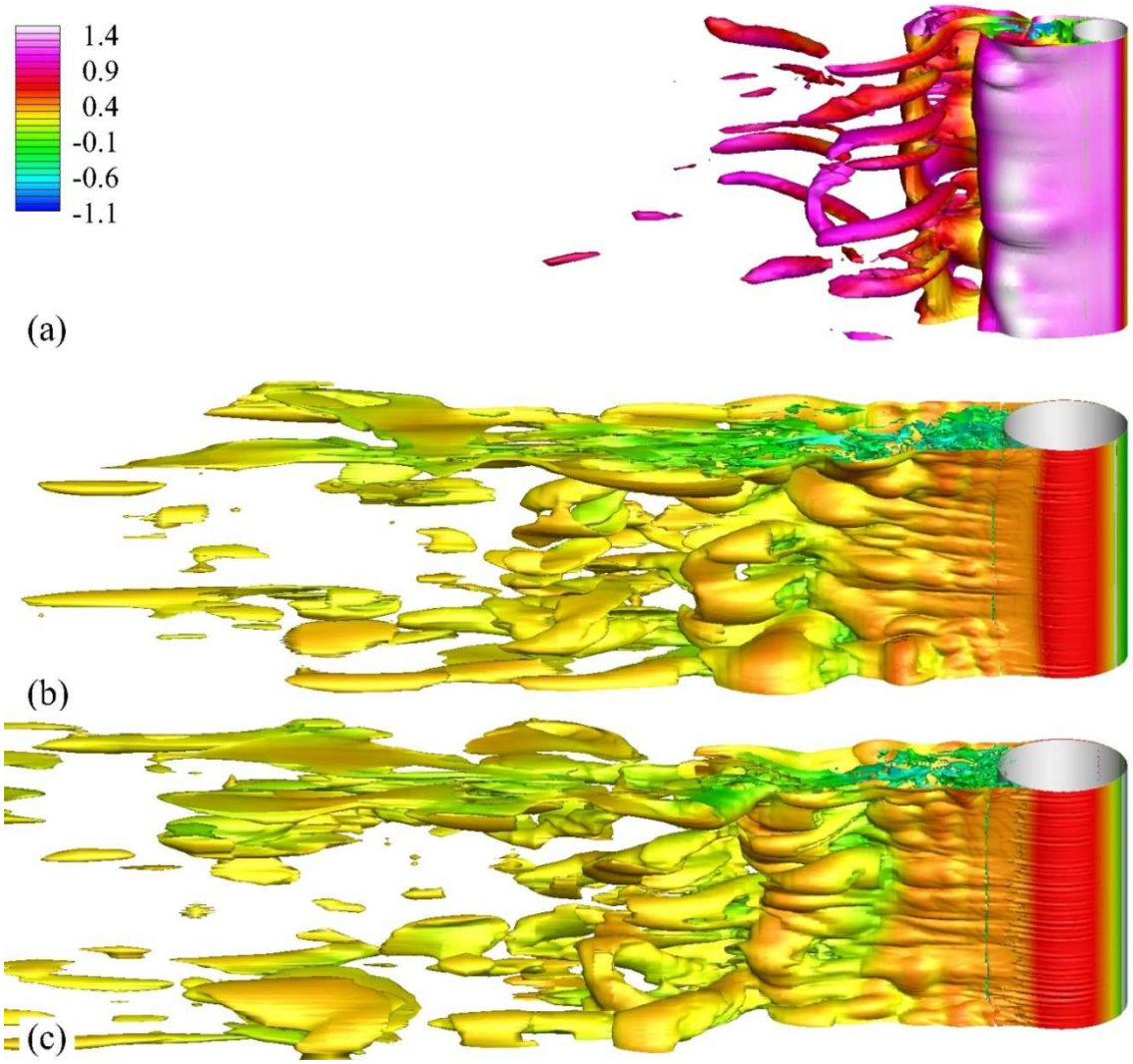

Figure 3.26 Iso-surfaces of the instantaneous vorticity magnitude (ω = 2.5): (a) 3900-CS-M (b) 5E5-CS; (c) 1E6-CS

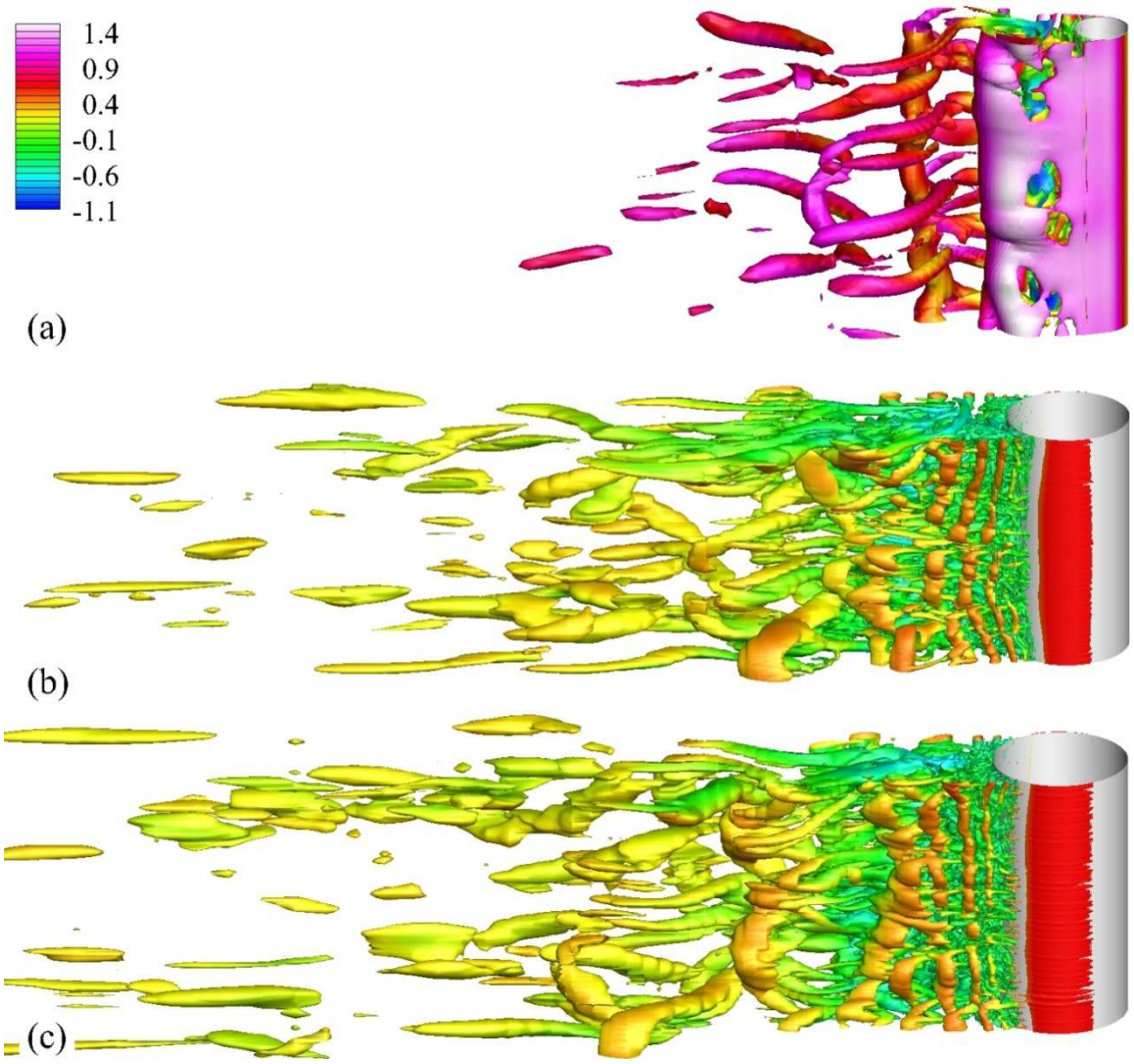

Figure 3.27 Iso-surfaces of the second invariant of the velocity gradient tensor (Q = 1): (a) 3900-CS-M (b) 5E5-CS; (c) 1E6-CS

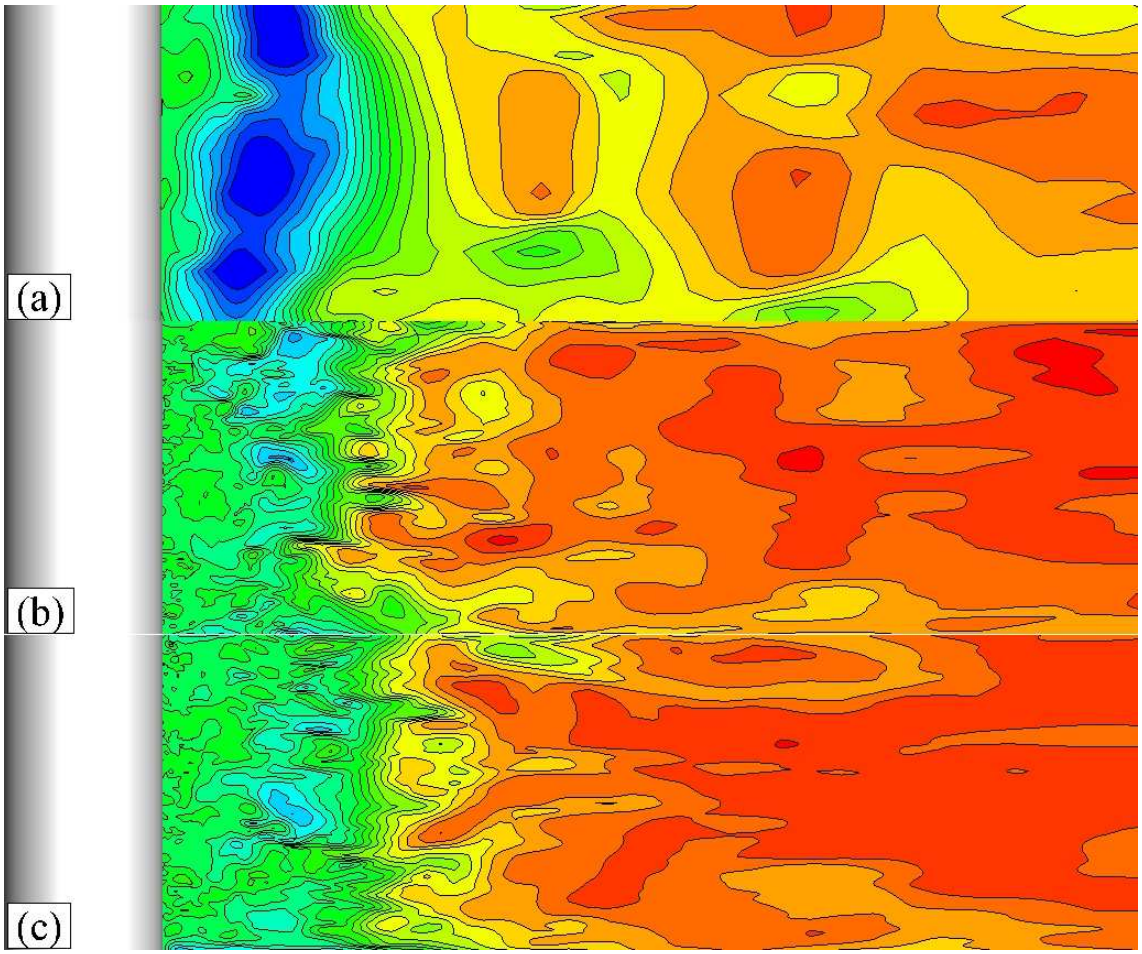

Figure 3.28 Instantaneous streamwise velocity on the center plane of the wake: (a) 3900-CS-M; (b) 5E5-CS; (c) 1E6-CS. The contour range is -0.8 – 1 with interval 0.1.

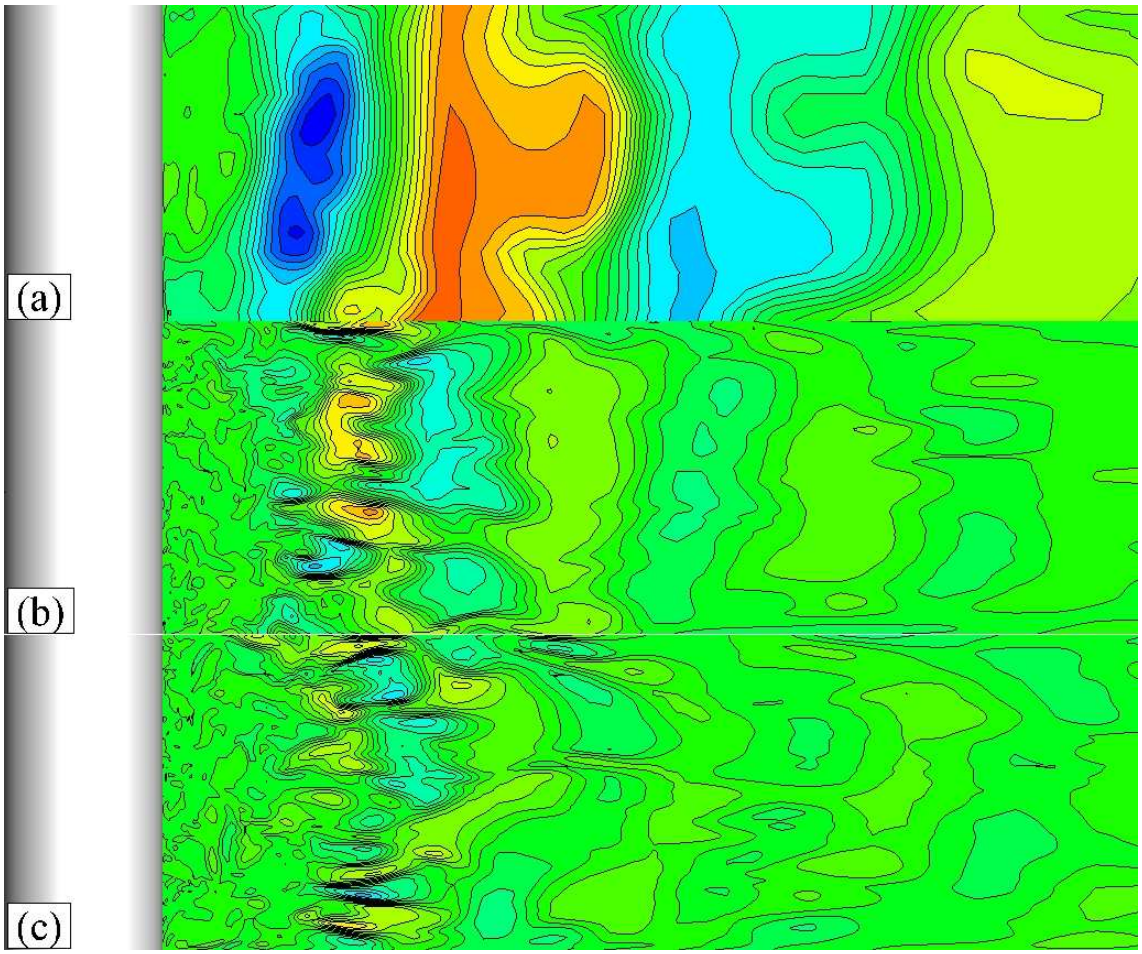

Figure 3.29 Instantaneous transverse velocity on the center plane of the wake: (a) 3900-CS-M; (b) 5E5-CS; (c) 1E6-CS. The contour range is -1 – 1 with interval 0.1.

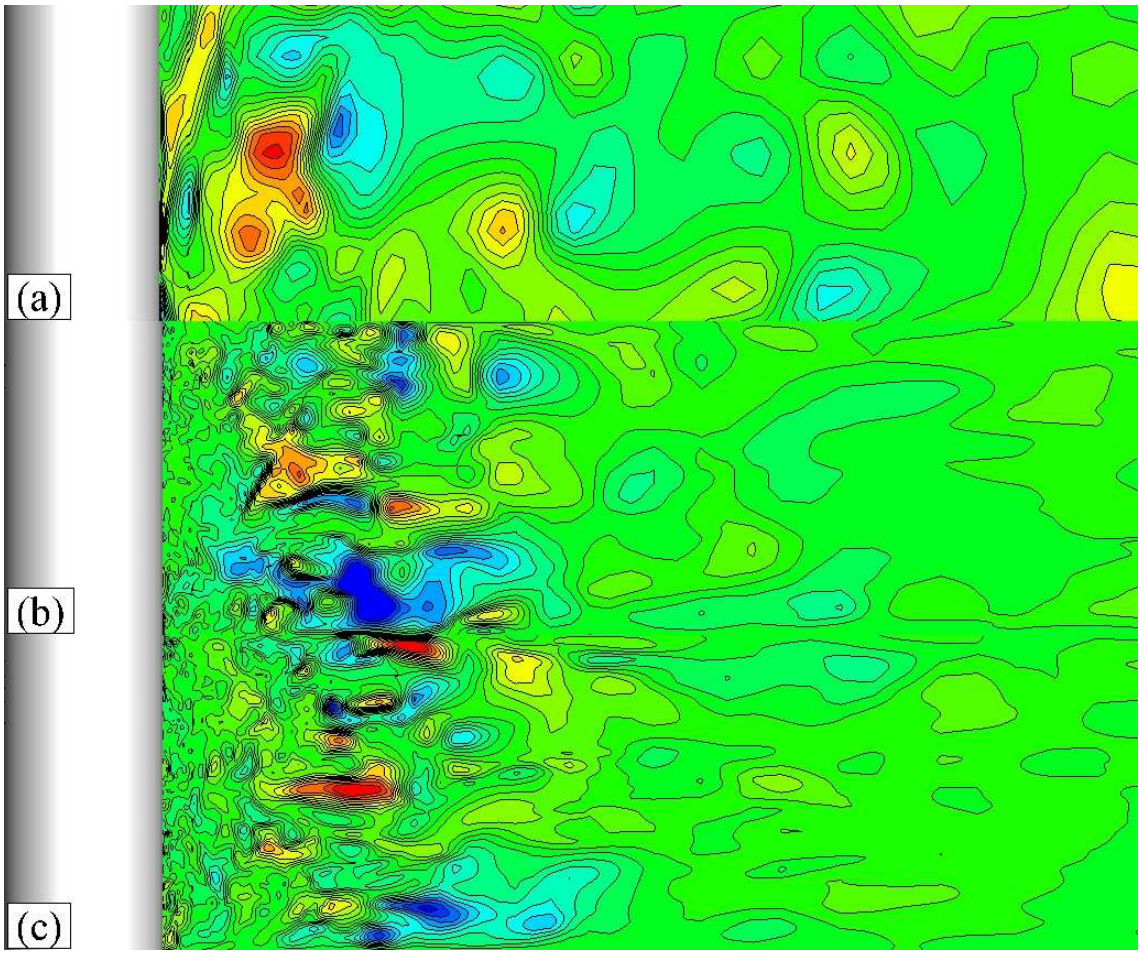

Figure 3.30 Instantaneous vertical velocity on the center plane of the wake: (a) 3900-CS-M; (b) 5E5-CS; (c) 1E6-CS. The contour range is -0.45 – 0.45 with interval 0.05.

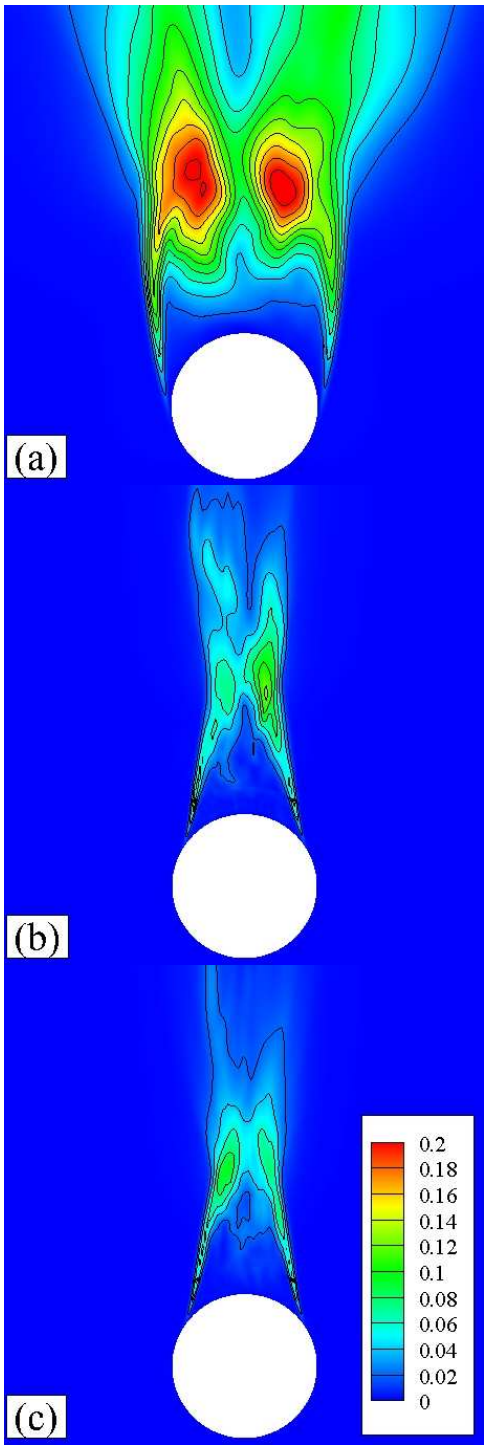

Figure 3.31 Streamwise Reynolds normal stress ($R_{xx} = \overline{u'u'}$) in the wake: (a) 3900-CS-M; (b) 5E5-CS; (c) 1E6-CS. The contour range is 0 – 0.2 with interval 0.02.

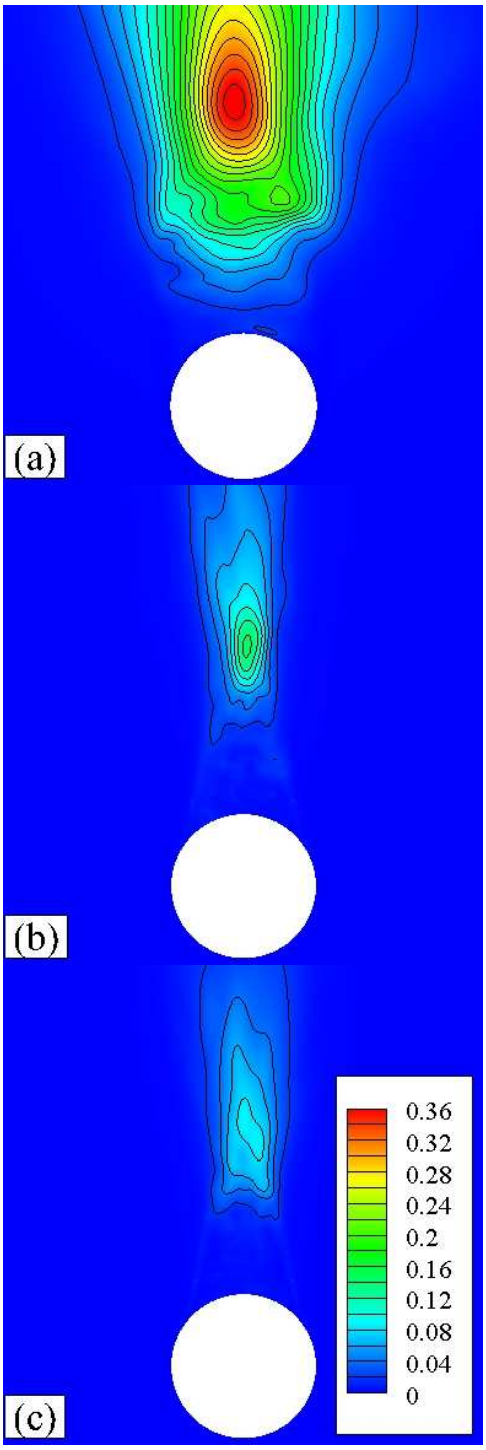

Figure 3.32 Transverse Reynolds normal stress ($R_{xx} = \overline{v'v'}$) in the wake: (a) 3900-CS-M; (b) 5E5-CS; (c) 1E6-CS. The contour range is 0 – 0.36 with interval 0.02.

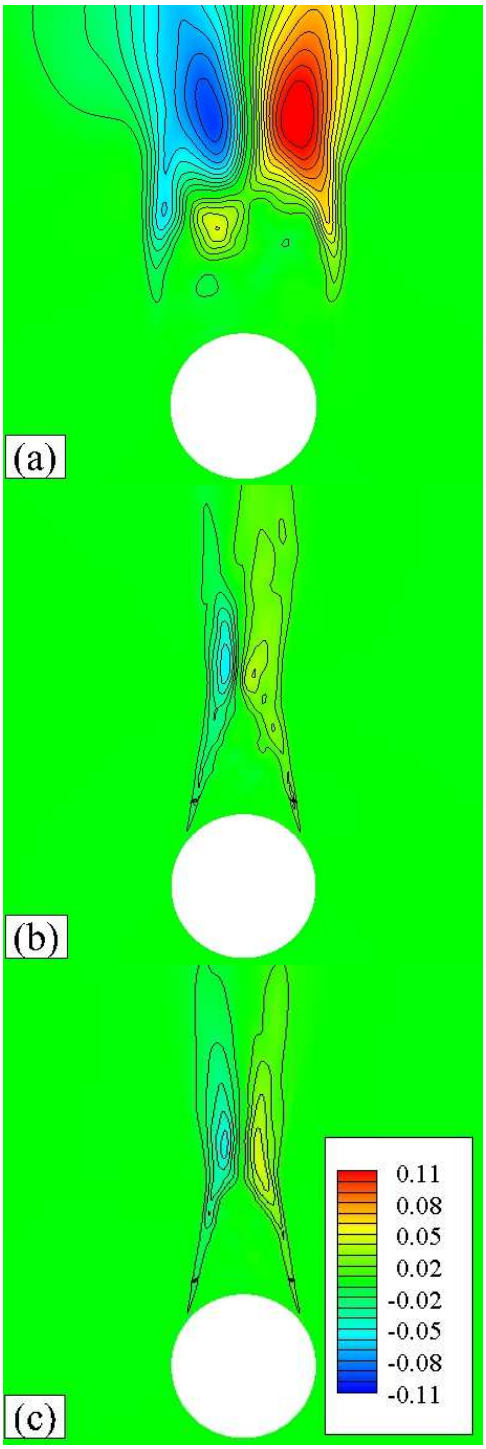

Figure 3.33 Reynolds shear stress ($R_{xx} = \overline{u'v'}$) in the wake: (a) 3900-CS-M; (b) 5E5-CS; (c) 1E6-CS. The contour range is -0.11 – 0.11 with interval 0.01.

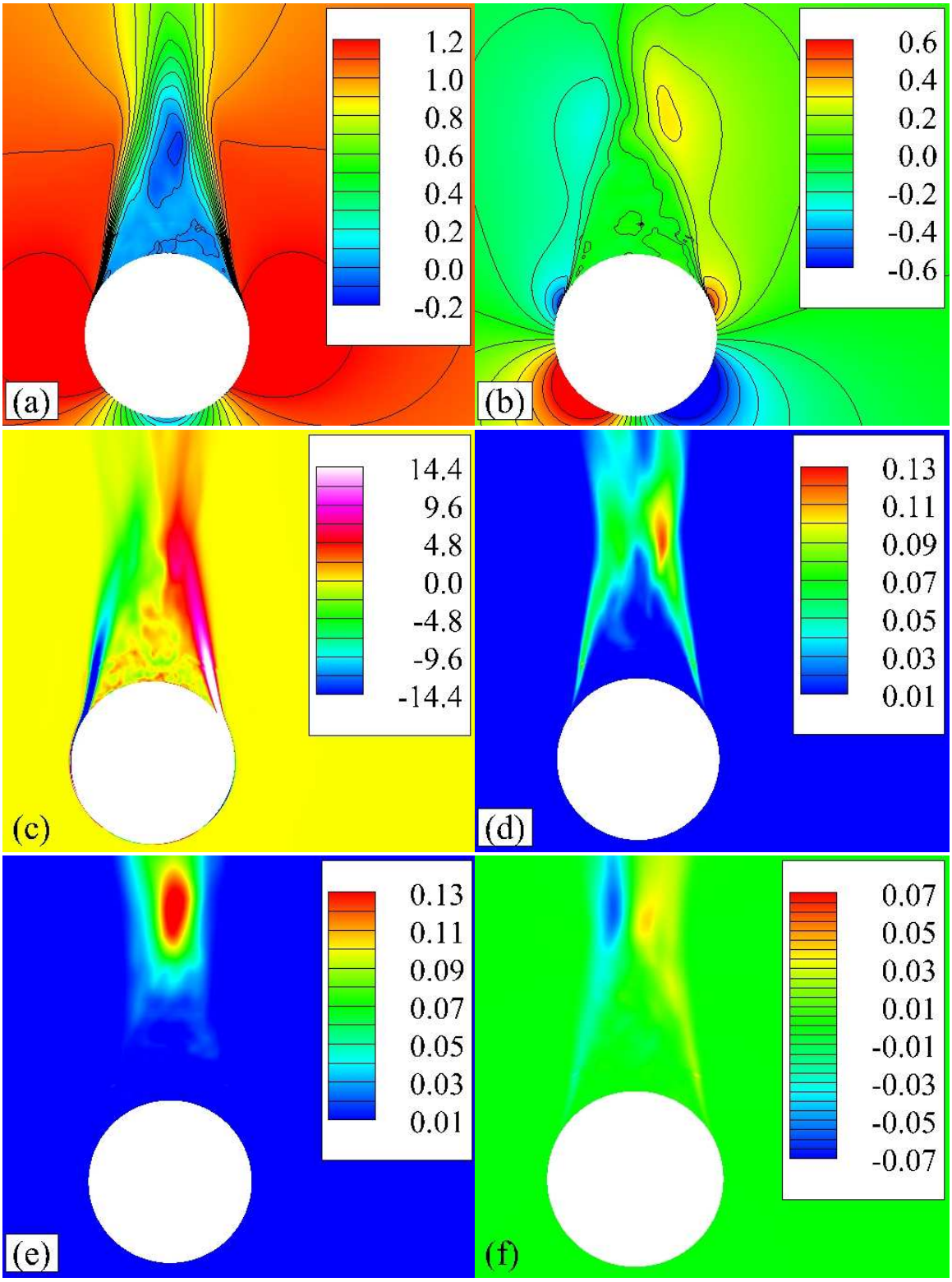

Figure 3.34 Mean flow fields and Reynolds stresses at Re = 5×10^5: (a) streamwise velocity; (b) transverse velocity; (c) vertical vorticity (d) R_{xx}; (e) R_{yy}; (f) R_{xy}

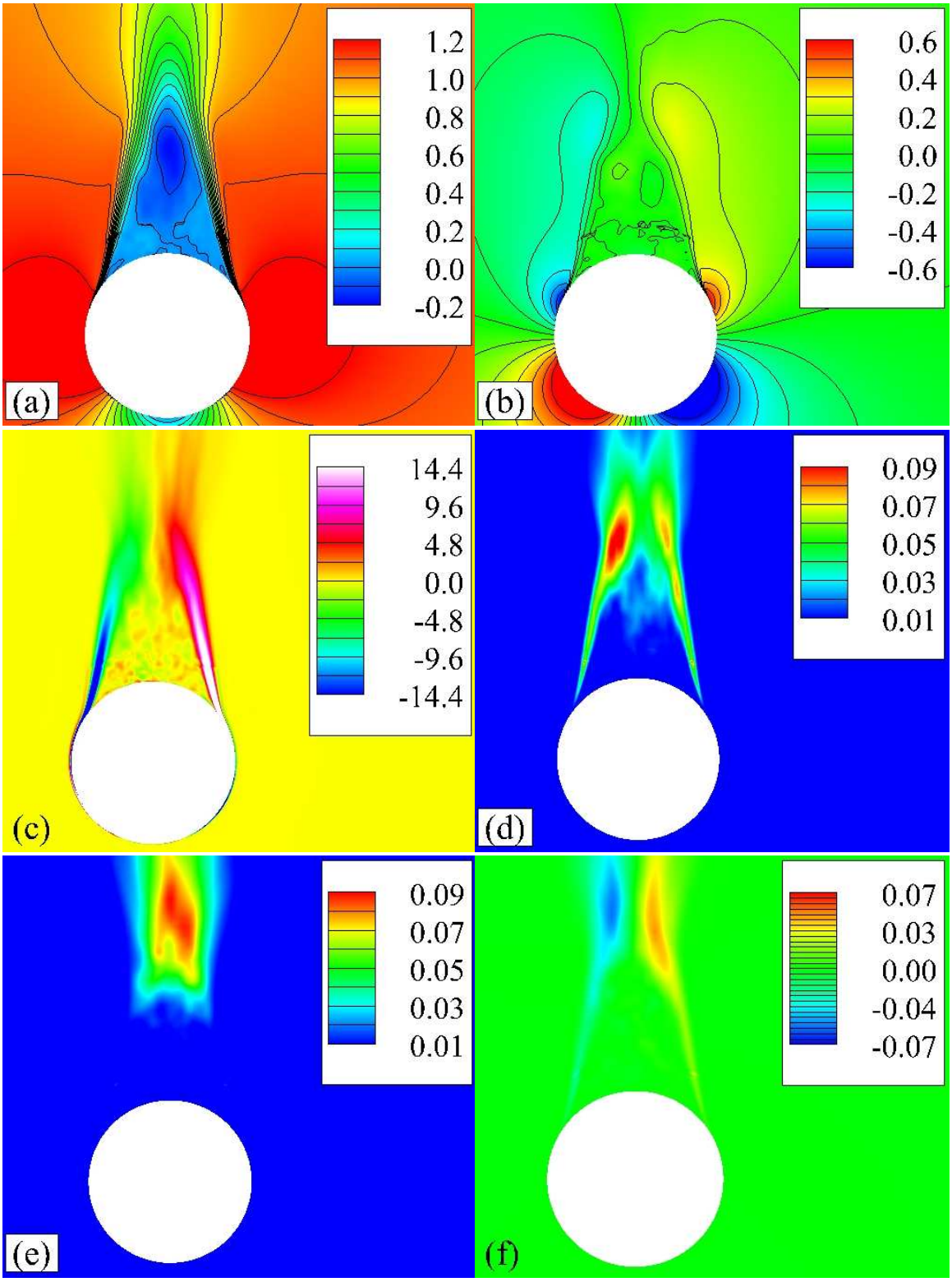

Figure 3.35 Mean flow fields and Reynolds stresses at Re = 1×10^6: (a) streamwise velocity; (b) transverse velocity; (c) vertical vorticity (d) R_{xx}; (e) R_{yy}; (f) R_{xy}

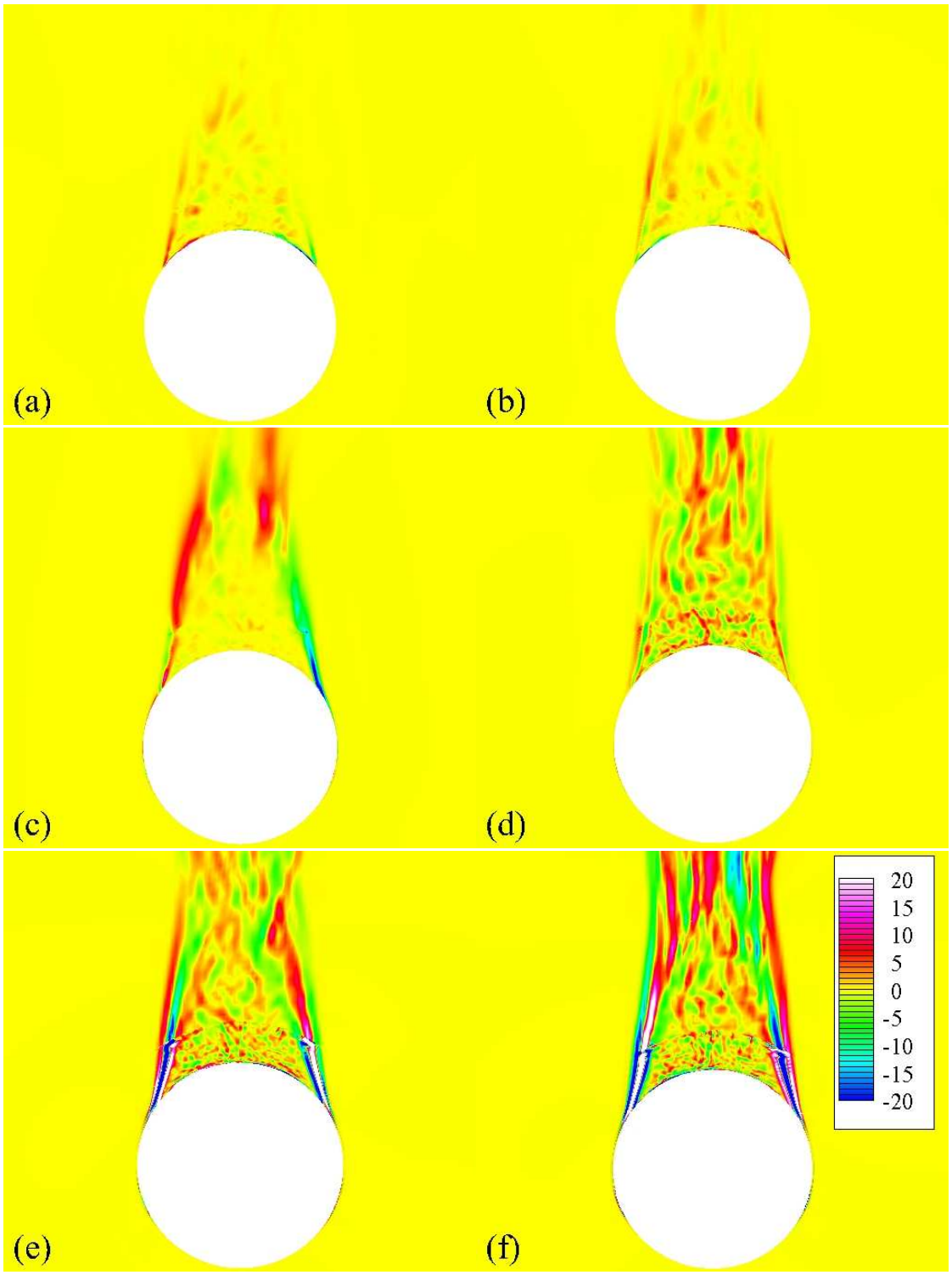

Figure 3.36 Source terms for the mean vertical vorticity at Re = 5×10^5: (a) x component of term (B); (b) y component of term (B); (c) z component of term (B); (d) term (D); (e) term (E); (f) term (F). The contour range is -20 – 20 with interval 1.

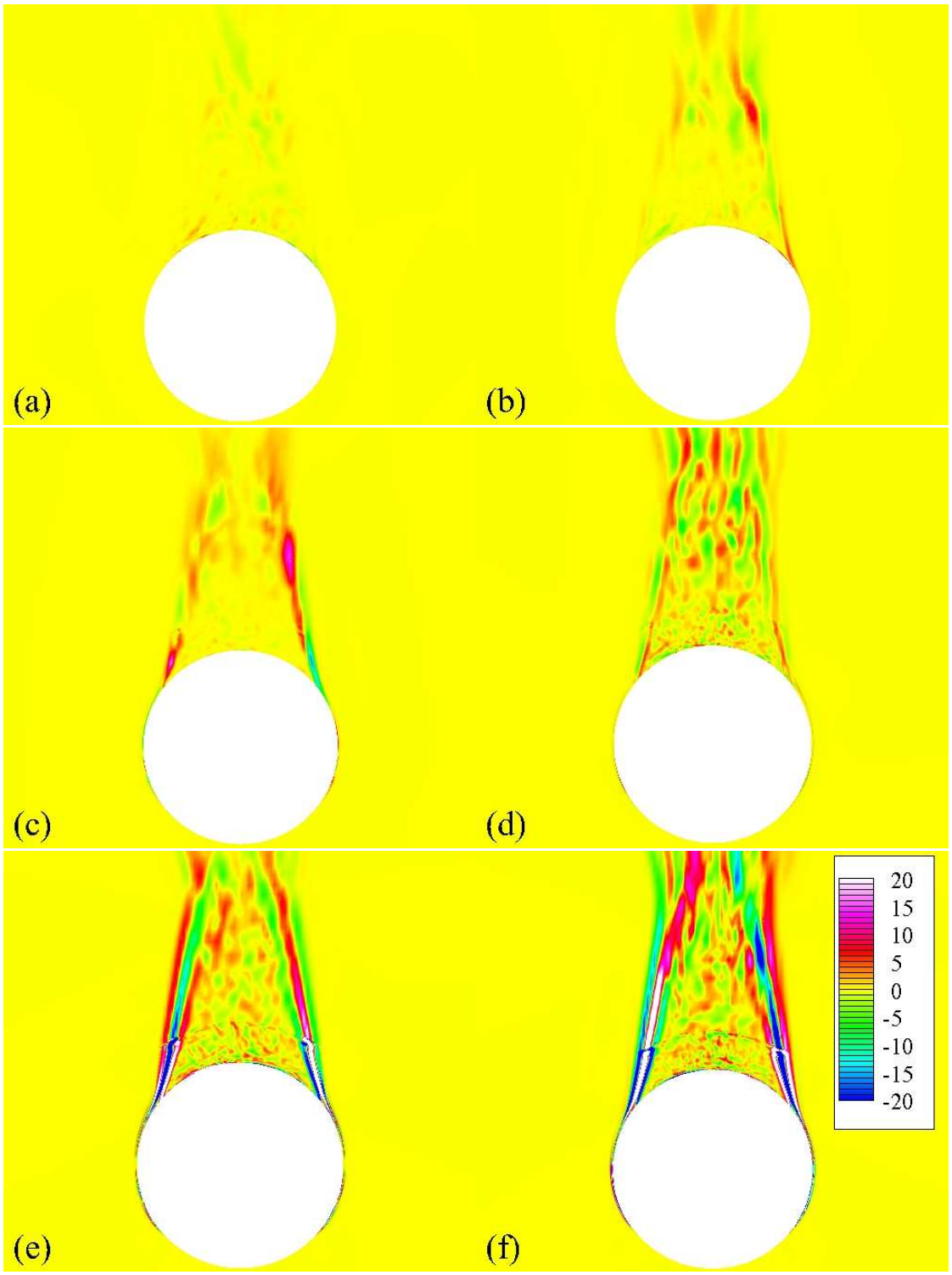

Figure 3.37 Source terms for the mean vertical vorticity at Re = 1×10^6: (a) x component of term (B); (b) y component of term (B); (c) z component of term (B); (d) term (D); (e) term (E); (f) term (F). The contour range is -20 – 20 with interval 1.

CHAPTER 4

NUMERICAL SIMULATIONS OF FLOWS PAST FREE SURFACE PIERCING CIRCULAR CYLINDERS

4.1 Introduction

Since flows past free surface piercing circular cylinders have received much less attention than the single-phase flows, only a few experimental and numerical studies on the two-phase flows around the circular cylinders are available in the literature. In spite of this, the two-phase flows past the circular cylinders still play important roles in various engineering applications including offshore structures and surface vessels. Moreover, the flows past the free surface piercing circular cylinders include complicated phenomena due to the generation of waves in various forms, the interactions of the waves with the body and vortices, the interfacial effects like bubble entrainment and surface tension, and three-dimensional flow separation, which are of great interest in fluid mechanics. In this study, CFDShip-Iowa version 6.2.5 is applied to the flows past a circular cylinder piercing the free surfaces vertically. It aims at investigating accuracy of the coupled orthogonal curvilinear/Cartesian grid solver in the simulation of the flows with free surfaces.

There are several experimental studies on the flows past the vertical circular cylinders piercing the free surfaces. In the study of Hay (1947), Froude numbers (Fr) and Reynolds numbers (Re) were determined by several ratios of those non-dimensional variables. For each ratio with different Fr, they measured the maximum heights of the bow waves in front of the circular cylinder and the depths of the depression on the center line behind the cylinder, and those data were plotted as a function of Fr. Chaplin and Teigen (2003) review the experimental study of Hay (1947). Inoue et al. (1993) conducted an experiment of the free surface flow past a circular cylinder at Re = 2.7×10^4 and Fr = 0.8. They measured the mean free surface elevations and the root mean square

(RMS) of the elevation fluctuations around the circular cylinder. Profiles of the streamwise velocity and the free surface elevation were also available in the literature.

Some numerical studies obtained the large eddy simulation (LES) results of the flows past vertical surface piercing circular cylinders. Kawamura et al. (2002) investigated interactions between surface waves and underlying viscous wakes around a free surface piercing circular cylinder at Re = 2.7×10^4 with three different Froude numbers Fr = 0.2, 0.5, and 0.8. The computational grid is fitted to the air-water interface and updated every time step by moving the grid points in the vertical direction. Yu et al. (2008) studied free surface flows past a circular cylinder at Fr up to 3.0 and Re up to 1.0×10^5. A volume-of-fluid method was employed to simulate the air-water interfaces. Suh et al. (2011) performed LES of the flows past a free surface piercing circular cylinder at Fr = 0.2 and 0.8 with the same Reynolds number Re = 2.7×10^4 using CFDShip-Iowa version 6.2 with a level set based sharp interface method. Koo (2011) extended the study of Suh et al. (2011) and used CFDShip-Iowa version 6.2 with a coupled level set and volume-of-fluid method to perform numerical simulations with conditions mainly based on the experiments of Chaplin and Teigen (2003). Those numerical studies show the detailed results of the free surfaces, the mean flow and turbulence statistics, the vortical structures, and the hydrodynamic forces at several Reynolds numbers up to Re = 4.58×10^5 and Froude numbers up to Fr = 1.64.

4.2 Large Eddy Simulations of Two-Phase Turbulent Flows

In order to assess the accuracy of CFDShip-Iowa version 6.2.5 in the flows with the free surfaces, numerical simulations using LES are performed for the two-phase turbulent flows past a circular cylinder piercing the free surfaces vertically at (Re, Fr) = (2.7×10^4, 0.20), (2.7×10^4, 0.80), and (4.58×10^5, 1.64), i.e., 2.7E4-0.20, 2.7E4-0.80, and 4.58E5-1.64 in Table 4.1. Those Re and Fr have been taken into account because several detailed results of those two-phase flows are available from the numerical and

experimental studies in the literature. Note that the Reynolds number is subcritical at the low (= 0.20) and medium (= 0.80) Fr while it is supercritical at the high Fr = 1.64. In this study, effects of the free surfaces on the vortical structures and the separated regions are also analyzed especially for 4.58E5-1.64 by comparing the results with those of the single-phase flow at the similar Re = 5×10^5, i.e., 5E5-CS.

Table 4.1 shows the simulation conditions at each Fr. For 2.7E4-0.20 and 2.7E4-0.80, the Cartesian domain size is $-10 \le x/D \le 15$, $-10 \le y/D \le 10$ and $-4 \le z/D \le 2$, and the grid consists of 9.4M points. For 4.58E4-1.64, the domain size is $-15 \le x/D \le 42$, $-20 \le y/D \le 20$ and $-4 \le z/D \le 2$, and the grid consists of 14.6M points.

The drag and lift coefficients are defined as

$$C_D = \frac{Drag}{\frac{1}{2}\rho_L U_\infty^2 DH} \quad C_L = \frac{Lift}{\frac{1}{2}\rho_L U_\infty^2 DH} \tag{4.1}$$

where H is the still water depth and ρ_L is the water density. The flows were regarded as statistically stationary when the fluctuations of the running mean are less than 1% of the mean C_D. After the flow was converged, flow field data covering up to $T = 80D/U_\infty$ were collected to obtain the time-averaged results. This procedure follows discussion in Suh et al. (2011) and Koo (2011). Fig. 4.1 shows the time histories of the drag and lift coefficients from which the instantaneous statistics were accumulated. The result of 4.58E5-1.64 is not shown since the vertical grid resolution is not fine enough to compute the forces accurately. Fast Fourier transform (FFT) of C_L is shown in Fig. 4.2. The peak values are at St = 0.2 for both 2.7E4-0.20 and 2.7E4-0.80. The Strouhal numbers correspond to the periods of vortex shedding at the subcritical Re = 2.7×10^4.

Table 4.2 compares the mean C_D and the root mean squares (RMS) of C_L (C_L^{RMS}). Unfortunately, no experimental data are available about the hydrodynamic forces of the circular cylinder in the two-phase flows at Fr = 0.2 and 0.8 with Re = 2.7×10^4. However, the experimental measurement of the single-phase flow at the same Re can be obtained from Szepessy and Bearman (1992). The predictions of 2.7E4-0.20 and 2.7E4-0.80 show

up to 18% lower C_D and up to 51% lower C_L^{RMS} than the experimental data of the single-phase flow at the same Re (Szepessy and Bearman, 1992). The effects of the deformation of the free surface probably result in the lower values of C_D and C_L^{RMS} (Kawamura et al., 2002; Yu et al., 2008). It is noted that the CFDShip-Iowa version 6.2.5 predictions approach the experimental data as Fr decreases. This trend is consistent with that observed in Kawamura et al. (2002). The predictions of both 2.7E4-0.20 and 2.7E4-0.80 compare within 4% of the LES results of Kawamura et al. (2002) and Suh et al. (2011).

Fig. 4.3 and 4.4 show instantaneous free surfaces computed by 2.7E4-0.20 and 2.7E4-0.80, and 4.58E5-1.64. In Fig. 4.3, the numerical results of CFDShip-Iowa version 6.2.5 show the similar characteristics to those predicted by CFDShip-Iowa version 6.2 (Koo, 2011). At Fr = 0.20, the deformation of the free surface is negligibly small and no waves are generated in the wake behind the cylinder. On the other hand, the free surfaces are deformed largely at higher Fr = 0.80 and 1.64. Bow waves are generated in front of the cylinder. The depressions exist on the downstream side of the cylinder. The free surfaces are very rough around the cylinder, and this indicates the existence of vortical structures below the free surface (Sarpkaya, 1996; Suh et al., 2011). Fig. 4.4 clearly shows Kelvin waves generated in the wake at Fr = 0.80 and 1.64. The wave lengths predicted by 2.7E4-0.80 and 4.58E5-1.64 are close to the theoretical values, i.e., $2\pi Fr^2$.

Some features of the mean free surfaces are compared qualitatively and quantitatively. Fig. 4.5 compares the maximum heights of the bow waves and the depths of the depressions on the center plane of the wake. The experimental data was obtained from Hay (1947) reviewed in Chaplin and Teigen (2003). The solid line shows Bernoulli equation result and indicates possible maximum bow wave heights ($=Fr^2/2$). The bow wave heights and depression depths predicted by CFDShip-Iowa version 6.2.5 are in fairly good agreement with the experimental data and the Bernoulli equation result.

Fig. 4.6 – 4.8 compare the near wake profiles of the mean free surface elevations (h_{mean}) and the RMS of the free surface fluctuations (h_{rms}) between the experimental data

(Inoue et al, 1993), the LES results in the literature (Kawamura et al., 2002; Suh et al., 2011; Koo, 2011), and the prediction of 2.7E4-0.20, 2.7E4-0.80, and 4.58E5-1.64. CFDShip-Iowa version 6.2.5 predicts both h_{mean} and h_{rms} at Fr = 0.20 in good agreement with the CFD results of Kawamura et al. (2002). Note that the differences between the numerical results are smaller than those observed at higher Fr. Although the numerical results of 2.7E4-0.80 agree well with the experimental data of Inoue et al. (1993), it under-predicts the depression on the profile at x = 0.9 near the center plane of the wake. The prediction is more similar to the CFDShip-Iowa version 6.2 result by Suh et al. (2011). The predictions of 4.58E5-1.64 are in good agreement with those of the CFDShip-Iowa version 6.2 by Koo (2011).

Inoue et al. (1993) shows the detailed measurement of the free surface elevations and the RMS of the free surface fluctuations around the circular cylinder at Re = 2.7×10^4 and Fr = 0.80. The experimental data are compared with the numerical results of 2.7E4-0.80 in Fig. 4.9. CFDShip-Iowa version 6.2.5 captures all the features of the mean free surface elevations in the experimental data well, i.e., the bow wave on the upstream side of the cylinder, an almost constant slope leading to the large depression on the downstream side, and the Kelvin waves diverging into the wake. The 2.7E4-0.80 result of the free surface fluctuations shows good agreement with the experimental data in terms of the overall distribution and the location of the peak value. The peak value is slightly under-predicted than the experimental data. CFDShip-Iowa version 6.2.5 predicts fluctuations on the front side of the cylinder. This trend is similar to the CFDShip-Iowa version 6.2 result in Suh et al. (2011), and it is explained that the front fluctuations are due to the presence of the necklace vortices.

Inoue et al. (1993) also measured the vertical profiles of the mean streamwise velocity in the wake at Re = 2.70×10^4 and Fr = 0.80. The profiles are compared in Fig. 4.10. The experimental data of Inoue et al. (1993) shows that the streamwise velocity is almost constant in the deep flow and decreases as the free surface is approached. This

trend corresponds to the recirculation region on the free surface, which is longer in the streamwise direction and wider in the transverse direction than that in the deep flow (Suh et al., 2011). The results of 2.7E4-0.80 capture the above features of the streamwise velocity and show fair agreement with the experimental data and the LES results of Kawamura et al. (2002), Yu et al. (2008), and Suh et al (2011).

Fig. 4.11 compares pressure distributions on the cylinder surface in the deep flow between the experimental data of the single-phase flows at similar Re = 2×10^4 (Norberg, 1992) and the numerical results by 2.7E4-0.20, 2.7E4-0.80, and Suh et al. (2011) using CFDShip-Iowa version 6.2. The experimental data at the subcritical Re shows decreasing pressure in the separated region after the separation point. All of the CFDShip-Iowa version 6.2.5 predictions in the deep flows are in good agreement with the experimental data at similar Re and the numerical result of Suh et al. (2011).

For all Fr = 0.20, 0.80, and 1.64, the CFDShip-Iowa version 6.2.5 predictions show good agreement with the experimental data available in the literature. In this study, the CFDShip-Iowa version 6.2.5 results are analyzed to discuss effects of the free surfaces on the turbulent flows around a circular cylinder. The numerical results are compared with those of the two-phase flows obtained by Kawamura et al. (2002) and Suh et al. (2011) and those of the single-phase flows obtained by 5E5-CS.

Fig. 4.12 and 4.13 show contours of the instantaneous vertical vorticity on the free surface and three horizontal planes at Fr = 0.20 and 0.80, respectively. The CFDShip-Iowa version 6.2.5 results are compared with those of CFDShip-Iowa version 6.2 obtained by Suh et al. (2011). The similar trends can be observed between CFDShip-Iowa version 6.2.5 and CFDShip-Iowa version 6.2. At both Fr = 0.20 and 0.80, organized vortex shedding, which is similar to that from an infinitely long circular cylinder in a single-phase flow, can be clearly observed in the deep flows at z = -3.5. In the deep flows, CFDShip-Iowa version 6.2.5 and CFDShip-Iowa version 6.2 show no significant differences in the characteristics of the vortex shedding in spite of Fr because of the same

Re. This indicates negligibly small effects of the free surface on the vortex shedding in the deep flows. As the free surface is approached, the large-scale periodic vortex shedding is attenuated and more vortices with smaller scales appear. The shear layers separating from the two sides of the cylinder interact with each other until at z = -1. While the shear layers still interact at the depth (z = -0.5) near the free surface at Fr = 0.20, they digress from each other at Fr = 0.80. On the free surfaces, the shear layers are deviating at both Fr. Large-scale vortex shedding can still be observed on the free surface at Fr = 0.20. On the other hand, the organized large-scale vortex shedding in the deep flow is no longer presented on the free surface at Fr = 0.80. Compared with the free surface at Fr = 0.20, more small-scale vortices are generated in the larger region of the free surface at higher Fr = 0.80. In addition, the necklace vortices exist on the front side of the cylinder on the free surface at Fr = 0.80.

For Fr = 0.20 and 0.80, the mean flow results are available from Suh et al. (2011) and Kawamura et al. (2002) for the comparison purpose. The effects of the free surfaces on the mean flows in the results of 2.7E-0.20 and 2.7E-0.80 are discussed by comparing with those LES results in the literature. Mean streamwise velocity and vorticity on the vertical planes at Fr = 0.20 are compared between CFDShip-Iowa version 6.2.5 and the numerical results of Kawamura et al. (2002) and Suh et al. (2011) in Fig. 4.14 and 4.15. Negative streamwise velocity can be observed at x = 1.0 and does not exist at x = 2.5. This indicates the streamwise locations at x = 1.0 and 2.5 are inside and outside of the recirculation region at Re = 2.7×10^4, respectively. The streamwise velocity contours show the wider wake at x = 2.5 than that at x = 1.0. At both x = 1.0 and 2.5, the wake width is slightly increased near the free surface, whereas the width is almost constant at the deeper level than about 0.5D. Small streamwise vortices can be seen only near the free surface at Fr = 0.20. The streamwise vortices near the free surface induce the outward transverse velocity which results in the separated region expanded in the transverse direction on the free surface (Suh et al., 2011). Fig. 4.16 clearly shows the

higher transverse velocity and the slightly wider separated region on the free surface than those at z = -3.5.

For steady flow of constant density, the transport equation of the streamwise vorticity can be written as Eq. (4.2). In Eq. (4.2), Ω_x, Ω_y, and Ω_z are the streamwise, transverse, and vertical components of the mean vorticity, respectively. Term (A) represents the material derivative of the mean streamwise vorticity. The first term of term (B) is the vorticity amplification by the streamwise stretching, while the other terms provide vortex-line bending effects. Term (C) suggests the vorticity damping by the viscous diffusion. Terms (D), (E), and (F) are the vorticity production by inhomogeneity in the Reynolds stress field.

$$\left(U\frac{\partial \Omega_x}{\partial x}+V\frac{\partial \Omega_x}{\partial y}+W\frac{\partial \Omega_x}{\partial z}\right) \quad \text{(A)}$$

$$=\left(\Omega_x\frac{\partial U}{\partial x}+\Omega_y\frac{\partial U}{\partial y}+\Omega_z\frac{\partial U}{\partial z}\right) \quad \text{(B)}$$

$$+\nu\left(\frac{\partial^2 \Omega_x}{\partial x^2}+\frac{\partial^2 \Omega_x}{\partial y^2}+\frac{\partial^2 \Omega_x}{\partial z^2}\right) \quad \text{(C)}$$

$$+\frac{\partial}{\partial x}\left(\frac{\partial \overline{u'v'}}{\partial z}-\frac{\partial \overline{u'w'}}{\partial y}\right) \quad \text{(D)}$$

$$+\frac{\partial^2}{\partial y \partial z}\left(\overline{v'v'}-\overline{w'w'}\right) \quad \text{(E)}$$

$$+\left(\frac{\partial^2}{\partial z^2}-\frac{\partial^2}{\partial y^2}\right)\overline{v'w'} \quad \text{(F)} \qquad (4.2)$$

As show in Fig. 4.17, the y and z components of term (B) and term (E) in Eq. (4.2) are the dominant source terms for the mean streamwise vorticity at Fr = 0.20. However, the y and z components of term (B) are canceled because they have the same magnitudes with the opposite signs. Hence, the term (E) is the main mechanism to generate the mean streamwise vorticity on the free surface at Fr = 0.20. These trends are similar to those at Fr = 0.80, as shown later, and consistent with those observed by Suh et al. (2011).

The predictions of 2.7E4-0.80 also show the similar trends to those in the numerical results obtained by CFDShip-Iowa version 6.2 at the same Re and Fr (Suh et al., 2011). Fig. 4.18 and 4.19 compare the mean streamwise velocity and vorticity components at Re = 2.7×10^4 and Fr = 0.80 between the CFDShip-Iowa version 6.2.5 predictions and the numerical results of Suh et al. (2011). At x = 1.0, the contours of the streamwise velocity show that the width of the wake increases significantly near the free surface, whereas the width is almost constant in the deep flow. It is obvious by comparing the streamwise velocity at x = 1.0 between Fr = 0.20 and 0.80 that the wake width is much larger at the higher Fr = 0.80 with the same Re. Since the plane at x = 1.0 is inside the recirculation region at this Re, negative mean streamwise velocities are observed in the deep flow and near the free surface. However, there is no negative streamwise velocity at around z = -1.5. Hence, the width of the recirculating zone increases as the free surface is approached. At x = 2.5, a negative streamwise velocity is still observed near the free surface, whereas the velocity in the deep flow increases to positive values, which indicates the slower velocity recovery in the wake on the free surface. On this vertical plane, the width of the wake is increased substantially near the free surface and slightly in the deep flow. The narrowest wake region locates at a slightly lower position (z = -1.1) on this vertical plane. This observation is consistent with Kawamura et al. (2002) and Suh et al. (2011).

The pair of strong counter-rotating streamwise vortices is responsible for the increased wake width and the large outward transverse velocity near the free surface. At x=2.5, streamwise vortices are only seen near the free surface. The locations of the mean streamwise vortices and the shapes of the wake on the free surface correlate well, indicating the effect of secondary swirl of the vortical structures on the wake structures (Kawamura et al., 2002; Suh et al., 2011). The mean transverse vorticity component is significant near the free surface only. Since the magnitude of the mean transverse vorticity is larger than that of the mean streamwise vorticity on the free surface between

the two surface-parallel vorticity components, the mean transverse vorticity is more responsible for the fluctuations of the free surface (Suh et al., 2011). The vertical distributions of the mean vertical vorticity component in the deep flow and the air region are due to the Karman vortex shedding. Its distribution near the free surface is inclined outward in the transverse direction, due to the outward mean transverse velocity generated near the free surface. The location of the high magnitude vorticity matches with the high gradient region of the mean streamwise velocity.

Fig 4.20 and 4.21 compare magnitudes of the Reynolds normal stresses and the shear stress at Re = 2.7×10^4 and Fr = 0.8 between the predictions of 2.7E-0.80 and the numerical results by CFDShip-Iowa version 6.2 (Suh et al., 2011). For the streamwise Reynolds normal stress $R_{xx} = \overline{u'u'}$, the peak values at x = 1 are produced near the free surface and along the separation region in the deep flow where the mean streamwise velocity is recirculated. Large R_{xx} is observed where the mean streamwise velocity gradients are very high, which indicates a region of high turbulent kinetic energy production. In addition, R_{xx} is increased locally near the edge of the separated region on the free surface, due to the increased velocity gradient by the outward transverse velocity generation. Relatively uniform distribution of R_{xx} inside the separated region at x = 1 is probably owing to the enhanced mixing by the complex streamwise vorticity inside the separated flow region.

For the transverse Reynolds normal stress $R_{yy} = \overline{v'v'}$, one or two peaks are observed in the deep flow near the symmetry plane**.** The peaks are due to the vortex shedding by the interaction of the shear layers separating from both sides of the cylinder. The behavior of R_{yy} near the free surface shows similar trends to those of R_{xx}. In the separated flow region, R_{yy} decreases as it approaches the free surface.

The vertical Reynolds normal stress $R_{zz} = \overline{w'w'}$ has a relatively large magnitude on the free surface and is directly related with the free surface fluctuations, which result in the significant streamwise vorticity and the outward transverse velocity on the free

surface. The feature of R_{zz} near the free surface is very similar to that of R_{xx}. Additional peaks are observed near the recirculation zone in the deep flow. R_{zz} in this deep region is also owing to the up- and downward flow through the vortex centers during the periodic vortex shedding.

On the free surface, the Reynolds shear stress $R_{xy} = \overline{u'v'}$ has an insignificant magnitude in the wake region because the shear layers from both sides deviate from each other and the interaction between them is restrained. Yu et al. (2008) also observed the decreased values of R_{xy} on the free surface.

Fig. 4.22 – 4.24 compares the dominant source terms for the mean vorticity components at x = 1.0 between CFDShip-Iowa version 6.2 (Suh et al., 2011) and CFDShip-Iowa version 6.2.5. For the mean streamwise vorticity, the y and z components of term (B) by the vortex bending are of a similar magnitude, but of opposite signs, so the total effect of them is canceled out. The remaining term (E) is the main production mechanism of the mean streamwise vorticity, which means the vertical and transverse gradients of the difference between R_{yy} and R_{zz} are partly responsible for the generation of the streamwise vorticity near the free surface and presumably cause the outward transverse velocity on the free surface.

The dominant terms for the mean transverse vorticity at x = 1.0 are the z component of term (B), term (E), and term (F). The z component of term (B) is from the bending of the vertical vorticity by the outward mean transverse velocity generation near the free surface. In other words, the swirling motion of the vortex shedding and shear-layer instability in the deep flow is changed to the free surface fluctuations via vortex bending.

In the deep flow, term (F) is the dominant source for the mean vertical vorticity. Hence, the shear stress is primarily responsible for the Karman vortex shedding and shear-layer instability in the deep flow. The dominant terms for the mean vertical vorticity near the free surface are the z component of term (B) and term (E), which are

the vortex stretching of the vertical vorticity and from the anisotropy between the streamwise and transverse Reynolds normal stresses, respectively.

In order to investigate the effect of the free surface on the flow at high Re = 4.58×10^5 and high Fr = 1.64, the numerical results of CFDShip-Iowa version 6.2.5 (4.58E5-1.64) are analyzed by comparing with those of the single-phase flow at the similar Re = 5×10^5 (5E5-CS). Fig. 4.25 compares the instantaneous vertical vorticity on the free surface of 4.58E5-1.64 with that on a horizontal plane of 5E5-CS. Compared to the single-phase flow at similar Re = 5×10^5, more small-scale vortices are generated over a large range of the wake on the free surface. Many vortices are located on the bow wave and depressions regions. In addition, more small-scale vortices are generated on the free surface in the further downstream direction and are inclined to the more outward transverse direction at higher Fr, as shown in Fig. 4.12, 4.13, and 4.25.

Fig. 4.26 – 4.28 compare the mean flows between 5E5-CS and 4.58E5-1.64. Fig. 4.27 shows the results of 4.58E5-1.64 on the curved plane which is 0.22D lower than the mean free surface. The plane near the free surface is always inside the water phase. On the plane, the mean vorticity components show similar magnitudes to those in the single-phase flow at Re = 5×10^5 shown in Fig. 4.26. On the other hand, the mean vertical velocity shows much higher magnitude than that of 5E5-CS. The magnitude correlates with the mean free surface elevations shown in Fig. 4.29, which includes very high bow wave, a pair of large symmetric depressions, and high elevations in the wake. In addition, the transverse velocity in the wake presents nonzero magnitudes in the further downstream direction and the more outward transverse direction.

The predictions of 2.7E4-0.20 and 2.7E4-0.80 show that the streamwise vorticity and the resulting outward transverse velocity generated near the free surface are primarily responsible for attenuation of the periodic vortex shedding, deviation of the separated shear layers, and the increased wake widths, which are consistent with the observation of Kawamura et al. (2002) and Suh et al. (2011). The mean flow on the free surface

computed by 4.58E5-1.64 also shows the high magnitudes of the streamwise vorticity and the transverse velocity. In the wake region, the positive streamwise vorticity induces the negative transverse velocity, while the negative vorticity results in generation of the positive velocity. The transverse velocity is inward and outward in the near and far wake region, respectively. These features of the transverse velocity cause the wake whose width is slightly shrunk near the cylinder and substantially expanded in the far region. The mean streamwise velocity contours in Fig. 4.28 (a) and the streamlines in Fig. 4.29 show the characteristics of the wake width clearly. The mean streamwise velocity contours also present the small recirculation region inside the cavity structure of the free surface. The mean vertical velocity contours correlate well with the deformations of the free surface including the high bow wave on the upstream side of the cylinder, the cavity structure immediately behind the cylinder, the large symmetric depressions behind the cavity, and the Kelvin waves. In addition, the mean transverse vorticity on the free surface shows the large magnitudes inside the symmetric depressions.

Reynolds stresses are compared between 5E5-CS and 4.58E5-1.64 in Fig. 4.30 – 4.32. R_{xx} on the curved plane 0.22D below the free surface shows the similar peak magnitude to that in the single-phase flow at Re = 5×10^5, whereas R_{yy} has the lower peak than that of 5E5-CS. R_{zz} near the free surface shows the higher peak near the circular cylinder presumably due to the free surface fluctuations inside the deep cavity structure. All shear stress components in the near wake region present similar magnitudes to those of 5E5-CS. The shear stresses near the free surface also have nonzero magnitudes in the far wake region, which is related to the free surface fluctuations.

The Reynolds stress contours on the free surface correlate well with the deformations of the free surface because the stresses are related to the free surface fluctuations. The normal components have the peak magnitudes near the center plane of the wake. The peak of R_{yy} is located near the downstream edge of the cavity on the free surface where the separated shear layers interact, as shown in Fig. 4.29. R_{zz} also shows

the peak near the edge of the cavity structure where the free surface fluctuations are presumably large. R_{xy} and R_{xz} have the larger magnitudes than that of R_{yz}. On the free surface, the Reynolds shear stress components have the smaller magnitudes than the normal components. Yu et al. (2008) and Suh et al. (2011) also observed the similar trend of R_{xy} on the free surface at Re = 2.70×10^4 and Fr = 0.80.

The source terms for the mean streamwise vorticity, as shown in Eq. (4.2), are compared between 5E5-CS and 4.58E5-1.64 in Fig. 4.33 – 4.35. As shown in Fig. 4.34, the mean streamwise vorticity near the free surface is dominantly produced by term (D), (E), and (F) which are due to the inhomogeneity in the Reynolds stress field. This trend is similar to that in the single-phase flow at Re = 5×10^5 shown in Fig. 4.33.

It is noted that term (E) and (F) on the free surface have the similar magnitude but the opposite signs as well as the y and z components of term (B). Therefore, term (D) and the x component of term (B) are the dominant source terms for the mean streamwise vorticity on the free surface. The difference of the gradients of two Reynolds shear stresses (R_{xy} and R_{xz}) and the streamwise vortex stretching are primarily responsible for generation of the mean streamwise vorticity on the free surface.

Fig. 4.36 – 4.38 compare the source terms for the mean transverse vorticity between 5E5-CS and 4.58E5-1.64. Similar to the mean streamwise vorticity, the terms due to the Reynolds stress gradients are the main mechanism to generate the mean transverse vorticity near the free surface, as shown in Fig. 4.37.

The source terms for the mean transverse vorticity on the free surface also show the similar characteristics to those of the source terms for the mean streamwise vorticity. Since the term (E) and (F) have the similar magnitudes but the opposite signs as well as the y and z components of term (B), the x component of term (B) and term (D) are mainly responsible for generation of the mean transverse vorticity on the free surface. The x component of term (B), $\Omega_x \partial V/\partial x$, is produced mainly by the strong streamwise

vorticity on the free surface, while term (D) is the difference of the gradients of two Reynolds shear stresses (R_{xy} and R_{yz}).

Fig. 4.41 – 4.43 compare the source terms for the mean vertical vorticity between 5E5-CS and 4.58E5-1.64. As shown in Fig. 4.42, the mean vertical vorticity near the free surface is generated mainly by the production terms due to the Reynolds stress gradients, which is similar to other vorticity components. The z component of term (B) shows the high magnitude in the shear layers because of the strong vertical vorticity, whereas other components of term (B) have smaller magnitudes. These features are similar to those in the single-phase flow at Re = 5×10^5 (5E5-CS).

On the free surface, the source terms for the mean vertical vorticity show the similar characteristics to those for other vorticity components. The y and z components of term (B) have the similar magnitudes with the opposite signs, so the dominant terms in the transport equation of the mean vertical vorticity are the x component of term (B) and the terms due to the Reynolds stresses. The x component of term (B), $\Omega_x \partial W/\partial x$, is produced mainly by the strong mean streamwise vorticity on the free surface.

4.3 Summary

CFDShip-Iowa version 6.2.5 has been applied to the flows past a circular cylinder piercing the free surfaces vertically in order to assess the accuracy of the coupled orthogonal curvilinear/Cartesian grid solver in the simulation of the flows with free surfaces. The numerical simulations have been performed for the two-phase turbulent flows past a surface-piercing circular cylinder at (Re, Fr) = (2.7×10^4, 0.20), (2.7×10^4, 0.80), and (4.58×10^5, 1.64) due to availability of several detailed results from both experimental and numerical studies in the literature. The effects of the free surfaces on the vortex shedding and the separated regions have also been analyzed by comparing the CFDShip-Iowa version 6.2.5 results with the LES results in the literature and those of the single-phase flow at the similar supercritical Re = 5×10^5, i.e., 5E5-CS in Chapter 3.

For the low (= 0.20) and medium (= 0.80) Fr cases, CFDShip-Iowa version 6.2.5 predicted the similar C_D and C_L^{RMS} to those obtained by the other numerical studies, which are up to 51% lower than the experimental data of the single-phase flow at the same Re.

CFDShip-Iowa version 6.2.5 appropriately captured the features of the instantaneous free surfaces for all Fr, which are shown in the experimental data and the numerical results. The CFDShip-Iowa version 6.2.5 predictions showed good agreement with the experimental and numerical results in terms of the profiles of the velocity and free surfaces and the variation of free surface elevations by Fr.

In the study of the effects of free surfaces, CFDShip-Iowa version 6.2.5 showed the similar results to those obtained by the past numerical studies using LES for Fr = 0.20 and 0.80. The organized vortex shedding observed in the deep flows is attenuated on the free surface, and many vortices with smaller scales are generated. On the free surface, the shear layers separating from the two sides of the cylinder digress, and the wake is substantially expanded in the transverse directions. The streamwise vorticity and the resulting outward transverse velocity, which are mainly produced by the vertical and transverse gradients of the difference between R_{yy} and R_{zz}, are primarily responsible for the deviation of the shear layers and the large wake widths. These trends of the vortex shedding, deviating shear layers, and the expanded wake on the free surface are more prominent in the flow at Fr = 0.80 than that at Fr = 0.20.

The numerical results of CFDShip-Iowa version 6.2.5 at Re = 4.58×10^5 and Fr = 1.64 have been compared with those of the single-phase flow at similar Re = 5×10^5 to analyze the effects of the free surface on the flows at the high Re and Fr. Compared to the single-phase flow at similar Re, more small-scale vortices are generated over a large range of the wake on the free surface at Fr = 1.64. Many vortices are located on the bow wave and depressions regions. While the mean vorticity near the free surface show similar trends to those in the single-phase flow, the mean velocity correlates with the

mean free surface elevations. The source terms for the vorticity near the free surface are mainly produced by the Reynolds stress gradients. The mean flow on the free surface at Fr = 1.64 shows the high magnitudes of the streamwise vorticity and the transverse velocity, which are responsible for the attenuation of periodic vortex shedding. The difference of the gradients of two Reynolds shear stresses and the streamwise vortex stretching are the main mechanism for generation of the mean streamwise vorticity on the free surface. In addition, the source terms due to the strong streamwise vorticity mainly generate both transverse and vertical vortices on the free surface.

Table 4.1 Conditions for CFDShip-Iowa version 6.2.5 simulations of two-phase turbulent flows

Case	Re	Fr	Domain size	Grid resolution	
				$N_x \times N_y \times N_z$	$N_r \times N_\theta \times N_z$
2.7E4-0.20	2.70×10^4	0.20	$-10 \le x/D \le 15$ $-10 \le y/D \le 10$ $-4 \le z/D \le 2$	264×264×128	28×128×128
2.7E4-0.80		0.80			
4.58E5-1.64	4.58×10^5	1.64	$-15 \le x/D \le 42$ $-20 \le y/D \le 20$ $-4 \le z/D \le 2$	336×328×128	28×128×128

Table 4.2 Drag coefficients and RMS of lift fluctuations of two-phase turbulent flows

Case	Fr	Re	C_D	C_L^{RMS}
Experiment	-	2.70×10^4	1.200	0.450
Kawamura et al. (2002) (E)	0.20		1.120 (-6.67%)	0.320 (-28.9%)
2.7E4-0.20 (E)			1.104 (-8.00%)	0.324 (-28.0%)
Kawamura et al. (2002) (E)	0.80		0.970 (-19.2%)	0.240 (-46.7%)
Suh et al. (2011) (E)			0.984 (-18.0%)	0.220 (-51.1%)
2.7E4-0.80 (E)			0.985 (-17.9%)	0.219 (-51.3%)

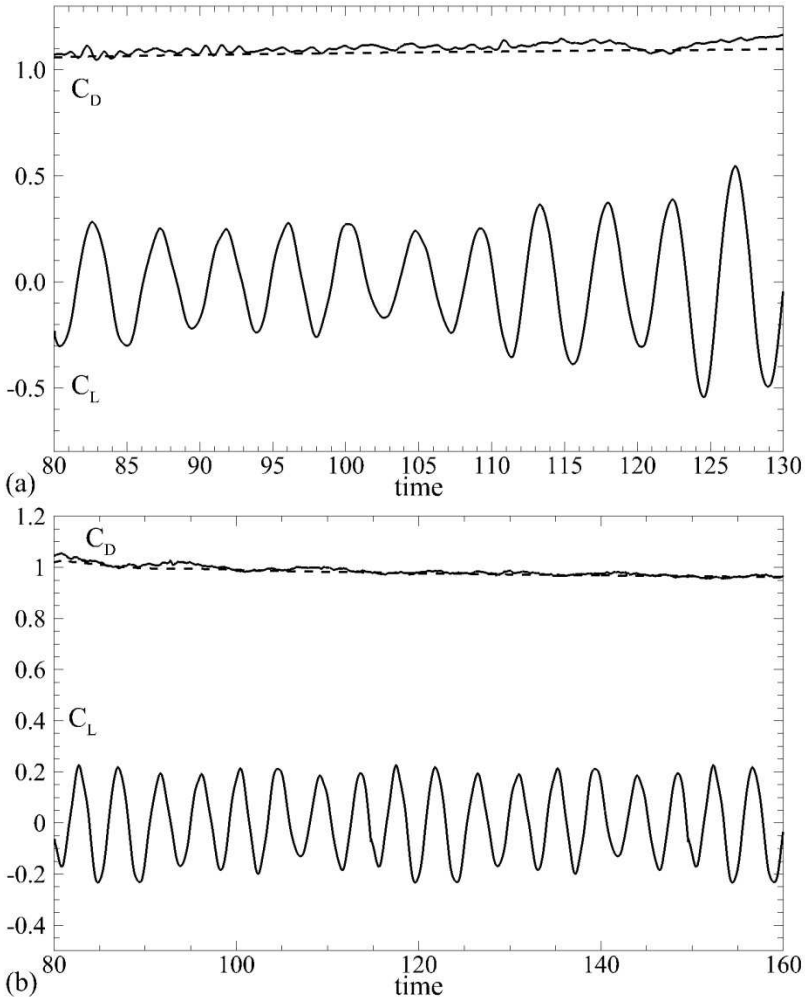

Figure 4.1 Time histories of the drag and lift coefficients. Dotted lines are the running mean of the drag coefficients: (a) 2.7E4-0.20; (b) 2.7E4-0.80

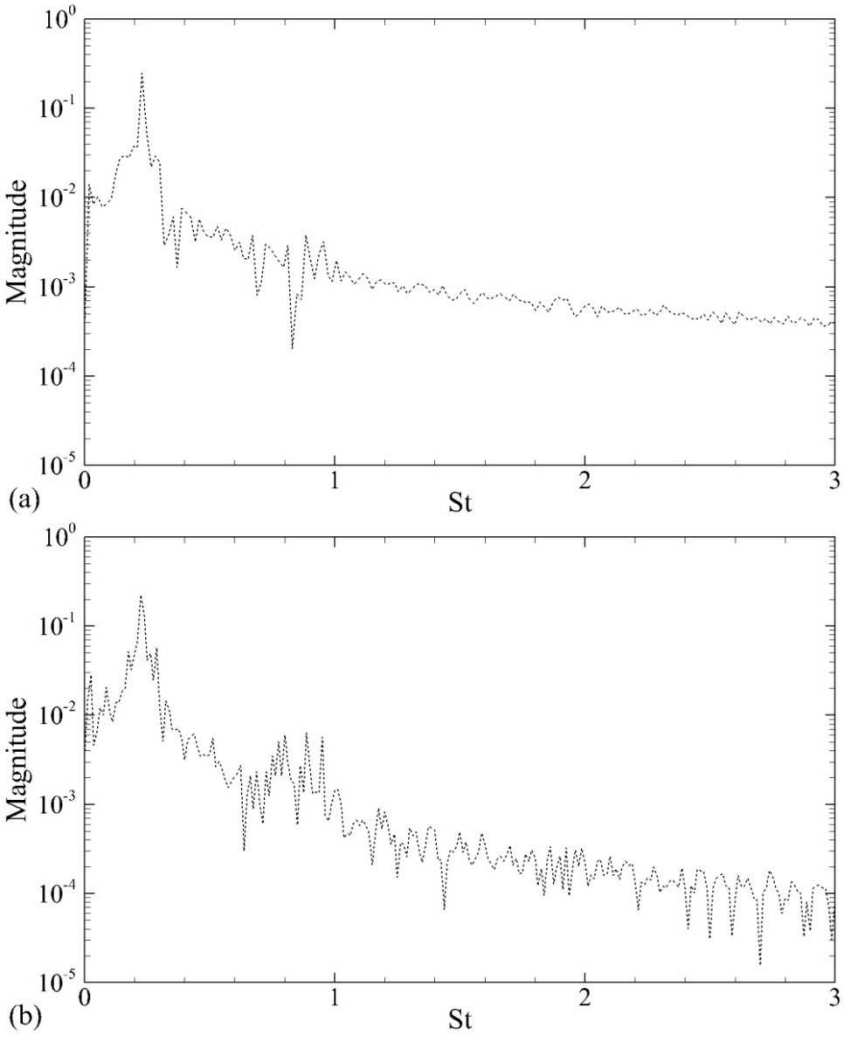

Figure 4.2 FFT of lift coefficients: (a) 2.7E4-0.20; (b) 2.7E4-0.80

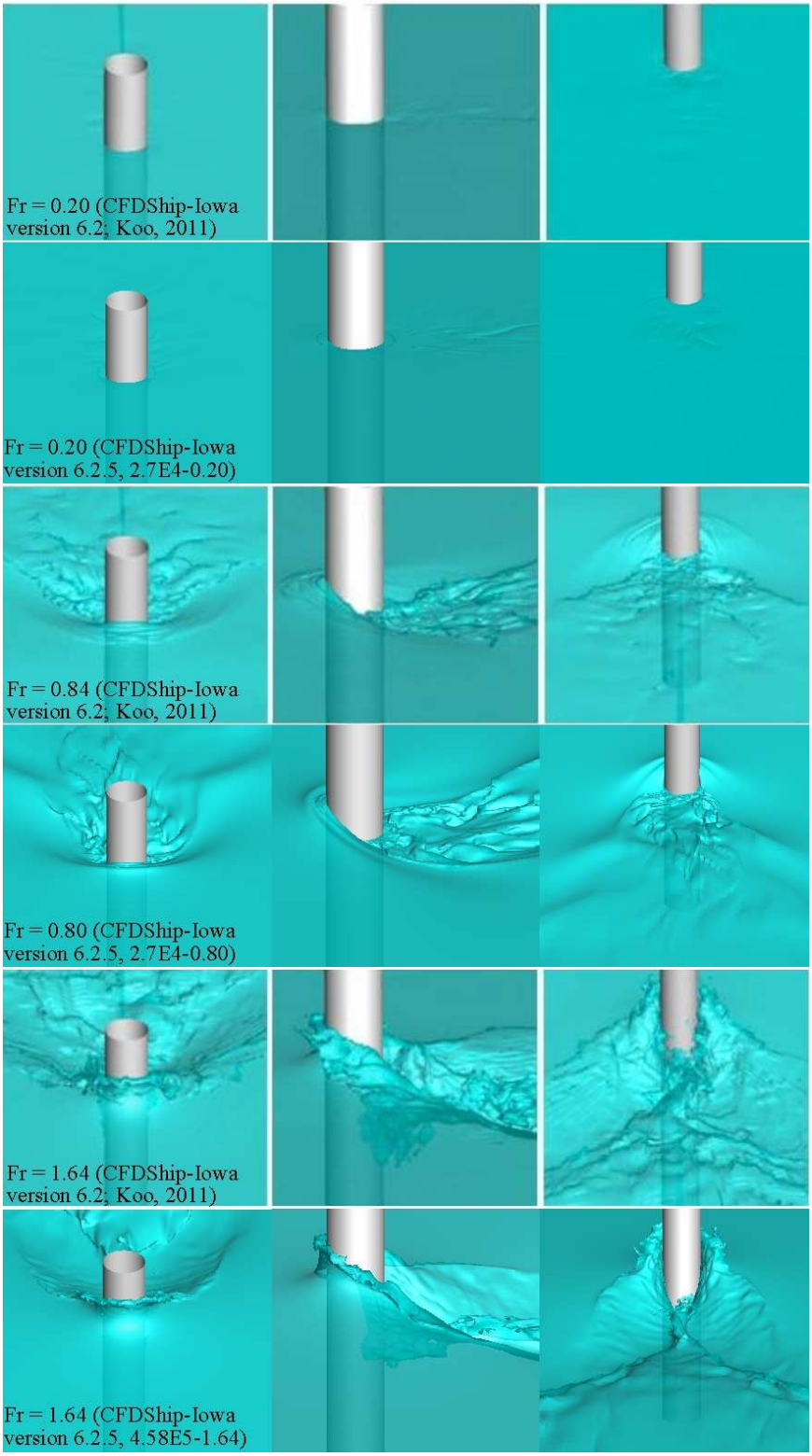

Figure 4.3 Instantaneous free surfaces around the circular cylinder

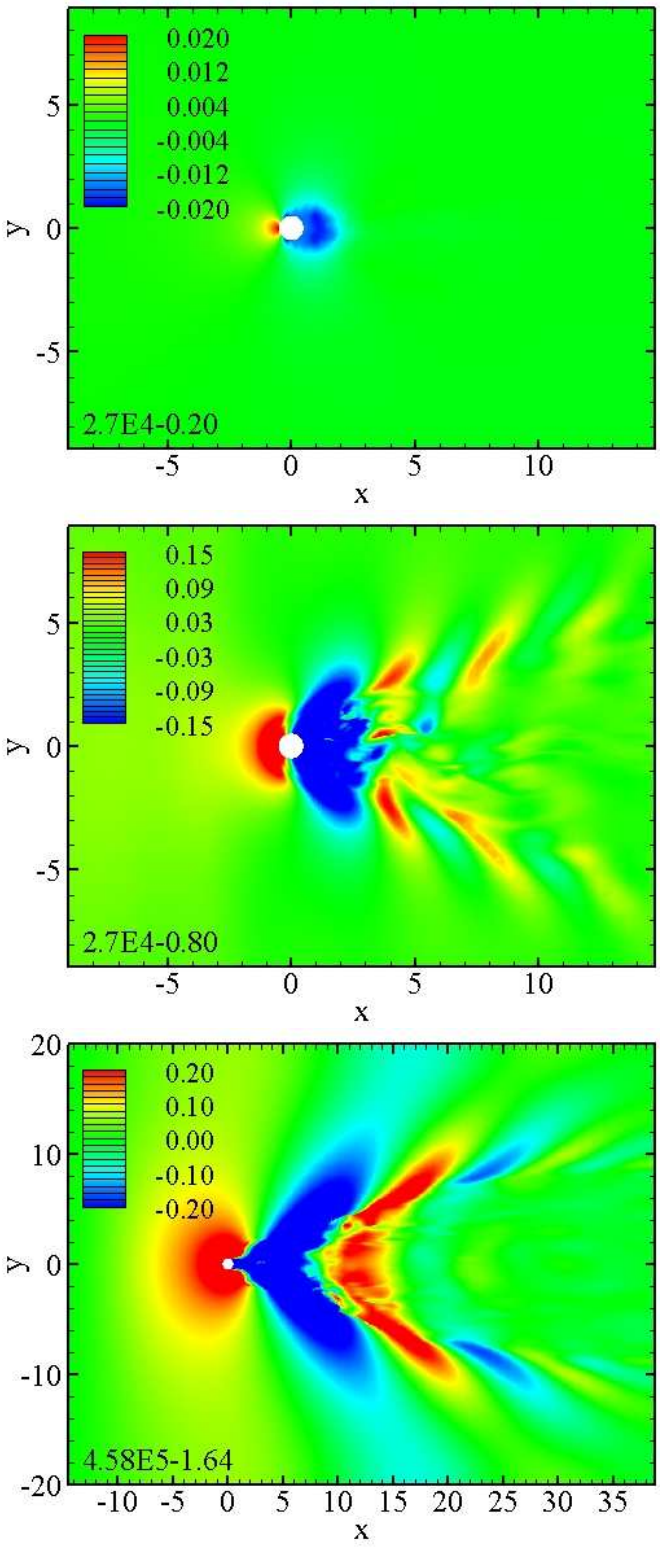

Figure 4.4 Instantaneous free surfaces in the wake behind the circular cylinder

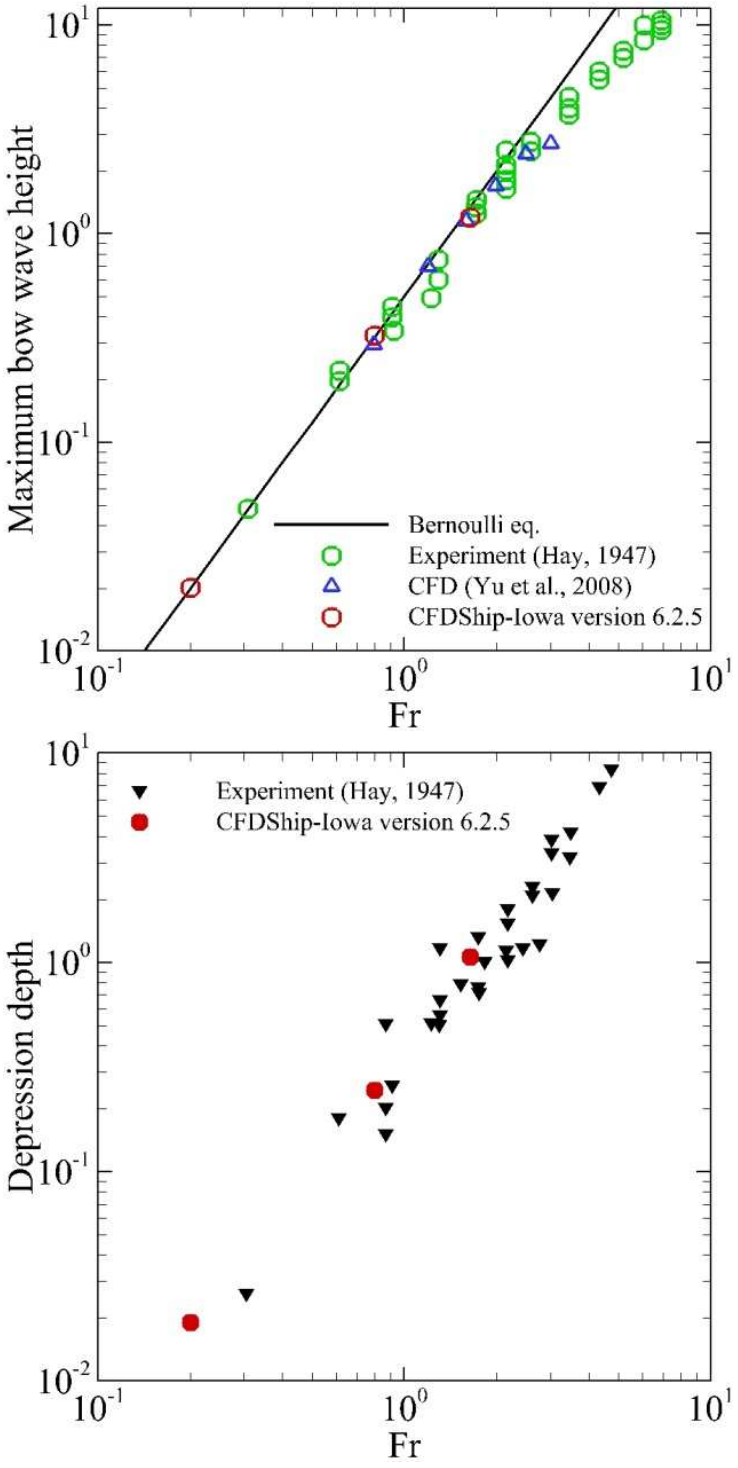

Figure 4.5 Comparison of mean free surfaces: (a) maximum heights of bow waves; (b) depths of depressions behind the cylinder on the center plane of the wake

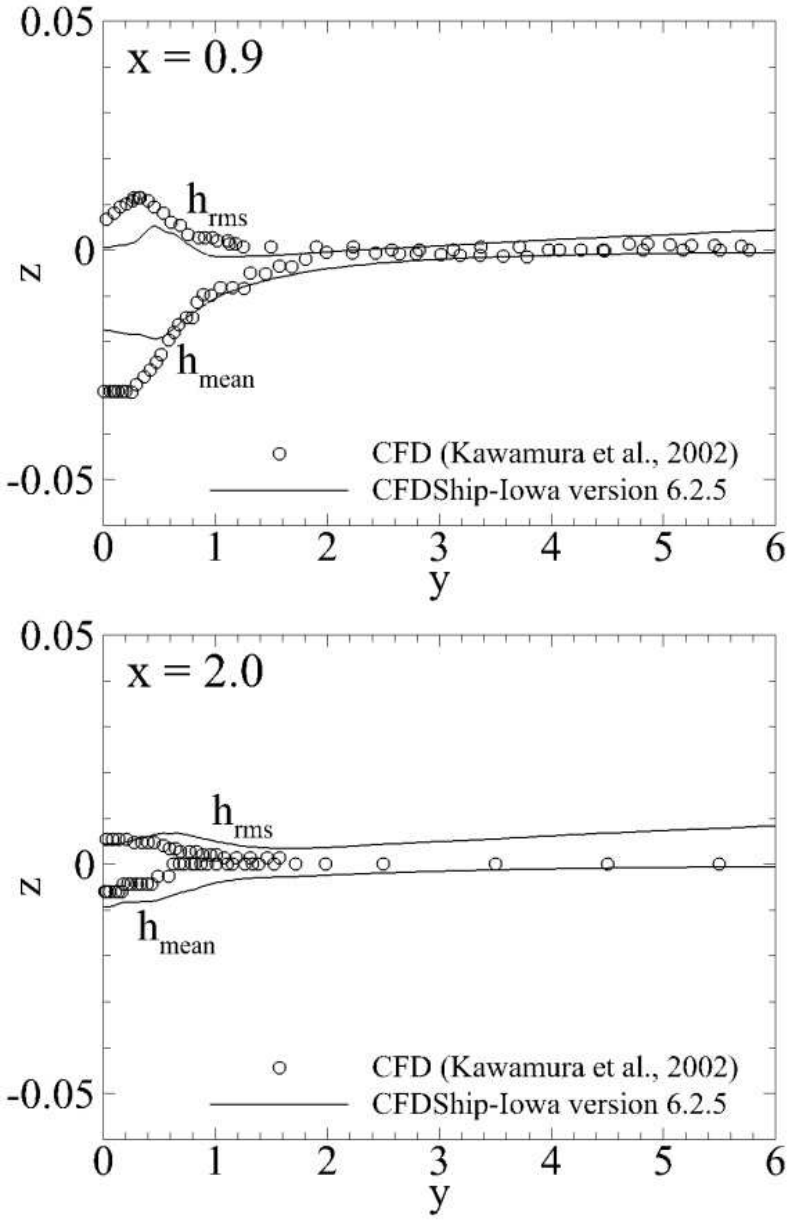

Figure 4.6 Transverse profiles of the mean free surface elevations at Re = 2.7×10^4 and Fr = 0.20

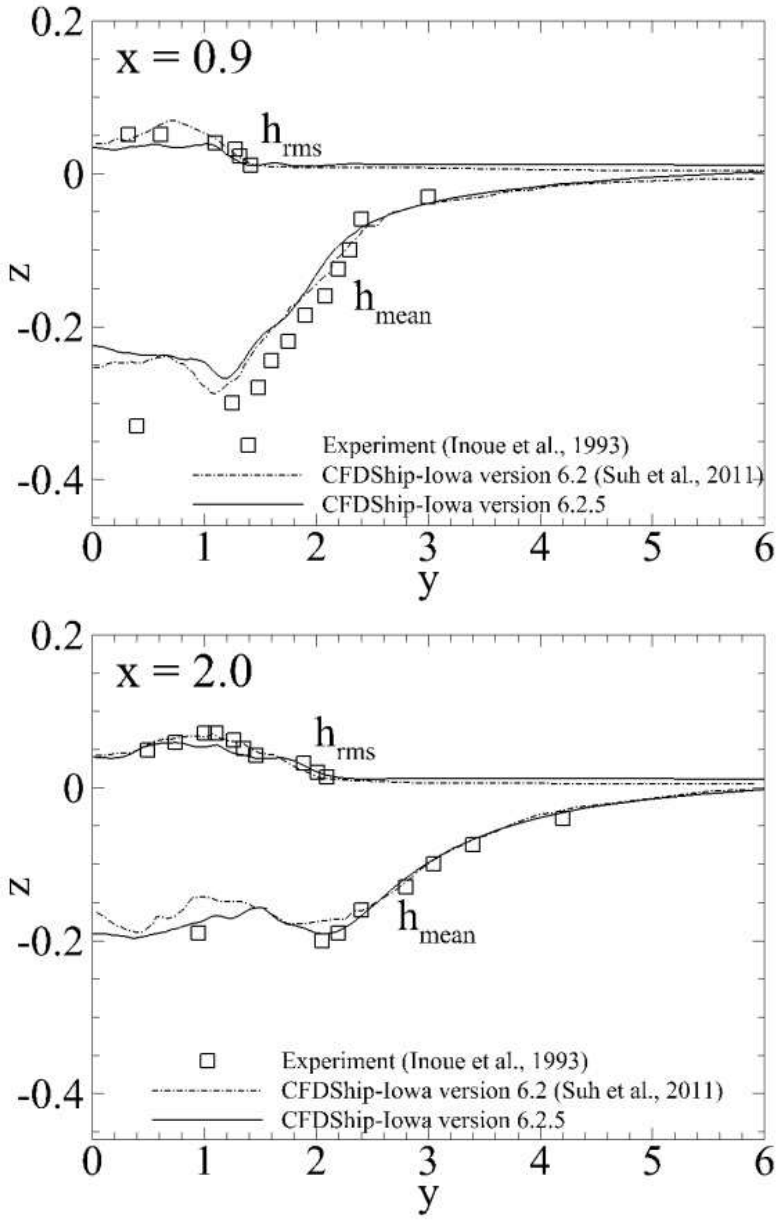

Figure 4.7 Transverse profiles of the mean free surface elevations at Re = 2.7×10^4 and Fr = 0.80

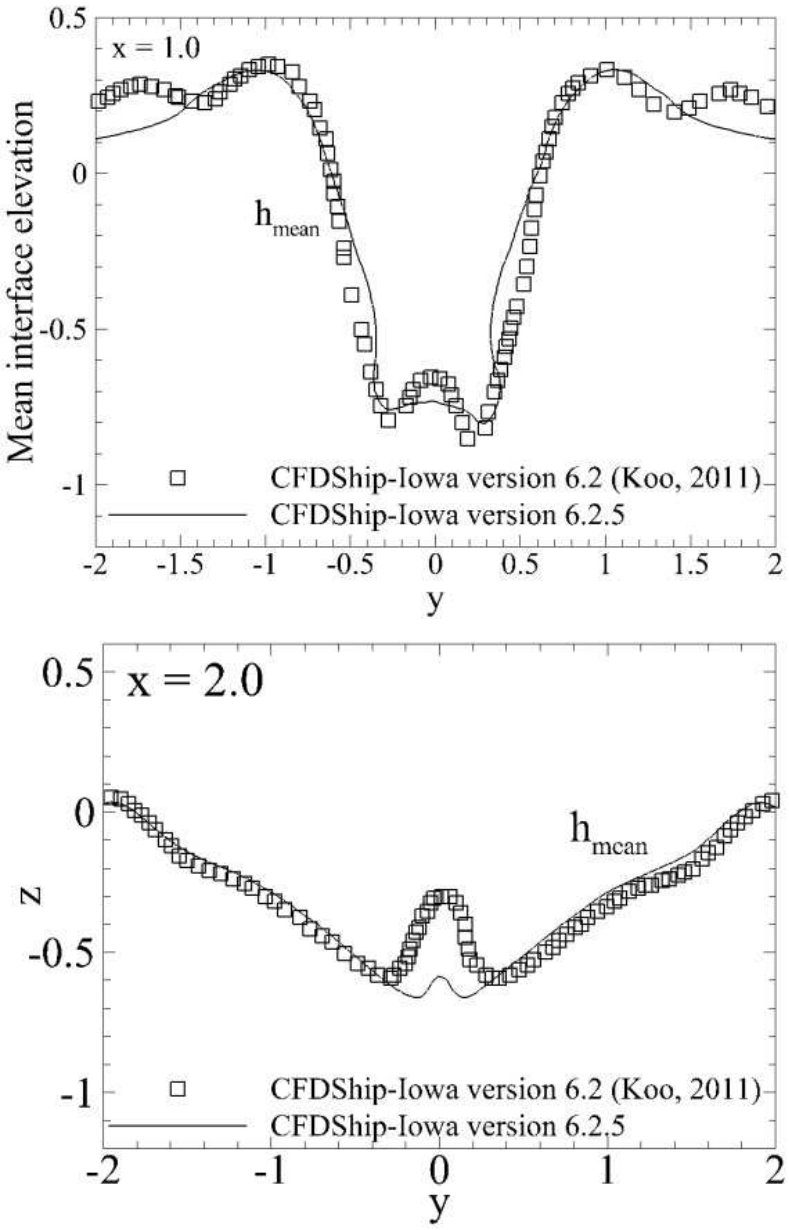

Figure 4.8 Transverse profiles of the mean free surface elevations at Re = 4.58×10^5 and Fr = 1.64

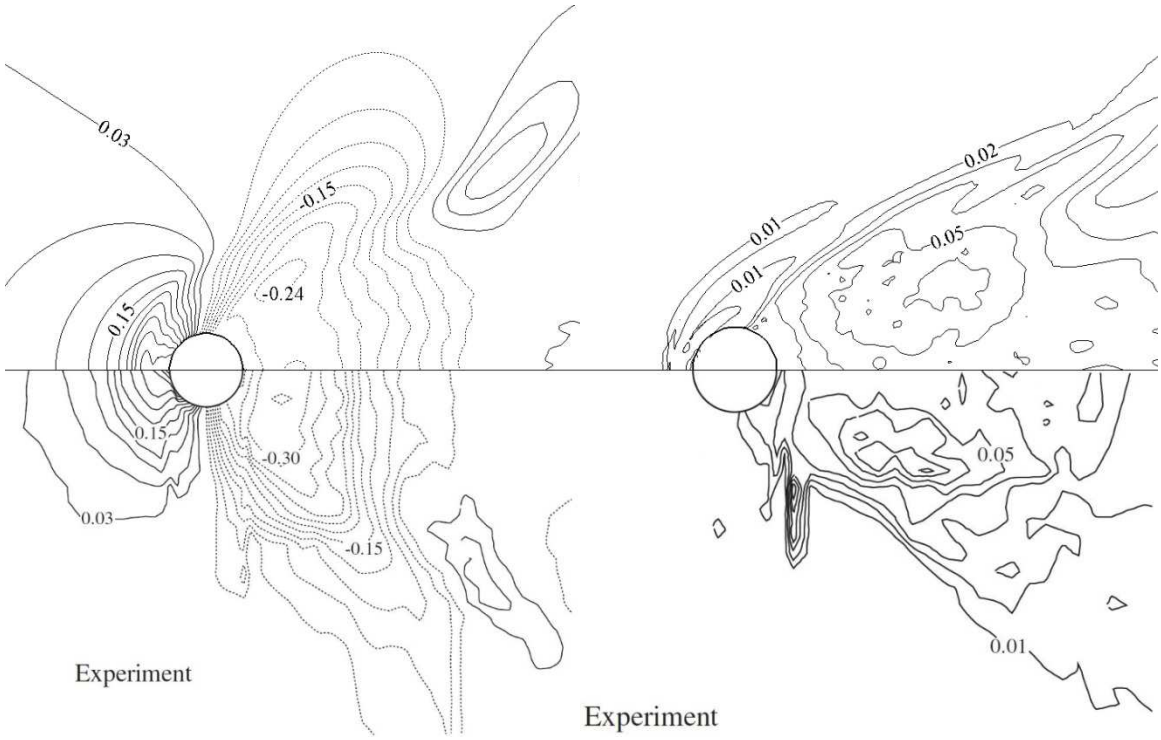

Figure 4.9 Mean free surface around the cylinder at Re = 2.7×10^4 and Fr = 0.80: (left panel) elevations; (right panel) RMS of the free surface fluctuations

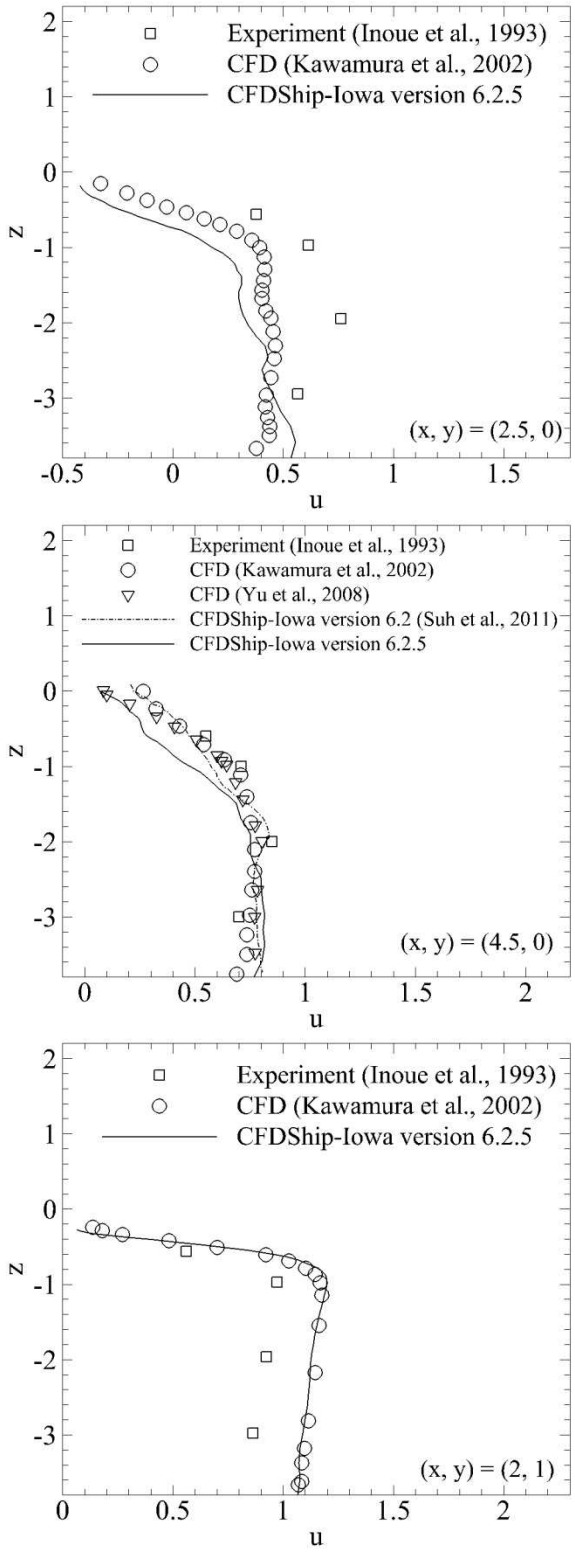

Figure 4.10 Vertical profiles of the mean streamwise velocity at Re = 2.7×10^4 and Fr = 0.80

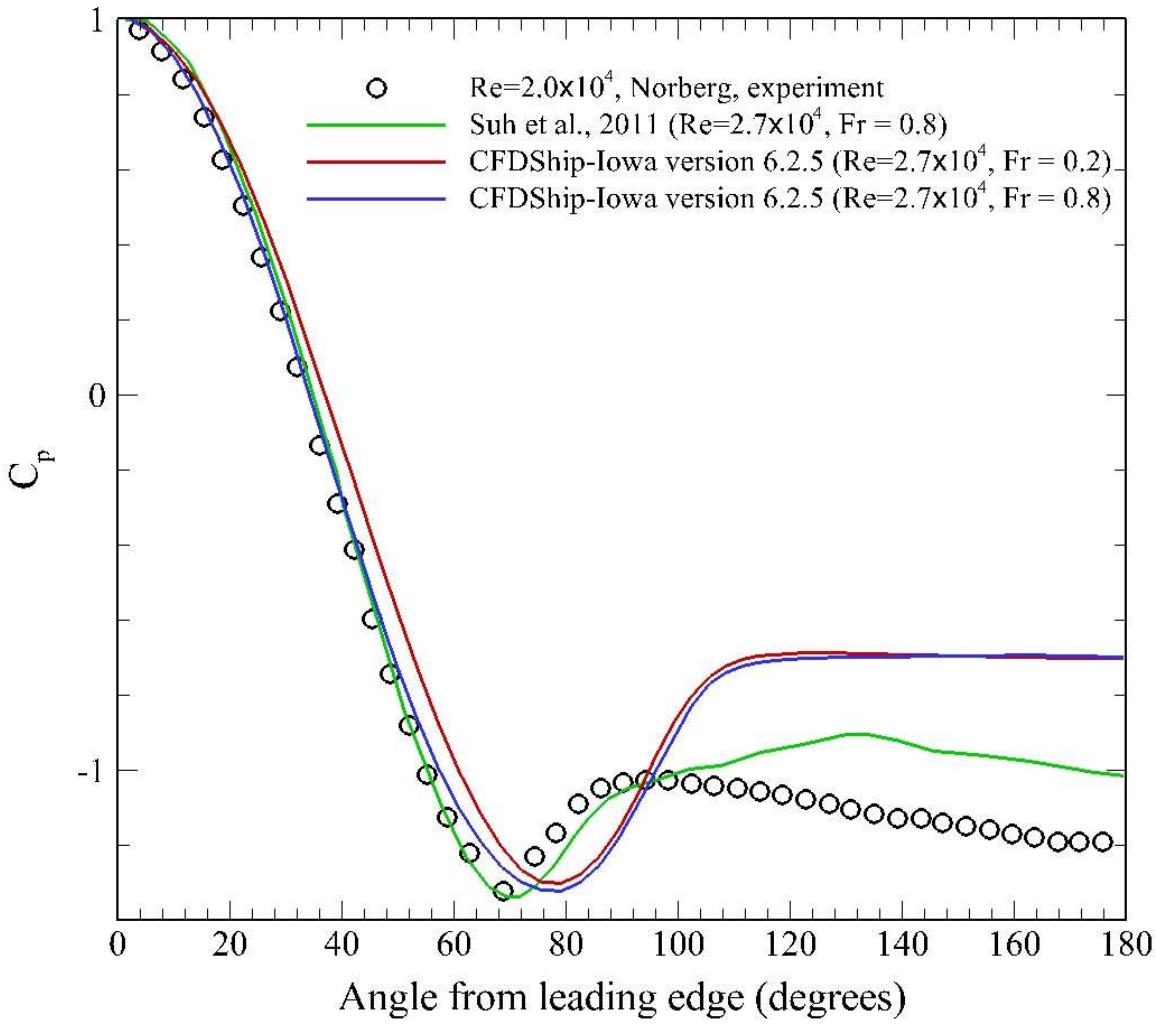

Figure 4.11 Pressure distributions on the cylinder surface in the deep flow region

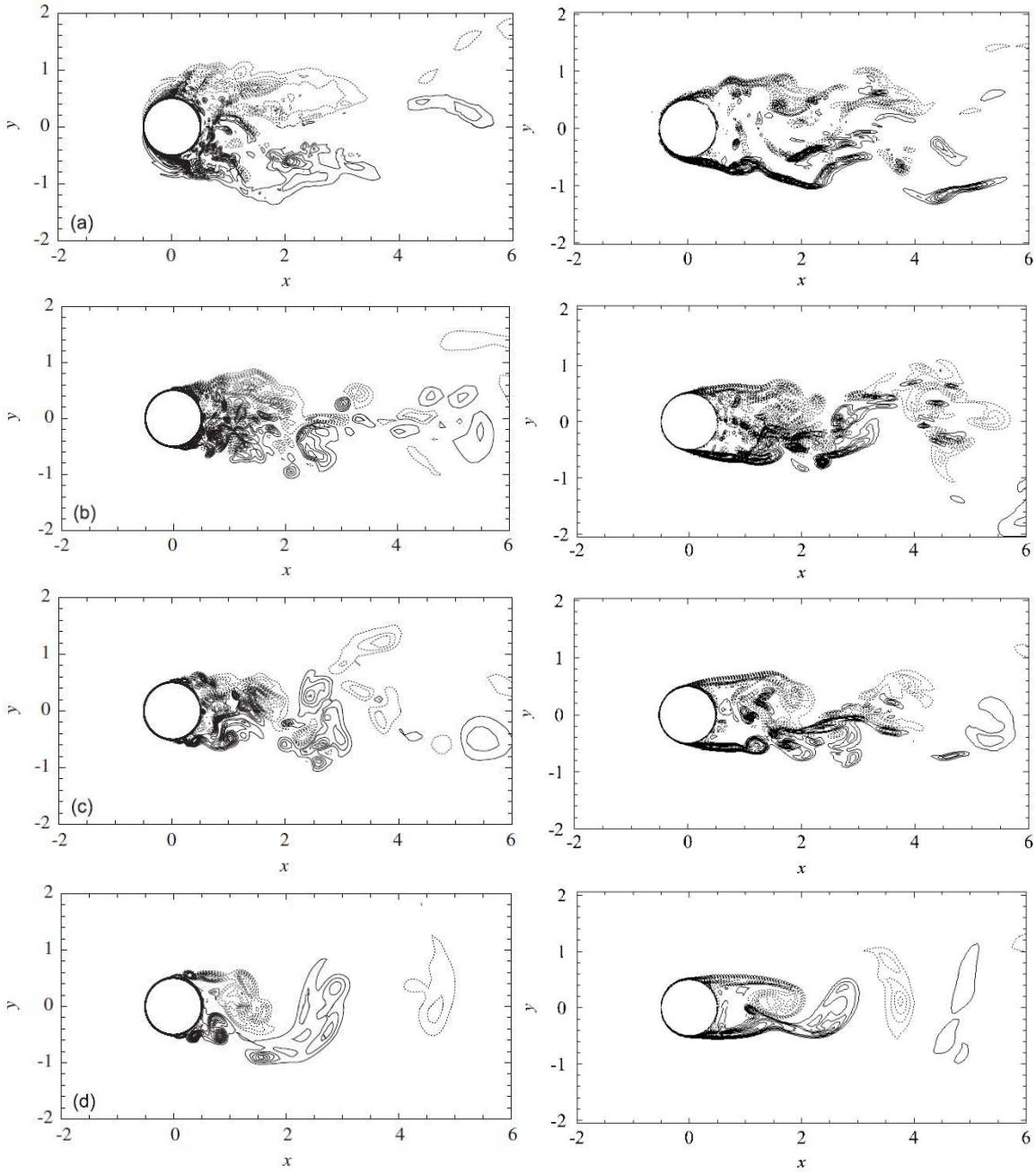

Figure 4.12 Instantaneous vertical vorticity at Re = 2.7×10^4 and Fr = 0.20 computed by CFDShip-Iowa version 6.2 (Suh et al., 2011) (left column) and CFDShip-Iowa version 6.2.5 (right column): (a) on the free surface; (b) z = -0.5; (c) z = -1; (d) z = -3.5. Contour interval is 1.2.

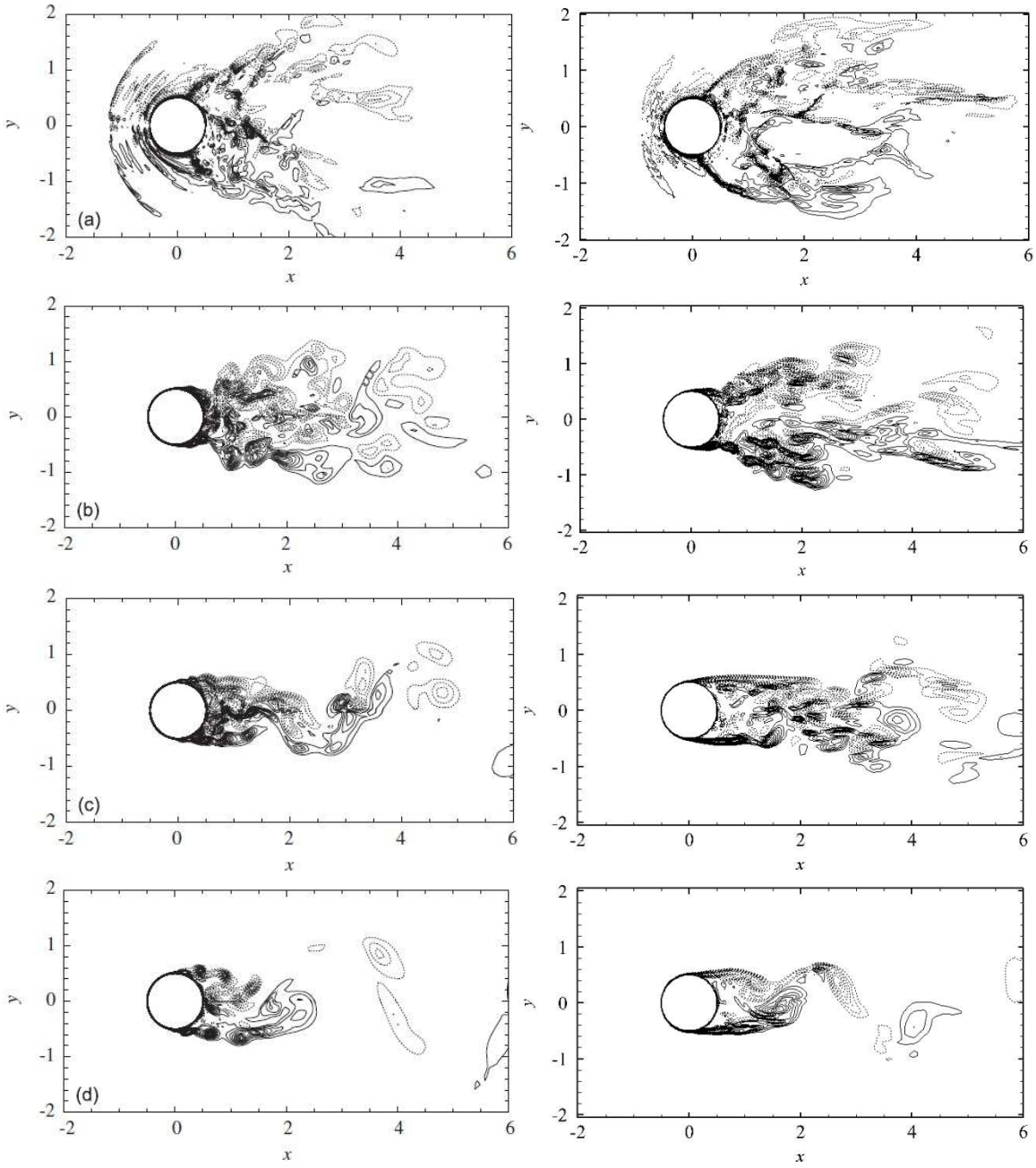

Figure 4.13 Instantaneous vertical vorticity at Re = 2.7×10^4 and Fr = 0.80 computed by CFDShip-Iowa version 6.2 (Suh et al., 2011) (left column) and CFDShip-Iowa version 6.2.5 (right column): (a) on the free surface; (b) z = -0.5; (c) z = -1; (d) z = -3.5. Contour interval is 1.2.

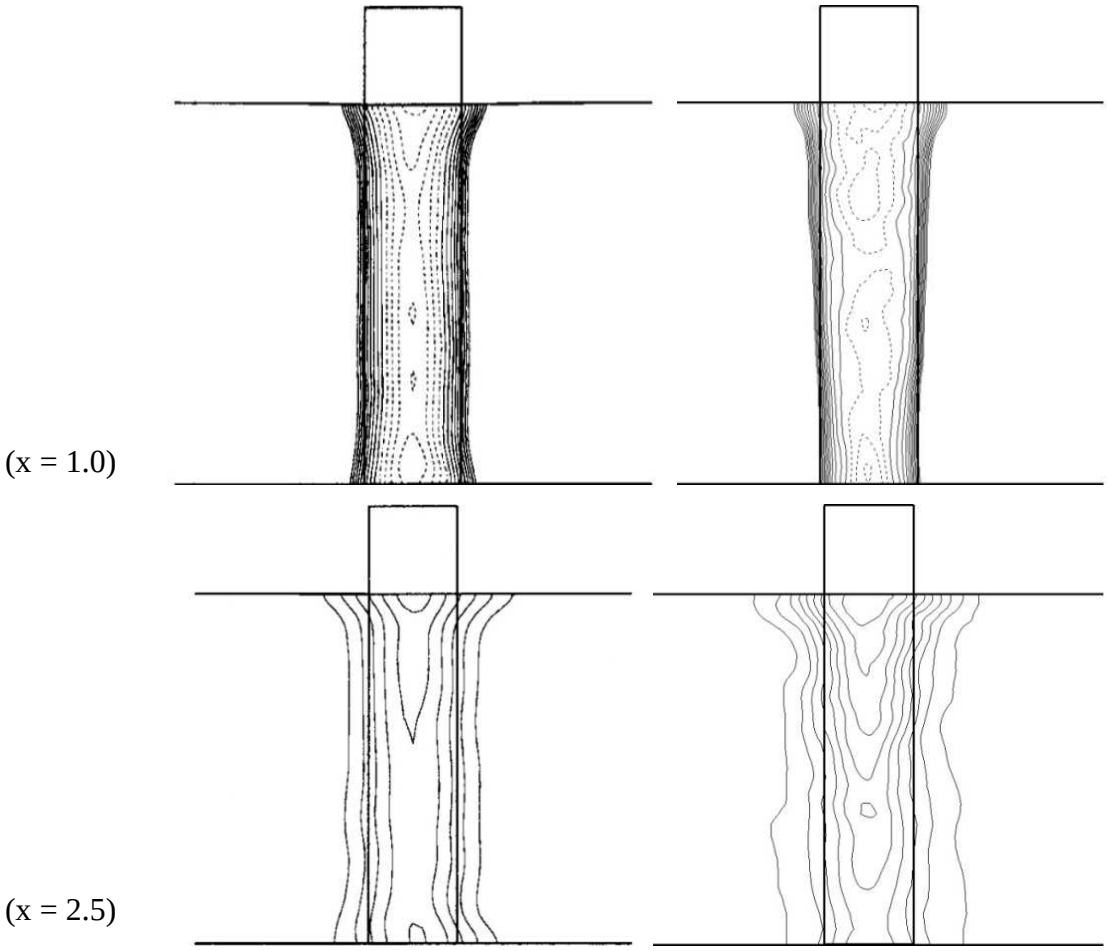

Figure 4.14 Mean streamwise velocity on vertical planes at Re = 2.70×10^4 and Fr = 0.2: (left column) Kawamura et al. (2002); (right column) CFDShip-Iowa version 6.2.5. Contour interval is 0.1.

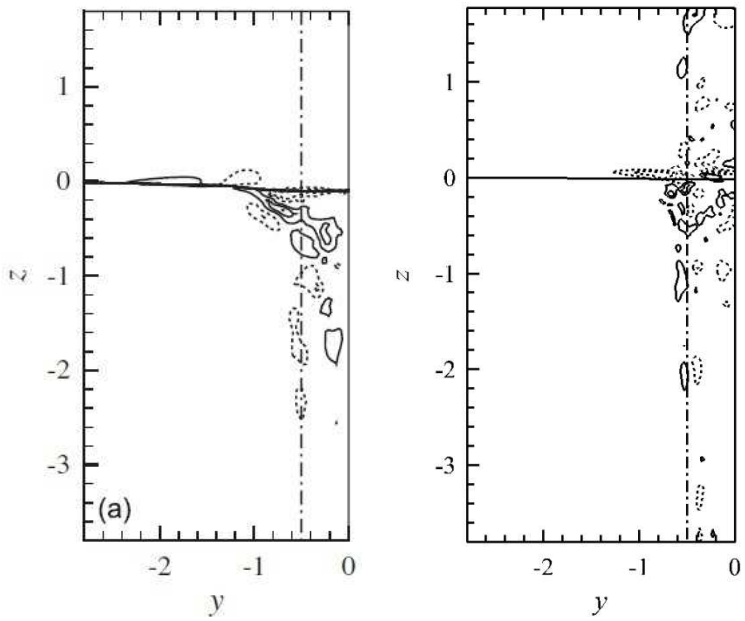

Figure 4.15 Mean streamwise vorticity at x = 1.0 at Re = 2.7×10^4 and Fr = 0.2: (left panel) CFDShip-Iowa version 6.2 (Suh et al., 2011); (right panel) CFDShip-Iowa version 6.2.5. Contour interval is 0.5.

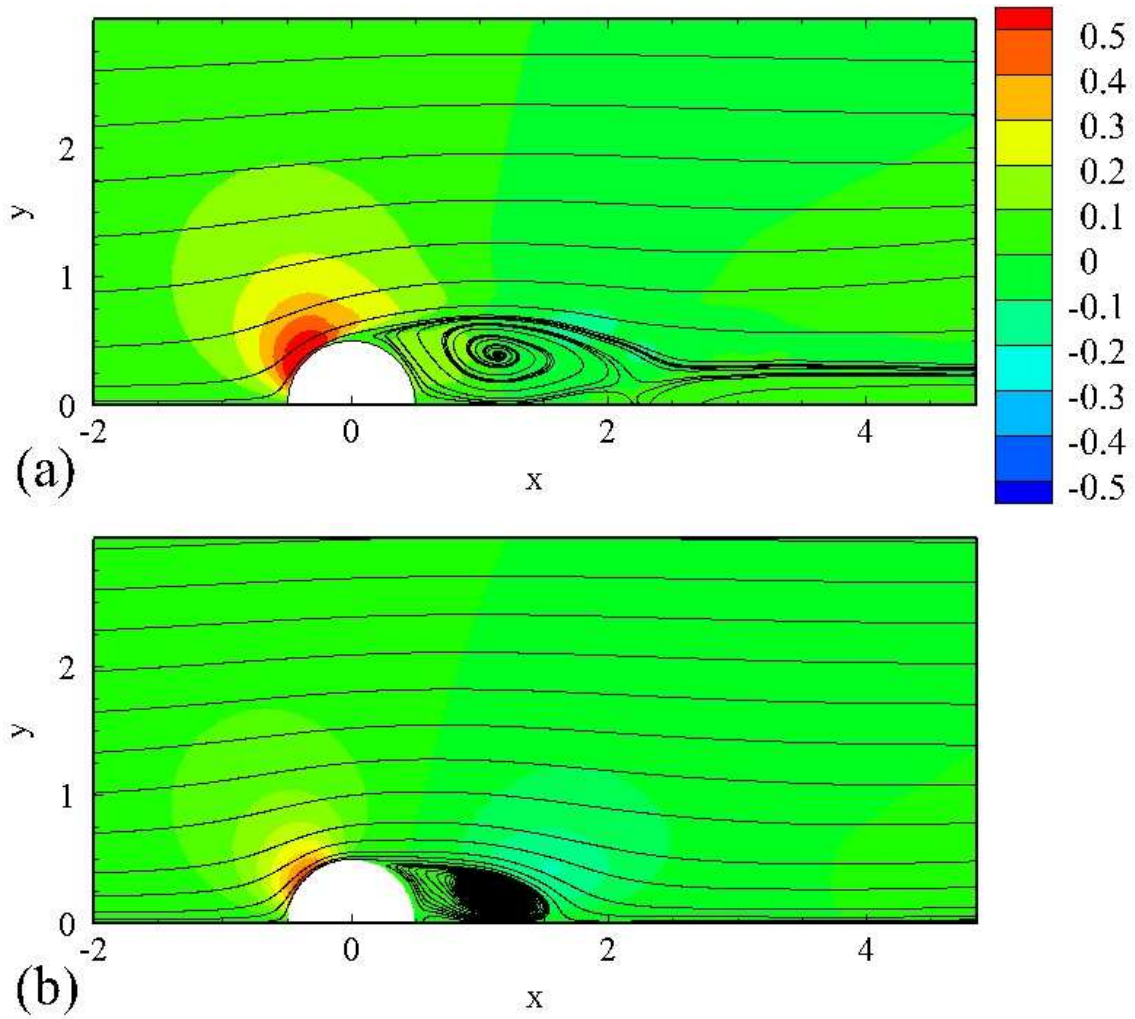

Figure 4.16 Mean transverse velocity computed at Re = 2.7×10^4 and Fr = 0.2: (a) on free surface; (b) z = -3.5

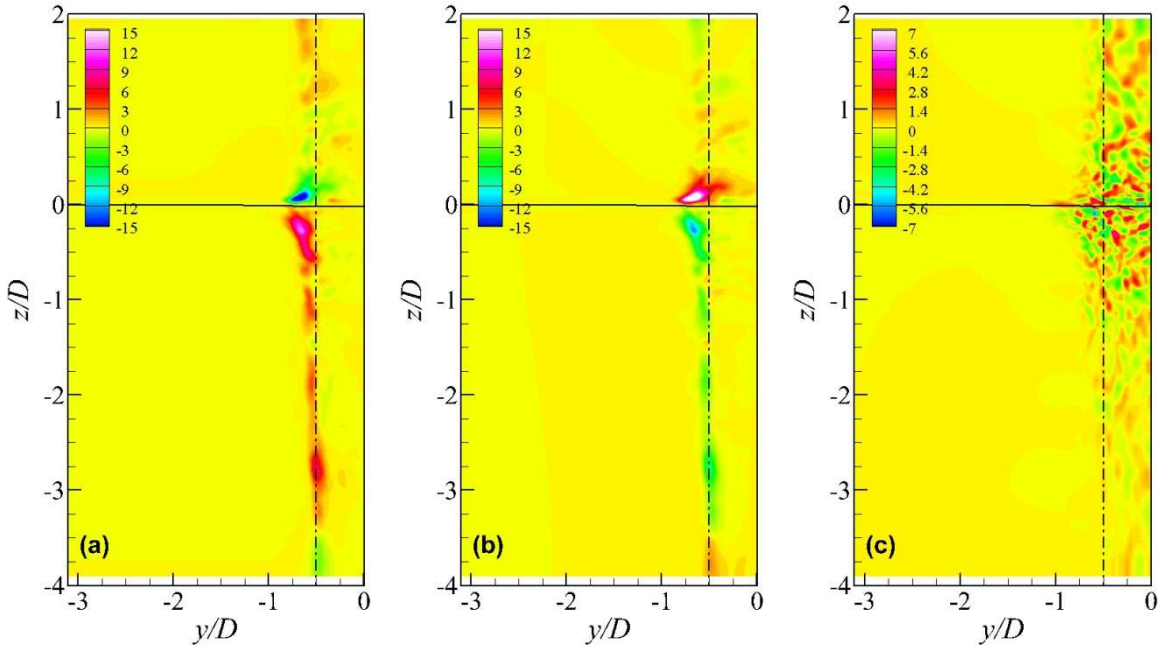

Figure 4.17 Dominant source terms for the mean streamwise vorticity at x = 1.0 computed at Re = 2.7×10^4 and Fr = 0.2: (a) y component of term (B); (b) z component of term (B); (c) term (E)

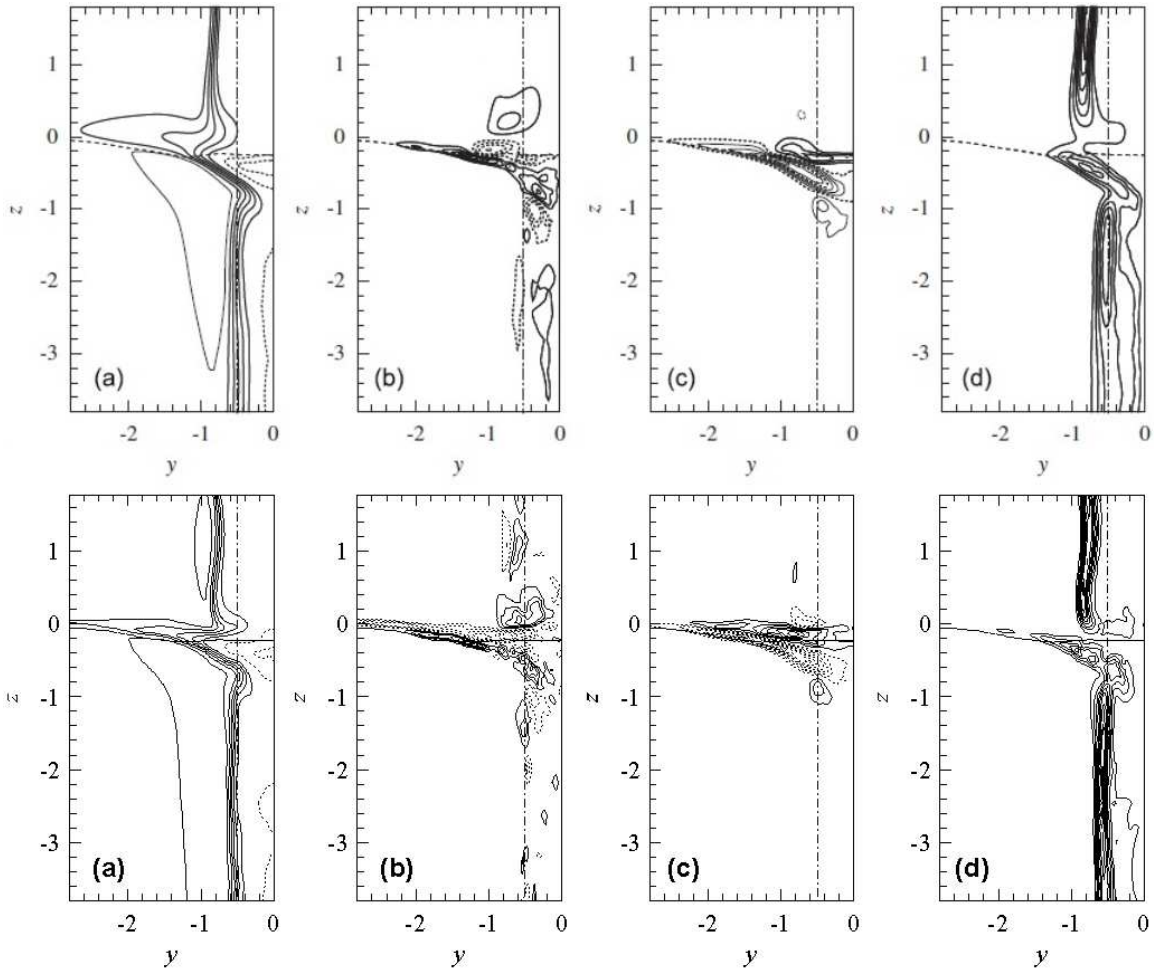

Figure 4.18 Mean flow at x = 1.0 computed at Re = 2.7×10^4 and Fr = 0.8 by CFDShip-Iowa version 6.2 (Suh et al., 2011) (top) and CFDShip-Iowa version 6.2.5 (bottom): (a) streamwise velocity with interval 0.2; (b) streamwise vorticity with interval 0.5; (c) transverse vorticity with interval 1.0; (d) vertical vorticity with interval 1.0

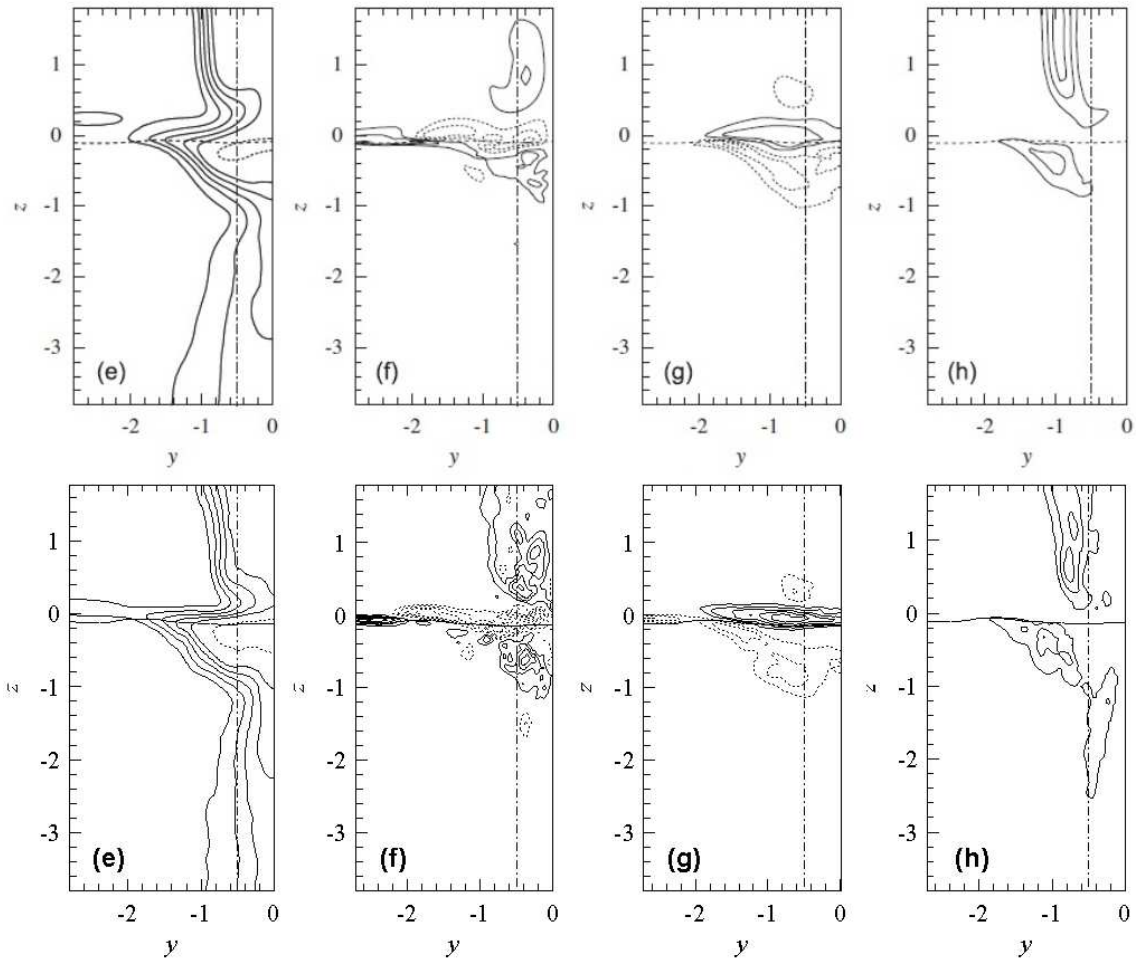

Figure 4.19 Mean flow at x = 2.5 computed at Re = 2.7×10^4 and Fr = 0.8 by CFDShip-Iowa version 6.2 (Suh et al., 2011) (top) and CFDShip-Iowa version 6.2.5 (bottom): (e) streamwise velocity with interval 0.2; (f) streamwise vorticity with interval 0.5; (g) transverse vorticity with interval 1.0; (h) vertical vorticity with interval 1.0

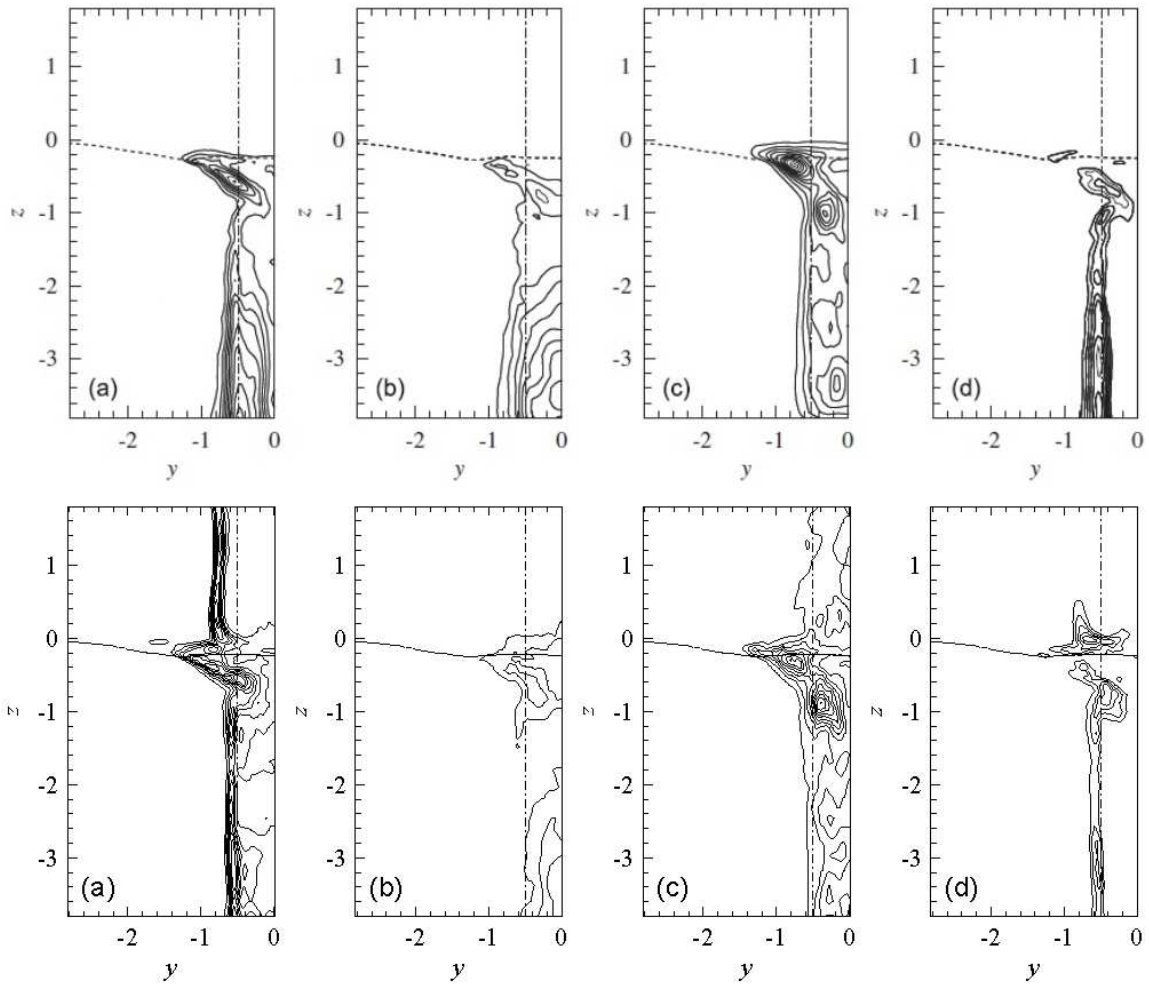

Figure 4.20 Reynolds stresses at x = 1.0 computed at Re = 2.7×10^4 and Fr = 0.8 by CFDShip-Iowa version 6.2 (Suh et al., 2011) (top) and CFDShip-Iowa version 6.2.5 (bottom): (a) R_{xx} with interval 0.025; (b) R_{yy} with interval 0.025; (c) R_{zz} with interval 0.01; (d) R_{xy} with interval 0.01

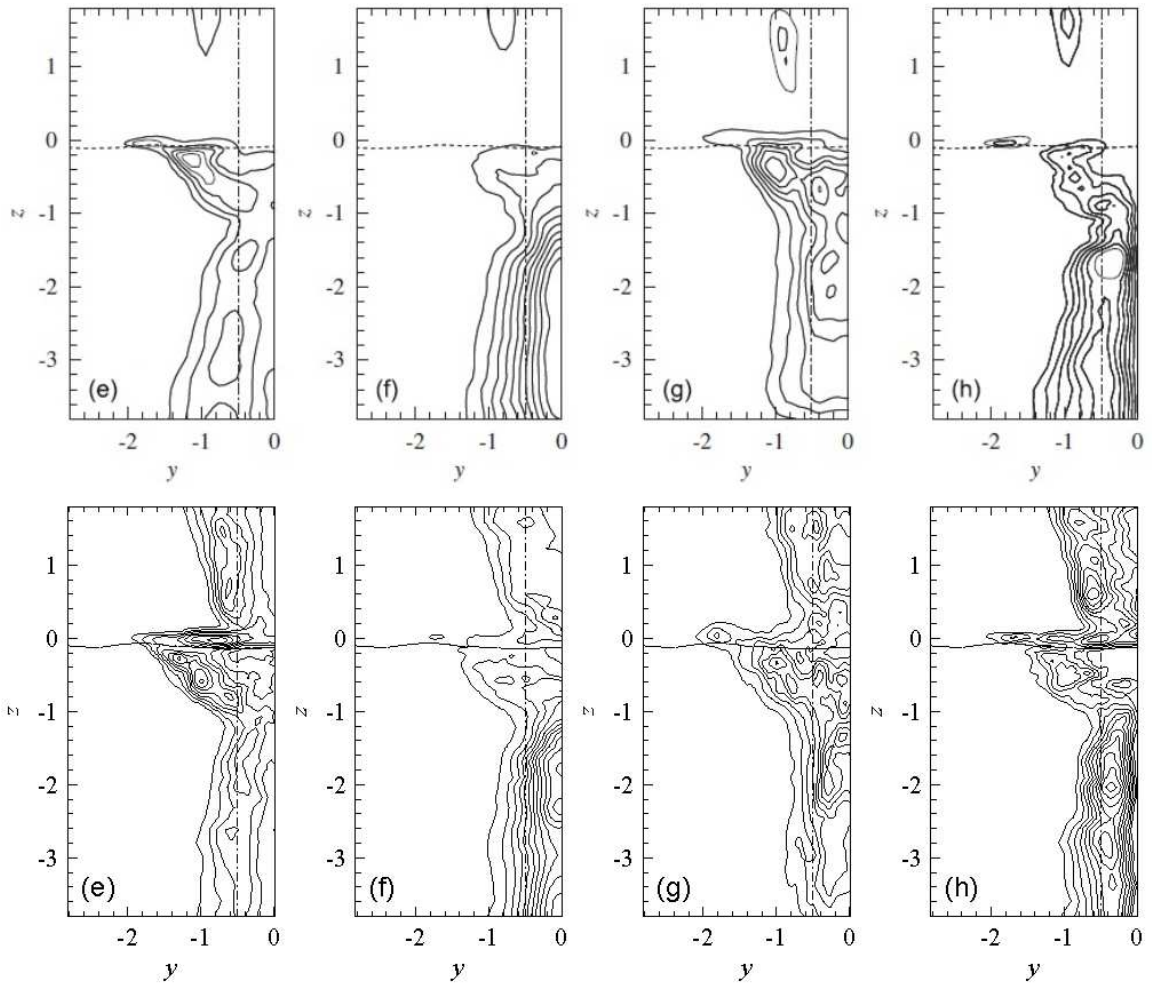

Figure 4.21 Reynolds stresses flow at x = 2.5 computed at Re = 2.7×10^4 and Fr = 0.8 by CFDShip-Iowa version 6.2 (Suh et al., 2011) (top) and CFDShip-Iowa version 6.2.5 (bottom): (e) R_{xx} with interval 0.025; (f) R_{yy} with interval 0.025; (g) R_{zz} with interval 0.01; (h) R_{xy} with interval 0.01

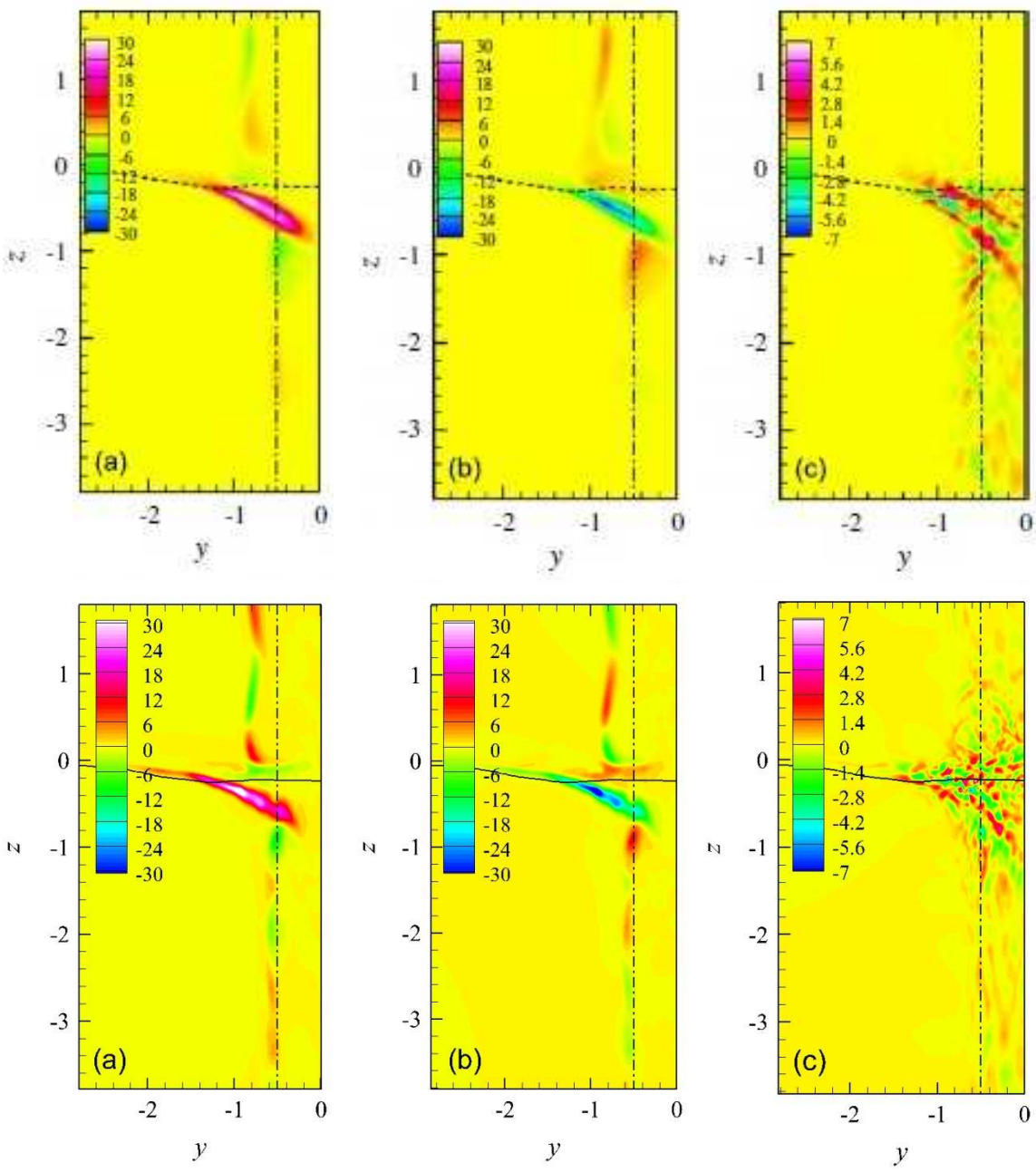

Figure 4.22 Dominant source terms for the mean streamwise vorticity at x = 1.0 computed at Re = 2.7×10^4 and Fr = 0.8 by CFDShip-Iowa version 6.2 (Suh et al., 2011) (top) and CFDShip-Iowa version 6.2.5 (bottom): (a) y component of term (B); (b) z component of term (B); (c) term (E)

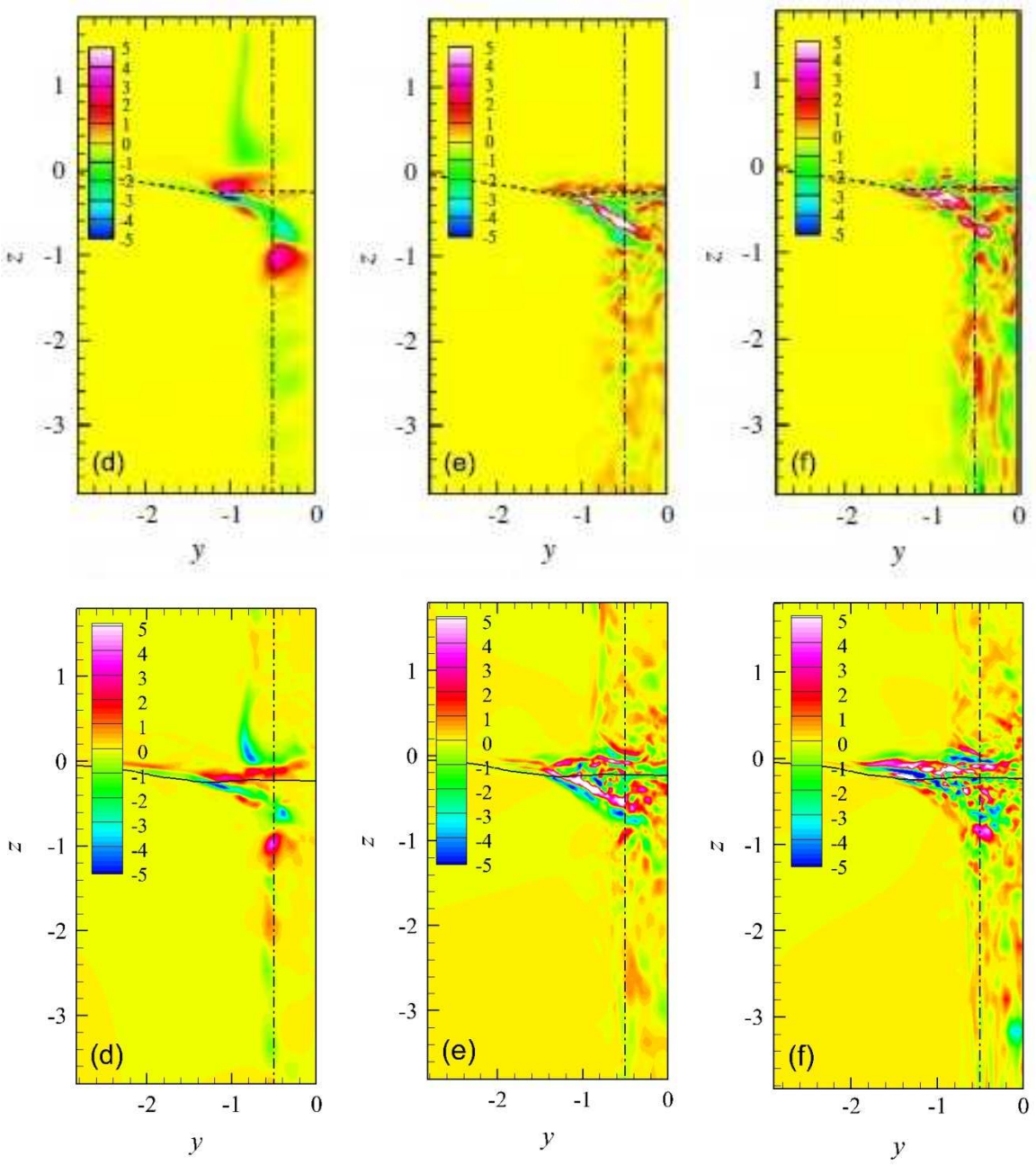

Figure 4.23 Dominant source terms for the mean transverse vorticity at x = 1.0 computed at Re = 2.7×10^4 and Fr = 0.8 by CFDShip-Iowa version 6.2 (Suh et al., 2011) (top) and CFDShip-Iowa version 6.2.5 (bottom): (d) z component of term (B); (e) term (E); (f) term (F)

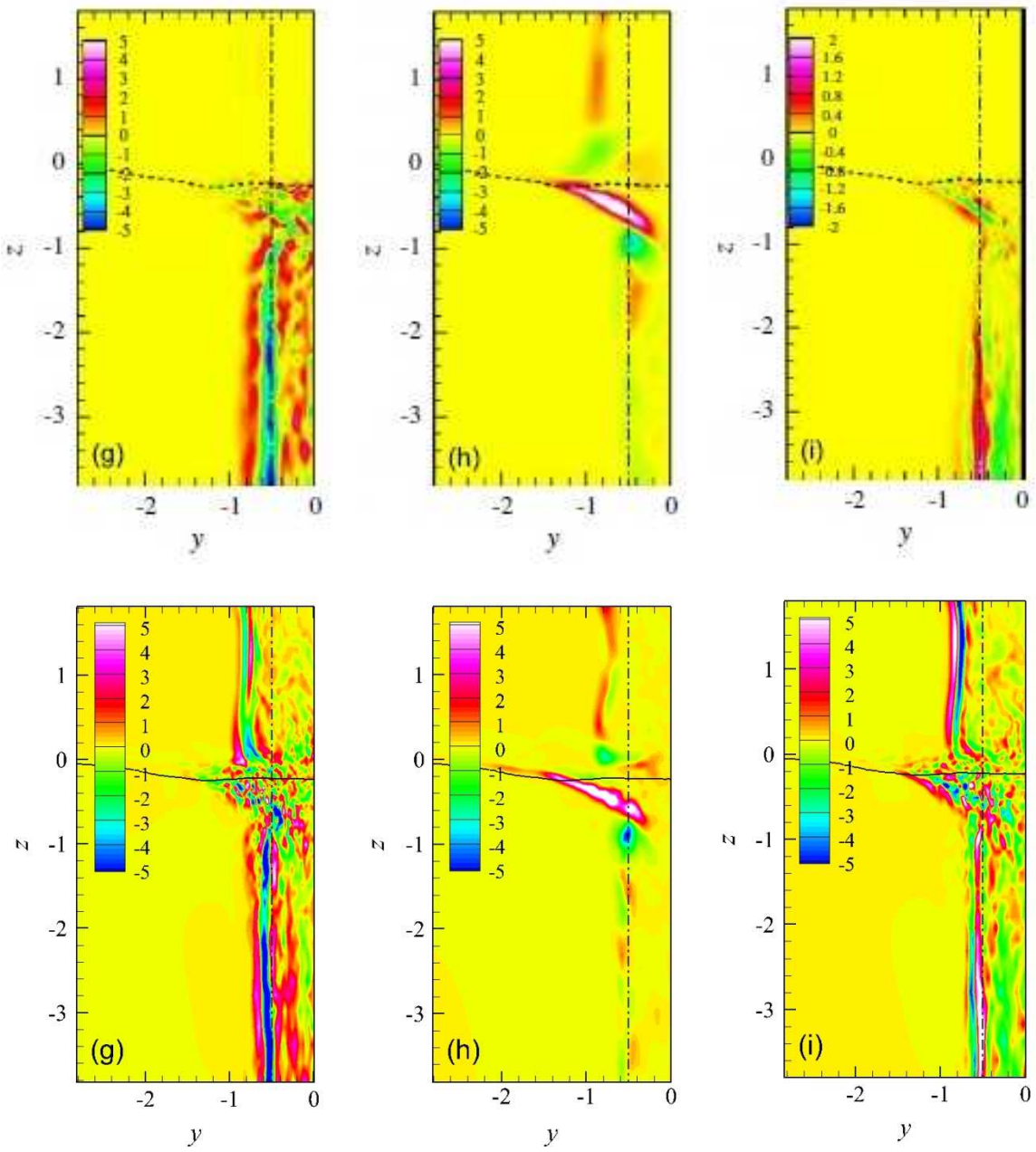

Figure 4.24 Dominant source terms for the mean vertical vorticity at x = 1.0 computed at Re = 2.7×10^4 and Fr = 0.8 by CFDShip-Iowa version 6.2 (Suh et al., 2011) (top) and CFDShip-Iowa version 6.2.5 (bottom): (g) term (F); (h) z component of term (B); (i) term (E)

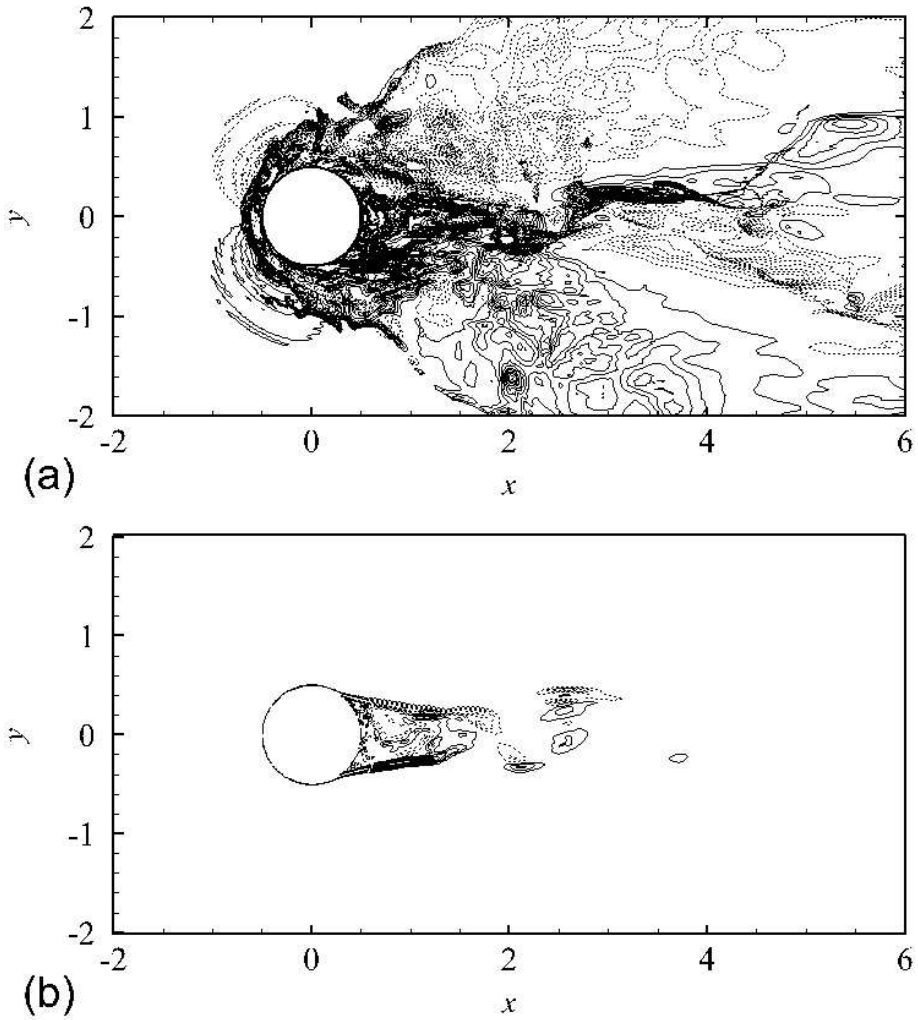

Figure 4.25 Instantaneous vertical vorticity computed by CFDShip-Iowa version 6.2.5: (a) on the free surface at Re = 4.58×10^5 and Fr = 1.64; (b) on a horizontal plane at Re = 5×10^5. Contour interval is 1.2.

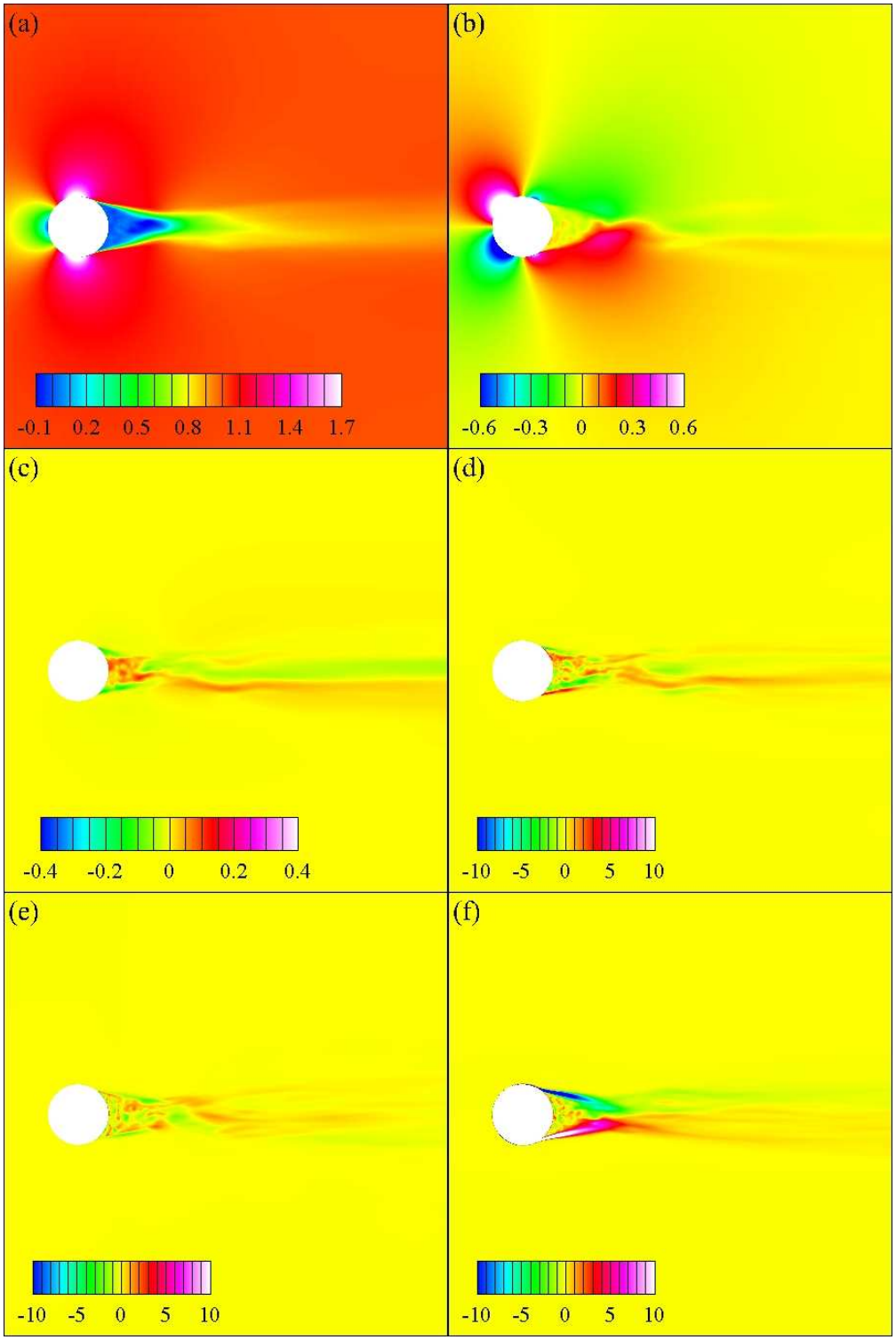

Figure 4.26 Mean flows computed at Re = 5×10^5: (a) streamwise velocity; (b) transverse velocity; (c) vertical velocity; (d) streamwise vorticity; (e) transverse vorticity; (f) vertical vorticity

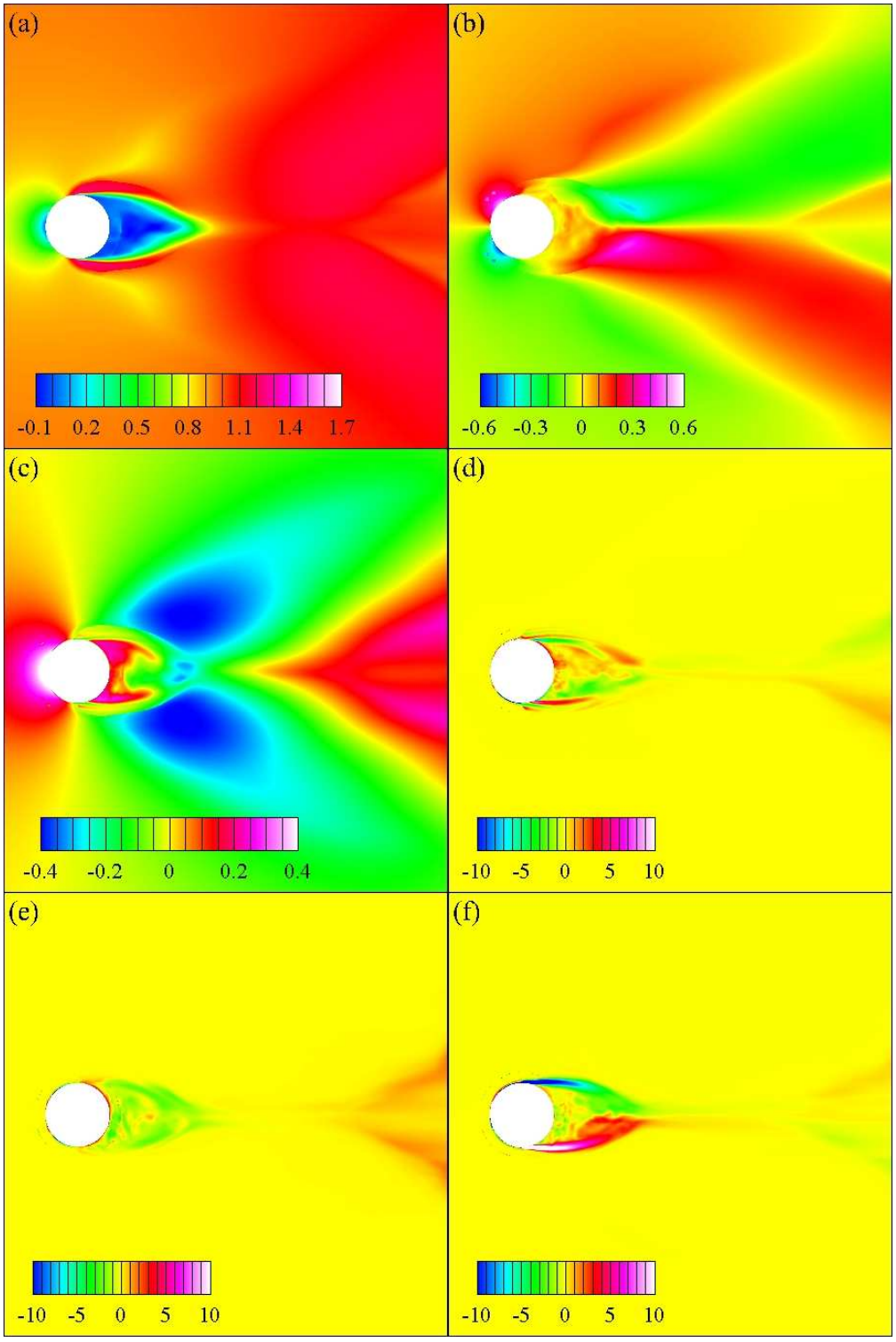

Figure 4.27 Mean flows on the curved plane which is 0.22D lower than the mean free surface computed at Re = 4.58×10^5 and Fr = 1.64: (a) streamwise velocity; (b) transverse velocity; (c) vertical velocity; (d) streamwise vorticity; (e) transverse vorticity; (f) vertical vorticity

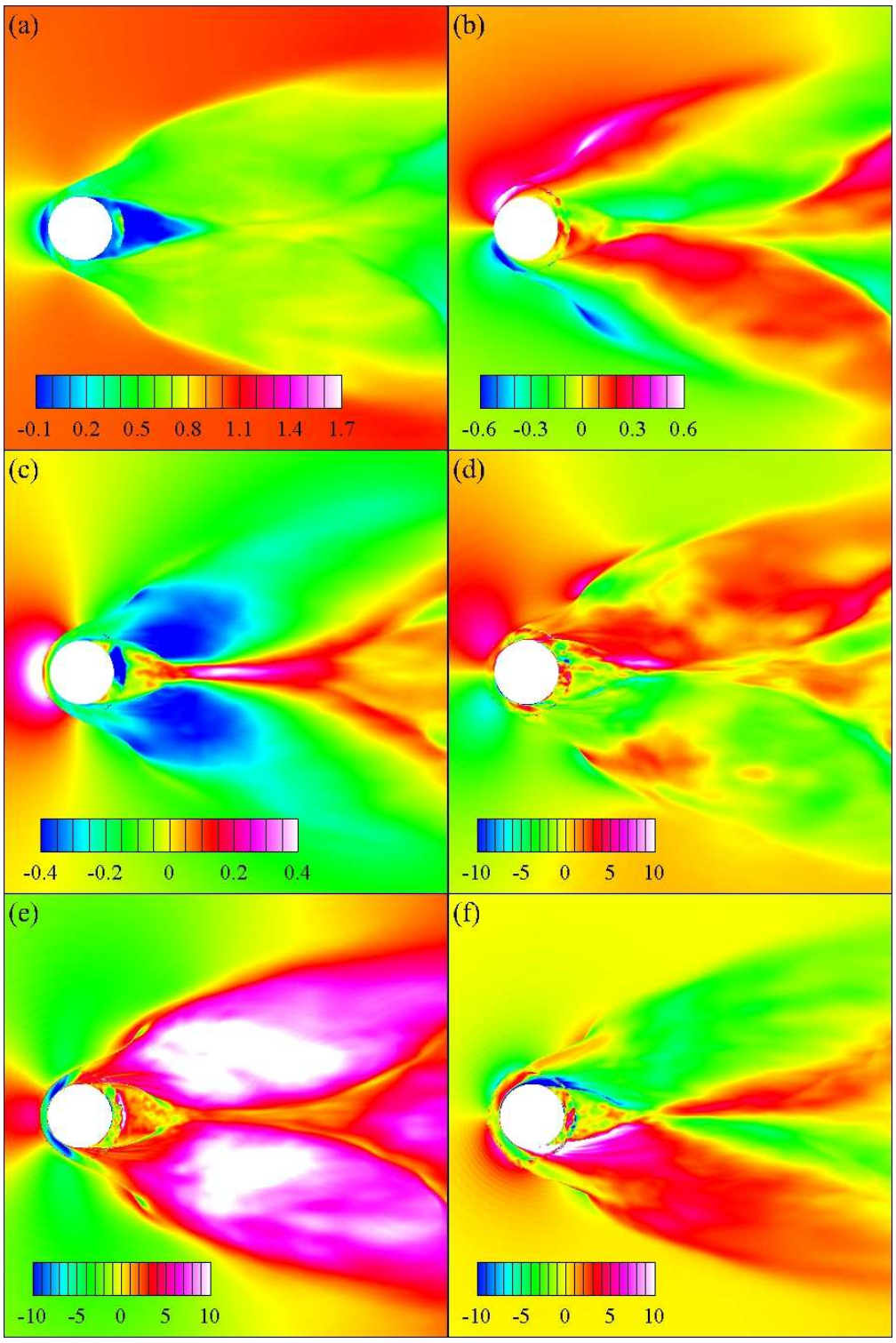

Figure 4.28 Mean flows on the free surface computed at Re = 4.58×10^5 and Fr = 1.64: (a) streamwise velocity; (b) transverse velocity; (c) vertical velocity; (d) streamwise vorticity; (e) transverse vorticity; (f) vertical vorticity

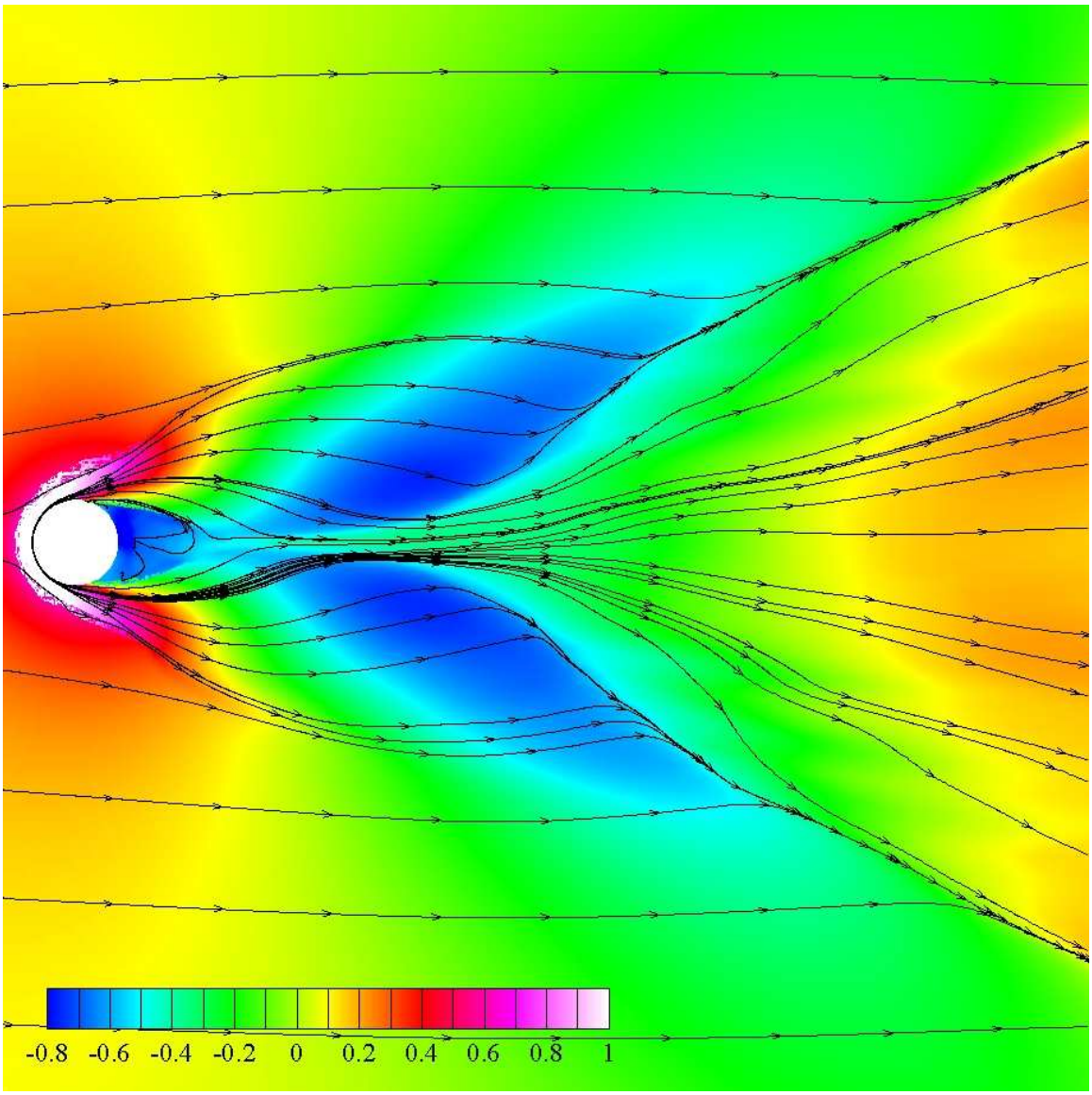

Figure 4.29 Elevations and streamlines on the mean free surface

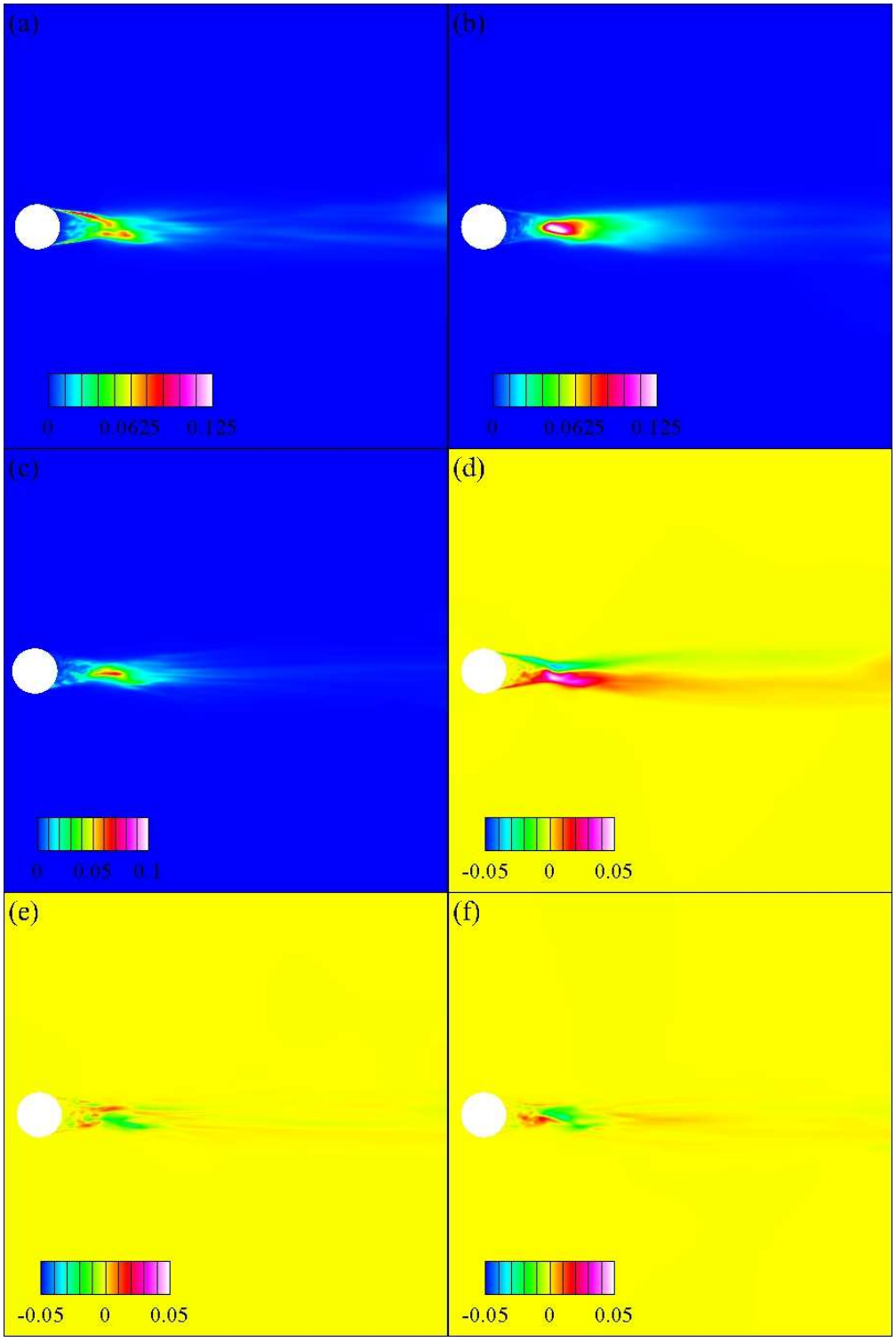

Figure 4.30 Reynolds stresses computed at Re = 5×10^5: (a) R_{xx}; (b) R_{yy}; (c) R_{zz}; (d) R_{xy}; (e) R_{xz}; (f) R_{yz}

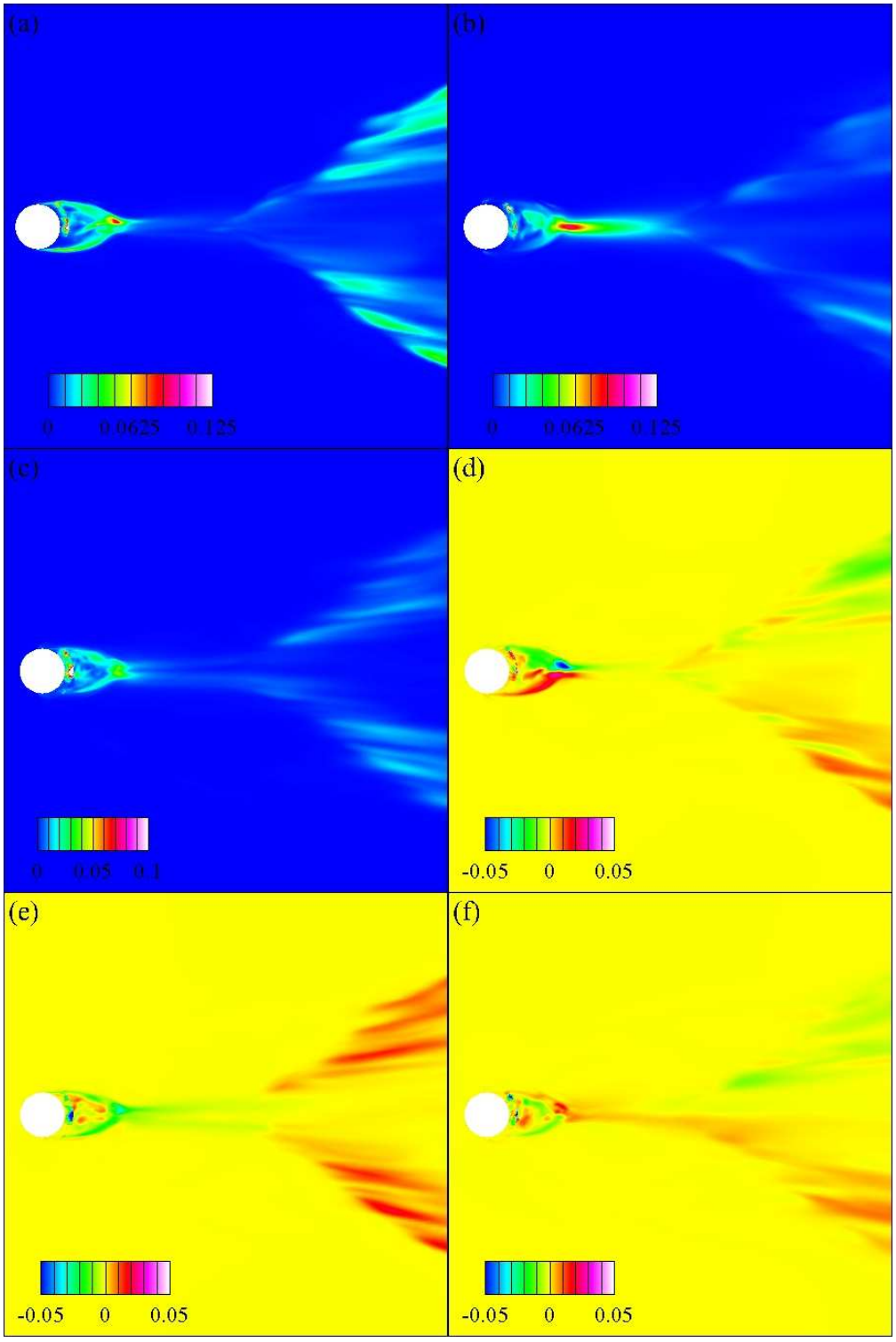

Figure 4.31 Reynolds stresses on the curved plane which is 0.22D lower than the mean free surface computed at Re = 4.58×10^5 and Fr = 1.64: (a) R_{xx}; (b) R_{yy}; (c) R_{zz}; (d) R_{xy}; (e) R_{xz}; (f) R_{yz}

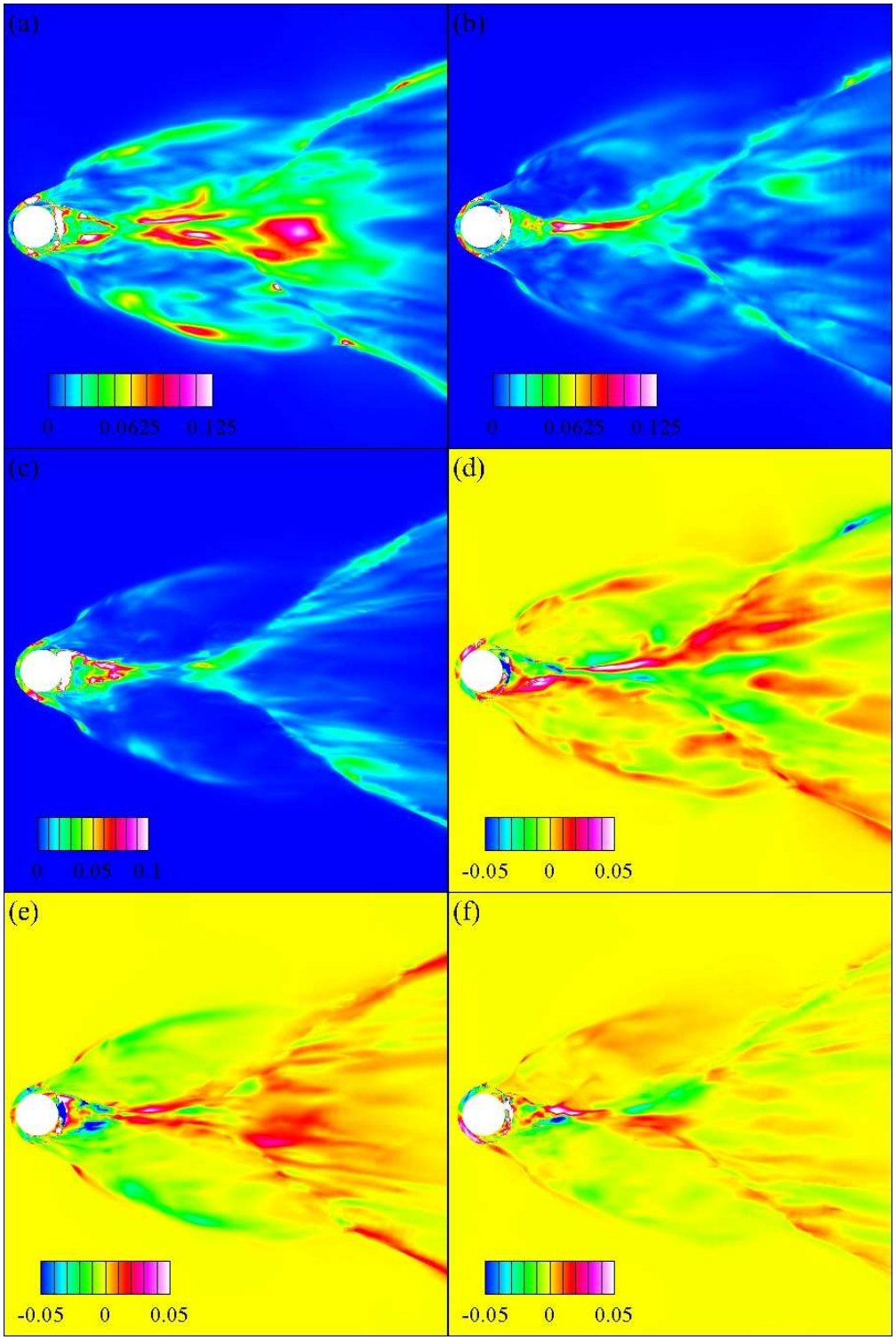

Figure 4.32 Reynolds stresses on the free surface computed at Re = 4.58×10^5 and Fr = 1.64: (a) R_{xx}; (b) R_{yy}; (c) R_{zz}; (d) R_{xy}; (e) R_{xz}; (f) R_{yz}

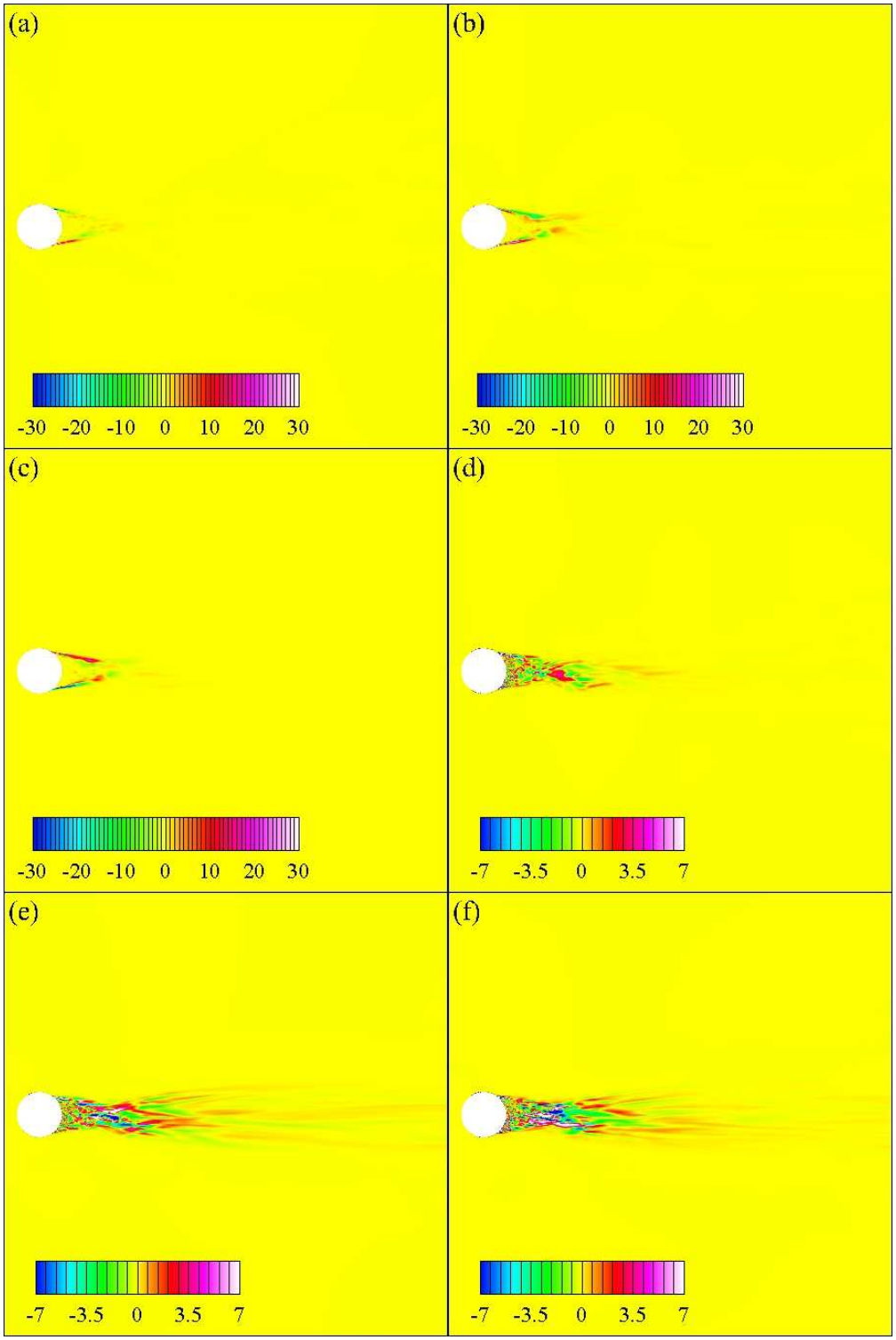

Figure 4.33 Source terms for the mean streamwise vorticity computed at Re = 5×10^5: (a) x component of term (B); (b) y component of term (B); (c) z component of term (B); (d) term (D); (e) term (E); (f) term (F)

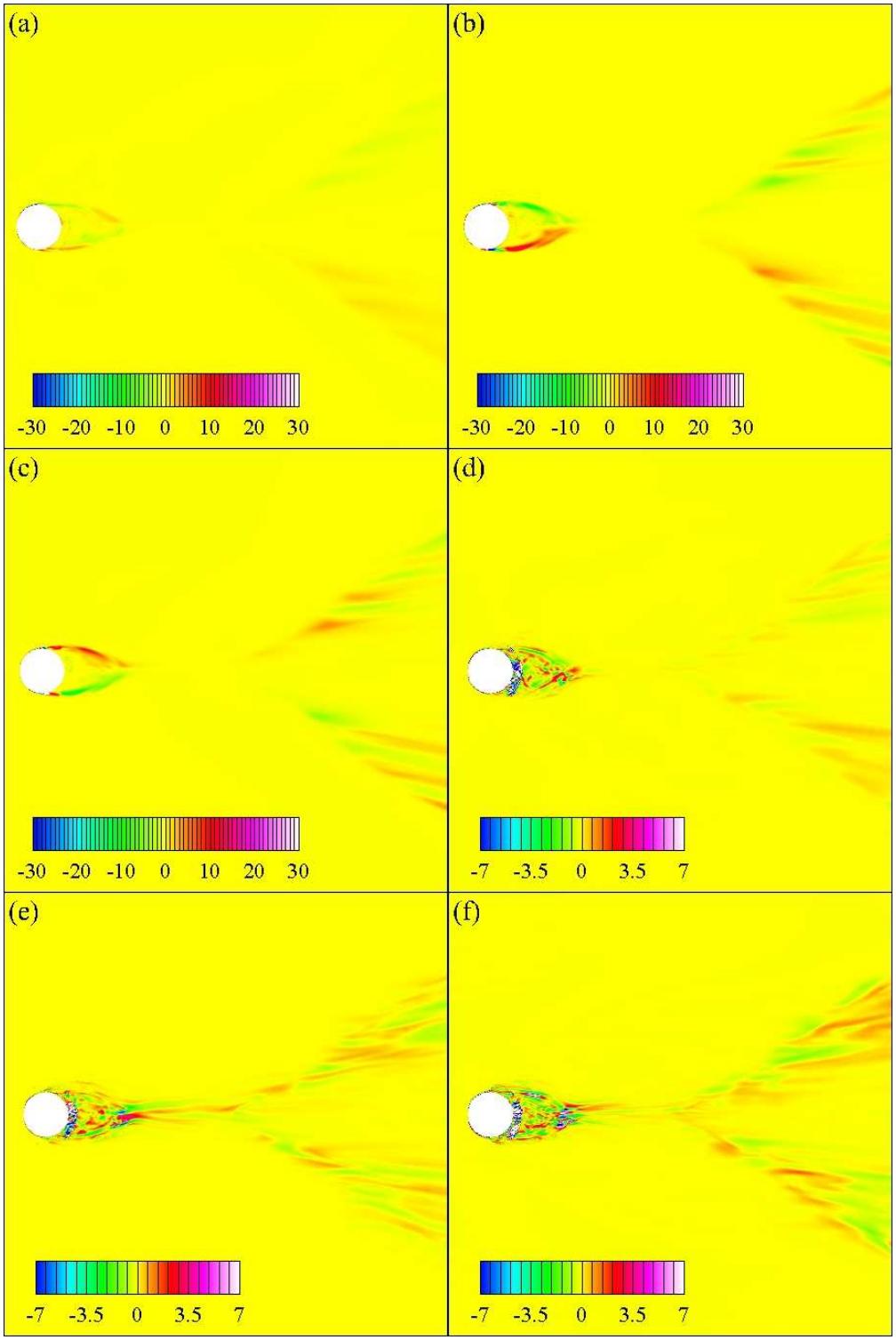

Figure 4.34 Source terms for the mean streamwise vorticity on the curved plane which is 0.22D lower than the mean free surface computed at Re = 4.58×10^5 and Fr = 1.64: (a) x component of term (B); (b) y component of term (B); (c) z component of term (B); (d) term (D); (e) term (E); (f) term (F)

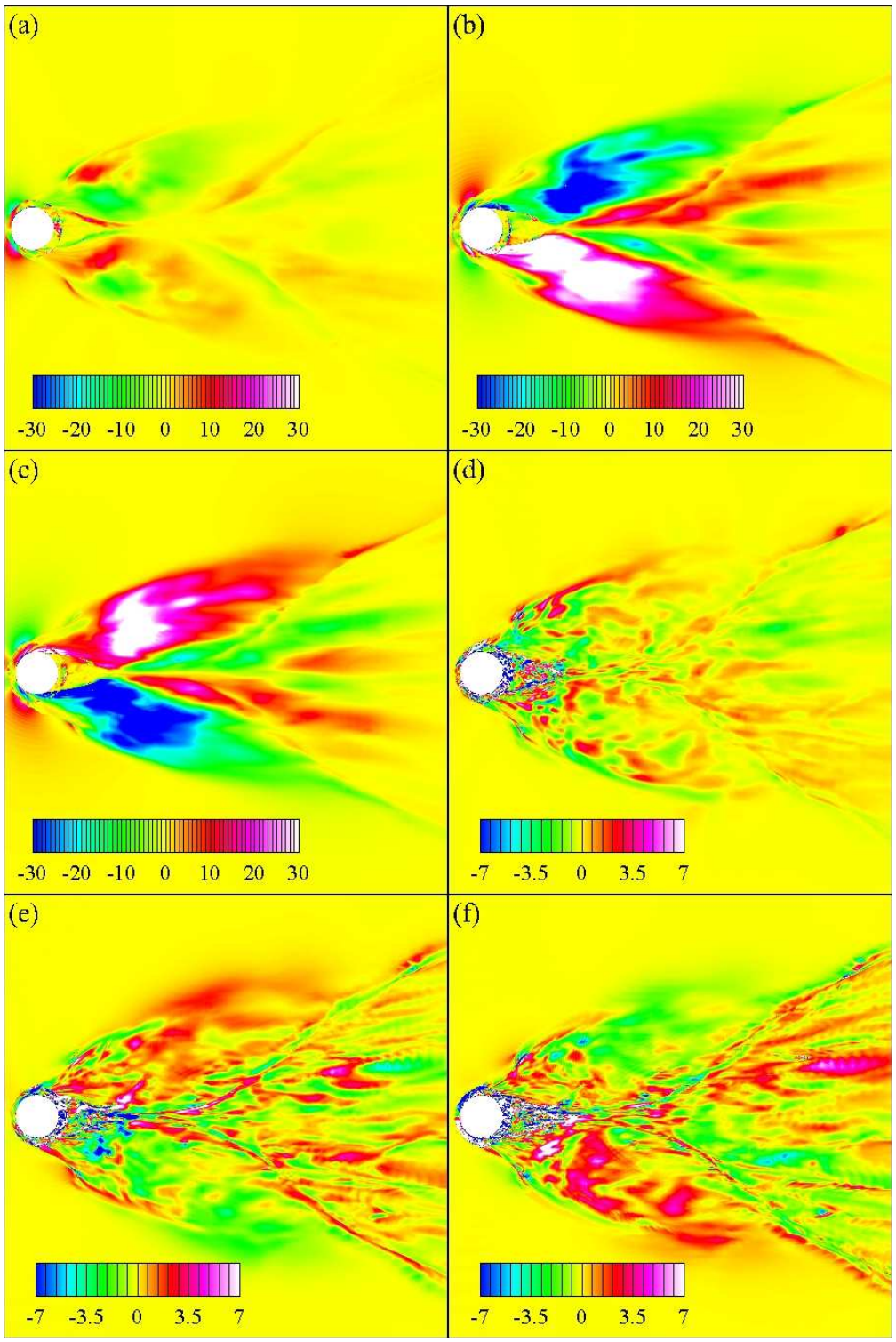

Figure 4.35 Source terms for the mean streamwise vorticity on the free surface computed at Re = 4.58×10^5 and Fr = 1.64: (a) x component of term (B); (b) y component of term (B); (c) z component of term (B); (d) term (D); (e) term (E); (f) term (F)

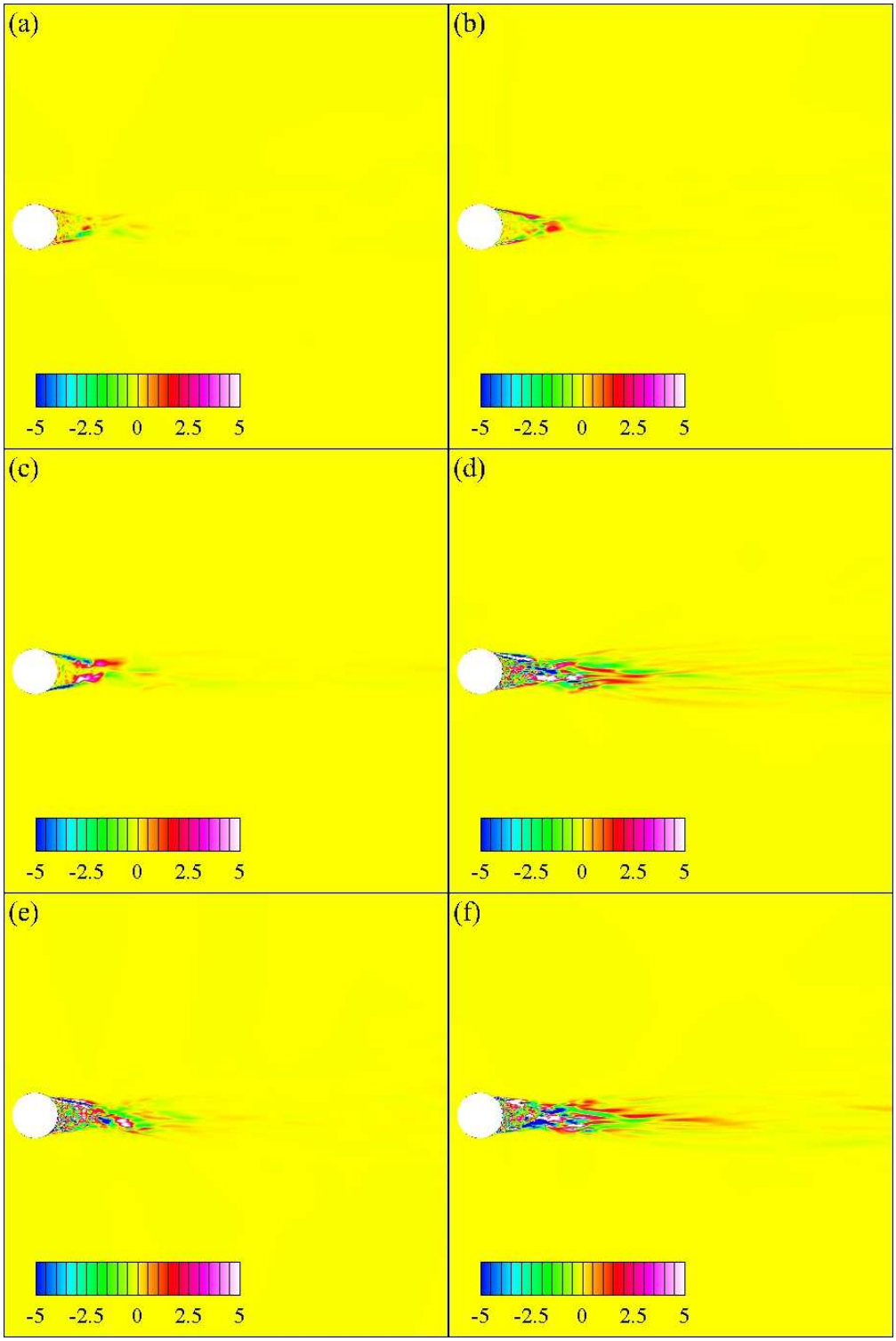

Figure 4.36 Source terms for the mean transverse vorticity computed at Re = 5×10^5: (a) x component of term (B); (b) y component of term (B); (c) z component of term (B); (d) term (D); (e) term (E); (f) term (F)

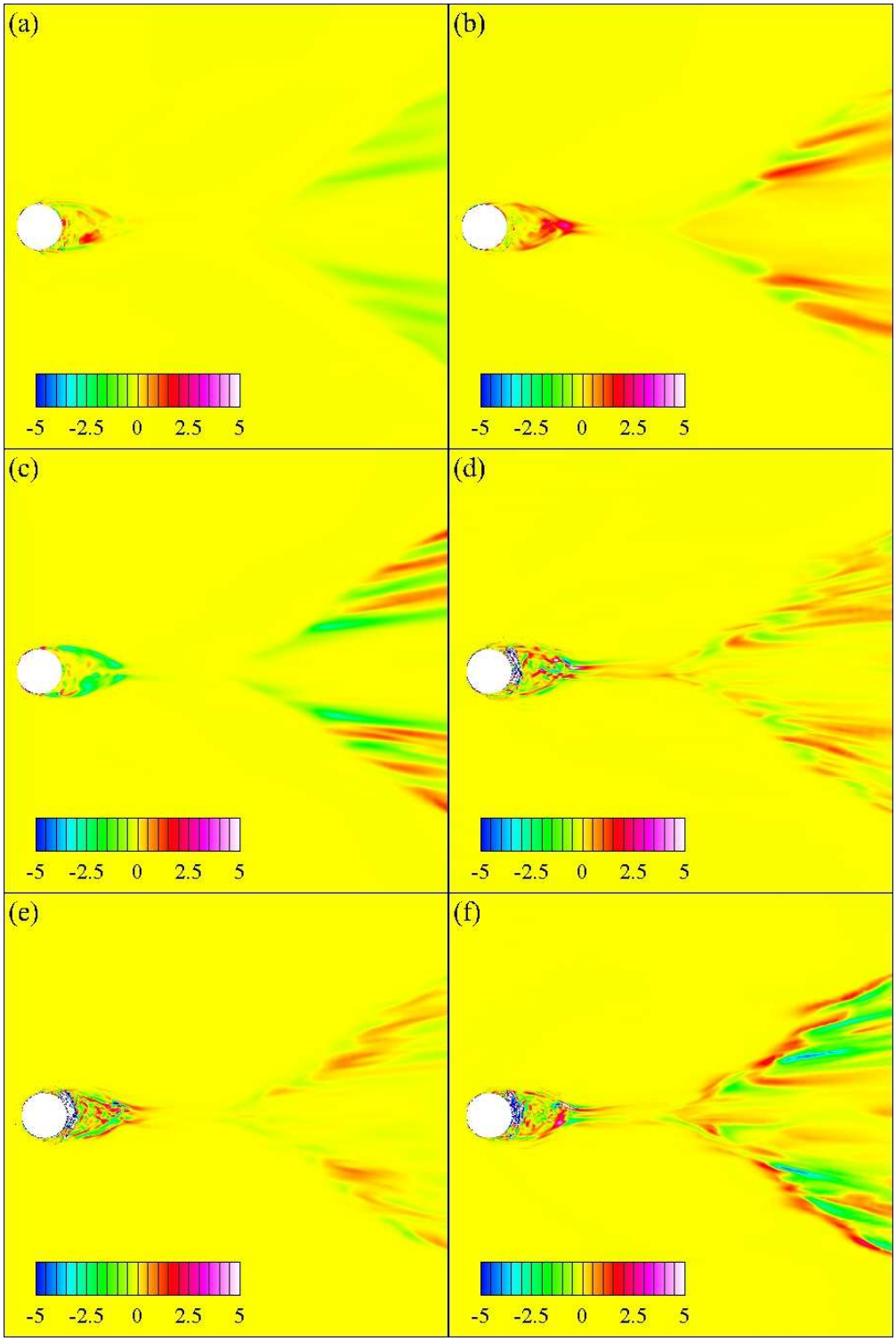

Figure 4.37 Source terms for the mean transverse vorticity on the curved plane which is 0.22D lower than the mean free surface computed at Re = 4.58×10^5 and Fr = 1.64: (a) x component of term (B); (b) y component of term (B); (c) z component of term (B); (d) term (D); (e) term (E); (f) term (F)

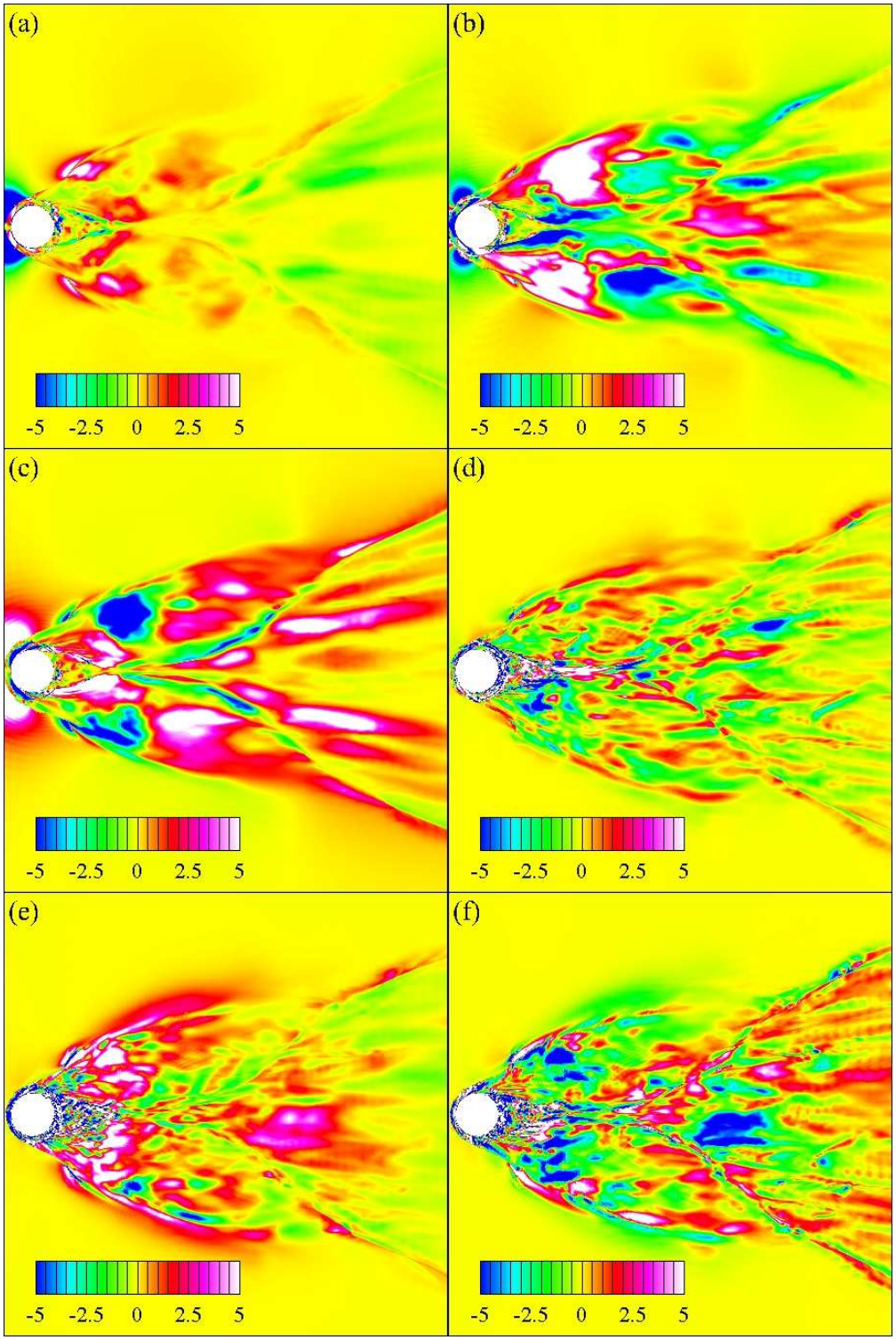

Figure 4.38 Source terms for the mean transverse vorticity on the free surface computed at Re = 4.58×10^5 and Fr = 1.64: (a) x component of term (B); (b) y component of term (B); (c) z component of term (B); (d) term (D); (e) term (E); (f) term (F)

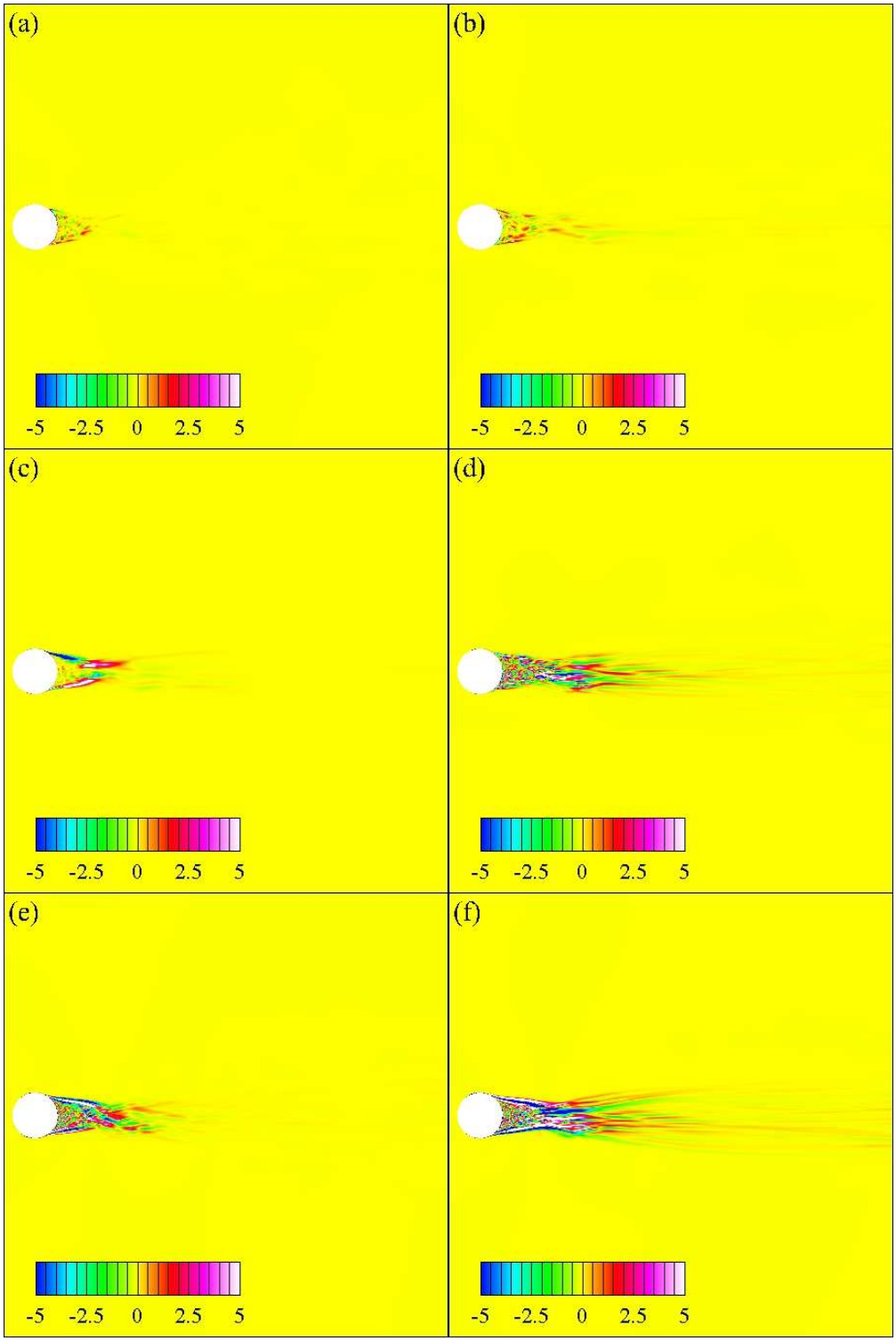

Figure 4.39 Source terms for the mean vertical vorticity computed at Re = 5×10^5: (a) x component of term (B); (b) y component of term (B); (c) z component of term (B); (d) term (D); (e) term (E); (f) term (F)

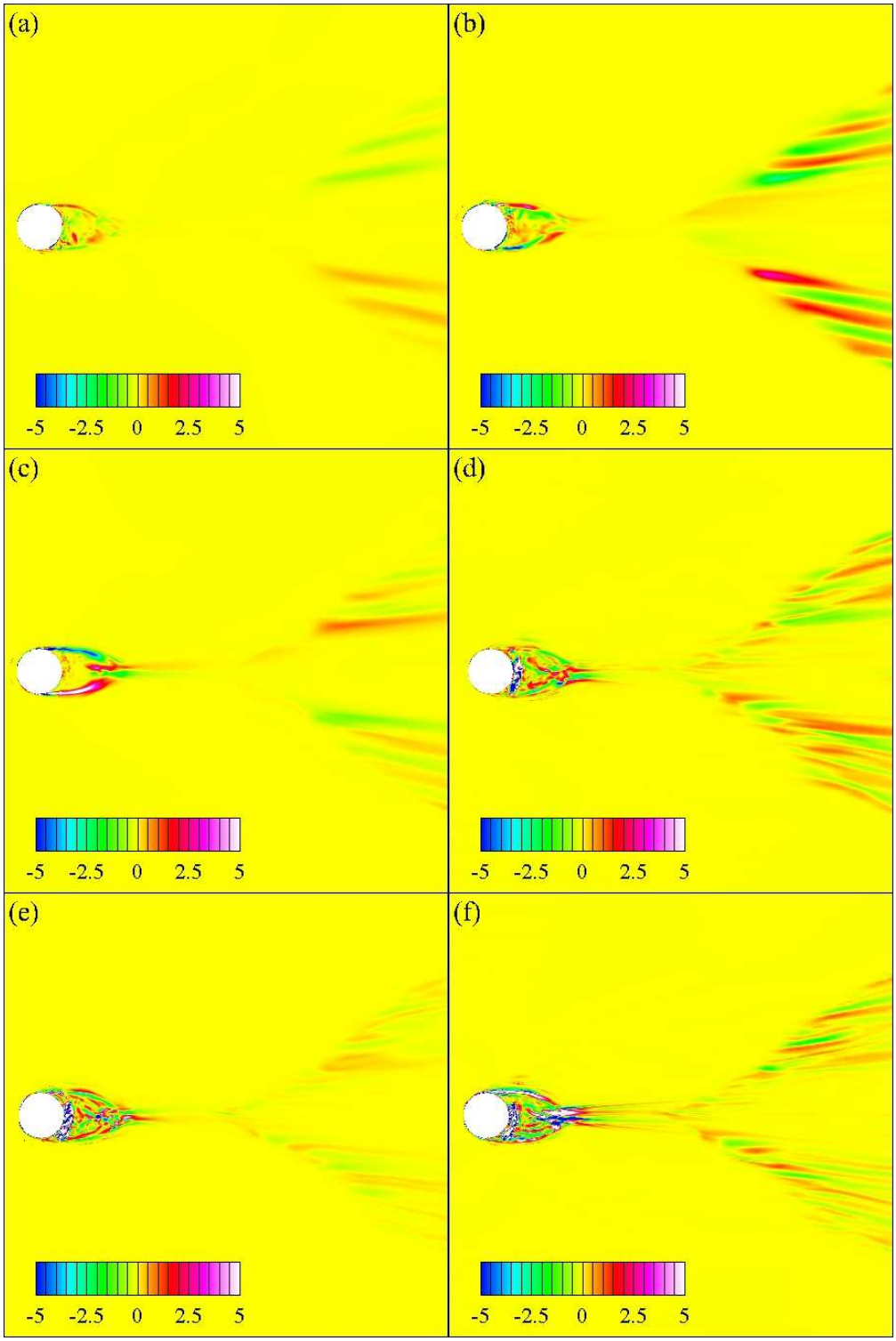

Figure 4.40 Source terms for the mean vertical vorticity on the curved plane which is 0.22D lower than the mean free surface computed at Re = 4.58×10^5 and Fr = 1.64: (a) x component of term (B); (b) y component of term (B); (c) z component of term (B); (d) term (D); (e) term (E); (f) term (F)

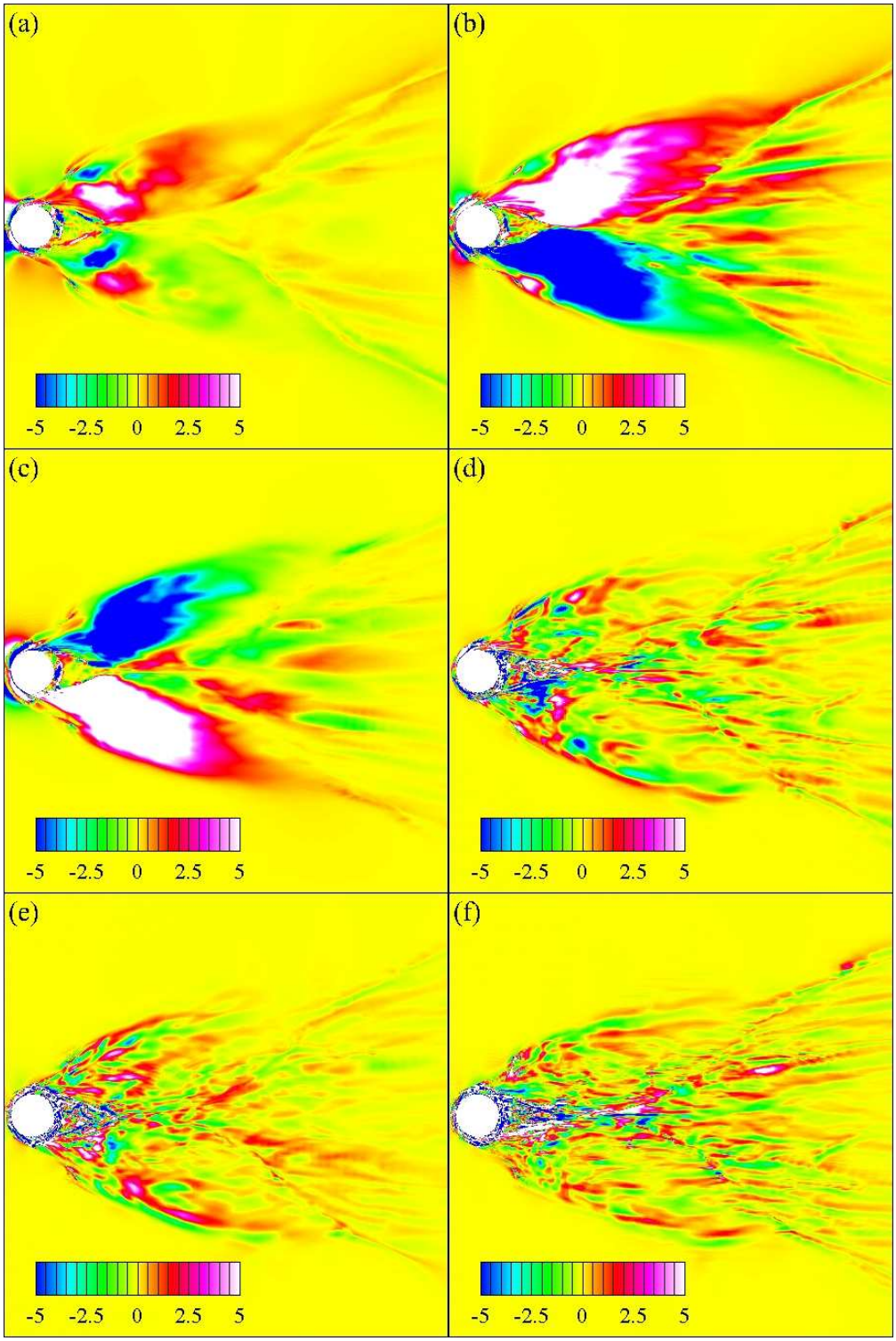

Figure 4.41 Source terms for the mean vertical vorticity on the free surface computed at Re = 4.58×10^5 and Fr = 1.64: (a) x component of term (B); (b) y component of term (B); (c) z component of term (B); (d) term (D); (e) term (E); (f) term (F)

CHAPTER 5

CONCLUSION AND FUTURE WORK

The objective of the current study is development of a coupled orthogonal curvilinear/Cartesian grid solver. The solver requires a thin structured boundary layer grid and a non-uniform Cartesian grid to resolve the boundary layer on a solid surface and the flow region away from the surface, respectively. The boundary layer grid is thin to keep its own orthogonality. Flows inside the orthogonal boundary layer and Cartesian background grids are solved by different CFD solvers which are coupled by an overset grid method. In the overset grid method, the flow variables are interpolated from one grid block to another through the interface between the boundary layer and Cartesian background grids. SUGGAR code writes the grid domain connectivity information into a file that identifies grid points necessary for the overset grid interpolation. In order to satisfy mass conservation across the overlapping region, the pressure Poisson equations and the overset interpolation equations are encompassed from both of the solvers and solved simultaneously by an iterative method.

Accuracy of the coupled orthogonal curvilinear/Cartesian grid solver was evaluated in terms of flows past circular cylinders because the orthogonal boundary layer grids can be generated easily due to its simple cylindrical shape. In addition, many results about the circular cylinder flows are available in the literature for the comparison purpose, which have been obtained from the experimental measurements or the numerical simulations. In this study, numerical simulations were also performed by the original orthogonal curvilinear and Cartesian grid solvers in order to obtain the benchmark data to compare with the results of the coupled orthogonal curvilinear/Cartesian grid solver.

The coupled orthogonal curvilinear/Cartesian grid solver predicted a pair of the symmetric counter-rotating vortices and periodic Karman vortex shedding in the laminar flows at Re = 40 and 200, respectively. The numerical results of the mean flow

parameters, such as the drag coefficient, are in good agreement with the experimental data and numerical results in the literature. The coupled orthogonal curvilinear/Cartesian grid solver also predicted the vorticity magnitude and pressure distributions on the cylinder surface 10% closer to the numerical results in the literature than the original Cartesian grid solver with the same Cartesian grid. This indicates that the near-wall region is resolved properly by the boundary layer grids for the coupled orthogonal curvilinear/Cartesian grid solver developed in this study.

At the subcritical Re = 3900, the coupled orthogonal curvilinear/Cartesian grid solver reproduced the long shear layers separating from both sides of the circular cylinder and the Karman vortices interacting with the vertical velocity component. The solver predicted the mean flow parameters and the wake profiles in good agreement with the experimental and numerical results in the literature. In the study of the effects of the vertical grid resolution, the coarse grid results showed better agreement with the experimental data, whereas the results given by the finer grids agreed better with the LES results in the literature. These trends with the vertical grid resolution were due to the earlier transitions of the shear layers to turbulence occurring in the experiments and the coarse grid simulation.

Numerical simulations were performed by the coupled orthogonal curvilinear/Cartesian grid solver for the flows at the supercritical Re = 5×10^5 and 1×10^6 in order to demonstrate the performance of the solver in the turbulent flows at very high Re. The numerical results were in good agreement with the experimental data in the literature. This study also showed the different flow characteristics between the current supercritical and subcritical Re. Much delayed separations of the boundary layers were predicted at the supercritical Re, which caused the narrower wakes and the shorter recirculation regions than those at the subcritical Re. The features of surface pressure corresponded to the separations. The main mechanism to generate the vertical vortices was the gradients of the Reynolds stresses and the vertical stretching effect.

The coupled orthogonal curvilinear/Cartesian grid solver was applied to the flows past a circular cylinder piercing the free surfaces vertically at (Re, Fr) = (2.7×10^4, 0.20), (2.7×10^4, 0.80), and (4.58×10^5, 1.64). It aimed at evaluating the accuracy of the solver in the simulation of the flows with free surfaces. The drag coefficients and the lift fluctuations were predicted very close to the numerical results in the literature. The solver also captured the features of the instantaneous and mean free surfaces for all Fr, which were shown in the experimental and numerical results.

The solver developed in this study showed the similar trends in its own numerical results to those observed by the past numerical studies using LES for Fr = 0.20 and 0.80. The organized vortex shedding observed in the deep flows is attenuated on the free surface, and many vortices with smaller scales are generated. On the free surface, the shear layers separating from the two sides of the cylinder deviate from each other, and the wake is substantially expanded in the transverse directions. The streamwise vorticity and the resulting outward transverse velocity, which are mainly produced by the vertical and transverse gradients of the difference between the transverse and vertical Reynolds normal stress components, are primarily responsible for the deviation of the shear layers and the large wake widths. These trends of the vortex shedding, deviating shear layers, and the expanded wake on the free surface are more prominent in the flow at Fr = 0.80 than that at Fr = 0.20.

The numerical results at Re = 4.58×10^5 and Fr = 1.64 were compared with those of the single-phase flow at similar Re = 5×10^5 to analyze the effects of the free surface on the flows at the high Re and Fr. Compared to the single-phase flow at similar Re, more small-scale vortices are generated over a large range of the wake on the free surface at Fr = 1.64. While the mean vorticity near the free surface show similar trends to those in the single-phase flow, the mean velocity correlates with the mean free surface elevations. The source terms for the vorticity near the free surface are mainly produced by the Reynolds stress gradients. The mean flow on the free surface at Fr = 1.64 shows the high

magnitudes of the streamwise vorticity and the transverse velocity, which are responsible for the attenuation of periodic vortex shedding. The difference of the gradients of two Reynolds shear stresses and the streamwise vortex stretching are the main mechanism for generation of the mean streamwise vorticity on the free surface. In addition, the source terms due to the strong streamwise vorticity mainly generate both transverse and vertical vortices on the free surface.

In the future work, the coupled orthogonal curvilinear/Cartesian grid solver will be applied to a flow around Wigley hull. Because the Wigley hull has a simple surface shape, an orthogonal curvilinear boundary layer grid is expected to be generated easily. The orthogonality correction term will be added into the governing equations to apply the solver to non-orthogonal boundary layer grids around more complicated shapes.

BIBLIOGRAPHY

Baker, Timothy J. 2005. “Mesh generation: Art or science?” *Progress in Aerospace Sciences* 41:29-63.

Balaras, Elias. 2004. “Modeling complex boundaries using an external force field on fixed Cartesian grids in large-eddy simulations.” *Computers & Fluids* 33:375-404.

Balay, S., Brown, J., Buschelman, K., Eijkhout, V., Gropp, W., Kaushik, D., Knepley, M., McInnes, L. C., Smith, B., and Zhang, H. 2012. “PETSc Users Manual Revision 3.3.” ANL-95/11 Argonne National Laboratory.

Batina, John. T. 1991. “Unsteady Euler algorithm with unstructured dynamic mesh for complex-aircraft aerodynamic analysis.” *AIAA Journal* 29:327-333.

Beam, R. M., and Warming, R. F. 1976. “An implicit finite-difference algorithm for hyperbolic systems in conservation-law form.” *Journal of Computational Physics* 22:87-110.

Beaudan, P., and Moin, P. 1994. “Numerical experiments on the flow past a circular cylinder at sub-critical Reynolds number.” *Report No. TF-62*, Department of Mechanical Engineering, Stanford University.

Bhushan, Shanti., Carrica, Pablo., Yang, Jianming., and Stern, Frederick. 2011. “Scalability studies and large grid computations for surface combatant using CFDShip-Iowa.” *International Journal for High Performance Computing Applications* 25:466-487.

Bhushan, S., Hanaoka, A., Yang, J., and Stern, Frederick. 2011. “Wall-layer modeling for Cartesian grid solver using an overset boundary layer orthogonal curvilinear grid.” *49th AIAA Aerospace Sciences Meeting including the New Horizons Forum and Aerospace Exposition* AIAA 2011-756.

Braza, M., Chassaing, P., Minh, H. Ha. 1986. “Numerical study and physical analysis of the pressure and velocity fields in the near wake of a circular cylinder.” *Journal of Fluids Mechanics* 165:79-130.

Breuer, Michael. 2000. “A challenging test case for large eddy simulation: high Reynolds number circular cylinder flow.” *International Journal of Heat and Fluid Flow* 21:648-654.

Caraeni, D., and Hill, D. C. 2010. “Unstructured-Grid Third-Order Finite Volume Discretization Using a Multistep Quadratic Data-Reconstruction Method.” *AIAA Journal* 48:808-817.

Cardell, G. S. 1993. “Flow past a circular cylinder with a permeable splitter plate.” PhD diss., California Institute of Technology.

Carrica, Pablo M., Wilson, Robert V., Noack, Ralph W., and Stern, Fred. 2007. “Ship motions using single-phase level set with dynamic overset grids.” *Computer & Fluids* 36:1415-1433.

Catalano, Pietro., Wang, Meng., Iaccarino, Gianluca., and Moin, Parviz. 2003. "Numerical simulation of the flow around a circular cylinder at high Reynolds numbers." *International Journal of Heat and Fluid Flow* 24:463-469.

Chaplin, J. R., and Teigen, P. 2003. "Steady flow past a vertical surface-piercing circular cylinder." *Journal of Fluids and Structures* 18:271-285.

Choi, H., and Moin, P. 1994. "Effects of the computational time step on numerical solutions of turbulent flow." *Journal of Computational Physics* 113:1-4.

Coutanceau, M., and Bouard, R. 1977. "Experimental determination of the main features of the viscous flow in the wake of a circular cylinder in uniform translation. Part 1. Steady flow." *Journal of Fluids Mechanics* 79:231-256.

Dennis, S. C. R., and Chang, Gau-Zu. 1970. "Numerical solutions for steady flow past a circular cylinder at Reynolds numbers up to 100." *Journal of Fluids Mechanics* 42:471-489.

Falgout, R. D., Jones, J. E., and Yang, U. M. 2006. "The design and implementation of HYPRE, a library of parallel high performance preconditioners." *Numerical Solution of Partial Differential Equations on Parallel Computers, Vol. 51.* Springrt-Verlag, pp. 267-294.

Fornberg, B. 1980. "A numerical study of steady viscous flow past a circular cylinder." *Journal of Fluids Mechanics* 98:819-855.

Ghias, R., Mittal, R., and Dong, H. 2007. "A sharp interface immersed boundary method for compressible viscous flows." *Journal of Computational Physics* 225:528-553.

Gullbrand, J., Bai, X. S., and Fuchs, L. 2001. "High-order Cartesian grid method for calculation of incompressible turbulent flows." *International Journal for Numerical Methods in Fluids* 36:687-709.

Hansen, Robert P., and Forsythe, James. 2004. "A Grid Convergence Study of a Highly Separated Turbulent Flow." *Computing in Science and Engineering* 6:30-37.

Hay, A. D. 1947. "Flow about semi-submerged cylinders of finite length." *Princeton University Report*.

Iaccarino, G., Kalitzin, G., Moin, P., and Khalighi, B. 2004. "Local Grid Refinement for an Immersed Boundary RANS Solver." *42nd AIAA Aerospace Sciences Meeting and Exhibit* AIAA 2004-586.

Inoue, M., Baba, N., and Himeno, Y. 1993. "Experimental and numerical study of viscous flow field around an advancing vertical circular cylinder piercing a free-surface." *Journal of Kansai Society of Naval Architecture of Japan* 220:57-64.

Jiang, G. S., and Peng, D. 2000. "Weighted ENO schemes for Hamilton-Jacobi equations." *SIAM Journal of Scientific Computing* 21:2126-2143.

Kang, M., Fedkiw, R. P., and Liu, X. D. 2000. "A boundary condition capturing method for multiphase incompressible flow." *Journal of Computational Physics* 15:323-360.

Kawamura, T., Mayer, S., Garapon, A., and Sørensen, L. 2002. “Large eddy simulation of a flow past a free surface piercing circular cylinder.” *Journal of Fluids Engineering* 124:91-101.

Kim, J., Kim, D., and Choi, H. 2001. “An immersed-boundary finite-volume method for simulations of flow in complex geometries.” *Journal of Computational Physics* 171:132-150.

Koo, G. K. 2011. “Numerical study of two-phase air-water interfacial flow: Plunging wave breaking and vortex-interface interaction.” PhD diss., The University of Iowa.

Koomullil, Roy., Cheng, Gary., Soni, Bharat., Noack, Ralph., and Prewitt, Nathan. 2008. “Moving-body simulations using overset framework with rigid body dynamics.” *Mathematics and Computers in Simulation* 78:618-626.

Kravchenko, Arthur G., and Moin, Parviz. 2000. “Numerical studies of flow over a circular cylinder at Re_D=3900.” *Physics of Fluids* 12:403-417.

Launder, B. E., and Rodi, W. 1983. “The turbulent wall jet-measurements and modeling.” *Annual Review of Fluid Mechanics* 15:429-459.

Le, D. V., Khoo, B. C., and Peraire, J. 2006. “An immersed interface method for viscous incompressible flows involving rigid and flexible boundaries.” *Journal of Computational Physics* 220:109-138.

Leonard, B. P. 1979. “Stable and accurate convective modeling procedure based on quadratic upstream interpolation.” *Computer Methods in Applied Mechanics and Engineering* 19:59-98.

Linnick, Mark N., and Fasel, Hermann F. 2005. “A high-order immersed interface method for simulating unsteady incompressible flows on irregular domains.” *Journal of Computational Physics* 204:157-192.

Liu, X. D., Fedkiw, R., and Kang, M. 2000. “A boundary condition capturing method for Poisson equation on irregular domains.” *Journal of Computational Physics* 154:151-178.

Liu, Xueqiang., Qin, Ning., and Xia, Hao. 2006. “Fast dynamic grid deformation based on Delaunay graph mapping.” *Journal of Computational Physics* 211:405-423.

Longo, J., Huang, H. P., and Stern, F. 1998. “Solid/free-surface juncture boundary layer and wake.” *Experiments in Fluids* 25:283-297.

Mahesh, K., Constantinescu, G., and Moin, P. 2004. “A numerical method for large-eddy simulation in complex geometries.” *Journal of Computational Physics* 197:215-240.

Mavriplis, D. J. 1997. “Unstructured Grid Techniques.” *Annual Review of Fluid Mechanics* 29:473-514.

Meneveau C., Lund, C. S., and Cabot, W. H. 1996. “A Lagrangian dynamic subgrid-scale model of turbulence.” *Journal of Fluids Mechanics* 319:353-385.

Mittal, Rajat., and Iaccarino, Gianluca. 2005. “Immersed Boundary Methods.” *Annual Review of Fluid Mechanics* 37:239-261.

Mittal, R., and Moin, P. 1997. “Suitability of upwind-biased finite-difference schemes for large-eddy simulation of turbulent flows.” *AIAA Journal* 35:1415-1417.

Moin, Parviz. 2002. “Advances in large eddy simulation methodology for complex flows.” *International Journal of Heat and Fluid Flow* 23:710-720.

Mulvihill, Lawrence P., and Yang, Cheng-I. 2007. “Numerical Simulation of Flow over Fully Appended ONR Body-1 with Overset Grid Scheme” *Proc. 9th International Conference on Numerical Ship Hydrodynamics.*

Noack, Ralph W. 2005. “SUGGAR: a General Capability for Moving Body Overset Grid Assembly.” *17th AIAA Computational Fluid Dynamics Conference* AIAA 2005-5117.

Norberg, C. 1992. “Pressure forces on a circular cylinder in cross flow.” *IUTAM Symposium on Bluff-Body Wakes, Dynamics and Instabilities* 275-278.

Ong, L., and Wallace, J. 1996. “The velocity field of the turbulent very near wake of a circular cylinder.” *Experiments in Fluids* 20:441-453.

Osher, S., and Sethian, J. 1988. “Fronts propagating with curvature-dependent speed: algorithms based on Hamilton-Jacobi formulations.” *Journal of Computational Physics* 79:12-49.

Pandya, Mohagna J., Frink, Neal T., and Noack, Ralph W. 2005. “Progress Toward Overset-Grid Moving Body Capability for USM3D Unstructured Flow Solver.” *17th AIAA Computational Fluid Dynamics Conference* AIAA 2005-5118.

Peng, D., Merriman, B., Osher, S., Zhao, H., and Kang, M. 1999. “A PDE-based fast local level set method.” *Journal of Computational Physics* 155:410-438.

Pope, S. B. 1978. “The calculation of turbulent recirculating flows in general orthogonal coordinates.” *Journal of Computational Physics* 26:197-217.

Ramakrishnan, Srinivas., Zheng, Lingxiao., Mittal, Rajat., Najjar, Fady., Lauder, George V., and Hedrick, Tyson L. 2009. “Large Eddy Simulation of Flows with Complex Moving Boundaries: Application to Flying and Swimming in Animals.” *39th AIAA Fluid Dynamics Conference* AIAA-2009-3976.

Russell, David., and Wang, Z. Jane. 2003. “A Cartesian grid method for modeling multiple moving objects in 2D incompressible viscous flow.” *Journal of Computational Physics* 191:177-205.

Sarghini, F., Piomelli, U., Balaras, E. 1999. “Scale-similar models for large-eddy simulations.” *Physics of Fluids* 11:1596-1607.

Schlüter, J. U., and Pitsch, H. 2005. “Anti-Aliasing Filters for Coupled Reynolds-Averaged/Large Eddy Simulations.” *AIAA Journal* 43:608-616.

Schlüter, J. U., Pitsch, H., and Moin, P. 2004. “Large Eddy Simulation Inflow Conditions for Coupling with Reynolds-Averaged Flow Solvers.” *AIAA Journal* 42:478-484.

Schlüter, J. U., Pitsch, H., and Moin, P. 2005a. "Outflow Conditions for Integrated Large Eddy Simulation/Reynolds-Averaged Navier Stokes Simulations." *AIAA Journal* 43:156-164.

Schlüter, J. U., Shankaran. S., Kim, S., Pitsch, H., Alonso, J. J., and Moin, P. 2003a. "Integration of RANS and LES Flow Solvers for Simultaneous Flow Computations." *41st Aerospace Sciences Meeting and Exhibit Conference* AIAA 2003-0085.

Schlüter, Jörg., Shankaran, Sriram., Pitsch, Heinz., Kim, Sangho., Moin, Parviz., and Alonso, Juan. 2003b. "Towards Multi-Component Analysis of Gas Turbines by CFD: Integration of RANS and LES Flow Solvers." *Proc. ASME TURBO EXPO 2003* ASME Paper No. GT2003-38350.

Sarpkaya, T. 1996. "Vorticity, free surface, and surfactants." *Annual Review of Fluid Mechanics* 28:83-128.

Schlüter, J. U., Wu, X., Kim, S., Shankaran. S., Alonso, J. J., and Pitsch, H. 2005b. "A Framework for Coupling Reynolds-Averaged With Large-Eddy Simulations for Gas Turbine Applications." *Journal of Fluids Engineering* 127:806-815.

Shankaran, S., Liou, M.-F., Liu, N.-S., Davis, R., and Alonso, J. J. 2001. "A Multi-Code-Coupling Interface for Combustor/Turbomachinery Simulations." *39th AIAA Aerospace Sciences Meeting and Exhibit* AIAA 01-0974

Shu, C. W., and Osher, S. 1988. "Efficient implementation of essentially non-oscillatory shock-capturing schemes." *Journal of Computational Physics* 77:439-471.

Smagorinsky, J. 1963. "General circulation experiments with the primitive equations I. The basic experiment" *Monthly Weather Review* 91:99-164.

Son, J., and Hanratty, T. J. 1969. "Velocity gradients at the wall for flow around a cylinder at Reynolds numbers 5×10^3 to 10^5." *Journal of Fluids Mechanics* 35:353-368.

Stern, F., Bhushan, S., Carrica, P. M., and Yang, J. 2009. "Large scale parallel computing and scalability study for surface combatant static maneuver and straight ahead conditions using CFDShip-Iowa." In *Proc. 21st Int. Conf. Parallel Comput. Fluid Dynamics.*

Suh, Jungsoo., Yang, Jianming., and Stern, Frederick. 2001. "The effect of air-water interface on the vortex shedding from a vertical circular cylinder." *Journal of Fluids and Structures* 27:1-22.

Sussman, M., Smereka, P., and Osher, S. 1988. "A level set approach for computing solutions to incompressible two-phase flow." *Journal of Computational Physics* 114:146-159.

Szepessy, S., and Bearman, P. W. 1992. "Aspect ratio and end plate effects on vortex shedding from a circular cylinder." *Journal of Fluids Mechanics* 234:191-217.

Tritton, D. J. 1959. "Experiments on the flow past a circular cylinder at low Reynolds numbers." *Journal of Fluids Mechanics* 6:547-567.

Warschauer, K. A., and Leene, J. A. 1971. "Experiments on mean and fluctuating pressures of circular cylinders at cross flow at very high Reynolds numbers." In *Proc. Int. Conf. on Wind Effects on Buildings and Structures.*

Williamson, C. H. K. 1996. “Vortex Dynamics in the Cylinder Wake.” *Annual Review of Fluid Mechanics* 28:477-539.

Xu, Sheng. 2008. “The immersed interface method for simulating prescribed motion of rigid objects in an incompressible viscous flow.” *Journal of Computational Physics* 227: 5045-5071.

Xu, Sheng., and Wang, Jane. 2006. “An immersed interface method for simulating the interaction of a fluid with moving boundaries.” *Journal of Computational Physics* 216:454-493.

Yang, J., and Balaras, E. 2006. “An embedded-boundary formulation for large-eddy simulation of turbulent flows interacting with moving boundaries.” *Journal of Computational Physics* 215:12-40.

Yang, Jianming., and Stern, Frederick. 2009. “Sharp interface immersed-boundary/level-set method for wave-body interactions.” *Journal of Computational Physics* 228:6590-6616.

Yu, G., Avital, E. J., and Williams, J. J. R. 2008. “Large eddy simulation of flow past free surface piercing circular cylinders.” *Journal of Fluids Engineering* 130:101304.1-101304.9.

Zhang, L. P., Chang, X. H., Duan, X. P., Wang, Z. Y., and Zhang, H. X. 2009. “A block LU-SGS implicit unsteady incompressible flow solver on hybrid dynamic grids for 2D external bio-fluid simulations.” *Computers & Fluids* 38:290-308.

Zhang, L. P., and Wang, Z. J. 2004. “A block LU-SGS implicit dual time-stepping algorithm for hybrid dynamic meshes.” *Computers & Fluids* 33:891-916.

Zhang, Yaoxin., Jia, Yafei., and Wang, Sam S. Y. 2006. “Structured mesh generation with smoothness controls.” *International Journal for Numerical Methods in Fluids* 51:1255-1276.

Zhang, Yaoxin., Jia, Yafei., and Wang, Sam S. Y. 2012. “An improved nearly-orthogonal structured mesh generation system with smoothness control functions.” *Journal of Computational Physics* 231:5289-5305.

Zdravkovich, M. M. 1997. “Flow Around Circular Cylinders. Fundamentals, vol. 1.” Oxford University Press.